Biopolymer-based smart sensitive composites with functionalized magnetic nanoparticles and their evaluation of biocompatibility

Alberto Varela Feijoo

Université de Paris

Ecole doctorale EDPIF 564

Laboratoire Matière et Systèmes Complexes

Biopolymer-based smart sensitive composites with functionalized magnetic nanoparticles and their evaluation of biocompatibility

Par Alberto Varela Feijoo

Thèse de doctorat de Physique

Dirigée par Alain Ponton

Présentée et soutenue publiquement le 13/12/2021

Devant un jury composé de :

Armelle Baeza, Professeur, Université de Paris, Examinatrice
Philippe Cassagnau, Professeur, Université Claude Bernard Lyon 1, Président
Socorro Castro, Professeur, Université de la Corogne, Rapporteur
Philippe Djemia, Professeur, Université Sorbonne Paris Nord, Examinateur
Dominique Dupuis, Professeur, Université de Mulhouse, Rapporteur
Tetsuharu Narita, Chargé de recherche, CNRS, Examinateur
Alain Ponton, Directeur de recherche, CNRS, Directeur de thèse
Valentina Sirri, Chargée de recherche, CNRS, Membre invitée

Composites intelligents à base de biopolymères avec nanoparticules magnétiques fonctionnalisées et évaluation de leur biocompatibilité

L'objectif de cette thèse est d'élaborer et d'étudier à différentes échelles des matériaux magnéto-stimulables afin de mieux comprendre leurs propriétés en vue d'applications potentielles en ingénierie tissulaire. Nous proposons une méthodologie d'élaboration basée sur des matrices de polymères de différentes natures contentant des nanoparticules magnétiques (NPMs) de maghémite (γ-Fe_2O_3) fonctionnalisées. La stratégie est une méthode *ex-situ* dans laquelle des solutions aqueuses de polymères et des dispersions de NPMs sont préparées séparément puis mélangées avant une réticulation pour élaborer des hydrogels nanocomposites. Les NPMs de maghémite synthétisées sont hautement cristallines et fonctionnalisées soit par greffage covalent avec un double ligand (l'acide 3-Aminopropylphophonique) portant une charge positive par ionisation d'une fonction amine soit par adsorption d'ion citrate chargé négativement. Deux polymères ont été choisis, l'un neutre, l'alcool polyvinylique, l'autre de nature polyélectrolyte avec une charge négative, l'alginate de sodium. Leur conformation en solution aqueuse a tout d'abord été étudiée afin de déterminer la gamme de concentration pour laquelle la taille de maille est similaire à celle des NPMs synthétisées. L'élaboration des nanocomposites a ensuite été réalisée par la dispersion des NPMs dans des solutions de polymères enchevêtrés conduisant à différentes microstructures, soit la formation d'agrégats dus aux interactions électrostatiques attractives entre les chaines de polymères et les NPMs, soit la formation de gouttelettes de démixtion. L'étude de l'effet de l'application d'un champ magnétique continu sur les propriétés mécaniques des nanocomposites en lien avec les microstructures induites a montré l'importance du rôle des interactions chaines de polymères - NPMs. Les hydrogels de nanocomposites magnétiques finaux ont ensuite été élaborés par la réticulation de ces solutions de nanocomposites en développant une méthodologie pour moduler la cinétique de la transition sol-gel et leurs propriétés mécaniques et structurelles finales en modifiant le degré de réticulation des réseaux de polymères et par l'application d'un champ magnétique. Enfin, les nanocomposites magnétiques élaborés ont été évalués par des études de viabilité cellulaire *in vitro* sur des fibroblastes par le test WST-1 identifiant les conditions expérimentales les plus prometteuses pour leur application potentielle en ingénierie tissulaire.

Mots clefs: hydrogel, nanoparticules, polymère, composite, magnétorhéologie, biocompatibilité, viscoélasticité.

Biopolymer-based smart sensitive composites with functionalized magnetic nanoparticles and their evaluation of biocompatibility

The aim of this PhD is to elaborate and to study at different scales magnetic sensitive materials to progress in the understanding of soft sensitive composites with potential applications in tissue engineering. For such purpose, we propose a methodology of elaboration consisting in the combination of polymer matrices of different natures with functionalized magnetic nanoparticles (MNPs) of maghemite (γ-Fe_2O_3) by an *ex-situ* method in which aqueous polymer solutions and MNPs dispersions are separately prepared and then mixed followed by the crosslinking to elaborate nanocomposite hydrogels. The synthetized maghemite MNPs are highly crystalline and surface functionalized either by covalent grafting of double ligand (3-Aminopropylphosphonic acid) bearing a positive charge due to the ionization of amino group or by the adsorption of citrate ions negatively charged. Two polymers have been selected, one of neutral nature (polyvinyl alcohol) and the other one which is a polyelectrolyte (sodium alginate) with a negative charge. Their conformation in aqueous solution has been firstly studied to determine the range of concentrations for which the mesh size is similar to the size of the synthetized MNPs. The elaboration of nanocomposites is firstly carried out by the dispersion of MNPs in entangled polymer solutions leading to different microstructures, either the formation of aggregates due to the attractive electrostatic interactions between the individual components or the formation of droplets of demixion originated by colloidal forces. The study of the effect of an applied magnetic field on the mechanical properties in relation with microstructures of the nanocomposites has underlined the key role of the interactions between polymer chains and MNPs. The final magnetic nanocomposite hydrogels have been then elaborated by the crosslinking of those nanocomposite solutions developing a methodology to modulate the kinetics of the sol-gel transition and their final mechanical and structural properties by varying the crosslinking degree of the polymer networks and by the application of a magnetic field. Finally, the elaborated magnetic nanocomposites have been evaluated by *in vitro* cell viability studies in fibroblast NIH-3T3 by the WST-1 assay identifying the more promising experimental conditions for their potential application in tissue engineering.

Keywords: hydrogel, nanoparticles, polymer network, composite, magnetorheology, biocompatibility, viscoelasticity.

Composites intelligents à base de biopolymères avec nanoparticules magnétiques fonctionnalisées et évaluation de leur biocompatibilité

L'objectif de cette thèse est d'élaborer et d'étudier à différentes échelles des matériaux magnéto-stimulables afin de mieux comprendre leurs propriétés mécaniques en lien avec leur microstructure. Nous proposons une méthodologie d'élaboration basée sur des matrices de polymères de différentes natures contentant des nanoparticules magnétiques (NPMs) de maghémite (γ-Fe_2O_3) fonctionnalisées. La stratégie d'élaboration développée consiste en une méthode *ex-situ* dans laquelle des solutions aqueuses de polymères et des dispersions aqueuses de NPMs sont préparées séparément puis mélangées avant une gélification pour élaborer des hydrogels nanocomposites.

Les premières étapes de la thèse sont focalisées sur les deux composants individuels, les NPMs et les solutions de polymères. Deux types de NPMs de maghémite sont obtenus suivant deux voies de synthèse, la méthode des polyols et la méthode de coprécipitation. Ensuite les NPMs obtenus par la méthode des polyols ont été greffées de manière covalente par un double ligand (l'acide 3-Aminopropylphosphonique (APPA)) portant une charge de surface positive (APPA-NPMs). Tandis que les NPMs obtenus pas coprécipitation ont été stabilisées par adsorption d'ions citrate portant une charge négative (NPMs-citratées). Les propriétés structurales et morphologiques des deux types de NPMs ont été étudiées par diffraction de rayons X, spectroscopie Infra Rouge à transformée de Fourier, spectrométrie de photoélectrons induits par rayons X, microscopie électronique, analyse thermogravimétrique et analyse thermique différentielle. Leur stabilité en dispersion aqueuse a été évaluée par mesure du rayon hydrodynamique et du potentiel zêta et leur propriétés magnétiques ont été quantifiées avec un magnétomètre à échantillon vibrant. Les deux types de particules sont cristallines, sphériques avec une taille nanométrique (diamètre de l'ordre de 10 nm) et superparamagnétiques sans coercivité. Les APPA-NPMs ont une distribution en taille plus uniforme mais ont tendance à former des agrégats en dispersion aqueuse contrairement aux NPMs-citratées. Ceci est un inconvénient important pour obtenir une dispersion aqueuse homogène d'APPA-NPMs à mélanger avec la matrice polymérique dans des conditions neutres pour élaborer des nanocomposites. En conséquence, les NPMs-citratées ont été retenues pour la suite de l'étude.

Pour choisir la matrice avec les propriétés les plus appropriées pour l'élaboration de nanocomposites, nous avons d'abord étudié quatre polymères hydrosolubles, biocompatibles, biodégradables et pouvant former des gels (alginate de sodium, gélatine, alginate diAldheyde (ADA) et Poly(VinylAlcohol) (PVA)). Une méthodologie expérimentale a été développée pour

préparer des solutions aqueuses des quatre polymères de manière reproductible permettant de contrôler précisément leurs propriétés. Ensuite, des films polymères ont été préparés afin d'identifier les principaux groupes chimiques des chaînes polymères par spectroscopie infrarouge à transformée de Fourier qui peuvent servir de base à la caractérisation ultérieure des nanocomposites. La mesure du potentiel zêta dans des solutions de polymères diluées permet de confirmer le comportement de polyélectrolyte anionique de l'alginate de sodium et de l'ADA, un comportement de polyélectrolyte cationique faible de la gélatine et un comportement neutre du PVA. Ces différents comportements sont très importants, non seulement pour l'interprétation de la conformation du polymère en solution, mais aussi pour les éventuelles interactions particules-polymère dans l'élaboration ultérieure des nanocomposites. Une étude complète de l'écoulement rhéologique a été réalisée afin de déterminer les trois régimes de concentration : dilué, semi-dilué et concentré. La viscosité intrinsèque [η] a été déterminée par les méthodes de Huggins et Kraemer dans le régime dilué en déduisant la masse moléculaire moyenne par l'équation de Mark-Houwink. La faible valeur de [η] pour la gélatine et le PVA a suggéré une conformation compacte en solution aqueuse. Au contraire, la valeur plus élevée de [η] pour l'alginate de sodium a confirmé la rigidité de la chaîne et la forte répulsion électrostatique entre les monomères qui conduisent à une conformation étendue en solution aqueuse. Cependant, [η] diminue lorsque l'alginate de sodium est oxydé en ADA, ce qui s'explique par la scission de la chaîne et la rupture des liaisons C-C entre les carbones 2 et 3. Des mesures d'écoulement ont été effectuées dans des solutions aqueuses de PVA et d'alginate de sodium dans le régime concentré, révélant un comportement rhéofluidifiant lié à l'enchevêtrement/désenchevêtrement des chaînes de polymère. Cette étude complète permet de mieux comprendre la microstructure des solutions aqueuses de polymères de différentes natures. Même si aucune différence importante n'a été trouvée entre les masses moléculaires, les différences dans la rigidité de la chaîne et les interactions entre les monomères conduisent à des conformations différentes qui changent radicalement leurs propriétés. L'application potentielle pour l'élaboration de nanocomposites requiert des solutions polymères avec une viscosité modérée avec des enchevêtrements entre les chaînes qui permettent de créer un réseau dans lequel les NPMs sont stables. Pour cette raison, les solutions d'ADA et de gélatine ont été écartées pour l'élaboration de nanocomposites en raison de leur conformation compacte et de leur faible viscosité même à des concentrations élevées, ce qui a ainsi conduit à choisir l'alginate de sodium et le PVA pour la matrice polymère.

En plus, une étude multi-échelle a été réalisée dans les solutions aqueuses d'alginate de sodium pour mieux comprendre sa microstructure dans le régime semi-dilué et concentré. Une

caractérisation viscoélastique complète de ces matériaux a été obtenue sur une large gamme de fréquences, allant de 10^{-2} à 10^{5} Hz par une combinaison des résultats de la macrorhéologie et de la microrhéologie avec une très bonne continuité entre les résultats obtenus à partir des deux techniques. La longueur de persistance des chaînes d'alginate a été déterminée en fonction de la concentration à partir des mesures de microrhéologie par l'identification de la fréquence caractéristique correspondant à la transition entre un comportement suivant le mode de flexion et le mode de Zimm-Rouse. La dépendance en concentration de la viscosité et du module de compressibilité dans le domaine GHz a également été déterminée à partir des spectres obtenus par diffusion Brillouin. Des expériences complémentaires de diffusion des rayons X aux petits angles ont été également réalisées pour sonder directement les propriétés structurelles. L'évolution de l'intensité diffusée en fonction du vecteur d'onde q montre un comportement de loi de puissance pour les valeurs élevées de q. L'exposant obtenu suggère une conformation de pelote statistique due à l'écrantage de charge par comparaison avec les valeurs théoriques de l'approche statistique de la physique des polymères pour une large gamme de concentrations (4-32 g/L). De plus, le facteur de structure S(q) montre clairement des maxima à partir desquels la taille de la maille de la solution enchevêtrée peut être déduite. En conclusion, il a été confirmé que la taille caractéristique (taille de la maille et longueur de persistance) des solutions aqueuses d'alginate de sodium enchevêtrées est du même ordre de grandeur que la taille des NPMs déterminée précédemment (~10 nm).

Ensuite, des hydrogels d'alginate de calcium ont été élaborés par réticulation ionique de l'alginate de sodium avec deux sources différentes de Ca^{2+} (complexe de $CaCl_2$-EDTA et carbonate de calcium) conduisant à une matrice tridimensionnelle avec des zones de jonction de structure en boîte à œufs. La libération des ions Ca^{2+} est obtenue par l'ajout de glucono-delta-lactone (GDL) induisant une diminution du pH. En plus, des hydrogels de PVA avec des zones cristallines ont été élaborés par cycles de congélation-décongélation des solutions aqueuses de PVA. L'étude de la transition sol-gel des hydrogels d'alginate de calcium a été réalisée par spectroscopie mécanique à résolution temporelle (SMRT). Il a été montré que la cinétique de la transition sol-gel (temps de gélification t_g) et les propriétés des hydrogels critiques à t_g (la « force » du gel S et l'exposant de relaxation Δ.) peuvent être modulées par le rapport molaire entre le calcium ajouté et les groupes carboxylates ($R_{Ca} = [Ca^{2+}]/[COO^-]$) et la source de calcium utilisée. Le $CaCO_3$ conduise à des gels plus rigides et des cinétiques plus rapides. Ceci est confirmé par les mesures du module Young obtenue par compression uniaxiale. L'étude du gonflement montre deux comportements différents après l'immersion des hydrogels totalement gélifiés dans l'eau pure. Pour les hydrogels d'alginate de calcium, la

pénétration de l'eau dans le réseau entraîne un allongement des chaînes polymères et donc une rigidification du réseau. Pour les hydrogels de PVA l'adsorption de l'eau conduit à une diminution de la réticulation physique et la dissolution des chaînes ne participant pas à la formation des cristallites mais ces deux effets deviennent négligeables si le nombre de cycles de congélation-décongélation est suffisant. La raideur mécanique et la porosité sont corrélées avec le degré de réticulation.

Dans un premier temps, trois solutions nanocomposites ont été préparées et étudiées par l'introduction de NPMs de maghémite soit greffées avec le double ligand APPA(APPA-NPMs) soit stabilisées par adsorption d'ions citrate (NPMs-citratées) dans une solution de polyélectrolyte chargé négativement (alginate de sodium) et par l'introduction des NPMs-citratées dans une solution de polymère neutre (PVA). L'étude des propriétés d'écoulement, viscoélastiques et structurelles des différents nanocomposites met en évidence l'importance des interactions polymère-particules et les relations entre la microstructure et renforcement magnéto-induite des propriétés viscoélastiques. Pour les trois nanocomposites étudiés, nous avons montré que l'introduction de NPMs dans des solutions de polymères conduit à des nanocomposites homogènes à l'échelle macroscopique alors qu'ils sont non homogènes à l'échelle microscopique avec la formation de gouttelettes sphériques de démixtion pour les NPMs-citratées ou d'agrégats entre chaînes de polymères et NPMs pour les NPMs-APPA. Ceci pourrait s'expliquer par la modification de la force ionique due aux ions libres citratés non absorbés à la surface des NPMs ou par des attractions électrostatiques entre les NPMs-APPA chargées positivement et les chaînes d'alginate de sodium chargées négativement respectivement. L'étude combinée des mesures rhéologiques et de l'observation optique dans une cellule de magnéto-opto-rhéologie développée au laboratoire de Matière et Systèmes Complexes permet d'analyser les résultats d'écoulement et viscoélastiques sous champ magnétique. Dans les domaines viscoélastiques linéaires ou à faible taux de cisaillement, des modifications structurelles produits sous l'application de champ magnétique induisent un renforcement des propriétés mécaniques. D'une part les gouttelettes sphériques de démixtion s'allongent de manière réversible dans la direction du champ magnétique appliqué pour les nanocomposites avec NPMs-citratées. D'autre part les agrégats entre chaînes de polymères et particules deviennent plus compacts et s'orientent perpendiculairement au cisaillement pour les nanocomposites avec les NPMs-APPA. Lorsque les contraintes ou les taux de cisaillement augmentent, ces microstructures s'orientent progressivement dans la direction du cisaillement avant de se rompre car l'effet du taux de cisaillement prédomine sur celui du champ magnétique. En tenant compte du fait que la réversibilité de la microstructure induite par le champ devrait

être plus favorable que la dispersion d'agrégats polydisperse dans des solutions de polymères pour élaborer des hydrogels nanocomposites, les solutions aqueuses d'alginate de sodium ou de PVA incorporant les NPMs-citratées sont retenues pour l'étude des hydrogels magnétiques. La principale différence trouvée entre ces deux types de solutions de nanocomposite est la distribution en taille des gouttelettes de démixtion avec un diamètre moyenne de 3.3 μm dans l'alginate de sodium et de 8.5 μm dans le PVA.

La modulation des propriétés finales des hydrogels magnéto-stimulables a été obtenue par l'étude de différents paramètres expérimentaux. L'effet de l'introduction de NPMs citratées sur la transition sol-gel des hydrogels d'alginate de calcium a été étudié par SMRT mettant en évidence un ralentissement notable de la cinétique pour les deux sources de calcium utilisées (complexe de $CaCl_2$-EDTA et carbonate de calcium). De plus, des gels critiques plus mous et un module d'élasticité plus élevé aux temps longs (G'_∞) en présence de NPMs citratées conduisent à poursuivre l'élaboration des hydrogels magnétiques avec le carbonate de calcium. Ensuite, l'effet d'un champ magnétique appliqué sur la transition sol-gel est étudié par SMRT pour la première fois en montrant qu'il permet de moduler les propriétés viscoélastiques avant le point de gel mais pas la cinétique de la transition sol-gel et les propriétés structurelles de l'hydrogel critique puisqu'ils dépendent des caractéristiques du réseau formé. De plus, l'étude mécanique et structurale des hydrogels magnéto-stimulables d'alginate de calcium et de PVA à l'état totalement gélifié permet de corréler l'effet de l'introduction de NPMs citratées sur les propriétés mécaniques et structurales. Les résultats obtenus des modules viscoélastiques (G' et G'') en fonction de la déformation à une fréquence de 1Hz ainsi que les déformations critiques correspondant respectivement à la limite du domaine linéaire et au maximum de G'' montrent deux effets différents lorsque des NPMs citratées sont introduites. Nous avons ainsi observé une diminution de la rigidité et du degré de réticulation dans les réseaux d'alginate de calcium alors que des réseaux plus rigides sont obtenus avec le PVA en raison des interactions polymère-particules dues à des liaisons hydrogène entre les chaînes PVA et les NPMs-citratées. Ces résultats sont confirmés par la mesure des modules en compression uniaxiale. La cinétique de gonflement est plus rapide pour les nanocomposites gélifiés à base d'alginate, comparés au PVA. L'ajout des NPMs-citratées à la matrice polymère conduit à une augmentation du degré de gonflement à l'équilibre dans le cas de l'alginate de calcium contrairement au PVA. Cet effet est associé à un plus faible degré de réticulation dans le cas de l'alginate de calcium favorisant l'absorption d'eau. Ceci est confirmé par la forte augmentation du module de compression des hydrogels totalement gonflés. Cette augmentation est relativement faible dans le cas du PVA du fait d'une plus grande rigidité du réseau au départ.

Finalement, la biocompatibilité des nanocomposites magnétiques élaborés et étudiés dans les chapitres précédents a été évaluée par des études de viabilité cellulaire *in vitro* avec les fibroblastes NIH-3T3 par le test WST-1. A partir de la mise en place de protocoles expérimentaux très stricts ainsi qu'une analyse statistique des résultats, la biocompatibilité est caractérisée par la viabilité des cellules, comparée à des échantillon témoins traités avec du milieu de culture. Les résultats ont confirmé la biocompatibilité de l'alginate de sodium et un effet cytotoxique modéré des NPMs citratées. Lorsque les NPMs sont dispersées dans la solution d'alginate, la viabilité des cellules augmente et n'est pas significativement différente de celle du témoin. Cet effet est attribué à une diffusion limitée des particules dans une matrice polymère de viscosité relativement élevée. Ce n'est pas le cas du PVA qui, de ce fait, ne contribue pas à réduire la cytotoxicité des NPMs mais semble au contraire l'augmenter. Pour les hydrogels nanocomposites, la cytotoxicité semble être bloquée par enrobage des NPMs par des chaînes de PVA. Par contre, dans le cas de l'alginate, il faut recourir à une augmentation du degré de réticulation afin de limiter la relargage des NPMs en dehors des hydrogels nanocomposites.

Acknowledgments

I would first like to thank my supervisor, Alain Ponton, for welcoming me in the laboratory Matière et Systèmes Complexes (MSC) as well as for his help and guidance. His expertise was indispensable in formulating the research questions, methodology and the presentation of the results. I would also like to thank my colleagues of the MSC laboratory with a special mention to the PhD students with whom I worked more closely, Yu Lei and Souhmia Ikhaddalene. The positive feedback between us was a very strong support for solving the little daily difficulties. I would also like to acknowledge Véronique Thévenet for her support in the experimental chemistry work and Arnaud Grados, Williams Brett Mathieu Receveur and Laurent Rea for their expertise in the development of the magneto-opto-rheological cell essential for this PhD.

I wish to offer my profound thanks to my PhD referees (Socorro Castro and Dominique Dupuis) for accepting to spend their precious time to evaluate my PhD manuscript as well as the other members of the committee.

I would like to acknowledge my colleagues from the ITODYS laboratory for their collaboration and good advices in the synthesis and characterization of nanoparticles. I would particularly like to single out Walid Mnasri, Nancy Flores-Martinez and Alexandre Chevillot for all their support in the experimental work and the group leader Souad Ammar-Merah.

I would like to acknowledge the fantastic collaboration in the different laboratories where I have developed important parts of the experimental work of this PhD. Tetsuharu Narita (École supérieure de physique et de chimie industrielles de la ville de Paris) initiates me to microrheology in order to investigate the viscoelastic properties of the polymer solutions at small scales. Philippe Djemia (Laboratoire des Sciences des Procédés et des Matériaux) introduces me to the Brillouin spectroscopy and opens me the doors of his laboratory even when Paris looks like a desert.

I am also thankful to the colleagues of the laboratory Biologie Fonctionnelle Adaptative, Armelle Baeza for her good advices and Valentina Sirri to initiate me in the world of the cell viability and for her valuable guidance throughout the experimental studies. You provided me with the tools that I needed to choose the right direction and to complete successfully the last chapter of this PhD.

I want also to thank Philippe Pignon and Florent Carn to open the opportunity to perform small-angle X-ray measurements in the Synchrotron SOLEIL and the European Synchrotron Radiation Facility.

I would like also to acknowledge the fantastic collaboration with the colleagues of the Centre of Nanotechnology and Tissue Engineering of the Photobiology and Photomedicine research Group (São Paulo University). I would particularly like to single out the group leader Antonio Tedesco, for inviting me to do a short stage in his laboratory and for all the good advises to expand the scope of this PhD and Maryanne Trafani for all the explanations about the experimental work.

In addition, I would like to thank my parents for their support throughout my life. Their provision of emotional and financial support has allowed me to accomplish tasks that would have otherwise been impossible.

Finally, I could not have completed this dissertation without the support of my Galician friends, who provided me happy distractions to rest my mind outside of my research in every moment that I was able to return to this little piece of heaven on earth. I would particularly like to single out those who have already gone through the experience of a PhD paving the way with their great advice.

Summary

Introduction

Hydrogels are an interesting class of materials formed when a three-dimensional polymer network is crosslinked and swollen by water but without dissolving in it [1]. Both synthetically prepared and natural derived polymers are used to prepare hydrogels with a common characteristic, the hydrophilicity that permits a high degree of water absorption. They can be classified depending on the crosslinking method in reversible (physical crosslinking) and irreversible (chemical crosslinking). Some examples reported in the literature to prepare physically crosslinked hydrogels [2] include heating or cooling a polymer solution, ionic interactions, hydrogen bonding or freezing-thawing cycles. The chemical crosslinking involves the formation of covalent bonds either during polymerization of monomers or crosslinking of polymer precursors. The biocompatibility of hydrogels, their capability to retain water similarly to natural tissues and to form different shapes make them widely used in biomedical applications [3] such as tissue engineering [4], drug delivery [5] and extracellular matrices for biological studies [6].

However, some of these biomedical applications are currently limited due to the poor mechanical properties and insufficient adhesion of hydrogels [7]. Thus, different strategies have been explored to design hydrogels with enhanced mechanical properties such as the development of new methods of chemical and physical crosslinking [8] or the elaboration of double network hydrogels [9]. Another proposed alternative is the introduction of fillers to elaborate hydrogel composites with reinforced mechanical properties. The size of filler materials has a profound effect on the resulting properties of the composite. This is because surface interactions with the matrix, adhesion, particle motion, dispersion, bonding, etc., increase with decrease in filler size making the choice of nanofillers a promising approach. More precisely, the assembly of inorganic nanofillers in hydrogel matrices to elaborate hybrid nanocomposites has become increasingly attractive in recent years [10]. When the two components are placed together, the polymer can interact with the nanofiller and behaves as though it is part of them (Figure 1), leading to the increase in the apparent volume fraction and, thus, increasing the mechanical properties of the nanocomposite [11]. Thus, these inorganic nanofillers can induce new and unique properties not only by their own related nanoscale properties but also due to the nanoscale interfacial interactions between the organic matrix and the inorganic filler [11]. In addition to the enhancement of the mechanical properties, some

non-conventional properties can be achieved in those hybrid nanocomposites such as barrier properties [12–14], electrical and magnetic properties [15,16], thermal properties [17,18] and shape-memory properties [19,20]. There are different key points for the development of such nanocomposites: the chemical nature, concentration, type and surface modification of nanofillers the properties of the organic matrix and the way they are mixed and possibly linked, and the dispersion that is finally obtained [21].

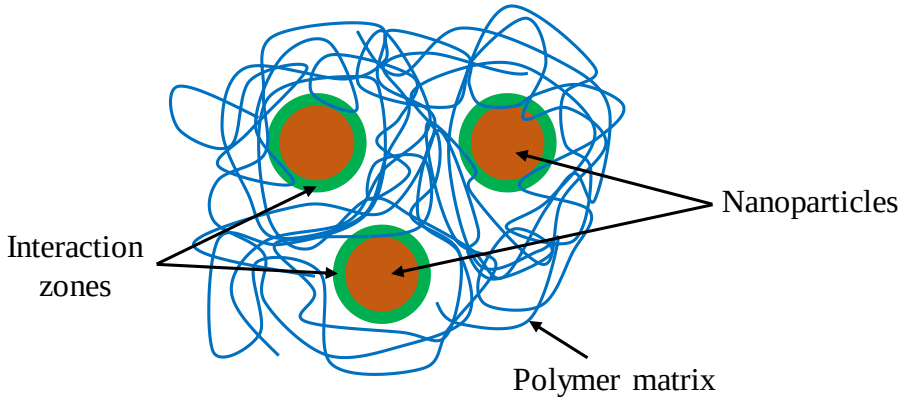

Figure 1: importance of interactions in the final properties of hybrid nanocomposites.

The special features of nanofillers are sustained in the fact that when the dimensions of a material are reduced (typically below 100 nm) dramatic alterations may occur in their properties [29] based on the dominance of size confinement, distribution and morphology, interfacial phenomena and quantum effects [30]. Nanofillers can be classified accordingly with different parameters. Regarding the shape, they are commonly classified in zero- one- or two-dimensional (0D, 1D, 2D) [22]. In 0D nanomaterials all the dimensions are measured within the nanoscale. Most commonly 0D nanomaterials are nanoparticles, nanocrystals and quantum dots. In 1D nanomaterials, one dimension is outside the nanoscale. This class includes nanotubes, nanorods, and nanowires. In 2D nanomaterials, two dimensions are outside the nanoscale. This class exhibits plate-like shapes and includes nanofilms, nanolayers, and nanocoatings. Nanofillers can be also classified depending on the chemical composition in: (1) metal [23], such as gold, iron, silver with unusual chemical, optical, and electrical properties as compared to bulk materials; (2) metal oxides [24] including titanium oxide (TiO_2), silicon (SiO_2), iron oxide (Fe_2O_3 and Fe_3O_4), zinc oxide (ZnO), gallium oxide (Ga_2O_3), nickel oxide (NiO) and copper oxide (CuO) with interesting electrical, magnetic, mechanical, optical and catalytic properties; (3) carbon-based [25] with outstanding mechanical and electrical properties; (4) bimetallic [26] with a variety of properties due to the synergistic effect created when two different metals are combined; (5) zeolite and silica-based [27] widely used for catalysis and gas absorption due to their favourable surface chemistry and mesoporous

structure; (6) ceramic [28] made up of oxides, carbides, phosphates and carbonates of metals and metalloids with high heat resistance and chemical inertness extensively used in biomedicine for bone tissue engineering and (7) semiconductors such as quantum dots with size and composition-dependent optoelectrical properties.

Another important feature is the selected methodology to elaborate the nanocomposite, that can be classified in two main groups: compounding *ex-situ* methods [31], in which nanofillers and organic matrix are separately prepared and then mixed, and *in-situ* methods [32], in which the synthesis of the nanofillers is carried out using the organic matrix as support. The advantage of the *in-situ* methods is that they allow a one-step elaboration preventing particle agglomeration while maintaining a good spatial distribution in the polymer matrix. However, for *ex-situ* methods, the individual preparation of both components gives more flexibility in their synthesis controlling better their morphology and physicochemical properties.

Depending on the elaboration conditions, the particle shape and the affinity between constituents, different morphologies can be obtained. For 0D and 1D nanomaterials, three arrangements can be observed, *i.e.* (i) well-dispersed, (ii) agglomerated, or (iii) percolating systems [12]. A very promising methodology is the control of the microstructure of the elaborated nanocomposites based on noncovalent interactions between the individual components, such as electrostatic forces, hydrogen bonding, van der Waals or hydrophobic forces. Thus, the state of the nanofiller dispersion is controlled by the filler-filler and filler-polymer interactions inducing a self-assembling into the energetically most favourable system. For a better control of these interactions, nanofillers are commonly functionalized with ligands and either dispersed in a solution with the hydrogel precursor followed by the crosslinking or precipitated after the synthesis of the hydrogel [33]. For all the strategies to control the interactions and the microstructure of the nanocomposites, the synthesis and elaboration of the individual components with the desired physicochemical properties are key steps including the functionalization of the nanofillers, the study of the polymer conformation in aqueous solution and the sol-gel transition during the crosslinking to elaborate hydrogels.

An important class of these nanocomposites aims to integrate the specific characteristics of each individual component into stimuli-responsive nanocomposites [34]. They can significantly change their properties such as shape, mechanical properties, phase separation, surface, permeability, optical properties, and electrical properties upon small variation of environmental conditions such as temperature, electric field, pH, light, magnetic field, solvent, ions, enzymes and glucose [19]. The case of the combination of magnetic nanoparticles (MNPs)

and hydrogels is of particular interest for the development of magnetic-sensitive nanocomposites with rapid response time [35], high penetration and low invasiveness [36] compared to other external stimuli-sensitive materials making them ideal candidates for a lot of biomedical applications [37].

MNPs with sizes below 15 nm exhibit superparamagnetic activities [38] and even after being introduced in the polymer matrices, the magnetic moment of each MNP will align in the direction of an applied magnetic field. By merging these superparamagnetic properties of MNPs and mechanical properties of a biocompatible polymer matrix, one can obtain magnetic responsive nanocomposites with potential biomedical applications [37]. One of the advantages is that biological tissues are much more transparent to magnetic fields than to electric fields [39] without a destructive effect on living tissues [40]. These nanocomposites can be then deformed in a controlled manner in homogeneous fields or gradients, used for magnetic guidance of drug delivery systems [41,42] or remotely activated using alternating magnetic fields to locally heat-up the regions in the proximity of MNPs [43], and for actuators with shape memory effect [19,44]. If a lot of studies are concerned by the synthesis of MNPs and their use as nanofillers in polymer matrices, there is to our knowledge no investigation in which interactions between MNPs and polymer chains are modulated with a complete study of the mechanical properties at different stages during the elaboration of the nanocomposite hydrogels.

The general objective of this PhD project is focused on the elaboration and study at different scales of magnetic sensitive materials to progress in the understanding of soft sensitive composites by linking properties of the MNPs, their interaction with the polymer chains, mechanical and structural properties of nanocomposites and the evaluation of their biocompatibility. For this purpose, we propose a methodology to elaborate magnetic nanocomposites combining neutral and polyelectrolyte polymer matrices with functionalized MNPs of maghemite (γ-Fe_2O_3). The selected strategy for their elaboration is an *ex-situ* method in which aqueous polymer solutions and MNPs dispersions are separately prepared and then mixed followed by the crosslinking to elaborate nanocomposite hydrogels. In these conditions, the MNPs-MNPs and polymer-MNPs interactions play a key role in the microstructure and therefore in the properties of the obtained nanocomposites. Then viscoelastic and structural properties are studied combining several complementary methods before the evaluation of their biocompatibility. The manuscript is divided in six chapters:

Chapter I: synthesis and characterization of magnetic nanoparticles (MNPs)

A co-precipitation and a polyol route are used for the synthesis of maghemite MNPs. These later are then functionalized either by adsorption of ions or by grafting double ligands to obtain positively and negatively charged MNPs who can interact with the polymer matrix of the nanocomposites. The functionalized MNPs are characterized by different techniques to investigate their composition and crystallinity, their magnetic properties and their stability in aqueous colloidal dispersions.

Chapter II: polymer solutions

Neutral and polyelectrolyte polymers (sodium alginate, polyvinyl alcohol (PVA), gelatin and alginate dialdehyde) are first chosen as organic matrix of the nanocomposites. A study of their viscoelasticity and structural properties in aqueous solution is performed to select the best candidates depending on the interactions with the MNPs.

Chapter III: polymer hydrogels

Two crosslinking methodologies are developed to elaborate hydrogels from the sodium alginate and PVA solutions based on a crosslinking with calcium and a freezing-thawing method respectively. The effect of the amount of calcium and the number of freezing-thawing cycles are studied to control the crosslinking density, the sol-gel transitions and the structural and mechanical properties of the gelled samples in order to determine the more favourable conditions for the elaboration of nanocomposites.

Chapter IV: magnetic nanocomposite solutions

Nanocomposites prepared by the dispersion of MNPs in entangled polymer solutions with different electrostatic affinities between them are studied macroscopically with an opto-magneto-rheological cell. The formation of different microstructures leading to different magnetic behaviours are identified and characterized for the different alternatives including the dispersion of either positively or negatively charged MNPs in an entangled negatively charged sodium alginate solution and the dispersion of negatively charged MNPs in an entangled neutral PVA solution.

Chapter V: magnetic nanocomposite hydrogels

The two methodologies for the elaboration of hydrogels proposed in chapter III are applied for the crosslinking of the most promising nanocomposite solutions studied in the chapter IV. The effect of the volume fraction of MNPs and the application of a continuous magnetic field during the sol-gel transition is studied by time-resolved mechanical spectroscopy

(TRMS) as well as the final mechanical and structural properties of the nanocomposite hydrogels.

Chapter VI: biocompatibility of nanocomposites

The first evaluation of the biocompatibility of the nanocomposites is carried out by cell viability tests in fibroblast NIH-3T3 for the individual components and for nanocomposites in solution and hydrogel states.

References

[1] J. Jagur-Grodzinski, Polymeric gels and hydrogels for biomedical and pharmaceutical applications, Polym. Adv. Technol. 21 (2010) 27–47. https://doi.org/10.1002/pat.1504.

[2] M. Djabourov, K. Nishinari, S.B. Ross-Murphy, Physical Gels from Biological and Synthetic Polymers, Cambridge University Press, Cambridge, 2013. https://doi.org/10.1017/CBO9781139024136.

[3] Q. Chai, Y. Jiao, X. Yu, Hydrogels for Biomedical Applications: Their Characteristics and the Mechanisms behind Them, Gels. 3 (2017) 6. https://doi.org/10.3390/gels3010006.

[4] S. Van Vlierberghe, P. Dubruel, E. Schacht, Biopolymer-Based Hydrogels As Scaffolds for Tissue Engineering Applications: A Review, Biomacromolecules. 12 (2011) 1387–1408. https://doi.org/10.1021/bm200083n.

[5] T.R. Hoare, D.S. Kohane, Hydrogels in drug delivery: Progress and challenges, Polymer. 49 (2008) 1993–2007. https://doi.org/10.1016/j.polymer.2008.01.027.

[6] M.W. Tibbitt, K.S. Anseth, Hydrogels as extracellular matrix mimics for 3D cell culture, Biotechnol. Bioeng. 103 (2009) 655–663. https://doi.org/10.1002/bit.22361.

[7] J. Xiang, L. Shen, Y. Hong, Status and future scope of hydrogels in wound healing: Synthesis, materials and evaluation, Eur. Polym. J. 130 (2020) 109609. https://doi.org/10.1016/j.eurpolymj.2020.109609.

[8] W.E. Hennink, C.F. van Nostrum, Novel crosslinking methods to design hydrogels, Adv. Drug Deliv. Rev. 64 (2012) 223–236. https://doi.org/10.1016/j.addr.2012.09.009.

[9] Q. Chen, H. Chen, L. Zhu, J. Zheng, Fundamentals of double network hydrogels, J. Mater. Chem. B. 3 (2015) 3654–3676. https://doi.org/10.1039/C5TB00123D.

[10] C. Sanchez, B. Julián, P. Belleville, M. Popall, Applications of hybrid organic–inorganic nanocomposites, J. Mater. Chem. 15 (2005) 3559–3592. https://doi.org/10.1039/B509097K.

[11] J. George, H. Ishida, A review on the very high nanofiller-content nanocomposites: Their preparation methods and properties with high aspect ratio fillers, Prog. Polym. Sci. 86 (2018) 1–39. https://doi.org/10.1016/j.progpolymsci.2018.07.006.

[12] C. Wolf, H. Angellier-Coussy, N. Gontard, F. Doghieri, V. Guillard, How the shape of fillers affects the barrier properties of polymer/non-porous particles nanocomposites: A review, J. Membr. Sci. 556 (2018) 393–418. https://doi.org/10.1016/j.memsci.2018.03.085.

[13] T.-S. Chung, L.Y. Jiang, Y. Li, S. Kulprathipanja, Mixed matrix membranes (MMMs) comprising organic polymers with dispersed inorganic fillers for gas separation, Prog. Polym. Sci. 32 (2007) 483–507. https://doi.org/10.1016/j.progpolymsci.2007.01.008.

[14] H. Cong, M. Radosz, B.F. Towler, Y. Shen, Polymer–inorganic nanocomposite membranes for gas separation, Sep. Purif. Technol. 55 (2007) 281–291. https://doi.org/10.1016/j.seppur.2006.12.017.

[15] G. Gorrasi, E. Piperopoulos, M. Lanza, C. Milone, Effect of morphology of the filler on the electrical behaviour of poly(l-lactide) nanocomposites, J. Phys. Chem. Solids. 74 (2013) 1–6. https://doi.org/10.1016/j.jpcs.2012.08.006.

[16] F. Ridi, M. Bonini, P. Baglioni, Magneto-responsive nanocomposites: Preparation and integration of magnetic nanoparticles into films, capsules, and gels, Adv. Colloid Interface Sci. 207 (2014) 3–13. https://doi.org/10.1016/j.cis.2013.09.006.

[17] C. Huang, X. Qian, R. Yang, Thermal conductivity of polymers and polymer nanocomposites, Mater. Sci. Eng. R Rep. 132 (2018) 1–22. https://doi.org/10.1016/j.mser.2018.06.002.

[18] S.N. Leung, Thermally conductive polymer composites and nanocomposites: Processing-structure-property relationships, Compos. Part B Eng. 150 (2018) 78–92. https://doi.org/10.1016/j.compositesb.2018.05.056.

[19] H. Meng, G. Li, A review of stimuli-responsive shape memory polymer composites, Polymer. 54 (2013) 2199–2221. https://doi.org/10.1016/j.polymer.2013.02.023.

[20] W. Wang, Y. Liu, J. Leng, Recent developments in shape memory polymer nanocomposites: Actuation methods and mechanisms, Coord. Chem. Rev. 320–321 (2016) 38–52. https://doi.org/10.1016/j.ccr.2016.03.007.

[21] M. Šupová, G.S. Martynková, K. Barabaszová, Effect of Nanofillers Dispersion in Polymer Matrices: A Review, Sci. Adv. Mater. 3 (2011) 1–25. https://doi.org/10.1166/sam.2011.1136.

[22] J. Hu, T.W. Odom, C.M. Lieber, Chemistry and Physics in One Dimension: Synthesis and Properties of Nanowires and Nanotubes, Acc. Chem. Res. 32 (1999) 435–445. https://doi.org/10.1021/ar9700365.

[23] M. Nasrollahzadeh, S.M. Sajadi, M. Sajjadi, Z. Issaabadi, Chapter 1 - An Introduction to Nanotechnology, in: M. Nasrollahzadeh, S.M. Sajadi, M. Sajjadi, Z. Issaabadi, M. Atarod (Eds.), Interface Sci. Technol., Elsevier, 2019: pp. 1–27. https://doi.org/10.1016/B978-0-12-813586-0.00001-8.

[24] N. Karak, Chapter 1 - Fundamentals of Nanomaterials and Polymer Nanocomposites, in: N. Karak (Ed.), Nanomater. Polym. Nanocomposites, Elsevier, 2019: pp. 1–45. https://doi.org/10.1016/B978-0-12-814615-6.00001-1.

[25] T.A. Saleh, Nanomaterials: Classification, properties, and environmental toxicities, Environ. Technol. Innov. 20 (2020) 101067. https://doi.org/10.1016/j.eti.2020.101067.

[26] S.R.V.S. Prasanna, K. Balaji, S. Pandey, S. Rana, Chapter 4 - Metal Oxide Based Nanomaterials and Their Polymer Nanocomposites, in: N. Karak (Ed.), Nanomater. Polym. Nanocomposites, Elsevier, 2019: pp. 123–144. https://doi.org/10.1016/B978-0-12-814615-6.00004-7.

[27] G. Mittal, V. Dhand, K.Y. Rhee, S.-J. Park, W.R. Lee, A review on carbon nanotubes and graphene as fillers in reinforced polymer nanocomposites, J. Ind. Eng. Chem. 21 (2015) 11–25. https://doi.org/10.1016/j.jiec.2014.03.022.

[28] R. Stephanie, M.W. Kim, S.H. Kim, J.-K. Kim, C.Y. Park, T.J. Park, Recent advances of bimetallic nanomaterials and its nanocomposites for biosensing applications, TrAC Trends Anal. Chem. 135 (2021) 116159. https://doi.org/10.1016/j.trac.2020.116159.

[29] S. Lehman, S. Larsen, Zeolite and Mesoporous Silica Nanomaterials: Greener Syntheses, Environmental Applications and Biological Toxicity, Environ. Sci. Nano. 1 (2014) 200. https://doi.org/10.1039/c4en00031e.

[30] N. Wang, S. Thameem Dheen, J.Y.H. Fuh, A. Senthil Kumar, A review of multi-functional ceramic nanoparticles in 3D printed bone tissue engineering, Bioprinting. 23 (2021) e00146. https://doi.org/10.1016/j.bprint.2021.e00146.

[31] M.S. Kim, Y.D. Liu, B.J. Park, C.-Y. You, H.J. Choi, Carbonyl iron particles dispersed in a polymer solution and their rheological characteristics under applied magnetic field, J. Ind. Eng. Chem. 18 (2012) 664–667. https://doi.org/10.1016/j.jiec.2011.11.062.

[32] Y. Wu, Y. Wang, G. Luo, Y. Dai, In situ preparation of magnetic Fe_3O_4-chitosan nanoparticles for lipase immobilization by cross-linking and oxidation in aqueous solution, Bioresour. Technol. 100 (2009) 3459–3464. https://doi.org/10.1016/j.biortech.2009.02.018.

[33] N.S. Satarkar, D. Biswal, J.Z. Hilt, Hydrogel nanocomposites: a review of applications as remote controlled biomaterials, Soft Matter. 6 (2010) 2364–2371. https://doi.org/10.1039/B925218P.

[34] K. Haraguchi, Stimuli-responsive nanocomposite gels, Colloid Polym. Sci. 289 (2011) 455–473. https://doi.org/10.1007/s00396-010-2373-9.

[35] Q. Shi, H. Liu, D. Tang, Y. Li, X. Li, F. Xu, Bioactuators based on stimulus-responsive hydrogels and their emerging biomedical applications, NPG Asia Mater. 11 (2019) 1–21. https://doi.org/10.1038/s41427-019-0165-3.

[36] F. Ridi, M. Bonini, P. Baglioni, Magneto-responsive nanocomposites: Preparation and integration of magnetic nanoparticles into films, capsules, and gels, Adv. Colloid Interface Sci. 207 (2014) 3–13. https://doi.org/10.1016/j.cis.2013.09.006.

[37] Y. Li, G. Huang, X. Zhang, B. Li, Y. Chen, T. Lu, T.J. Lu, F. Xu, Magnetic Hydrogels and Their Potential Biomedical Applications, Adv. Funct. Mater. 23 (2013) 660–672. https://doi.org/10.1002/adfm.201201708.

[38] K.J. Sreeram, M. Nidhin, B.U. Nair, Synthesis of aligned hematite nanoparticles on chitosan–alginate films, Colloids Surf. B Biointerfaces. 71 (2009) 260–267. https://doi.org/10.1016/j.colsurfb.2009.02.015.

[39] D. Formica, S. Silvestri, Biological effects of exposure to magnetic resonance imaging: an overview, Biomed. Eng. OnLine. 3 (2004) 11. https://doi.org/10.1186/1475-925X-3-11.

[40] V.V. Spiridonov, I.G. Panova, L.A. Makarova, S.B. Zezin, A.A. Novakova, T.G. Baluyan, A.V. Sybachin, V.V. Kuznetsov, A.A. Yaroslavov, Magneto-sensitive hybrid nanocomposites of water-soluble sodium alginate cross-linked with calcium ions and maghemite, Express Polym. Lett. 12 (2018) 452–461.

[41] R. Hernández, J. Sacristán, L. Asín, T.E. Torres, M.R. Ibarra, G.F. Goya, C. Mijangos, Magnetic Hydrogels Derived from Polysaccharides with Improved Specific Power Absorption: Potential Devices for Remotely Triggered Drug Delivery, J. Phys. Chem. B. 114 (2010) 12002–12007. https://doi.org/10.1021/jp105556e.

[42] R. Tietze, J. Zaloga, H. Unterweger, S. Lyer, R.P. Friedrich, C. Janko, M. Pöttler, S. Dürr, C. Alexiou, Magnetic nanoparticle-based drug delivery for cancer therapy, Biochem. Biophys. Res. Commun. 468 (2015) 463–470. https://doi.org/10.1016/j.bbrc.2015.08.022.

[43] J.A. Medford, J.W. Hubbard, F. Orange, M.J.-F. Guinel, B.O. Calcagno, C. Rinaldi, Magnetothermal repair of a PMMA/iron oxide magnetic nanocomposite, Colloid Polym. Sci. 292 (2014) 1429–1437. https://doi.org/10.1007/s00396-014-3194-z.

[44] M.Y. Razzaq, M. Behl, A. Lendlein, Memory-effects of magnetic nanocomposites, Nanoscale. 4 (2012) 6181–6195. https://doi.org/10.1039/c2nr31332d.

Chapter I: synthesis and characterization of magnetic nanoparticles (MNPs)

1. Introduction

The first component required to elaborate magneto-sensitive nanocomposites are the magnetic nanoparticles (MNPs) acting as fillers with the main function of providing the ability to respond to the application of a magnetic field. The definition of a nanoparticle is a collective of atoms bonded together with an average diameter between 1 and 100 nm, typically consisting of 10^2–10^5 atoms, showing properties that are not found in bulk samples of the same material. The emergence of these size-related properties comes from a sharp increase in the surface-to-volume ratio. From among a wide range of exceptional properties such as optical [1] or electrical [2] ones; the interest, for the present case, is focused on the unique magnetic properties that can be achieved by processing particles at the nanoscale [3] that are not found in microparticles or bulk materials.

The applications of MNPs are quite extensive and the use as constituents of magneto-responsive systems in nanomedicine and biology is one of the main fields [4–11]. Superparamagnetic iron oxide (magnetite and maghemite) MNPs are the most suitable option for the elaboration of these materials due to the best compromise between good magnetic properties [12] and low toxicity [13]. To prepare such kind of MNPs, a variety of chemical methods have been developed during the last decades from which we have selected two alternatives emphasising the more relevant properties for their application as fillers of magnetic responsive nanocomposites. Among them, the most important are high crystallinity, monodisperse size distribution below the critical value that enables superparamagnetic properties and the coating with appropriate ligands to ensure a good colloidal stability in aqueous dispersions.

The outline of this chapter is the following. After a description of the two proposed synthesis protocols to prepare maghemite MNPs, the results of their characterization are discussed focused on their potentiality to elaborate magnetic nanocomposites. Firstly, thermogravimetric analysis (TGA), Fourier transform infrared spectroscopy (FTIR), X-ray

photoelectron spectroscopy (XPS) and X-ray powder diffraction (XRD) results are presented to discuss the composition and crystallinity of the obtained MNPs powders while the size and morphology are studied by transmission electron microscopy (TEM). Secondly, the magnetic properties are discussed to quantify the magnetic response under an applied continuous magnetic field. Finally, the stability of aqueous colloidal dispersions of MNPs is studied based on the determination of the hydrodynamic size and Zeta potential by dynamic light scattering (DLS).

2. Magnetic iron oxides: theoretical background

Iron oxide – magnetite (Fe_3O_4) and maghemite (γ-Fe_2O_3) – nanoparticles are the most used constituents of magneto-responsive materials. Both, magnetite and maghemite, are paramagnetic materials. Below their Curie temperature (850 K and 986 K respectively), they undergo a transition to a magnetically ordered state and become ferrimagnetic. It is important to remark, that even if some authors consider them ferromagnetic, they are in fact ferrimagnetic due to opposite spin in tetrahedral and octahedral sites in the crystalline structure (Figure 1).

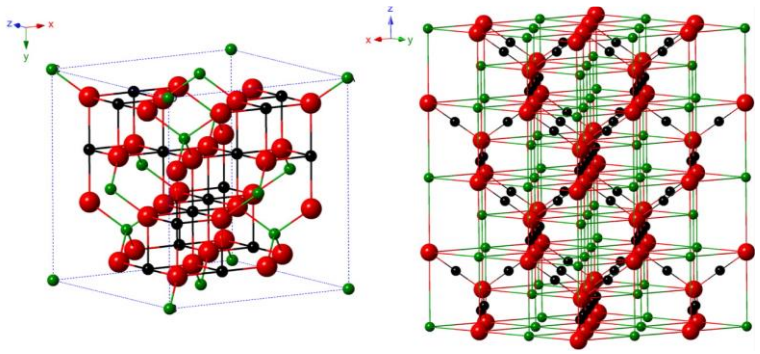

(a) Magnetite (b) Maghemite

Figure 1: crystal structure of (a) magnetite and (b) maghemite (the black ball is Fe^{2+}, the green ball is Fe^{3+} and the red ball is O^{2-}). Obtained from [14].

The behaviour of both ferri- and ferromagnetic materials is characterized by a strong attraction under the application of a magnetic field due to the presence of unpaired electrons whose moments can be aligned under the application of the field. As can be observed in Figure 2, the difference between them is the totally parallel spin alignment for the case of ferromagnetic, while for ferromagnetic, the alignment is antiparallel with the prevalence of one of the orientations. As result it is obtained a net magnetic moment in both cases.

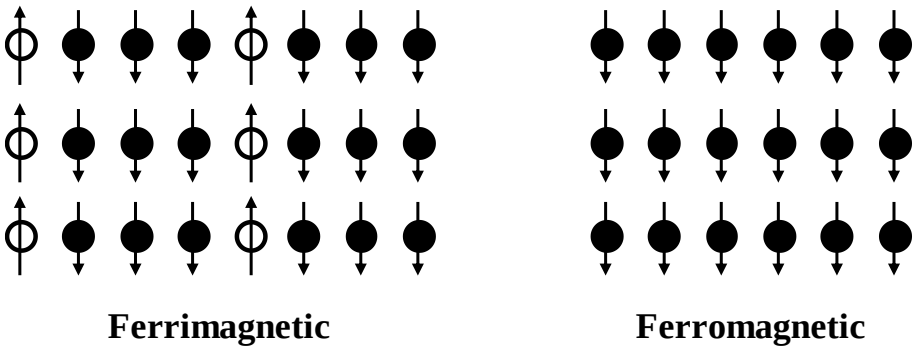

Figure 2: magnetic moment arrangements in ferromagnetic and ferromagnetic materials.

Any ferri- or ferromagnetic material is composed of small-volume regions in which there is a mutual alignment in the same direction of all magnetic dipole moments. Such regions are called domains. Under application of an external magnetic field all the domains tend to be oriented in the same direction increasing the net contribution to the magnetization. At a high enough magnetic field, saturation magnetization (M_s) is reached, *i.e.,* the orientation of all the domains is parallel. The value of M_s depends on the crystalline structure and the density of unpaired electrons whose moments can be aligned in the direction of the field. Experimentally, at T=300K, it was found a slightly higher value for magnetite, M_s = 90-92 $A.m^2/kg$, than for maghemite, M_s = 84-88 $A.m^2/kg$ concluding that both – magnetite and maghemite – show appropriate magnetic properties to elaborate magneto-responsive materials. However, maghemite is chosen in this study over magnetite mainly because magnetite is easily oxidized in the presence of air and in water or alkali solutions under hydrothermal conditions that could lead to water soluble but non-magnetic products. In contrast, maghemite has been demonstrated to be chemically stable in physiological solution [15] and it only undergoes a phase transition into hematite at very high temperatures and/or very long times.

As indicated above, bulk state maghemite present a multi-domain magnetic structure. But, reducing the volume of a material below the size of a domain, the magnetic properties are no longer similar to bulk materials. This is the case of subdomain maghemite MNPs, that are superparamagnetic. The response of superparamagnetic MNPs to the application of an external magnetic field is the magnetization by the orientation of the magnetic moment by rotation of each of the single-domain MNP until it becomes parallel to the applied magnetic field, and they will lose the magnetization when removing the field. These interesting properties strongly depend on the size, shape and coating amount and type, making the development of a suitable synthesis method and the characterization key steps to ensure good quality maghemite MNPs with controlled properties.

3. Synthesis and functionalization of maghemite MNPs

3.1. Introduction

The scheme of the protocols proposed in the present chapter to synthetize maghemite MNPs are composed by three steps: (1) synthesis of nanosized magnetite MNPs, (2) oxidation of magnetite to maghemite and (3) surface treatment to improve the stability in the form of colloidal dispersions.

The selected synthesis mechanism has an important effect on the particle size and shape, size distribution, surface chemistry and the degree of structural defects or impurities. It represents the key-step since the interesting properties found in MNPs strongly depend on all these mentioned characteristics. Different strategies can be found in the literature for the synthesis of magnetite MNPs including physical (gas phase deposition or power ball milling), chemical (co-precipitation, sol-gel or microemulsions) and biological methods (using bacteria and plants). An exhaustive description for each of the methods and a discussion of their advantages and drawbacks can be found in the literature [16,17]. For the present case, two different chemical routes have been selected, sol-gel method in a polyol solvent and co-precipitation. Chemical methods are generally composed of two steps, the formation of magnetite clusters followed by the deposition of more magnetite in the surface of those clusters. The different strategies are based on the control of several parameters which enable to initiate numerous initial clusters and to slow down the growth reaction in order to depose more magnetite in the initiated clusters in a controlled way. The specific characteristics and detailed experimental protocols for the methodologies selected will be presented subsequently.

The second step consists in the oxidation of magnetite into the desired maghemite. This phase transition takes place just by mixing the obtained magnetite powder in boiling pure water. A simple way to confirm the oxidation is the transformation of the black-coloured powder of magnetite into a brown-coloured powder of maghemite. If the oxidation is too intensive a non desired red-coloured powder of hematite can be obtained. Oxidation of maghemite in the appropriate conditions will not affect the crystal morphology.

The third step is the treatment of the maghemite MNPs surface. An aqueous dispersion of as-obtained bare maghemite MNPs is non-stable due to their hydrophobic characteristics coming from a neutral surface charge and magnetic-dipole attractive forces between the particles. MNPs in this state will become aggregated and sediment in water dispersion due to their high density. To avoid this inconvenience, different strategies can be found in the literature to modify the hydrophobic surface of maghemite MNPs that can be classified in *in-situ* coating,

post-synthesis adsorption and post-synthesis grafting. All these methods are based on the introduction of repulsive steric or/and electrostatic interactions between MNPs that avoid the agglomeration when particles collide due to thermal motion. This stage is especially important for MNPs more than for other nanoparticles due to the attractive magnetic-dipole forces between MNPs that can easily lead to aggregation. A more complete discussion about the alternatives of surface functionalization of nanoparticles can be found in the literature [18,19]. For the present case the strategy of functionalization has been chosen to elaborate nanocomposites with different electrostatic interactions between the MNPs and the polymer chains. Thus, positively and negatively charged MNPs have been synthetized and functionalized by two methods described in the next paragraphs.

3.2. Polyol method

Polyol method is an easy and versatile route to prepare inorganic nanoparticles with controlled morphology that can be included in the sol-gel techniques. It consists in the reduction of a metal salt in a polyol medium. It was successfully applied for the synthesis of metal and metal oxide nanoparticles with a very wide range of chemical compositions and morphologies [20,21]. Polyol solvents presents some interesting physico-chemical properties, including their reducing and coordinating capacity and the relatively higher boiling temperatures and viscosities. This set of unique properties allow to provide the adequate synthesis conditions to obtain monodisperse shape-controlled nanometric particles.

Likewise, magnetite MNPs can be prepared in a polyol solvent by forced hydrolysis of an iron salt allowing to better control their shape, their size distribution and therefore, their structural and magnetic properties [22]. The polyol will serve as solvent and surfactant during the synthesis controlling the nucleation and growth of the particles and preventing the agglomeration. The synthesis protocol and the characterization of the obtained MNPs has been developed in collaboration with the ITODYS laboratory (Université de Paris et Centre national de la recherche scientifique). Diethylene glycol (DEG) and iron acetate were chosen as solvent and iron precursor, based on the literature [23–27] and the previous experience in the ITODYS laboratory in the synthesis of MNPs of different nature [28,29].

Precisely, 4 g of iron acetate $Fe(CH_3CO_2)_2$ (ACROS, 95%) were dissolved in 250 mL of DEG. A volume of distilled water (1 mL) was also added to get a hydrolysis ratio (h), defined as the molar ratio between water and iron cations (h =1.6). The value of h is the main factor governing the formation of either magnetite or maghemite, obtaining higher proportions of maghemite as the value of h increases. However, it was decided to maintain h relatively low to

avoid the risk of formation of non-magnetic hematite. The mixture was then heated until boiling at a rate of 6 °C/min under mechanical stirring and maintained under reflux for 3 hours. In these operating conditions, forced hydrolysis of iron acetate leads to the production of magnetite MNPs of a size ranging between 10 and 12 nm in diameter. The black magnetic powder, assumed to be magnetite (Fe_3O_4), was then isolated by addition of acetone (DEG/acetone = 1/2 v/v) and centrifugation at 22000 rpm for 20 minutes. The recovered powder was then washed with boiling water several times, to oxidize magnetite into maghemite. A dark brown magnetic powder was then recovered by centrifugation and finally dried at atmospheric pressure in an oven at 50°C.

Afterwards, MNPs were functionalized by the grafting of 3-Aminopropylphosphonic acid (APPA). This molecule presents a posphonic group able to bond to the particle surface by covalent linkage and, at the same time, a terminal amino group ($-NH_2$) which can be ionized (NH_3^+) leading to positively charged MNPs (Figure 3). Thus, electrostatic repulsion between MNPs will prevent the aggregation in aqueous dispersion and could interact electrostatically with a polyelectrolyte matrix in the prepared nanocomposites. The experimental protocol consists in preparing a dispersion of bare MNPs (600 mg) in deionized water (150 mL). 130 mg of APPA were then added and the resulting mixture was kept at 60°C under mechanical stirring for 12 hours. The functionalized MNPs (APPA-MNPs) were rapidly isolated by a magnet and washed with deionized water, before to be dried in air overnight at 50°C.

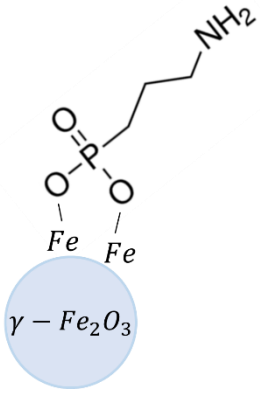

Figure 3: schematic representation of the maghemite nanoparticles functionalized by APPA.

The obtained final product consists in a brown-colored powder that was stored in the desiccator for further characterization and use. From a practical point of view, it is important to remark that this methodology allows to obtain a relatively small quantity of around 500 mg of APPA-MNPs from 4 g of iron acetate with no-possibility to scale-up the synthesis with the materials and equipment available in the laboratory. This is not an inconvenience for the characterization of APPA-MNPs due to the small masses of few milligrams required. However,

it is an important limit for the elaboration of nanocomposites that requires big amount of MNPs.

3.3. Co-precipitation

Co-precipitation is a well-known and reproducible method that allow to synthesize magnetite MNPs with reasonably good magnetic and structural properties. This route consists in the mixing of soluble iron salts containing Fe^{2+} and Fe^{3+} in a determined proportion followed by the addition of a base under continuous stirring inducing a direct precipitation in the form of magnetite MNPs. Afterwards, these magnetite MNPs can be easily oxidized to maghemite. In the literature we can find extensive information about this method [6,30,31] to obtain monodisperse and shape controlled MNPs depending on several parameters: (1) ratio Fe^{3+}/Fe^{2+}, (2) temperature, (3) salt concentration, (4) type and concentration of the base and (5) presence of surfactants. Among all the alternatives, iron oxide maghemite (γ-Fe_2O_3) were synthetized following the co-precipitation method of iron salts in ammonia proposed by Massart [32].

Briefly, 214 mL of aqueous solution of ferric chloride hexahydrate 0.43M ($FeCl_3.6H_2O$, SIGMA-ALDRICH, ≥99%) was prepared in a 3-necked flask. Freshly dissolved in 35 mL of 2M HCl (aq) ferrous chloride tetrahydrate 0.4M ($FeCl_2.4H_2O$, Acros Organics, ≥99%) were dropped in the 3-necked flask under mechanical stirring at room temperature. Rapidly, 71 mL of ammonia (NH_3, Technic 28-30% v/v) were added and maintained under the stirring at 400 rpm for 30 minutes to obtain magnetite MNPs. The precipitate consisting of anionic magnetite particles (Fe_3O_4) was isolated with a magnet and then washed in distilled water. The precipitate was then stirred in a solution of nitric acid (HNO_3, 1.98M, V = 250 mL) for 30 minutes to prepare the surface of the MNPs for the following step. The obtained magnetite particles were oxidized to maghemite at 90°C with ferric nitrate ($Fe(NO_3)_3.9H_2O$ Merck, 1.67M, V = 57 mL) for 30 minutes. The produced maghemite ($\gamma-Fe_2O_3$) was then washed 3 times with acetone and twice with ether.

This protocol allows to obtain maghemite MNPs with a diameter around 10 nm. Such small particles tend to form agglomerates to reduce the energy associated with the high surface area/volume ratio. To avoid this inconvenience, MNPs were immersed in aqueous sodium citrate solution ($Na_3C_6H_5O_7$ Sigma-Aldrich, 0.1M, V = 71 mL) during 30 minutes at 80ºC and the dispersion was stabilized by the adsorption of negatively charged citrate ions on the surface of MNPs. Finally, the citrated-MNPs, represented in Figure 4, were washed twice with acetone and twice with diethyl ether before being dispersed in amount of pure water depending on the volume fraction desired. The residual diethyl ether was evaporated heating at 40ºC.

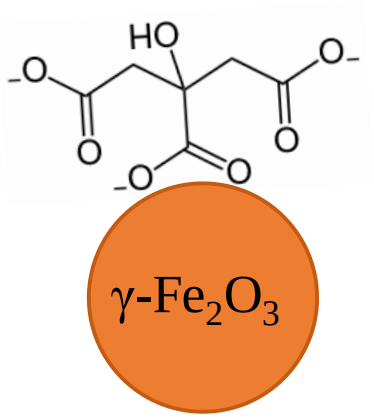

Figure 4: schematic representation of the maghemite nanoparticles with absorbed citrated ions.

The final product consists in an aqueous dispersion of maghemite MNPs stabilized by the adsorption of citrated ions, named citrated ferrofluid. This dispersion has demonstrated to have high stability and if it is stored hermetically closed at room temperature and protected from the light to be used during two months. From a practical point of view, it is important to remark that this methodology allows to obtain around 8 g of citrated-MNPs (around 40 mL with approximatively 20 % w/w of citrated-MNPs). This is an important advantage in comparison to the previous APPA-MNPs, allowing to have enough quantity to prepare nanocomposites in a less restrictive way.

4. Characterization of MNPs

4.1. Introduction

The two different experimental protocols lead to the production of MNPs in different states. Through the polyol method, APPA-MNPs were obtained in powder, while co-precipitation method leads to the production of a concentrated aqueous dispersion of MNPs stabilized by citrated ions named citrated ferrofluid. In order to carry out a comparative study, depending on the different experimental techniques, the MNPs prepared by the two methods require different pre-treatments to achieve an equivalent state. For the experiments which require MNPs in powder, citrated ferrofluids were firstly dried in oven at 80ºC during 12 hours. The obtained powder was then milled and dried in the oven at 50ºC during 12 hours and stored in the desiccator in order to obtain dried citrated-MNPs (Figure 5). On the contrary, APPA-MNPs obtained in the form of dried powder were stored in the desiccator after the synthesis and do not require any pre-treatment.

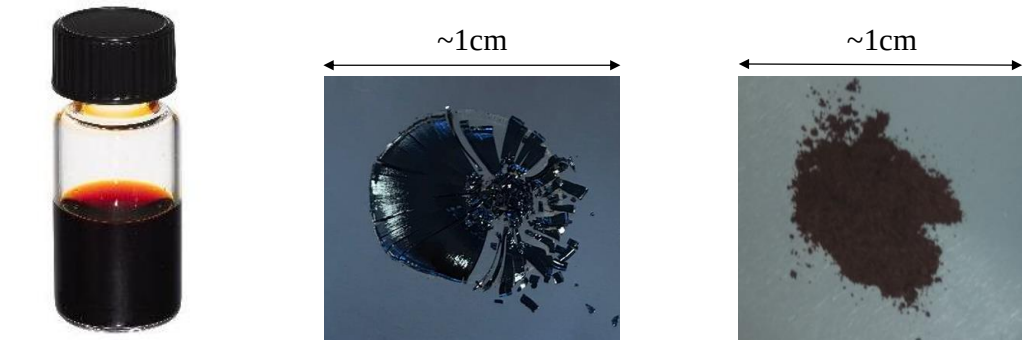

Figure 5: MNPs prepared by co-precipitation with adsorbed citrated ions in different states.

For the experiments which require aqueous dispersions of MNPs they were prepared by dilution of either concentrated citrated ferrofluids or APPA-MNPs powders and sonicated during 10 minutes to ensure a good dispersion. The only requirement to adjust these experimental conditions is the determination of the concentration of MNPs. For the polyol method, as obtained APPA-MNPs powders were considered 100% w/w MNPs after drying in the oven at 50ºC during 24 hours. For citrated ferrofluids obtained by co-precipitation the concentration of MNPs in % w/w was estimated for each of the synthesis as the dried mass after 24 hours at 80°C and verified by atomic absorption spectroscopy for one of the cases. For the cases where it is necessary to provide the concentration of MNPs in % v/v, it was recalculated based on the assumption of a density, ρ_{MNPs} = 4.90 g/cm^3 [33].

The performed characterization on the maghemite MNPs has been divided in the three sections presented above. Firstly, a study was performed on dried powders of the products to evaluate their structure, size, morphology, and composition. This study will provide the base to understand the differences in the properties of the MNPs prepared by the two proposed methods. In a second section, the magnetization of MNPs powders was measured with a vibration sample magnetometer (VSM) to quantify their magnetic response. In addition, MNPs have to be dispersed in water before introducing them in the polymeric matrix for the elaboration of nanocomposites. For this reason, a third section focused on the study on the colloidal stability of aqueous dispersions of MNPs was also included as an important evaluation before their final application as fillers in magnetic-responsive nanocomposites.

4.2. Structural and morphological analysis

4.2.1. Experiments

The crystalline structure of bare and functionalized MNPs was characterized by X-Ray Powder Diffraction (XRD) on a Empyream (Malvern-Panalytical) device using the CuKα

radiation (λ_1=1.5406 Å, λ_2=1.544 Å) in Bragg−Brentano reflection configuration in the 10º−100º angular range. The cell parameter and the size of coherent diffraction domain (crystalline size) were determined with MAUD software which is based on the Rietveld method combined with Fourier analysis, well-adapted for broadened diffraction peaks.

The structural analysis was complemented with Fourier Transform InfraRed (FTIR) spectroscopy and ThermoGravimetric Analysis (TGA) coupled with Differential Thermal Analysis (DTA) to confirm the production of maghemite and to evaluate the presence and the amount of ligands in the surface of MNPs that have a strong influence on their physicochemical properties. The FTIR spectra was recorded in a Bruker Equinox spectrometer in the range 400-4000 cm^{-1}. KBr pellets of dried MNPs were prepared and the spectra was recorded in transmission mode at room temperature. The TGA-DTA scans were conducted in a SERATAM TGA-DTA-92 device. A small mass (10 – 20 mg) of MNPs powder dried overnight at 50ºC was introduced in the sample holder. Scans were performed under air flow (80 mL/min) between 10 and 1000ºC with a heating rate of 10ºC/min and the mass loss and the differential temperature were measured simultaneously. The mass loss data can be used for a quantitative analysis while differential temperature data can be interpreted to obtain qualitative information about the phenomena inducing changes in heat and temperature.

X-ray Photoelectron Spectroscopy (XPS) has been performed in bare and grafted APPA-MNPs powders to confirm the covalent linkage of APPA molecules in a K-Alpha+ (ThermoFisher Scientific) spectrometer. XPS in a non-invasive surface analysis technique based on the photoelectric effect. The measurement of the kinetic energy of the photoelecctroltrons submitted to X-ray are used to obtain the binding energy, characteristic of the chemical linkage. Thus, this technique allows to identify the atoms presented in the MNPs surface. The penetration of the analysis in the sample is between 1 and 12 nm which allows to determine a surface concentration.

The morphology of MNPs was visualized on a Tecnai12 Transmission Electron Microscope (TEM). Diluted dispersions of MNPs were prepared by mixing a calculated mass of MNPs powder in pure water to obtain the final concentration of 0.05% w/w. The sample was sonicated to ensure a good dispersion and a small droplet was placed in a copper grid. The sample was then dried in a vacuum oven and the grid was inserted in the TEM device.

4.2.2. XRD results

The XRD patterns of the MNPs prepared by both methods are presented in Figure 6 and Figure 7 respectively. For all cases, the broadened diffraction peaks obtained confirm the

crystallinity of MNPs and can be unambiguously attributed to an iron oxide phase with cubic spinel structure of maghemite JCPDS file, No. 04-0755 [34]. The diffraction pattern obtained for both bare and grafted MNPs prepared by the polyol method is almost identical confirming good stability of the crystalline structure of maghemite when MNPs are dispersed in the aqueous solutions of APPA at moderate temperatures (APPA-grafting implies 12 hours at 60ºC). Rietveld refinement has been applied for the estimation of the mean coherent diffraction domain size – crystallite size. A least-squares procedure has been used to compare intensities and width of the experimental peaks to those calculated from the peak shape function [35], which is a convolution of the instrumental broadening, the wavelength dispersion and the specimen function; defined in this case by the cubic Fd3m phase assigned to maghemite. The crystallite sizes are found to be 9.1±0.2 nm and 9.6±0.1 nm for bare and APPA-MNPs respectively. The differences in both the average crystallite size and the error between bare and grafted MNPs can be explained by a tendency of separation of the smallest MNPs during the dispersing/washing steps during the grafting protocol.

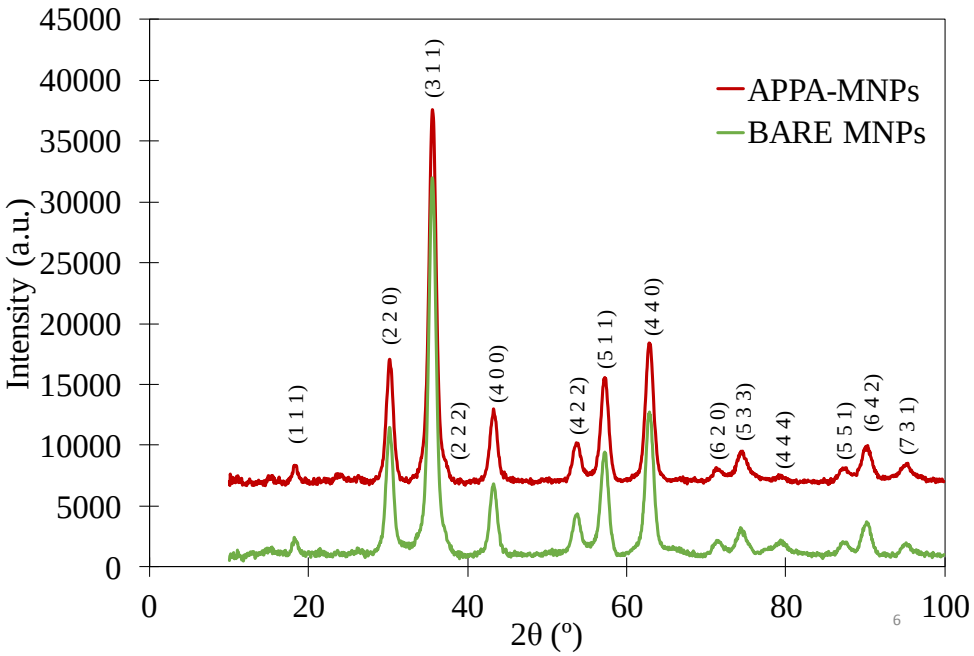

Figure 6: XRD pattern of bare and APPA-grafted MNPs prepared by the polyol method.

The XRD pattern of the MNPs prepared by co-precipitation method is obtained only for the final product, citrated-MNPs. The XRD pattern is nearly identical of those of MNPs prepared by the polyol method demonstrating the feasibility of the synthesis of maghemite MNPs with high degree of crystallinity by a simpler method without requiring high temperatures. The mean crystallite size, determined as previously, is found to be 8.6±0.1 nm, slightly smaller than for APPA-MNPs.

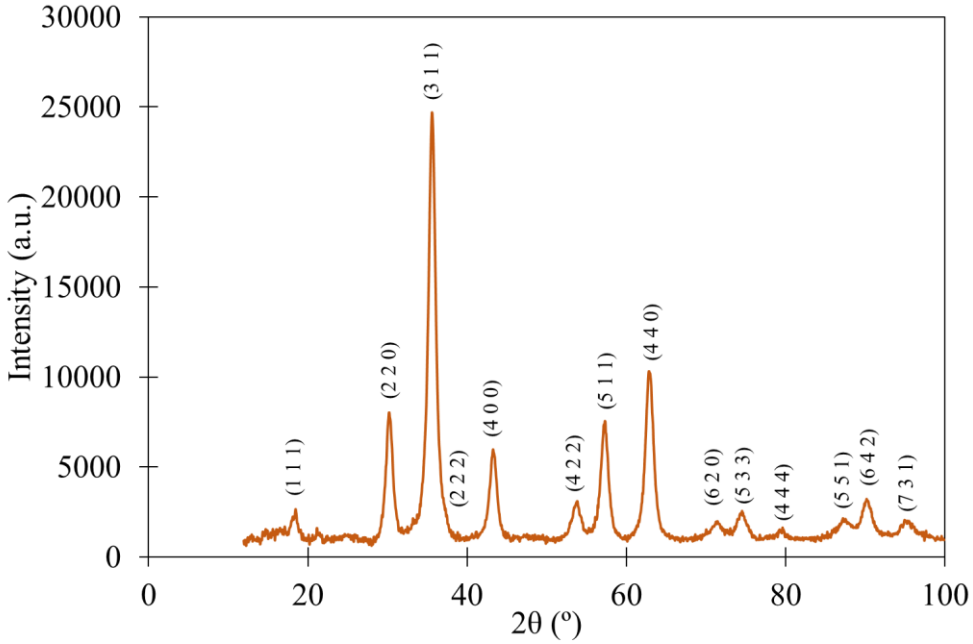

Figure 7: XRD pattern of citrated-MNPs prepared by co-precipitation method.

4.2.3. FTIR results

The FTIR spectra of bare MNPs and APPA-MNPs prepared by polyol method are compared in Figure 8. The band at 3428 cm^{-1} can be assigned to hydrogen bonded O-H stretching vibration coming from water and diethylene glycol while the band at 1633 cm^{-1} corresponds to H-O-H scissoring coming from water. The bands at 2965, 2928 and 2868 cm^{-1} can be assigned to C-H stretching while at 1119 and 1072 cm^{-1} to C-O stretching coming from DEG adhered into the MNPs surface. Characteristic bands at 629 and 588 corresponds with Fe-O confirming the oxidation to maghemite (for magnetite only a single peak at 590 cm^{-1} is expected) [36]. Small differences can be observed between bare MNPs and APPA-MNPs. No intense peaks corresponding with phosphonic and amino groups presented in APPA were found. This can be explained by the overlapping of characteristic bands of N-H with those of O-H. P-O and P=O bonds can be proved generally by a band in the range of 1320-1140 cm^{-1} related to their stretching vibration but in the obtained spectrum cannot be clearly assigned to any of the observed peaks. The presence of these groups could be explained by a change on the position and number of peaks presented in the region 1000-1500 cm^{-1} in comparison with bare MNPs.

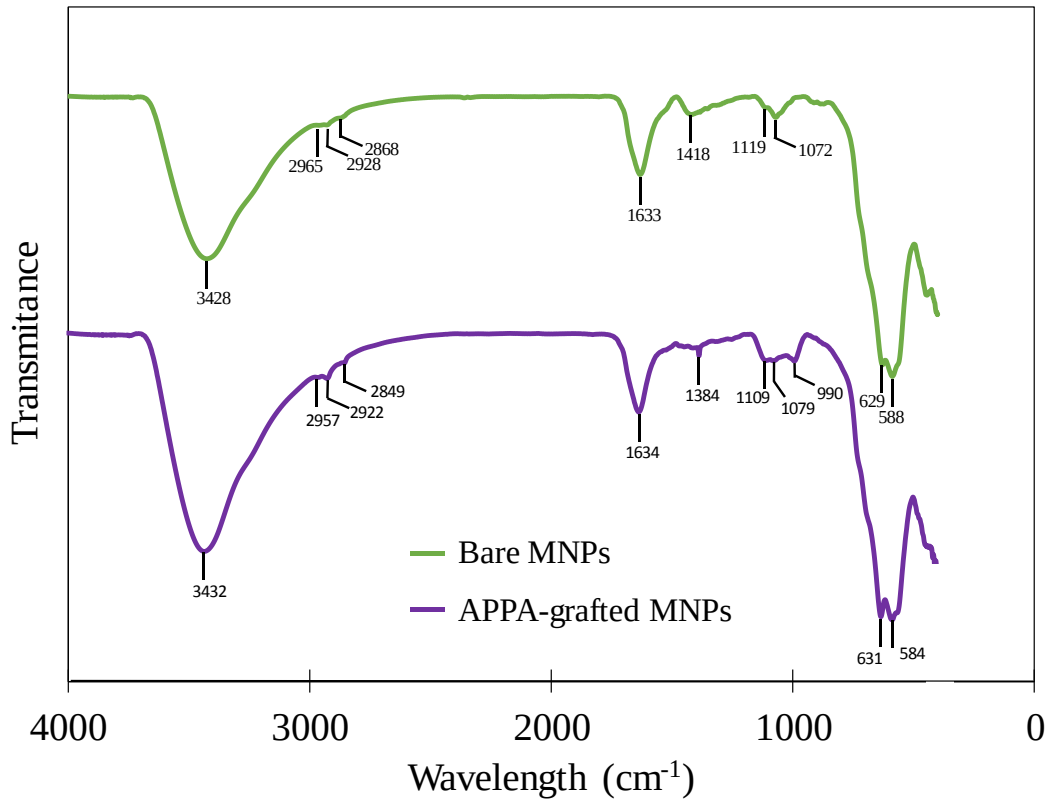

Figure 8: FTIR spectra of bare and APPA-grafted maghemite nanoparticles prepared by polyol method.

The FTIR spectra of the citrated-MNPs prepared by co-precipitation method is presented in Figure 9. The characteristic band at 3383 cm^{-1} can be assigned to hydrogen bonded O-H stretching vibration. Bands at 1595 and 1384 cm^{-1} correspond to the anti-symmetric and symmetric stretching of carboxylic groups (COOH) confirming the presence of citrated ions adsorbed in the surface of the MNPs. As for polyol obtained MNPs, the bands at 631 and 583 cm^{-1} are assigned to Fe-O confirming the presence of iron oxide in the form of maghemite (for magnetite only a single peak at 590 cm^{-1} is expected) [36].

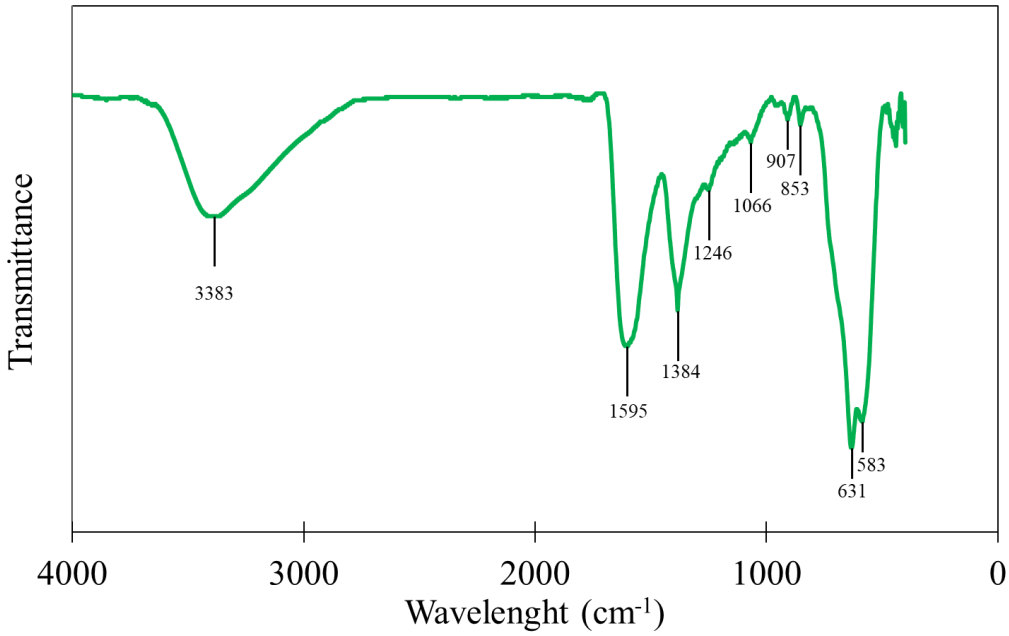

Figure 9: FTIR spectra of maghemite nanoparticles with absorbed citrated ions prepared by co-precipitation.

4.2.4. TGA-DTA results

TGA-DTA thermograms are presented in Figure 10 and 11 for bare and APPA-grafted MNPs synthetized by the polyol method. For both cases, a first endothermic step below 160ºC is observed coming from the drying of the free water on the surface of MNPs. Even after drying the MNPs at 50ºC overnight, the environmental humidity can be adsorbed by the MNPs. The difference in the mass loss in this step between bare and APPA-grafted MNPs can be explained by the effect of the grafting in the MNPs surface. Indeed, Bare MNPs have a hydrophobic surface while APPA-grafted MNPs have a more hydrophilic positively charged surface that could have an influence on the interactions with the environmental humidity. The second exothermic step is related with organic compounds decomposition. This step for bare MNPs is assigned to the DEG elimination, not separated during the washing steps, representing a 3.5% of the total mas of the MNPs. For APPA-MNPs, it is a combination of the DEG elimination and the partial degradation of the APPA that occur simultaneously. Analysing in detail the peak between 200 and 400ºC in Figure 11, it can be observed a broadening at high temperatures in the heat flow peak and the increase of the mass loss, coming both from the APPA degradation. However, it is very difficult to determine the APPA amount grafted in the surface of the MNPs due to the variable content on DEG. For more details, an exhaustive study should be applied by elemental analysis or FTIR analysis of the gases during TGA. Finally, at higher temperature, it can be observed an exothermic peak accompanied by a small mass loss representative of the maghemite to hematite phase transition. The shift of this transition to higher temperature for

APPA-grafted MNPs reveals that the grafting enhances the γ-Fe_2O_3 stability, increasing the transition temperature up to 650ºC, comparable to other cation modifications on maghemite MNPs [37].

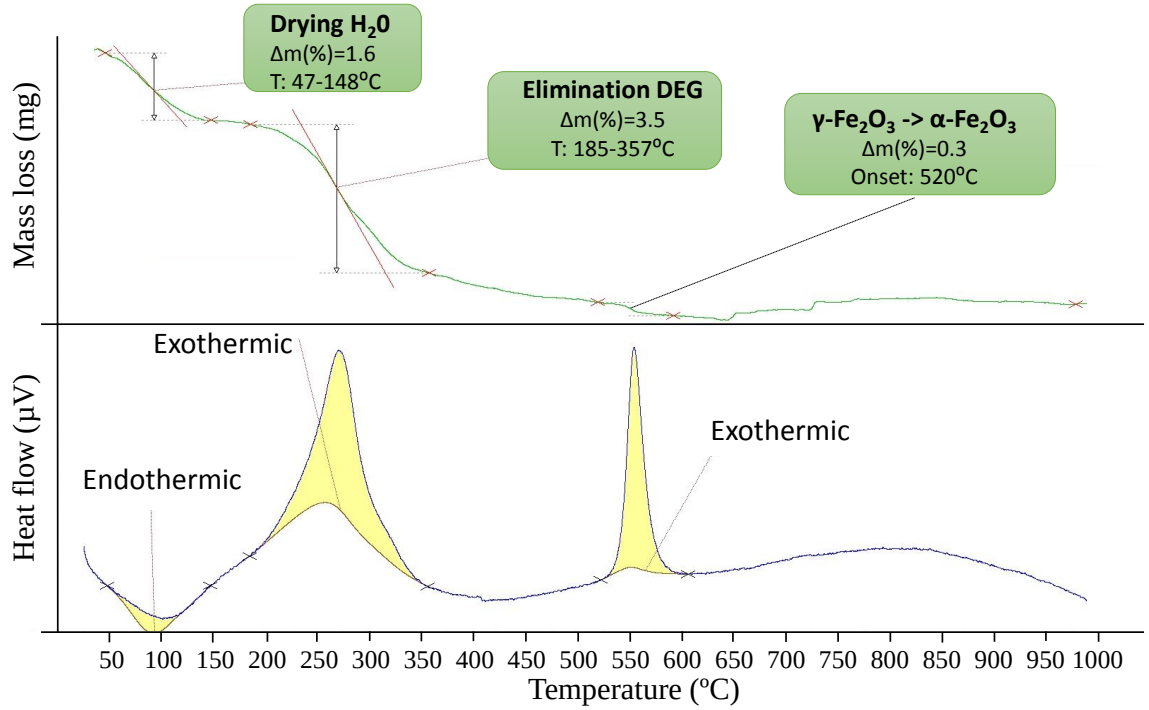

Figure 10: TGA-DTA scan between 10 and 1000ºC of bare maghemite MNPs synthetized by the polyol method at 10ºC/min.

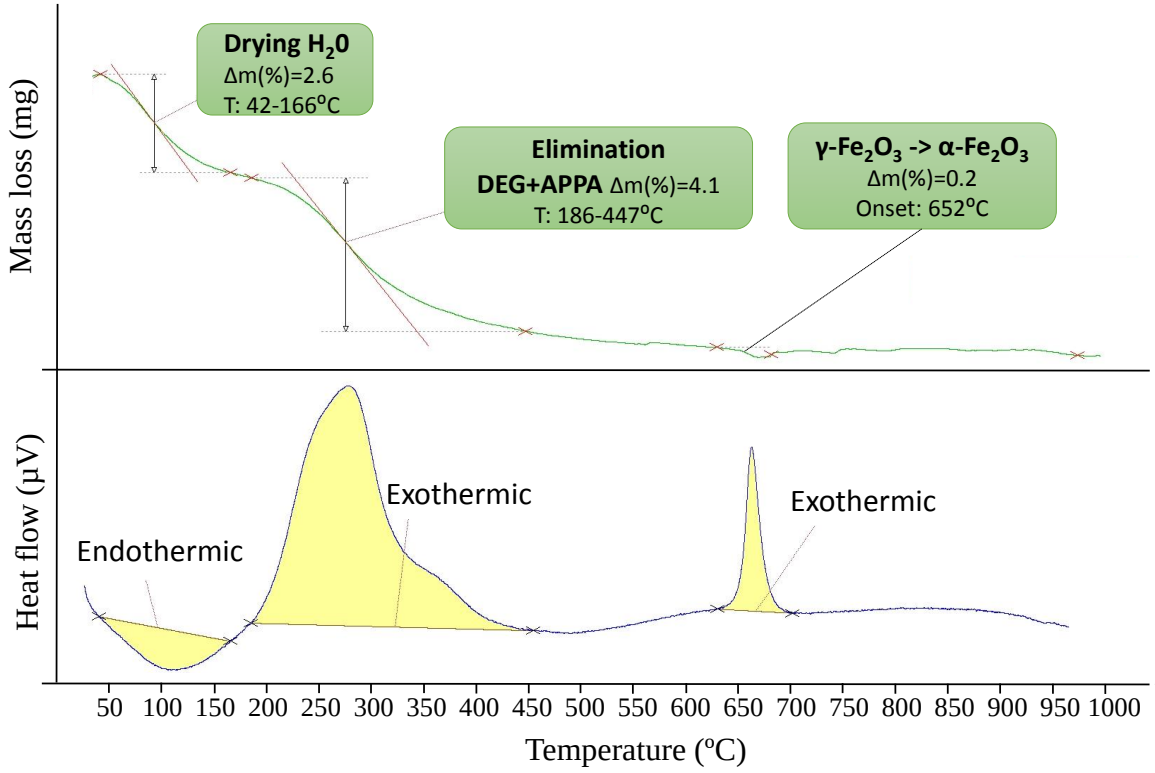

Figure 11: TGA-DTA scan between 10 and 1000ºC of maghemite MNPs synthetized by the polyol method and grafted with APPA at 10ºC/min.

From the thermogram presented in Figure 12 three steps in the mass loss can be identified for citrated-MNPs. The first step, between 36 and 155ºC, is assigned to the dehydration of the sample consisting in the evaporation of free water but probably also to the dehydration of sodium citrate to sodium aconitate [38]. The second step, taking place between 170 and 310ºC, is assigned to the partial degradation of citrate ions. This step, strongly exothermic according with the heat flow data, correspond to the degradation of carboxylic groups of citrated ions and the consequent departure of CO_2(g). The third step is assigned to the decomposition of citrate residues. In addition, an exothermic peak was found around 550ºC with a small mass loss of 0.3% coming as previously from the phase transformation of maghemite to hematite. The observed peak for this transition in the heat flow is less sharply than in the previous APPA-MNPs synthetized by polyol method that could be related with a less controlled morphology for the case of citrated-MNPs.

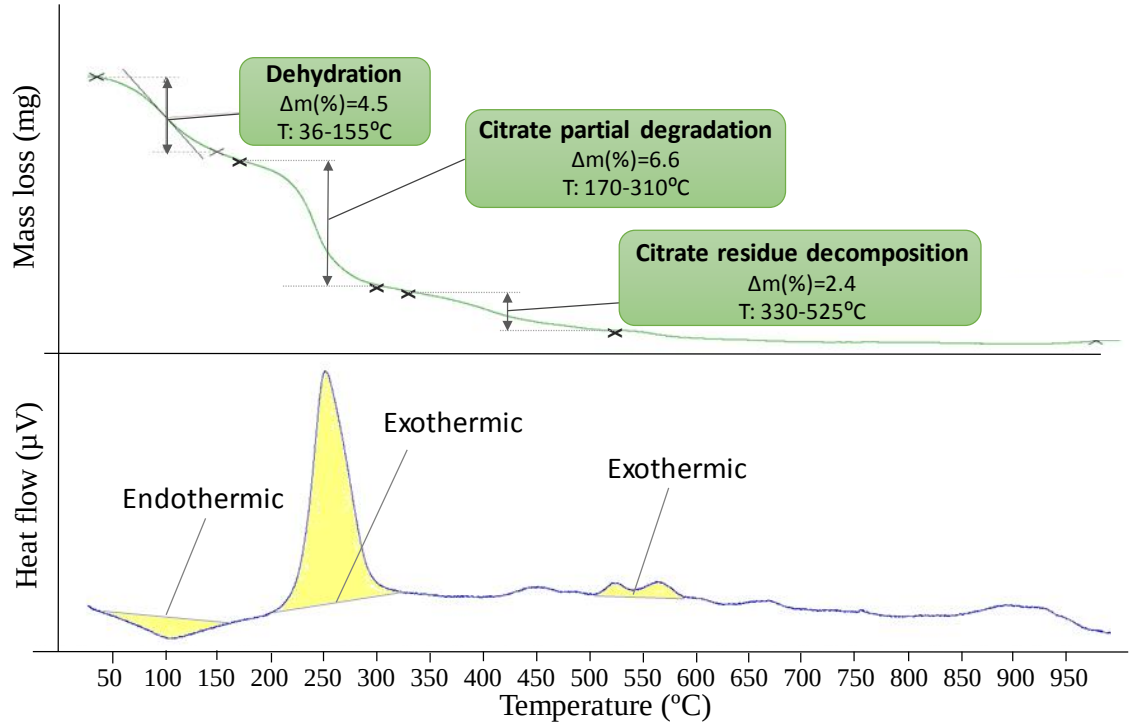

Figure 12: TGA-DSC scan between 10 and 1000ºC of maghemite nanoparticles synthetized by co-precipitation with absorbed citrated ions at 10ºC/min.

By comparison of the compositions for APPA-MNPs and citrated-MNPS estimated from the TGA/DTA analysis it can be concluded that citrated-MNPs have a bigger content in non-magnetic compounds. In the one hand, the humidity is higher in citrated-MNPs probably from a higher hydrophilicity of the surface and the presence of free citrate ions even if the drying was carried out in identical conditions. From the other hand, the quantity of citrate ligands in citrated-MNPs is also more important than the amount of APPA double ligands in APPA-

MNPs. This is a characteristic that will have an important effect on both properties of interest that will be discussed below, magnetic properties and colloidal stability in water dispersion.

4.2.5. XPS results

The recorded spectra of bare and grafted APPA-MNPs prepared by the polyol method are shown in the Figure 13a. The spectra were then deconvoluted to obtain the signal of to the atoms of interest (nitrogen, iron and phosphorus) shown in the Figures 13b, 13c and 13d in their respective intervals of binding energy. It can be clearly identified the characteristic peak of phosphorus in the APPA-MNPs that did not appear in the bare-MNPs unambiguously assigned to the APPA grafted in the surface of the MNPs. An equivalent analysis can be done with the nitrogen coming from the amino group of the APPA molecule.

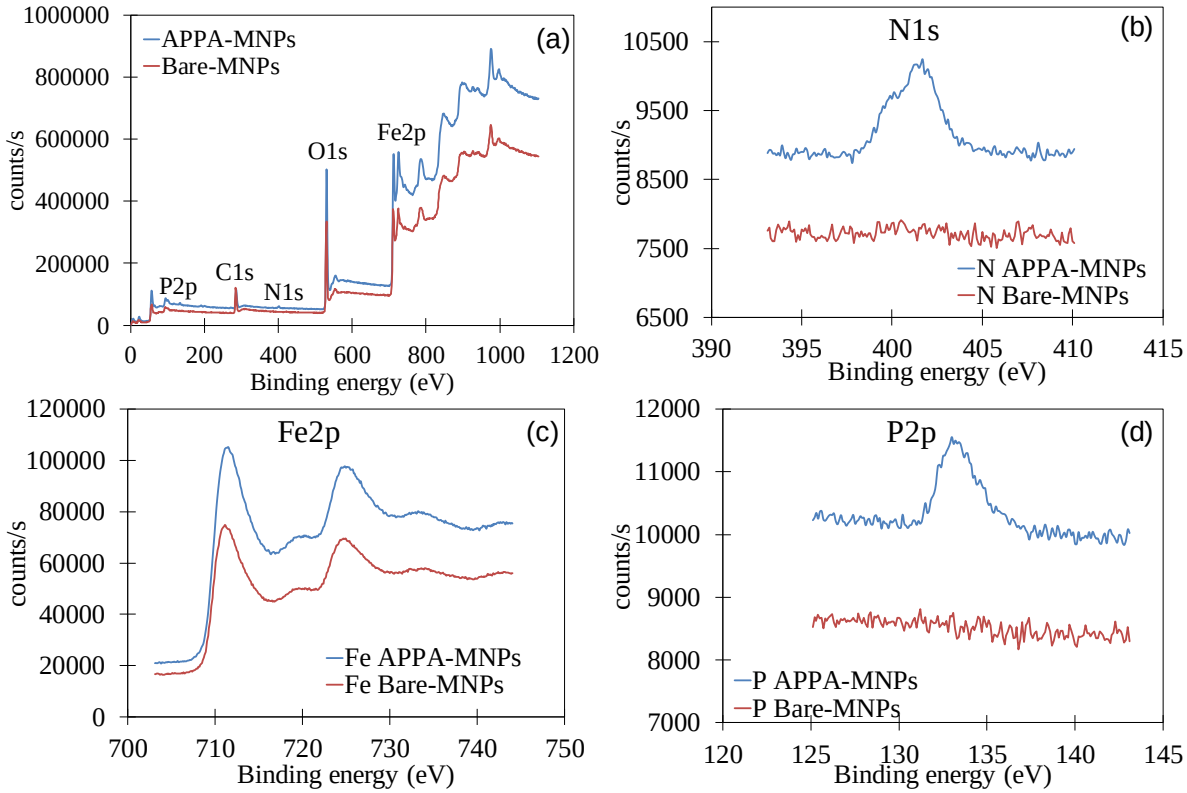

Figure 13: XPS spectra for bare and APPA-grafted MNPs prepared by the polyol method: (a) complete spectra, (b) nitrogen, (c) iron and (d) phosphorus spectra obtained by deconvolution in the intervals of interest.

By comparison of the intensities of the peaks obtained for phosphor and iron (Table 1), a surface concentration of APPA can be determined obtaining a value of 10.6% w/w. However, the unknown degree of penetration of the XPS measurement in the sample do not allow to define a volume concentration to more clearly quantify the amount of APPA grafted on the APPA-MNPs surface.

Table 1: comparison of the intensity of the XPS peaks observed for iron (Fe) and phosphor (P)

Atoms	% Atoms	N molecules	Surface concentration (% w/w)
Fe	25.17	12.59 (Fe_2O_3)	89.4 (Fe_2O_3)
P	1.72	1.72 (APPA)	10.6 (APPA)

4.2.6. TEM visualization

TEM images carried out in dried samples (Figure 14) show that both methods lead to roughly spherical, highly crystallized, and almost uniform in size MNPs. The average particle diameter was determined from the recorded TEM images by counting about 200 particles considered to be perfectly spherical. Mean diameter, obtained by fitting to a log-normal distribution (Figure 15) is 8.1±1.4 nm for citrated-MNPs and 10.9±1.2 nm for APPA-MNPs. These results are in good agreement with the results of the crystallite size obtained by XRD (8.6±0.1 nm and 9.6±0.1 nm respectively) and confirms that co-precipitation method allows to obtain maghemite MNPs with slightly smaller size than polyol method. Nevertheless, APPA-MNPs present more uniform size distribution demonstrating the better regulation of the crystallization conditions leading to a more controlled nucleation and growth of crystals in the presence of the DEG solvent.

(a) Citrated-MNPs (b) APPA-MNPs

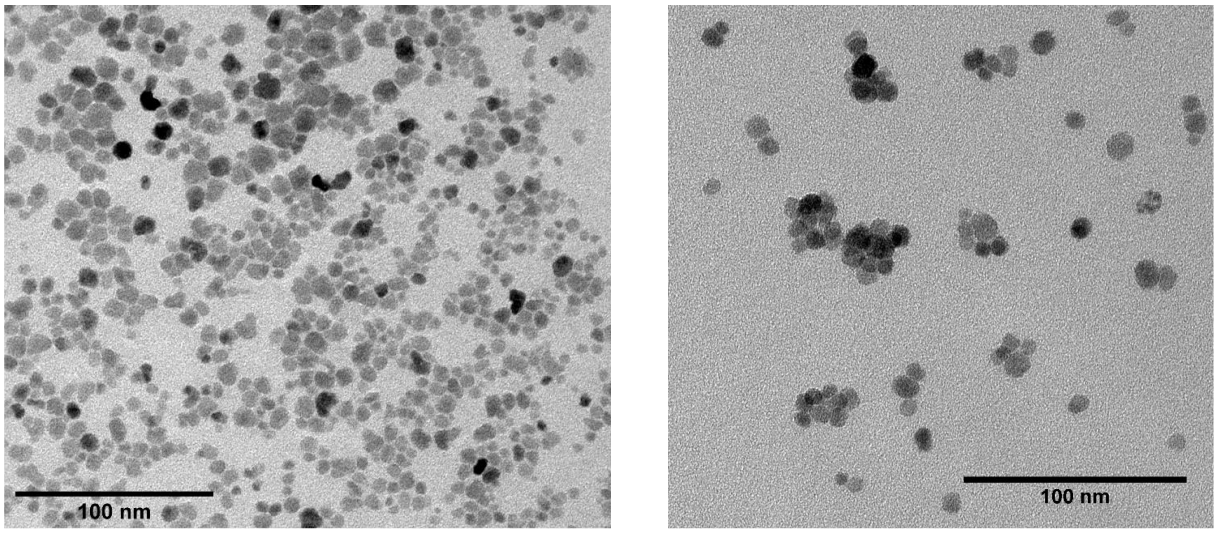

Figure 14: TEM images for citrated-MNPs and APPA-MNPs prepared respectively by coprecipitation and polyol method.

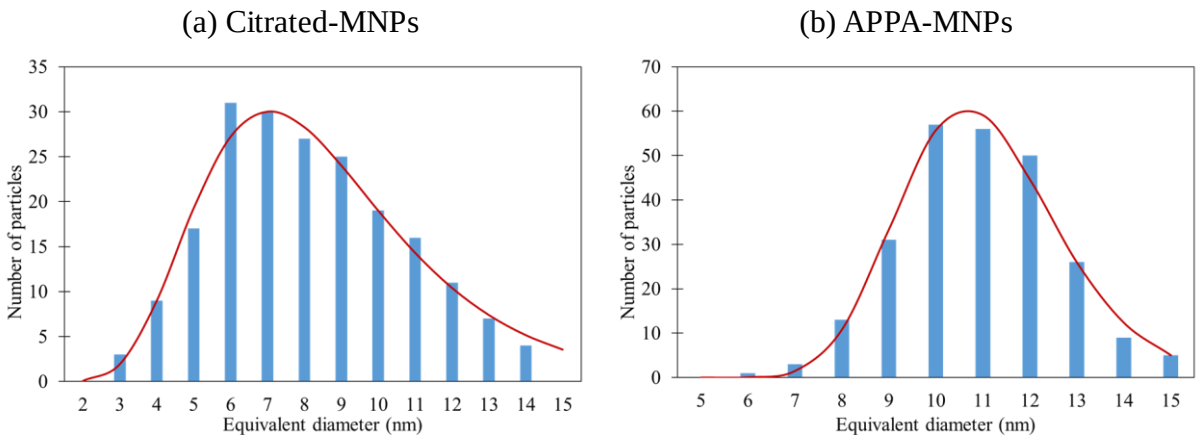

Figure 15: particle diameter distribution for citrated-MNPs and APPA-MNPs prepared respectively by coprecipitation and polyol method. Red lines correspond to a fitting with a log-normal distribution.

4.3. Magnetization in a vibrating sample magnetometer (VSM)

The magnetization as function of the applied magnetic field was measured with a vibrating sample magnetometer (VSM). To perform the measurement, a small amount of dried powder of citrated-MNPs or APPA-MNPs was weighted and introduced in a glass cup connected to a vibration unit and a continuous magnetic field was applied between −1600 and +1600 kA/m with an electromagnet in an environmental controlled area at T = 293K. The magnetization was deduced from the magnetic flux generated by the sample by tracking the voltage generated by the varying magnetic flux in the coils.

The obtained results of magnetization versus applied magnetic field are presented in Figure 16 for maghemite MNPs prepared by the two methods. A superparamagnetic behaviour with no coercivity is confirmed for both, showing that sizes are smaller enough to entail that each particle is composed by a single nanocrystal having the behaviour of individual magnetic domains. These results are in agreement with other studies that established a critical size of 15 nm [11] below which maghemite MNPs show a superparamagnetic behaviour and the results of TEM presented previously with a size of 8.1±1.4 nm for citrated-MNPs and 10.9±1.2 nm for APPA-MNPs.

The saturation magnetization of both MNPs (M_s = 51 $A.m^2.kg^{-1}$ for citrated-MNPs and M_s = 72 $A.m^2.kg^{-1}$ for APPA-MNPs) are lower than the value of bulk maghemite found in the literature (M_s = 84-88 $A.m^2.kg^{-1}$) showing a more important decrease for citrated-MNPs than for APPA-MNPs. There are two reasons to explain those different decreases. Firstly, it is important to remember that the measurements were performed in dried powders of MNPs either with grafted APPA or adsorbed citrated ions. They were prepared with the same conditions as the samples for TGA-DTA. Then, in some extent, the difference in the value of M_s can be

explained by the higher amount of non-magnetic material (water and organic ligands) in citrated-MNPs (~13.5% w/w) than in APPA-MNPs (~6.7% w/w) estimated by the TGA-DTA measurements. Moreover, the size and the morphology of the MNPs influence the observed saturation magnetization. Particularly, the spin disorder at the surface of MNPs has an important effect on the magnetization for very small maghemite MNPs leading to a magnetic core surrounded by a "dead" magnetic layer. Studies on the effect of the size of maghemite MNPs on the saturation magnetization established a clear dependence between the saturation magnetization and the specific surface area of the MNPs [39]. For the present case, the difference in size found in TEM images and the crystallite size obtained by XRD between both types of MNPs leads to a higher specific surface for the smaller citrated-MNPs contributing to their lower saturation magnetization.

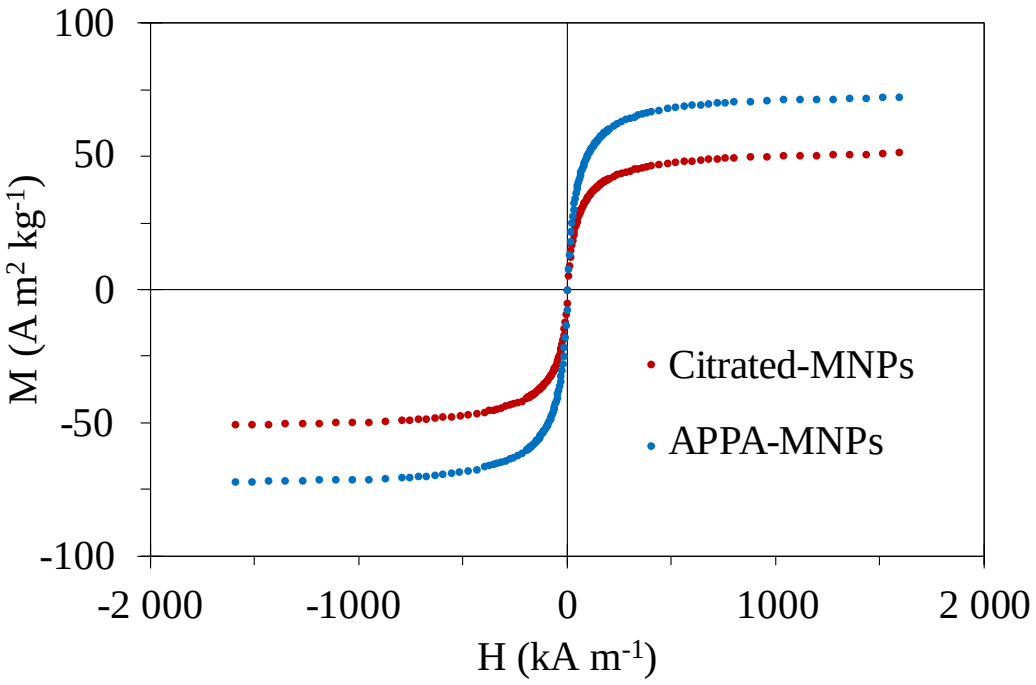

Figure 16: variation of the magnetization versus the applied magnetic field at 293K for citrated-MNPs and APPA-MNPs powders.

4.4. Hydrodynamic size and zeta potential results

The measurements were performed using the Zetasizer nano ZS (Malvern instruments). For the determination of the hydrodynamic size, citrated-MNPs and APPA-MNPs were dispersed in pure water (η=0.89 mPa.s at 25°C) and sonicated for a final concentration of 0.01 % w/w of MNPs. For each measurement 1 mL of sample was placed in a cubic cuvette and the measurement of the temporal fluctuation of the scattering intensity was performed at the constant temperature of 25°C. Through a process of correlating the intensity of scattered photons at various time points, the corresponding decay in correlation is used to determine the diffusion

rate for the MNPs following the Brownian motion due to their thermal energy (kT). More precisely, the hydrodynamic diameter (D_H) of MNPs, defined as the diameter of a sphere that diffuses with the same velocity as the targeted MNPs, was calculated by the software by the fitting of the correlation function with an algorithm based on Einstein-Stokes equation that defines the diffusion coefficient (D) of small particles through a liquid and assuming a logarithmic distribution [40].

$$D = \frac{kT}{3\pi\eta D_H} \quad (1)$$

In the same equipment and equivalent conditions, the electrophoretic mobility of charged MNPs was determined from the particle velocity under an applied electric field using a folded capillary cell. The zeta potential was then calculated from the obtained electrophoretic mobility, by using Henry's equation:

$$\zeta = \frac{3\eta U_E}{2\varepsilon f(ka)} \quad (2)$$

where U_E is the electrophoretic mobility, ε is dielectric constant and f(ka) is the Henry's function with a value of 1.5 following the Smoluchowski approximation for aqueous media and moderate electrolyte concentration [41].

The results of D_H for both types of MNPs are presented in the Figure 17 in the form of distribution of sizes in number per cent corresponding with the recorded signal during 60 seconds with a count rate of 280 and 360 kcounts/s for APPA-MNPs and citrated-MNPs respectively. The mean hydrodynamic diameter and standard deviation can be obtained by adjusting these values by a log-normal distribution. The result for citrated-MNPs shows a single peak with D_H = 9.5±3.1 nm while for APPA-MNPs two peaks were observed with D_H = 99.7±22.8 nm (82%) and D_H = 441±137 nm (18%). For the case of citrated-MNPs, the value is slightly higher than the core diameter determined by TEM (8.1±1.4 nm) as expected for well dispersed MNPs. This slight increase is explained by the presence of citrated ions and roughness in the surface of the MNPs. By contrast, the presence of two peaks and higher values of the D_H for APPA-MNPs indicates a moderate aggregation of particles with a tendency to the sedimentation. It is important to remember that maghemite is a dense material in comparison to water and, as a rule of the thumb, aggregates of MNPs of sizes higher than 100 nm dispersed in water at room temperature have a tendency to precipitate in a few minutes.

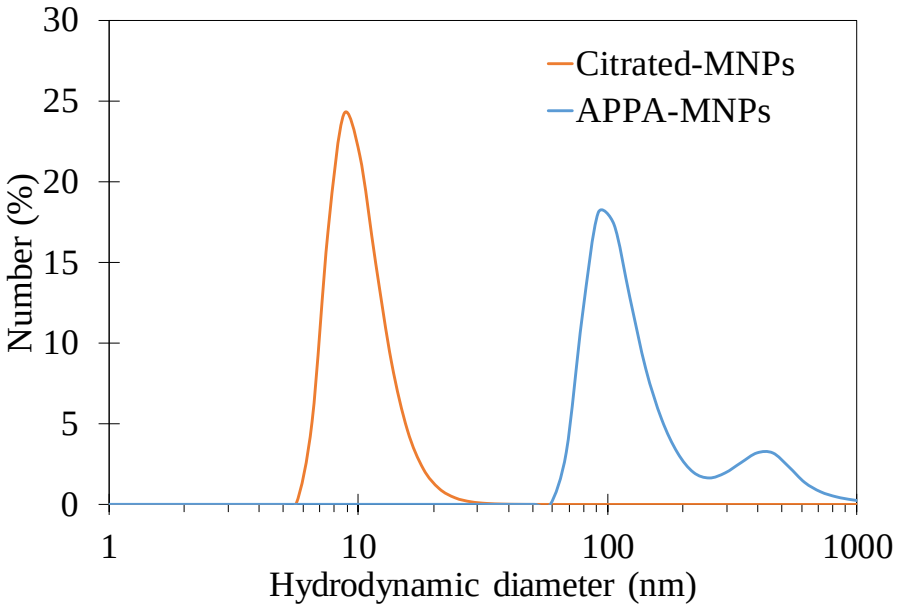

Figure 17: hydrodynamic diameter for MNPs diluted aqueous dispersions

Colloidal stability of MNPs is a key characteristic that is defined as the ability to remain monodispersed in a suspension as a colloid. This is extremely important because superparamagnetic properties of MNPs can be degraded when the aggregation takes place. The stability of the particles in water is determined by attractive magnetic and Van der Waals forces that should be prevented by repulsive electrostatic forces by the surface treatment with either positively charged APPA or negatively charged citrate ions.

A practical way to evaluate that, it is the determination of the Zeta Potential (ZP) directly related to the surface charge presented on the MNPs. A general rule is that a value of the ZP higher than ±30 mV is enough to ensure stable dispersions. The measured values are ZP = -46 mV at pH = 7.5 for citrated-MNPs dispersions in pure water and ZP = +19 mV at pH = 6.6 for APPA-MNPs dispersions in pure water. The higher ZP and therefore higher surface electrostatic charge of citrated-MNPs is in a good agreement with the lower D_H and it confirms a better stability in aqueous dispersion than APPA-MNPs.

5. Conclusions

The synthesis and characterization of the MNPs by two different methodologies lead to the production of high quality maghemite MNPs with the remarkable properties that are summarized in Table 2. Maghemite MNPs covalently grafted with APPA bearing positive surface charge and maghemite MNPs stabilized by adsorption of citrate ions negatively charged were obtained using polyol method and coprecipitation method respectively. For both cases the size is small enough to get single-domain nanometric MNPs with narrow size distribution and

superparamagnetic properties with high magnetization and no-coercivity. Despite the stronger magnetic properties of APPA-MNPs, these MNPs show aggregation and much worse colloidal stability in aqueous dispersion than citrated-MNPs explained by higher hydrodynamic diameter as measured by dynamic light scattering (Table 2) and lower zeta potential in neutral conditions (Table 2). This is an important drawback to obtain a homogeneous dispersion of APPA-MNPs in aqueous dispersion to be mixed with the polymeric matrix in neutral conditions to elaborate nanocomposites. In addition, the quantities of produced APPA-MNPs are quite limited with respect to the required amounts to prepare nanocomposites with the fixed conditions for the present study. Accordingly, citrated-MNPs were considered as the more promising candidate for the development of nanocomposites.

Table 2: summary of properties of MNPs prepared by co-precipitation and polyol method

	Citrated-MNPs	**APPA-MNPs**
Production	8 g/batch	0.6 g/batch
Crystallite size	8.6±0.1 nm	9.6±0.1 nm
TEM Diameter	8.1±1.4nm	10.9±1.2nm
Hydrodynamic diameter	9.5±3.1 nm	100±23 nm (82%) / 441±137 nm (18%)
Saturation magnetization	51.4 $A.m^2kg^{-1}$	72.3 $A.m^2/kg^{-1}$
Zeta potential in pure water	-46 mV	+19 mV

6. References

[1] R. Sardar, A.M. Funston, P. Mulvaney, R.W. Murray, Gold Nanoparticles: Past, Present, and Future, Langmuir. 25 (2009) 13840–13851. https://doi.org/10.1021/la9019475.

[2] D. Chen, X. Qiao, X. Qiu, J. Chen, Synthesis and electrical properties of uniform silver nanoparticles for electronic applications, J. Mater. Sci. 44 (2009) 1076–1081. https://doi.org/10.1007/s10853-008-3204-y.

[3] G.C. Papaefthymiou, Nanoparticle magnetism, Nano Today. 4 (2009) 438–447. https://doi.org/10.1016/j.nantod.2009.08.006.

[4] M. Amiri, M. Salavati-Niasari, A. Akbari, Magnetic nanocarriers: Evolution of spinel ferrites for medical applications, Adv. Colloid Interface Sci. 265 (2019) 29–44. https://doi.org/10.1016/j.cis.2019.01.003.

[5] L. Arias, J. Pessan, A. Vieira, T. Lima, A. Delbem, D. Monteiro, L.S. Arias, J.P. Pessan, A.P.M. Vieira, T.M.T. de Lima, A.C.B. Delbem, D.R. Monteiro, Iron Oxide Nanoparticles for Biomedical Applications: A Perspective on Synthesis, Drugs, Antimicrobial Activity, and Toxicity, Antibiotics. 7 (2018) 46. https://doi.org/10.3390/antibiotics7020046.

[6] P. Azcona, R. Zysler, V. Lassalle, Simple and novel strategies to achieve shape and size control of magnetite nanoparticles intended for biomedical applications, Colloids Surf. Physicochem. Eng. Asp. 504 (2016) 320–330. https://doi.org/10.1016/j.colsurfa.2016.05.064.

[7] S.M. Dadfar, K. Roemhild, N.I. Drude, S. von Stillfried, R. Knüchel, F. Kiessling, T. Lammers, Iron oxide nanoparticles: Diagnostic, therapeutic and theranostic applications, Adv. Drug Deliv. Rev. 138 (2019) 302–325. https://doi.org/10.1016/j.addr.2019.01.005.

[8] A.K. Gupta, M. Gupta, Synthesis and surface engineering of iron oxide nanoparticles for biomedical applications, Biomaterials. 26 (2005) 3995–4021. https://doi.org/10.1016/j.biomaterials.2004.10.012.

[9] K.K. Kefeni, T.A.M. Msagati, T.TI. Nkambule, B.B. Mamba, Spinel ferrite nanoparticles and nanocomposites for biomedical applications and their toxicity, Mater. Sci. Eng. C. 107 (2020) 110314. https://doi.org/10.1016/j.msec.2019.110314.

[10] M. Mahdavi, M. Ahmad, M. Haron, F. Namvar, B. Nadi, M. Rahman, J. Amin, M. Mahdavi, M.B. Ahmad, M.J. Haron, F. Namvar, B. Nadi, M.Z.A. Rahman, J. Amin, Synthesis, Surface Modification and Characterisation of Biocompatible Magnetic Iron Oxide Nanoparticles for Biomedical Applications, Molecules. 18 (2013) 7533–7548. https://doi.org/10.3390/molecules18077533.

[11] P. Tartaj, M. a del P. Morales, S. Veintemillas-Verdaguer, T.G. lez-Carre o, C.J. Serna, The preparation of magnetic nanoparticles for applications in biomedicine, J. Phys. Appl. Phys. 36 (2003) R182–R197. https://doi.org/10.1088/0022-3727/36/13/202.

[12] A.S. Teja, P.-Y. Koh, Synthesis, properties, and applications of magnetic iron oxide nanoparticles, Prog. Cryst. Growth Charact. Mater. 55 (2009) 22–45. https://doi.org/10.1016/j.pcrysgrow.2008.08.003.

[13] A. Hanini, A. Schmitt, K. Kacem, F. Chau, S. Ammar, J. Gavard, Evaluation of iron oxide nanoparticle biocompatibility, Int. J. Nanomedicine. 6 (2011) 787–794. https://doi.org/10.2147/IJN.S17574.

[14] W. Wu, Z. Wu, T. Yu, C. Jiang, W.-S. Kim, Recent progress on magnetic iron oxide nanoparticles: synthesis, surface functional strategies and biomedical applications, Sci. Technol. Adv. Mater. 16 (2015) 023501. https://doi.org/10.1088/1468-6996/16/2/023501.

[15] V.V. Spiridonov, I.G. Panova, L.A. Makarova, S.B. Zezin, A.A. Novakova, T.G. Baluyan, A.V. Sybachin, V.V. Kuznetsov, A.A. Yaroslavov, Magneto-sensitive hybrid nanocomposites of water-soluble sodium alginate cross-linked with calcium ions and maghemite, Express Polym. Lett. 12 (2018) 452–461.

[16] H. Shokrollahi, A review of the magnetic properties, synthesis methods and applications of maghemite, J. Magn. Magn. Mater. 426 (2017) 74–81. https://doi.org/10.1016/j.jmmm.2016.11.033.

[17] A.V. Samrot, C.S. Sahithya, J. Selvarani A, S.K. Purayil, P. Ponnaiah, A review on synthesis, characterization and potential biological applications of superparamagnetic iron oxide nanoparticles, Curr. Res. Green Sustain. Chem. 4 (2021) 100042. https://doi.org/10.1016/j.crgsc.2020.100042.

[18] E. Tombácz, R. Turcu, V. Socoliuc, L. Vékás, Magnetic iron oxide nanoparticles: Recent trends in design and synthesis of magnetoresponsive nanosystems, Biochem. Biophys. Res. Commun. 468 (2015) 442–453. https://doi.org/10.1016/j.bbrc.2015.08.030.

[19] S. Liu, B. Yu, S. Wang, Y. Shen, H. Cong, Preparation, surface functionalization and application of Fe3O4 magnetic nanoparticles, Adv. Colloid Interface Sci. 281 (2020) 102165. https://doi.org/10.1016/j.cis.2020.102165.

[20] S. Ammar, F. Fiévet, Polyol Synthesis: A Versatile Wet-Chemistry Route for the Design and Production of Functional Inorganic Nanoparticles, Nanomaterials. 10 (2020) 1217. https://doi.org/10.3390/nano10061217.

[21] F. Fiévet, R. Brayner, The Polyol Process, in: Nanomater. Danger Promise, Springer, London, 2013: pp. 1–25. https://doi.org/10.1007/978-1-4471-4213-3_1.

[22] H. Basti, L. Ben Tahar, L.S. Smiri, F. Herbst, M.-J. Vaulay, F. Chau, S. Ammar, S. Benderbous, Catechol derivatives-coated Fe3O4 and γ-Fe2O3 nanoparticles as potential MRI contrast agents, J. Colloid Interface Sci. 341 (2010) 248–254. https://doi.org/10.1016/j.jcis.2009.09.043.

[23] B. Zhang, Z. Tu, F. Zhao, J. Wang, Superparamagnetic iron oxide nanoparticles prepared by using an improved polyol method, Appl. Surf. Sci. 266 (2013) 375–379. https://doi.org/10.1016/j.apsusc.2012.12.032.

[24] W. Cai, J. Wan, Facile synthesis of superparamagnetic magnetite nanoparticles in liquid polyols, J. Colloid Interface Sci. 305 (2007) 366–370. https://doi.org/10.1016/j.jcis.2006.10.023.

[25] M. Abbas, B. Parvatheeswara Rao, S.M. Naga, M. Takahashi, C. Kim, Synthesis of high magnetization hydrophilic magnetite (Fe3O4) nanoparticles in single reaction—Surfactantless polyol process, Ceram. Int. 39 (2013) 7605–7611. https://doi.org/10.1016/j.ceramint.2013.03.015.

[26] R.J. Joseyphus, K. Shinoda, D. Kodama, B. Jeyadevan, Size controlled Fe nanoparticles through polyol process and their magnetic properties, Mater. Chem. Phys. 123 (2010) 487–493. https://doi.org/10.1016/j.matchemphys.2010.05.001.

[27] J. Vega-Chacón, G. Picasso, L. Avilés-Félix, M.J. Jr, Influence of synthesis experimental parameters on the formation of magnetite nanoparticles prepared by polyol method, Adv. Nat. Sci. Nanosci. Nanotechnol. 7 (2016) 015014. https://doi.org/10.1088/2043-6262/7/1/015014.

[28] L. Poul, S. Ammar, N. Jouini, F. Fievet, F. Villain, Synthesis of Inorganic Compounds (Metal, Oxide and Hydroxide) in Polyol Medium: A Versatile Route Related to the Sol-Gel Process, J. Sol-Gel Sci. Technol. 26 (2003) 261–265. https://doi.org/10.1023/A:1020763402390.

[29] J. Fouineau, K. Brymora, L. Ourry, F. Mammeri, N. Yaacoub, F. Calvayrac, S. Ammar-Merah, J.-M. Greneche, Synthesis, Mössbauer Characterization, and Ab Initio Modeling of Iron Oxide Nanoparticles of Medical Interest Functionalized by Dopamine, J. Phys. Chem. C. 117 (2013) 14295–14302. https://doi.org/10.1021/jp4027942.

[30] S. Mohapatra, P. Pramanik, Synthesis and stability of functionalized iron oxide nanoparticles using organophosphorus coupling agents, Colloids Surf. Physicochem. Eng. Asp. 339 (2009) 35–42. https://doi.org/10.1016/j.colsurfa.2009.01.009.

[31] S. Babay, T. Mhiri, M. Toumi, Synthesis, structural and spectroscopic characterizations of maghemite γ-Fe2O3 prepared by one-step coprecipitation route, J. Mol. Struct. 1085 (2015) 286–293. https://doi.org/10.1016/j.molstruc.2014.12.067.

[32] R. Massart, Magnetic fluids and process for obtaining them, US4329241A, 1982. https://patents.google.com/patent/US4329241A/en (accessed November 17, 2020).

[33] I.T. Lucas, S. Durand-Vidal, E. Dubois, J. Chevalet, P. Turq, Surface Charge Density of Maghemite Nanoparticles: Role of Electrostatics in the Proton Exchange, J. Phys. Chem. C. 111 (2007) 18568–18576. https://doi.org/10.1021/jp0743119.

[34] J. Mürbe, A. Rechtenbach, J. Töpfer, Synthesis and physical characterization of magnetite nanoparticles for biomedical applications, Mater. Chem. Phys. 110 (2008) 426–433. https://doi.org/10.1016/j.matchemphys.2008.02.037.

[35] V. Pecharsky, P. Zavalij, Fundamentals of Powder Diffraction and Structural Characterization of Materials, Second Edition, 2nd ed., Springer US, 2009. https://doi.org/10.1007/978-0-387-09579-0.

[36] C. Galindo-Gonzalez, S. Gantz, L. Ourry, F. Mammeri, S. Ammar-Merah, A. Ponton, Elaboration and Rheological Investigation of Magnetic Sensitive Nanocomposite Biopolymer Networks, Macromolecules. 47 (2014) 3136–3144. https://doi.org/10.1021/ma402655g.

[37] V. Rocher, J. Manerova, M. Kinnear, D. J. Evans, M. G. Francesconi, Direct amine-functionalisation of γ-Fe_2O_3 nanoparticles, Dalton Trans. 43 (2014) 2948–2952. https://doi.org/10.1039/C3DT52386A.

[38] Thermal decomposition of citric acid, Thermochim. Acta. 98 (1986) 119–126. https://doi.org/10.1016/0040-6031(86)87081-2.

[39] A.G. Roca, R. Costo, A. Rebolledo, S. Veintemillas-Verdaguer, P. Tartaj, T. Gonzalez-Carreno, M. del P. Morales, C. Serna, The preparation of magnetic nanoparticles for applications in biomedicine, J. Phys. Appl. Phys. 42 (2009) 224002. https://doi.org/10.1088/0022-3727/42/22/224002.

[40] I. Ostolska, M. Wiśniewska, Application of the zeta potential measurements to explanation of colloidal Cr2O3 stability mechanism in the presence of the ionic polyamino acids, Colloid Polym. Sci. 292 (2014) 2453–2464. https://doi.org/10.1007/s00396-014-3276-y.

[41] R.J. Hunter, Zeta Potential in Colloid Science: Principles and Applications, Academic Press, 2013.

Chapter II: polymer solutions

1. Introduction

The second component required to elaborate a magneto-sensitive nanocomposite is the polymer matrix with the main role of providing a support for the MNPs, imparting stability and processability. Moreover, the use of biopolymers with numerous applications in biomedical science and tissue engineering [1] allow to implement other interesting properties such as biocompatibility, biodegradability and ease of gelation. For the present case we are focused on aqueous solution of water-soluble polymers and polyelectrolytes in which previously synthetized MNPs can be dispersed to elaborate nanocomposite solutions.

The use of polymeric materials for the elaboration of such nanocomposites with application in tissue engineering have attracted a lot of attention since 1990 and many alternatives can be found in the literature [2–5]. Depending on their origin, they can be classified in two main groups: natural or synthetic. The choice of natural polymers [6] (proteins, polysaccharides, polyhydroxyalkanoates and polynucleotides) possesses the advantages of presenting high biocompatibility and biodegradability, while synthetic polymers [7] (polyvinyls, poly(ethylene glycol) and polyesters) are more stable and show more tractable and reproducible properties. These different polymers can be crosslinked to elaborate networks by a wide range of methodologies [8,9] either by covalent bonds (chemical gels) or by physical interactions (physical gels) as it will be discussed in the chapter III.

The outline of this chapter is the following. After a theoretical description of the dynamical properties of polymer and polyelectrolyte solutions, four polymers are characterized in order to select the ones to elaborate hydrogels and nanocomposites. Firstly, a general study including rheology, FTIR and zeta potential experiments on aqueous solutions of the four polymers is presented in order to link their viscoelastic properties with their chemical composition, conformation and structure in aqueous solution. Secondly a multiscale investigation of the viscoelastic properties of the selected polymer is presented coupled with SAXS measurements to measure directly the structural properties.

2. Neutral polymers and polyelectrolytes

In this chapter, theoretical concepts on polymer conformation and their dynamical behaviour in aqueous solution [10,11] will be introduced to understand and to describe the microstructure of the polymeric matrix of nanocomposites. Different strategies will be firstly presented for the characterization of individual polymer coils underlying the most relevant parameters. Then, the dynamics of neutral polymer and polyelectrolyte solutions will be discussed to establish a base on different behaviours and microstructures that can be found in a polymer solution depending on the polymer nature, the interactions between polymer coils and monomers and the polymer concentration.

2.1. Generalities on polymer

In 1920, H. Staudinger proposed the macromolecular hypothesis. This revolutionary concept, involving the formation of very long molecules by the repetition of a large number of elementary monomers linked through covalent bonds, was acknowledged by the award of the Nobel Prize for Chemistry and marked the beginning of the high molecular weight structural and functional polymeric materials. The number of monomers (N) in a giant molecule is the degree of polymerization. A polymer can be defined by his contour length (L_c) that is the result of the multiplication of N and the monomer length (a) or by his molecular weight (M_w) depending on N and the monomer molecular weight (M_i). A schematic representation of a polymer composed of fifteen monomers of length a is shown in Figure 1. For any polymer, the physical properties, such as viscosity or melting temperature, increase with the contour length or the molecular weight.

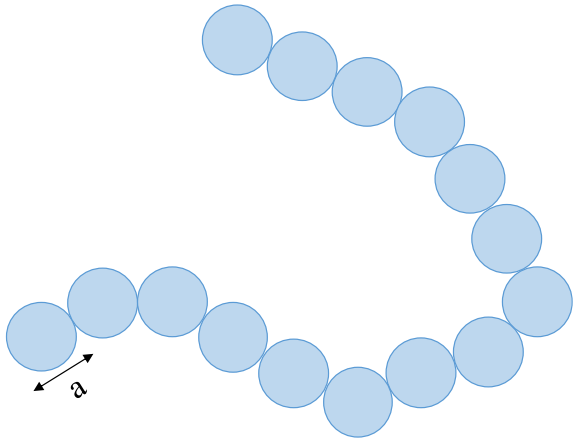

Figure 1: schematic representation of a polymer composed of fifteen monomers of length a.

Polymers can be classified depending on their monomer composition in homopolymers made by repetition of identical monomers and heteropolymers made by a combination of different types of monomers in the same chain. Another important feature controlling the

properties is the polymer architecture. Types of polymer architectures include linear, ring, star-branched, H-branched, comb, ladder, or randomly branched chains. However, we are focused in linear homopolymers in the present study. Polymer properties can be highly variable depending mainly on the chemical identity of monomers and the polymer microstructure (organization of atoms along the chain). Therefore, it will be presented and discussed the theoretical models and descriptions in this subchapter for a better understanding of the different possible conformations of polymer chains in solution.

2.2. Single chain conformations

Flexible polymers can have an enormous number of configurations by the rotation of chemical bonds that are controlled by the interactions with the solvent and with the other monomers of the chain. They can be divided in short range interactions, between adjacent or closer monomers, and long-range interactions, between monomers that are far apart along the chain. It will be first considered the simplest case of chains with no long-range interactions, named ideal chains. By representing the bond connecting two backbone atoms by a vector $\vec{r_i}$ defining their axis of rotation (Figure 2), the main source of flexibility is the variation of torsion angles (φ) and bond angles (θ) that will tend to the lowest energy conformation depending on the different steric interactions between the involved chemical groups.

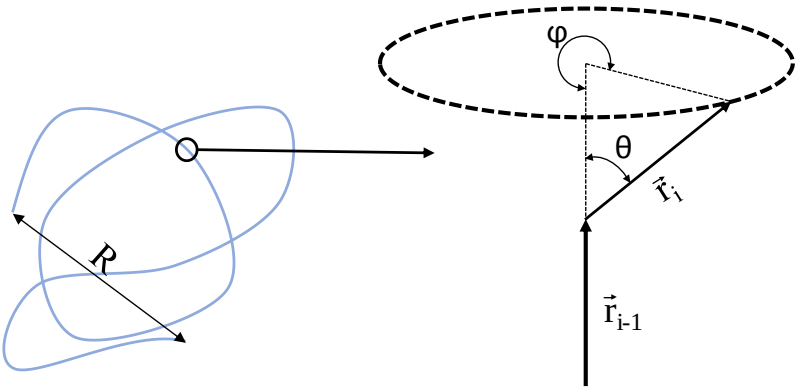

Figure 2: conformation of polymer and torsion and bond angle between two backbone atoms.

Whatever they are the angles θ and φ along the chain, the end-to-end distance (R) for an ideal polymer will be proportional to $a.C.N^{1/2}$ where C is the Flory's characteristic ratio which depends on the local stiffness of the polymer chain. A simple unified description can be provided by the concept of an equivalent chain with the same end-to-end distance (R) and the same contour length (L_c) as the actual polymer but has N' freely-jointed theoretical monomers of a length named Kunh length (b). This later is a sort of physical repeating unit that correspond to 1/2 of the persistence length (L_p), defined as the longest segment along the polymer backbone for which the orientation persists. L_p is a way to quantify the local stiffness of the polymer

chain, with higher value of L_p for stiffer chains with restrictive values of the angles θ and φ. Then the value of the end-to-end distance (R) for an ideal chain following Gaussian statistics can now be defined as $b.N'^{1/2}$ and the value of b or L_P can be either found in the literature or determined experimentally by scattering techniques.

However, long-range interactions neglected for the case of ideal chains are often important for the real polymers. An obvious interaction is the steric effect: two monomers cannot be present in the same positions at the same moment. This interaction swells the polymer increasing the coil size and it is named excluded volume effect in reference to the not available volume for a monomer because another is already there. The consideration of these steric effect in conjunction with Van de Waals attraction between monomers allow to perform a much more representative physical descriptions of real polymer conformation in solution. Considering these effects, R is not anymore proportional to $N^{1/2}$ but to N^{υ}. The value of the scaling exponent υ can be estimated based on some theories depending on the characteristics of the polymer-solvent system.

Regarding the polymer-solvent system, it is important to consider if polymer–solvent contacts are energetically more or less favourable than polymer-polymer contacts. If polymer-solvent contacts are more favourable, the chain will expand to minimize the contacts between monomers. For such case, it is considered a good solvent and υ=3/5 is a good estimation. In the opposite case in which polymer-polymer contacts are more favourable, the chain will contract to maximize the contacts between monomers. For such case, it is considered a bad solvent with υ=1/3. Between these two situations, it is defined the θ-solvent in which both contacts are equally favourable, and the conformation is given by Gaussian statistics with υ=1/2. The quality of the solvent depends on the polymer and solvent chemical compositions and the temperature of solution.

2.3. Dynamics of neutral polymer solutions

Polymer dynamics offer a powerful approach to study molecular-level interactions and dynamic microstructure in materials. Three different regimes with differentiated dynamical behaviours can be found depending on the interactions between the polymer coils. As schematized in Figure 3, diluted, semi-diluted and concentrated regimes are delimited by two critical concentrations named overlap concentration (c*) and crossover concentration (c**) that will be defined below in more detail.

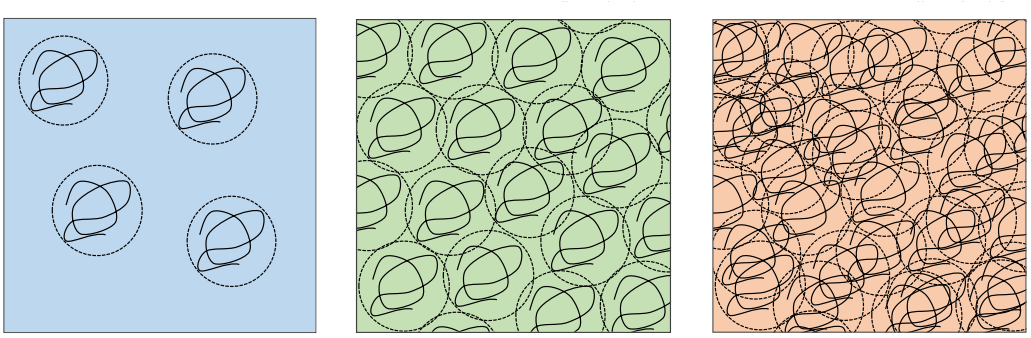

Figure 3: concentration regimes in polymer solution.

2.3.1. Diluted regime

At low concentrations, polymer coils are far from each other and behave as isolated real chains in the diluted regime. Then, the value of R is defined by the description of real chains considering the excluded volume as described previously ($R \approx a.N^{\upsilon}$) with the appropriate values of υ depending on the quality of the solvent. The viscosity of diluted polymer solutions is usually higher than just the viscosity of the solvent, due to the differences in size between the polymer and solvent molecules. For a solution of impenetrable spheres, the viscosity of the solution (η) can be determined by the Einstein equation:

$$\eta = \eta_0(1 + 2.5\phi) \quad (1)$$

where η_0 is the viscosity of the solvent and ϕ is the volume fraction of spheres in the solution and can be determined for the case of a polymer coil by:

$$\phi = \frac{4\pi N_A}{3M} R^3 C \quad (2)$$

where N_A is the Avogadro number, M is the polymer molecular mass, R is the radius of the sphere and C is the polymer concentration. Then, the viscosity of diluted solutions of polymers within the hypothesis of rigid spheres increases linearly with the polymer concentration.

2.3.2. Semi-diluted regime

Semi-diluted conditions are reached at the critical overlap concentration of polymer (c*), defined as the concentration within a given dilute conformation's pervaded volume is equal to the solution concentration [12]. In terms of number density of Kuhn monomers, the overlap can be estimate as $c^* \approx N/R^3$ [11] where N is the number of Kuhn monomers in the chain and R is the diluted solution size of the chain. Each monomer is surrounded at small distances by mostly solvent and a few monomers belonging to the same chain.

In semi-diluted regime the relevant length is the correlation length (ξ_c) rather than the radius of a single chain (R). Since the monomer interactions are screened out beyond the correlation distance, a single chain of N monomers may be viewed as a succession of subunits (blobs) of R = ξ_c, each containing g_c monomers. The conformations of the section of chain of size ξ_c containing g_c monomers are very similar to those for a chain in diluted solution. The correlation length can be defined (Figure 4) either as the distance of a monomer to nearest monomers on neighbouring chains (in this case named also mesh size) or as the radius of a blob containing a section of chain of g_c monomers that behaves in the similar way to the one of diluted regime.

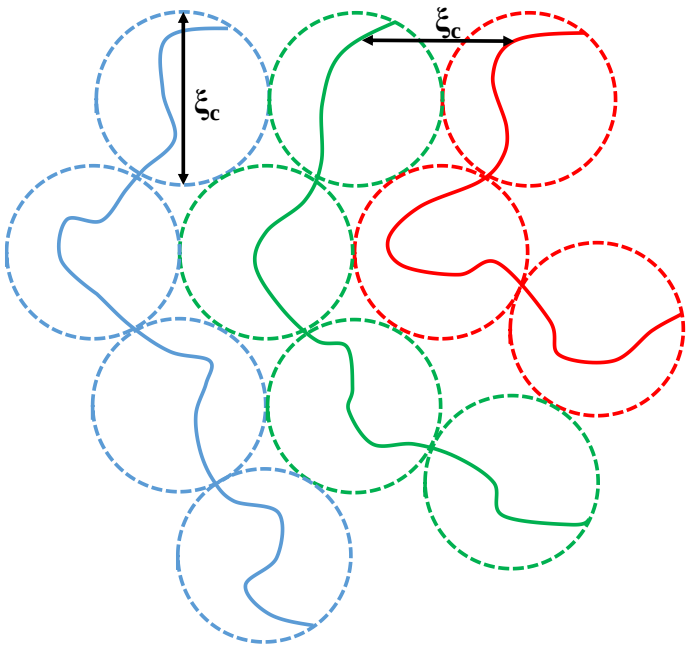

Figure 4: polymer solution in the semi-diluted regime described by the correlation length.

The interest for a solution in the semi-diluted regime is then focused on the estimation of ξ_c and the change in the properties of the polymer solution with the concentration. The value of ξ_c decreases and the viscosity (η) increases with the concentration because the higher number of molecules in solution promotes the occurrence of intermolecular interactions as well as the formation of entangled structures and structural contraction. In the Table 1 are summarized the relations of both η and ξ_c as function of c and N and for the neutral polymer in different solvent conditions accordingly with the values of υ presented previously. The correlation length depends on the concentration of monomers but no on the number of monomers (N) in each polymer chain while the viscosity depends on both parameters, as expected.

Table 1: concentration and N dependence of the correlation length, chain relaxation time and viscosity in the semi-diluted regime

Parameter	General	Θ-solvent	Good solvent
Scaling exponent	υ	1/2	3/5
Correlation length (ξ_c)	$\xi_c \sim c^{\frac{-\upsilon}{3\upsilon-1}}$	$\xi_c \sim c^{-1}$	$\xi_c \sim c^{-3/4}$
Chain relaxation time (τ)	$\tau \sim N^2 c^{\frac{2-3\upsilon}{3\upsilon-1}}$	$\tau \sim N^2 c$	$\tau \sim N^2 c^{1/4}$
Viscosity (η)	$\eta - \eta_S \sim N c^{\frac{1}{3\upsilon-1}}$	$\eta - \eta_S \sim N c^2$	$\eta - \eta_S \sim N c^{5/4}$

All the scaling laws in the semi-diluted regime summarized in Table 1 depend on the length scale for each polymer-solvent system. On length scales smaller than ξ_c, excluded volume interactions are strong enough to swell the chain, υ=3/5 (good solvent), while, on length scales larger than ξ_c, excluded volume interactions are screened by surrounding chains, υ=1/2 (θ-solvent).

Two main models have been proposed to describe a polymer coil [13]:

- The Zimm model considers hydrodynamic interactions and exclude volume describing the behaviour at length scales smaller than ξ_c. The Zimm relaxation time is defined by:

$$\tau_{Zimm} \approx \frac{\eta_s}{k_B T} R^3 \tag{3}$$

where η_s is the solvent viscosity, k_B is the Boltzmann constant and T is the absolute temperature.

- The Rouse model does not consider excluded volume and hydrodynamic interactions describing the behaviour for length scales larger than ξ_c. The Rouse relaxation time is defined by:

$$\tau_{Rouse} \approx \frac{\eta_s a}{k_B T} N . R^2 \tag{4}$$

The dynamical behaviour of a semi-diluted polymer solution can be described by a set of polymer blobs of size ξ_c containing g_c monomers, inside which, excluded volume and hydrodynamic effects are important. On the contrary, these excluded volume and hydrodynamic effects are not relevant between the sections of polymer contained in the different blobs. Then, the correct approach is to consider the Rouse relaxation time as a factor of the Zimm relaxation time by the number of units $(N/g_c)^2$ obtaining the following expression:

$$\tau_{Rouse} \approx \left(\frac{N}{g_c}\right)^2 \tau_{Zimm} \approx \frac{\eta_s}{k_B T} \cdot \left(\frac{N}{g_c}\right)^2 \xi_C^3 \tag{5}$$

The relation deduced previously for individual coils $R=a.N^{\upsilon}$ is fully applicable transformed to $\xi_c=g_c^{\upsilon}.a$. Combining this relation with the definition of ξ_c in Table 1 it is obtained:

$$g_c \propto c^{\frac{-1}{3\nu-1}} \tag{6}$$

Combining equations 4, 5 and 6 the following equation defining the concentration dependence of the relaxation time in a semi-diluted solution is obtained:

$$\tau_{Rouse} \propto N^2 \, c^{\frac{2-3\nu}{3\nu-1}} \tag{7}$$

The value of the viscosity is deduced by the multiplication of this relaxation time by the terminal modulus (G) defined by:

$$G \approx \frac{k_B T c}{N} \tag{8}$$

2.3.3. Concentrated regime

A polymer in the semi-diluted regime is defined by two characteristics lengths: the correlation length (ξ_c) and the Kuhn length (b). As it has been described previously the correlation length decrease as the polymer concentration is increased with an exponent -3/4 in a good solvent. On the contrary the Kuhn length does not depend on the polymer concentration. The crossover concentration (c**) that defines the beginning of the concentrated regime corresponds to the point at which the two characteristic distances are equal ($b= \xi_c$).

For $c \geq c^{**}$, the excluded volume interactions are weaker than the thermal energy at all length scales. The excluded volume interactions for length scales larger than ξ_c are screened by overlapping chains. To describe this behaviour of an entangled polymer solution, Doi-Edwards model can be applied based on the reptation model for a single chain developed by De Gennes [14,15]. This model describes the motion of a chain that is confined inside a tube of surrounding chains (Figure 5). This tube with a diameter (d_{tube}) is composed of N_e/g_c correlation blobs of size ξ_c, with each strand between entanglements of size d_{tube} containing N_e blobs. The results of this analysis are summarized in the Table 2.

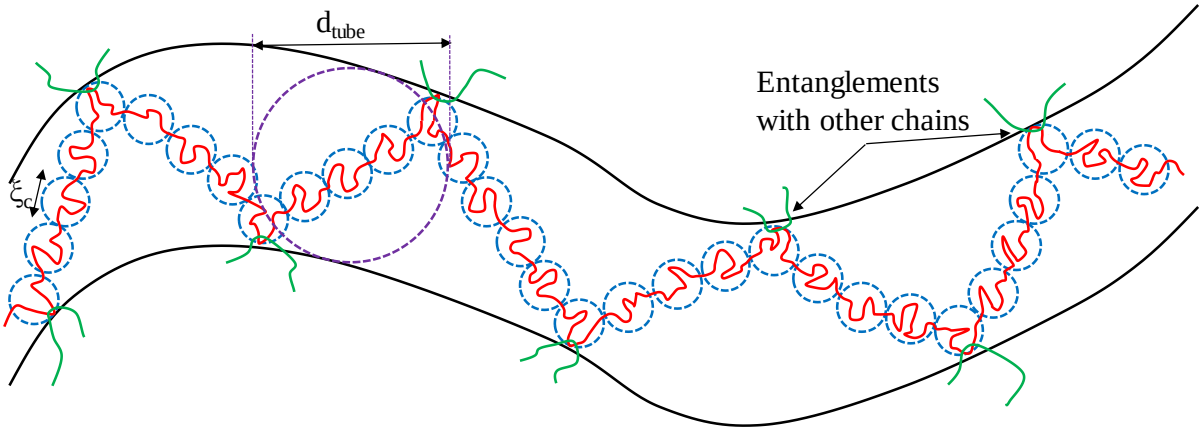

Figure 5: polymer solution in the concentrated regime described in a confined tube.

Table 2: concentration and N dependence of the number of monomers in a strand (N_e), chain relaxation time and viscosity in the concentrated regime.

Parameter	General	Good solvent
Scaling exponent	υ	3/5
Number of monomers in a strand (N_e)	$N_e \sim c^{\frac{-1}{3\upsilon-1}}$	$N_e \sim c^{-5/4}$
Chain relaxation time (τ)	$\tau \sim N^3 c^{\frac{3(1-\upsilon)}{3\upsilon-1}}$	$\tau \sim N^3 c^{3/2}$
Viscosity (η)	$\eta - \eta_S \sim N^3 c^{\frac{3}{3\upsilon-1}}$	$\eta - \eta_S \sim N^3 c^{\frac{15}{4}}$

Analysing the problem in different steps from the smaller to the larger scale, the behaviour inside a blob is the same as in a semi-diluted solution being described by the Zimm model (equation 3). The behaviour of a section composed of different blobs at length scales between ξ_c and d_{tube}, can be likewise described by the Rouse relaxation (equation 7) as the excluded volume and hydrodynamic effects are not relevant between the sections of polymer contained in the different blobs. However, this expression has to be adapted to the new constraints obtaining:

$$\tau_{Rouse} \approx \frac{\eta_s}{k_B T} \xi_c^3 \left(\frac{N_e}{g_c}\right)^2 \tag{9}$$

The reptation model describes the motion of the polymer as a diffusion of small loops, along the contour of the primitive path that is characterized by a curvilinear diffusion coefficient D_c:

$$D_C = \frac{k_B T}{N\zeta} \tag{10}$$

where $N\zeta$ is the Rouse friction coefficient. The reptation time is given by [11]:

$$\tau_{rep} \approx \tau_{Rouse}\left(\frac{N}{N_e}\right)^3 = \frac{\eta_s}{k_B T}\xi_c^3\left(\frac{N_e}{g_c}\right)^2\left(\frac{N}{N_e}\right)^3 \quad (11)$$

The diameter of the tube results by the addition of N_e/g_c blobs of size ξ_c:

$$d_{tube} = \left(\frac{N_e}{g_c}\right)^{1/2}\xi_c \quad (12)$$

Combining equations 6 and 12 and knowing that the diameter of the tube is bigger and proportional to the diameter of each of the blobs ($d_{tube} \propto \xi_c$) the concentration dependence of the number of blobs is:

$$N_e \propto c^{-1/(3\nu-1)} \quad (13)$$

Finally, combining equations 11 and 13 the concentration dependence of the relaxation time is obtained:

$$\tau_{rep} \sim N^3 c^{\frac{3(1-\upsilon)}{3\upsilon-1}} \quad (14)$$

The occupied volume of an entanglement strand is $\xi_c^3 N_e/g_c \approx a^2\xi_c$. Since the correlation volumes are space-fillings in solution, the number density of entanglement strands is simply the reciprocal of this volume. Then, the plateau modulus (G_e) of an entangled polymer solution is of the order of k_BT per entanglement strand:

$$G_e \approx \frac{k_B T}{a^2\xi_c} \sim c^{\frac{3\upsilon}{3\upsilon-1}} \quad (15)$$

The polymer contribution to the viscosity of an entangled polymer solution is estimated as the product of the plateau modulus (G_e) and the reptation relaxation time:

$$\eta - \eta_s \sim \eta_s N^3 c^{\frac{3}{3\upsilon-1}} \quad (16)$$

2.4. Dynamics of polyelectrolyte solutions

Polyelectrolytes (Figure 6) are defined as polymers built up of monomers with an ionisable group, i.e., a group that can dissociate in polar solvents into a chain-fixed cation or anion and a mobile counter-ion bearing the opposite charge [16]. This causes a chain stretching due to the repulsive electrostatic forces, changing dramatically the distribution of the chains in a solvent and their dynamical behaviour with respect to neutral polymers.

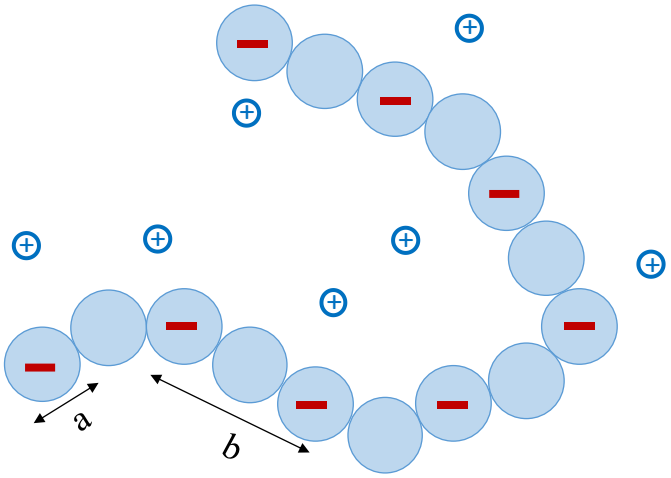

Figure 6: schematic representation of a polyelectrolyte negatively charged.

However, the interactions are not simply defined by the electrostatic repulsion between the chain-fixed ions. Free counter ions also play a key role. The strong attractive forces prevent them from diffusing away the chain. Part of them is kept as a condensate in the immediate neighbourhood of the chain-fixed ion so that the effective charge density is reduced screened by a shell of counter-ions. Then, the contribution of counterions leads to units with an elementary charge only at distances along the chain that are larger than the monomeric length. This characteristic minimum distance is known as the Bjerrum length (λ_B), while the length of the charge compensating cloud is known as the Debye length (λ_D). It varies with the ionic strength given by the total concentration of mobile ions.

These electrostatic interactions between charges lead to the rich behaviour of polyelectrolyte solutions qualitatively different from those of neutral polymers. For example [17]:

- The overlap concentration c* is much lower than in solutions of neutral chains.
- They have higher osmotic pressures.
- The viscosity is proportional to the square root of polyelectrolyte concentration (Fuoss' law [18]).
- Polyelectrolyte chains in semi-diluted regime follow unentangled dynamics in a much wider concentration range.

Polymer dynamics offers as for neutral polymers a powerful approach to study molecular-level interactions and dynamic microstructure in polyelectrolytes. As previously, three different regimes with differentiated dynamical behaviours can be found depending on the interaction between the coils. As schematized previously in Figure 3, diluted, semi-diluted and concentrated regimes are delimited by two critical concentrations named overlap concentration

(c*) and crossover concentration (c**). However, the electrostatic interactions occurring in polyelectrolytes make some important differences in the equations and relations presented previously for neutral polymer solutions as it will be discussed below.

2.4.1. Diluted regime

In diluted solutions below the overlap concentration c*, the intrachain interactions dominate over the interchain ones. To describe a diluted polyelectrolyte solution, each chain can be divided in electrostatic blobs of size ξ_e. Inside each of these blobs the electrostatic interactions are negligible, so that only electrostatic interactions with the other blobs are considered. The size of each of these blobs depends on the polyelectrolyte-solvent system and is given by the following equation in the case of good solvent [19]:

$$\xi_e \approx g_e^{3/5} a \tag{17}$$

where g_e is the number of monomers in an electrostatic blob and a is the size of a monomer.

The electrostatic repulsions between the different blobs lead to a tendency to stiffen in order to maximize the separation of ionic groups at scales larger than ξ_e while they have a conformation similar to neutral polymers at scales lower that ξ_e as schematized in Figure 7.

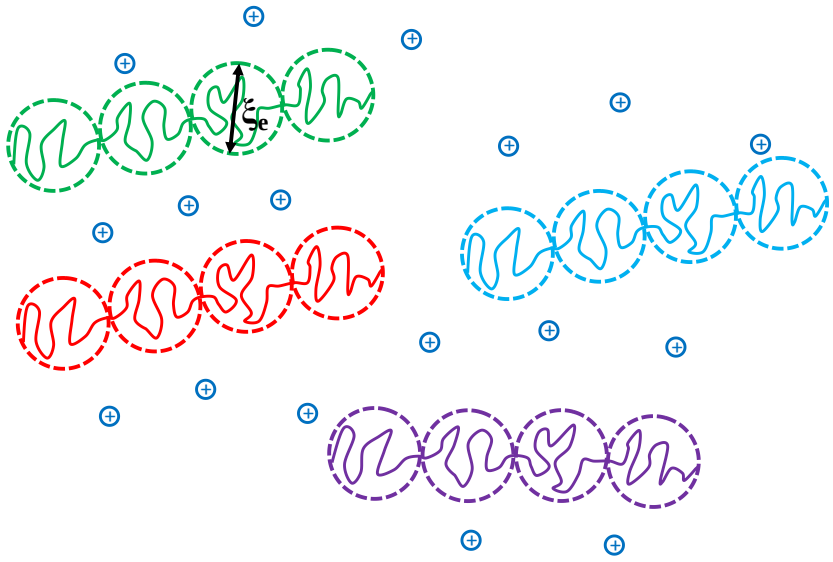

Figure 7: polyelectrolyte conformation in diluted conditions.

In order to describe the conformation of polyelectrolytes, Odijk [20] and Skolnick *et al.* [21] have deduced the following equation for the persistence length (L_p) based on definition of the free energy:

$$L_p = L_{pi} + L_{pe} \tag{18}$$

where L_{pi} is the intrinsic persistence length in the absence of charges and L_{pe} is the electrostatic persistence length related to the presence of electrostatic charges defined by:

$$L_{pe} = \frac{\lambda_B \lambda_D^2}{4b^2 \xi_M^2} \quad (19)$$

where λ_B and λ_D are the Bjerrum and Debye length respectively, as described previously, b is the distance between charges and ξ_M is the so-called Manning parameter ($\xi_M = \lambda_B/b$) that takes into account the effect of the counterions condensation along the polymer chain. More precisely Oosawa-Manning [22,23] model provides the means for obtaining the electrostatic contribution to the total free energy of the interaction considering two possible conformations of the counterions: free or condensed. This equation defines how a polyelectrolyte chain become more flexible in solvents with high ionic strength.

These effects of the ionic concentration on the persistence length also lead to a more complicate dynamical behaviour than in the case of neutral polymers since the electrostatic repulsions are also strongly influenced by the concentration and the mobility of free counterions. Unlike neutral polymers, two different behaviours inside the diluted regime can be differentiated depending on the concentration. For very diluted conditions, the size of an electrostatic blob ξ_e is higher than the distance between chains. In these conditions counterions are generally in solution not closely interacting with the chain. A critical concentration named interaction concentration (c_{int}), is achieved when the screening Debye length and the distance between chains are similar. For most of the cases, when $c>c_{int}$, the solution is still in the diluted regime below the overlap concentration c*, but the behaviour is drastically changed due to the increase of the concentration of counterions. Then, in the range $c_{int} < c < c^*$, each of the chains is associated to a cloud of counterions interacting with the other chains. This situation can be identified by a non-monotonous variation of the viscosity as function of the concentration inside the diluted regime.

2.4.2. Semi-diluted regime

As for neutral polymers, the main feature in the semi-diluted regime is the existence of a correlation length, ξ_c. On lengths scales smaller than ξ_c, the diluted solution scaling can be applied while on length scales larger than ξ_c, the chain is a random walk. The polyelectrolyte correlation length ξ_c can be described as for neutral polymers by a power law depending on the concentration c:

$$\xi_c = L\left(\frac{c}{c^*}\right)^m \quad (20)$$

From the molecular weight dependence of the overlap concentration $c^* \sim N^{-2}$ and the diluted chain size $L \sim N$, we find the exponent m=-1/2 and $\xi_c \sim c^{-1/2}$. The definition of the

number of monomers inside an electrostatic blob is $g_e \approx c.\xi_c^3$ and then $g_e \sim c^{1/2}$. Thus, a polyelectrolyte has a different concentration dependence of the correlation length than a neutral polymer ($\xi_c \sim c^{-3/4}$). It is important to remark than then in the semi-diluted regime there are two critical sizes: (1) electrostatic blob ξ_e limiting the length scales of electrostatic interactions and (2) correlation length ξ_c limiting the length scales of all kinds of interactions.

The approach applied previously for neutral polymers with equation 7 and Figure 4 can be now applied for polyelectrolytes taking into account the different concentration dependence of ξ_c obtaining the following concentration dependence for the relaxation time and the viscosity:

$$\tau_{Rouse} \propto c^{-1/2} \tag{21}$$

$$\eta_0 \propto c^{1/2} \tag{22}$$

2.4.3. Concentrated regime

Applying the approach explained previously for neutral polymers with the equation 11 and Figure 5, the concentration dependence of the relaxation time and the viscosity can be obtained as:

$$\tau_{rept} \propto c^0 \tag{23}$$

$$\eta_0 \propto c^{3/2} \tag{24}$$

However, for high polyelectrolyte concentrations, the concentration dependence of the viscosity can be described by scaling arguments like in a neutral polymer solution since entanglement effects dominate due to the screening of electrostatic, excluded volume, and hydrodynamic interactions [24]. For such case equations 14 and 16 are the best approach.

2.4.4. Effect of salt concentration

The electrostatic interactions between charged monomers in polyelectrolyte solutions can be screened by the presence of salt ions. Thus, a polyelectrolyte chain in salt solutions behaves as a semi-flexible polymer with salt concentration dependence stiffness and persistence length as schematized in Figure 8. This means that the size of a polyelectrolyte coil will decrease until a limit that corresponds with the total screening of electrostatic repulsions having an effect on the persistence length (equation 19) and on the critical concentrations that define the different regimes of concentration. Of course, the overlap concentration (c*) and the crossover concentration (c**) will increase by the addition of salt. This decrease of the coil size will also decrease the viscosity of the polyelectrolyte solution.

Polyelectrolyte in salt-free solution

Polyelectrolyte in solvent with salt

Figure 8: conformation of a polyelectrolyte in salt-free solution and in a salt solvent with a high ionic strength.

In the semi-diluted regime, the effect of added salt has been studied by Dobrynin *et al.* [17,19]. It is important to remember that the electrostatic interactions in salt-free solutions are screened at length scales below the correlation length ξ_c. The reason for such screening is that the Debye screening length is larger than the correlation length ξ_c. But this electrostatic screening length depends now on the ionic concentration. Under a number of assumptions developed in [17], it has been deduced that any quantity X^s characteristic of the polyelectrolyte solution with salt concentration c_s can be expressed in terms of the same property X in a salt-free solution as:

$$X^S = X\left(1 + \frac{2c_s}{fc}\right)^{\alpha} \qquad (25)$$

where f is the fraction of charged monomers and α is a characteristic exponent that depends on the regime of concentration. Based on the equation 25 and previously deduced concentration dependence of the relaxation time and the viscosity of salt-free polyelectrolyte solution (equations 22-25), scaling laws and exponents for a semi-diluted and concentrated polyelectrolyte solution in the presence of added salt can be deduced as summarized in Table 3.

Table 3: concentration dependence of the relaxation time and viscosity of a polyelectrolyte solution in the presence of salt.

Parameter	**Semi-diluted regime**		**Concentrated regime**	
Chain relaxation time (τ)	α = -3/4	$\tau \sim c^{-1/2} + c^{1/2}$	α = -3/2	$\tau \sim c^{0} + c^{3/2}$
Viscosity (η)	α = -3/4	$\eta_0 \sim c^{1/2} + c^{5/4}$	α = -9/4	$\eta_0 \sim c^{3/2} + c^{15/4}$

3. Description of the four studied polymers

3.1. Introduction

It is important to remember that the focus of this work is the elaboration of nanocomposites by introducing the previously synthetized MNPs in firstly the different polymer solutions and secondly the crosslinking of the polymer to elaborate nanocomposite

hydrogels. Within this general objective, the focus of this paragraph is the selection and study of four polymers used for the studied nanocomposites. Among the numerous biocompatible polymers and polyelectrolytes appropriate for the elaboration of hydrogels that can be found in the literature [5, 9, 21, 22], two natural derived polymers (sodium alginate (polysaccharide) and gelatin (protein)) and a synthetic polymer (poly (vinyl alcohol) (PVA)) have been chosen. In addition, alginate dialdehyde (ADA) obtained by the oxidation of sodium alginate was also included. This selection has been done with the objective of the modulation of the interactions between the polymer chains and MNPs (positive or negative electrostatic interactions, no interaction) and the crosslinking process of the polymer matrix (ionic, thermal cycles or covalent crosslinking without addition of crosslinking agent).

3.2. Sodium alginate

Alginates are the main structural component of the skeleton of brown algae such as, *Laminaria hyperborea*, *Laminaria digitata*, and *Macrocystis pyrifera*; with a structural function similar to that of cellulose in land plants. Structurally, alginates are linear unbranched polymers containing blocks of mannuronic acid (M block) guluronic acid (G block) or alternating (MG block) covalently linked by glycosidic linkage (Figure 9). Carboxylic groups presented in both monomers make alginate an anionic polyelectrolyte in aqueous solution. Electrostatic repulsion between the charged groups on the polymer chain, rigidity of six-membered sugar rings and restricted rotation around the glycosidic linkage that covalently links the different monomers contributes to the rigidity of the chains in solution.

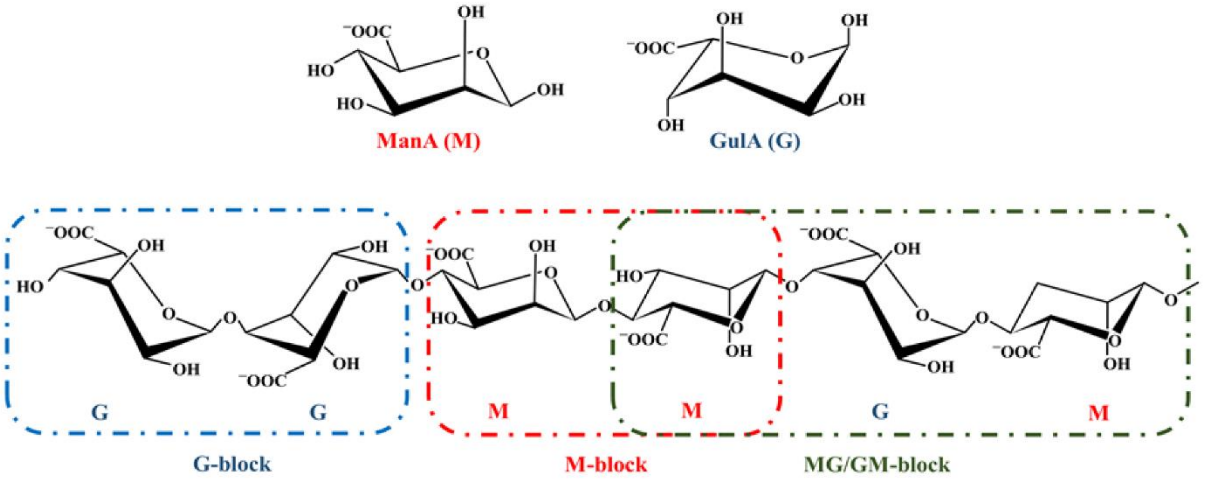

Figure 9: chemical structure of alginate polymer [27].

A special combination of properties such as the chain rigidity, hydrophilicity, and stability gives alginate the ability to form highly interconnected entangled networks in aqueous solution at concentrations as low as 1% w/w with a moderate chain contour length. Beyond multiple

application in the food, cosmetics, textile of pharmaceutical industry, its biocompatibility and ease of gelation with bivalent cations (for example Ca^{2+}) make alginate, mainly in hydrogel form, an excellent candidate for biomedicine in wound healing, drug delivery, and tissue engineering applications [28].

As a general characteristic of natural derived materials, the properties of alginate can vary depending on the source of origin. The chemical composition and sequence may vary widely between algae species and even between different parts of the algae and the time of year when it is harvested [29]. Some typical parameters that can contribute to identify the expected properties of a given alginate product are their molecular weight and ratio G/M. However, the length and distribution of the monomers along the polymer chain is not sufficient and it is necessary to determine the sequential structure of alginates that has an important effect on the properties coming from the different natures of the glycosidic linkages connecting the monomers depending on the block type (M-block, G-block or MG-block). The diaxial linkage in G-blocks results in a large hindered rotation, which combined with the polyelectrolyte nature of the alginate molecule, may account for its stiffness and expanded conformation in aqueous solution.

This variable chemical composition and structure of alginates have noticeable effects on their properties such as biocompatibility, ionic gelation or viscoelastic properties. For example, high molecular weight and high content in G-blocks alginate will show higher viscosities in aqueous solutions, faster gelation in the presence of calcium ions and higher mechanical properties in their hydrogel form. Otherwise, even if numerous studies were performed to study the effect of the structural and chemical properties on the biocompatibility of alginate, no clear evidences were founded due to the various impurities such as heavy metals, endotoxins, proteins, and polyphenolic compounds that could also be present modifying their biocompatibility [30].

Alginate hydrogel networks have demonstrated excellent properties as matrices for the elaboration of nanocomposites by the introduction of different types of fillers [31–33]. Different strategies can be found in the literature to crosslink alginate chains to elaborate hydrogels mainly by physical ionic crosslinks with bivalent cations [34].

3.3. Gelatin

Gelatin is a type of insoluble protein obtained by hydrolysis of collagen extracted from different animal sources such as the skin or the bones. Like all proteins, they are composed of many aminoacids joined together by amide bonds forming a linear chain (Figure 10). The

gelatin properties depend in both, the source of production as it will maintain the aminoacid composition of the original collagen, and the hydrolysis process applied during the manufacturing. Regarding the manufacturing process, gelatin is classified in two types. Type A or type B gelatin are obtained by acid-treated or basic-treated collagen respectively. The main difference between them is the isoionic point (pI) defined as the pH for which the gelatin backbone will present no electrolytes in solution. Type A gelatin presents a value of pI between 8 and 9 while type B gelatin has a value close to 5. Accordingly, gelatin is considered to be an amphoteric polyelectrolyte coming from a mixture of acidic and basic aminoacids. The amino groups ($-NH_2$) can be "dissociated" to $-NH_3^+$ ($-NH_2 + H^+ \leftrightarrow -NH_3^+$) while carboxylic groups (-COOH) can be "dissociated" to $-COO^-$ ($-COOH \leftrightarrow -COO^- + H^+$) depending on the pH. The value of pI defines the pH at which gelatin solution will present neutral behaviour with both carboxylic and amino ions present in the same amount. This is the bound between the cationic ($pH<pI$, $[NH_3^+]>[COO^-]$) and anionic ($pH>pI$, $[COO^-]>[NH_3^+]$) polyelectrolyte behaviours. The viscosity of gelatin aqueous solutions will present then a minimum at pH = pI corresponding with a minimum of the persistence length.

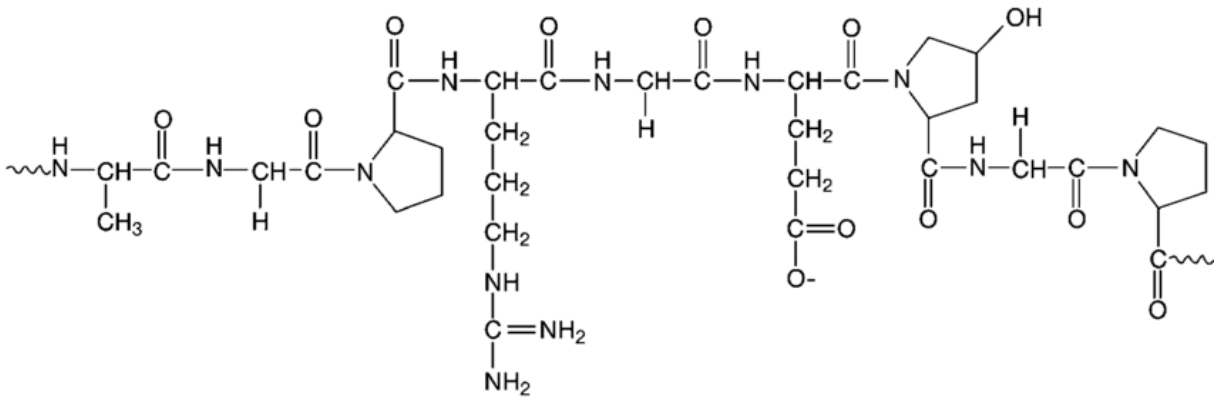

Figure 10: basic chemical structure of gelatin [35].

Other important properties are the gel strength and the viscosity that will depend mainly on the molecular weight and in the sequence of present aminoacids. In commercial gelatin, it is represented by the "bloom" value that usually lies between 30 g (low strength) and 300 g (high strength). This bloom value is defined as the weight required to push a cylindrical plunger of 12.7 mm diameter and 4 mm into a previously prepared gel of 6.66 % w/w concentration matured at 10ºC for 16-18h [36]. Gelatin hydrogel networks have demonstrated excellent properties as matrices for the elaboration of nanocomposites by the introduction of different types of fillers [37,38]. Even if the presence of reactive sites on gelatin molecules, such as amines, carboxylic acids, and hydroxyl groups, provides large opportunity for chemical crosslinking, the most widely used mechanism to create the polymer network consists in cooling

down a gelatin solution inducing the formation of a triple-helical structure physically crosslinked by hydrogen bond interactions.

3.4. Alginate DiAldehyde (ADA)

Alginate dialdehyde is the product of the oxidation of previously described sodium alginate. This chemical modification is an established strategy to introduce aldehyde groups with high reactivity in the alginate backbone [39]. Hydroxyl groups on carbons 2 and 3 of the alginate monomers are oxidized by sodium metaperiodate which leads to the formation of two aldehyde groups by rupture of C-C bond (Figure 11) with subsequent effects on their properties that will be discussed below.

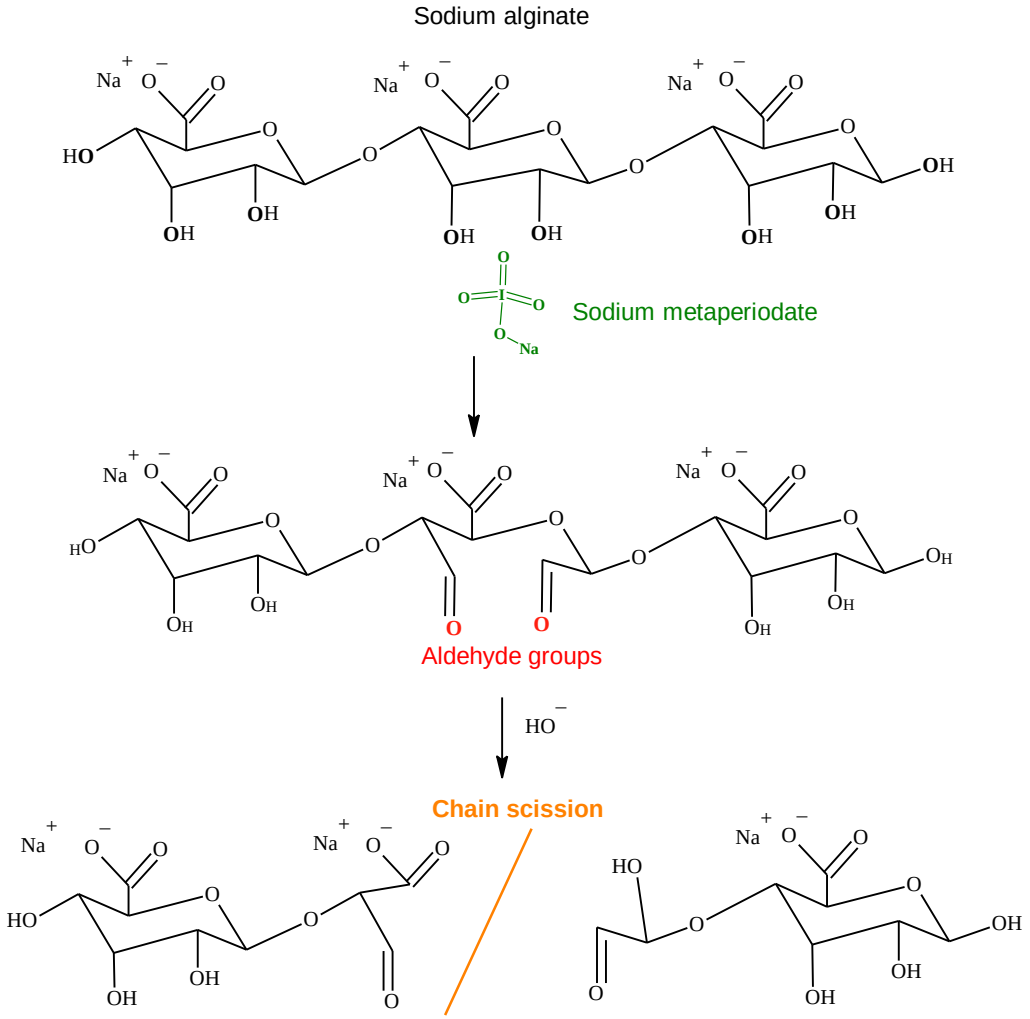

Figure 11: schematic mechanism of sodium alginate oxidation.

During the oxidation mechanism, alginate chain scission may occur due to the low stability of di-aldehyde of alginate in alkali conditions. Therefore, the oxidized polyelectrolyte will not conserve the polymerisation degree or molecular weight of the original sodium alginate. Moreover, the rotational freedom of each of the oxidized monomers is significantly increased by the rupture of the C-C bond between carbons 2 and 3 losing the stiffness and expanded

conformation in aqueous solution of the original sodium alginate. In view of this, it is extremely important to select the appropriate oxidation conditions in order to obtain an alginate dialdehyde with enough high oxidation degree but minimising the change of the dynamical properties of the original sodium alginate. Summarizing the information founded in the literature [39–43], there are three adjustable parameters in the oxidation proceed that will have an important effect on these characteristics of the produced ADA: (a) solvent: water or ethanol/water mixture, (b) ratio sodium metaperiodate/alginate monomer and (c) concentration of sodium alginate.

The selection of ethanol or water as solvent [39] is the parameter with the strongest influence in the decrease of the molecular weight of the ADA obtained in comparison with the original alginate. The main difference relies in the initial preparation of the alginate solution. In the case of water solvent, it is necessary to prepare an alginate aqueous solution with the correspondent limitations of concentration (< 80 g/L) due to the high viscosities. While, in the case of ethanol, we disperse the alginate in ethanol allowing to reach higher concentrations and therefore higher production with smaller volumes. Conversely, the drawback of using ethanol is the more frequent chain scission during the oxidation with a more important decrease of the molecular weight of the produced ADA in comparison with the original sodium alginate. Other adjustable parameter is the ratio sodium metaperiodate/alginate monomer**.** Different results can be found in the literature about the effect of this ratio on the properties of produced ADA; differentiating those studies performed for oxidation in aqueous media [36, 39] or ethanol/water mixture [42]. It can be concluded that, generally, an increase on the ratio will produce an alginate with a higher degree of oxidation and a lower molecular weight. The last adjustable parameter is the concentration of sodium alginate**.** For higher concentrations, the oxidation reaction and the chain scission will be faster and therefore the produced ADA will have higher degree of oxidation and a lower molecular weight. It is important to notice that as the concentration of alginate is increased it is more difficult to control chain scission and therefore produced ADA will have a lower molecular weight for similar degrees of oxidation.

The obtained ADA can be used for the elaboration of ADA-gelatin chemically crosslinked hydrogels without adding any supplementary chemical compound since the amino groups on gelatin and the aldehyde groups on ADA will form crosslinking points by Schiff's base formation [42].

3.5. Polyvinyl alcohol (PVA)

PVA is the synthetic and water-soluble polymer which is produced in the largest volume today via hydrolysis of polyvinyl acetate (PVAc) on an industrial scale [44]. Depending on the

hydrolysis conditions, two different types of PVA could be differentiated, hydrolyzed PVA and partially hydrolyzed PVA as shown in Figure 12. Among their multiple applications in textile, paper industry and food packaging industry, PVA has demonstrated to be an outstanding host polymer matrix for composite and it is the most commonly used water-soluble synthetic polymer for biomedical applications [45]. PVA has been considered biodegradable hydrophilic and biocompatible depending on the molecular weight, the degree of hydrolysis, and head-to-head junctions.

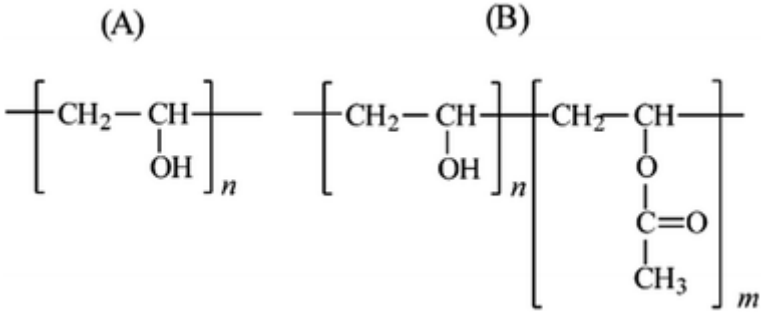

Figure 12: chemical structure of(A) fully-hydrolyzed PVA and (B) partial-hydrolyzed PVA) [46].

For most of their biomedical applications, PVA hydrogels are prepared to maintain the integrity either by chemical crosslinking with different ligands [47] or by physical reticulation applying freezing-thawing cycles [48]. PVA hydrogels are considered to be suitable host material for composites because of its high mechanical strength, hydrophilicity, easy processability, and good environmental stability [44]. Moreover, the carbon backbone of PVA contains hydroxyl groups which are a source of hydrogen bonding that can be used to promote interactions with the fillers enhancing the properties of nanocomposites [49].

3.6. Conclusions

As summarized in Table 4, the four selected polymers will enable to study the role of several key characteristics on the properties of polymer solutions, hydrogels and subsequently nanocomposites. These key characteristics are:

- Origin: the different advantages/disadvantages of natural and synthetic polymers has led to the choice of natural biopolymers composed of polysaccharides (sodium alginate and ADA) and amino-acids (gelatin) and a synthetic polymer (PVA).
- Molecular structure: the importance of the electrostatic interactions between polymeric chains and the MNPs with positively and negatively surface charge led to the selection of polymers with ionisable groups in aqueous solution leading to different behaviours; anionic polyelectrolyte (sodium alginate and ADA), amphoteric (gelatin) and neutral (PVA).

- Crosslinking method: it has also been established a preliminary strategy, that will be further developed in the chapter III, about the crosslinking of the different polymers for the elaboration of hydrogels by crosslinking of different nature, either physical (ionic, H-bonds or crystallization) or chemical covalent bonds.

Table 4: summary of selected polymers and their general characteristics

Polymer	Origin	Solution behaviour	Crosslinking method
Sodium alginate	Natural (brown seaweed)	Anionic polyelectrolyte	Ionic crosslinking (physical)
Gelatin	Natural (animal)	Amphoteric	Triple helix (physical)
ADA	Natural (sodium alginate)	Anionic polyelectrolyte	crosslinking with gelatin (chemical)
PVA	Synthetic	Neutral polymer	crystallization (physical)

4. Study of polymer solutions

4.1. Introduction

The importance of the study of polymer solutions relies in the fact that the physicochemical properties of the different polymers lead to very different dynamical behaviours in aqueous solution as discussed in the previous chapters. These properties will have important implications in the elaboration of nanocomposites since MNPs will be dispersed in them. One approach can be the presence of different chemical groups in the polymeric chain that can interact with the different organic ligands in the surface of MNPs, *i.e.* by electrostatic interaction if they bear chemical groups that are ionized in water solution with opposite charges. The polymer conformation and the entanglements can also play a key-role in the mixing procedure of the two components leading to nanocomposites with different microstructures and rheological behaviours. Each of the polymers was studied in a limited range of concentrations carefully chosen in a representative range linked with their application to elaborate magnetic nanocomposites based on the previous experience in the laboratory MSC and the information found in the literature.

4.2. Elaboration of polymer solutions

4.2.1. Sodium alginate

The selected sodium alginate is an alginic acid sodium salt of low viscosity (MP biomedicals). It consists in a cream-colored powder with a small amount of humidity (8%)

determined by measuring the mass before and after 24 hours in an oven at 80ºC. To prepare all the sodium alginate aqueous solutions, 50 mL of a concentrated mother solution (typically with a concentration, $C_{m.s}$ = 40 g/L) was previously prepared. For this purpose, the appropriate amounts of sodium alginate powder (2174 mg in 50 mL for 40 g/L) have been dispersed in pure water (50 mL) under continuous mechanical agitation of 400 rpm at room temperature for 14 hours. The homogeneity and transparency of the obtained samples contained in glass flask sealed with parafilm have been checked macroscopically before storage in the fridge for an use until ten days.The samples at different concentrations of sodium alginate (concentration C_{Alg}, volume V) have been prepared by dilution of mother solution (concentration $C_{m.s}$, volume $V_{m.s}$) with pure water (volume V_{H_2O}) by under magnetic stirring.

$$V_{m.s} = \frac{C_{Alg} \times V}{C_{m.s}} \quad (26)$$

$$V_{H_2O} = V - V_{m.s} \quad (27)$$

4.2.2. Gelatin

The selected gelatin is a type A gelatin from porcine skin with a bloom value of 300 (Sigma-Andrich). It consists in a cream-colored powder with a small amount of humidity (5%) determined by measuring the mass before and after 24 hours in an oven at 80ºC. To prepare all the gelatin aqueous solutions, the proper amount of gelatin powder and pure water have been mixed in 20 mL sealed glass flasks during 30 minutes at room temperature. Afterwards, the mixture has been stored in the fridge at 4ºC during 12 hours in order to swell the gelatin powder without dissolving. Finally, the mixture has been mechanically stirred in a thermostatic bath at 50ºC during 30 minutes to homogeneously dissolve the gelatin just before their characterization.

4.2.3. Alginate DiAldehyde (ADA)

The protocol for the oxidation of sodium alginate to produce ADA uses an ethanol/water mixture (1:1) as solvent in order to maximize the production of ADA. The ratio sodium metaperiodate/sodium alginate has been fixed to 0.32 according to the recommended value in the literature [42]. However, the concentration of alginate and the volume of the mixture have been varied to select the conditions to have a higher production with an enough high degree of oxidation and minimizing the decrease of the molecular weight. The general procedure is:

- Dispersion of the appropriate amount of sodium alginate in absolute ethanol in a glass flask of 500 mL following the selected concentration of alginate.

- Dissolution of the appropriate amount of sodium metaperiodate in pure water following the selected ratio alginate/sodium metaperiodate.
- Adding slowly, using a burette, the solution of $NaIO_4$ into the flask with the sodium alginate dispersion under continuous stirring and dark conditions.
- After 6 hours under continuous stirring the reaction has been quenched by adding 10 mL of diethylene glycol and left under continuous stirring for 30 minutes more.
- The obtained mixture has been then purified filling different dialysis membranes (3,4 kDa) to dialyze against pure water during 5 days with daily change of pure water. The absence of $NaIO_4$ has been checked by adding a 1 mL aliquot of dialysate to 1 mL of a 1% (w/w) solution of silver nitrate and ensuring the absence of any precipitate.
- The purified ADA solution contained in the dialysis membranes has been then divided in several glass balloons (< 50 mL/balloon). Each of the ADA containing balloon has been frozen by immersing it in liquid nitrogen during at least 15 minutes. Subsequently, the flasks have been introduced in a freeze-dryer with a vacuum system and left for 24-72h until no water remains in the sample.
- The obtained ADA powder has then been stored in a desiccator.
- The appropriate amounts of ADA and pure water have been mixed by magnetic stirring at room temperature until a homogeneous mixture has been obtained (~2 hours) to prepare the ADA solutions.

Each of the synthetized powder of ADA have been evaluated by the determination of the oxidation degree (DO) by titration. The methodology used is based in the reaction of hydroxylamine hydrochloride with the aldehyde groups presented in the ADA. Briefly, 0.1 g of ADA powder have been dissolved in 20 mL of 0.25M hydroxylamine hydrochloride solution containing methyl orange and stirred during 2 hours taking place the following reaction:

$$ADA-(CHO)_n + n(H_2N-OH.HCl) \longrightarrow ADA-(CH=N-OH)_n + nH_2O + nHCl$$

The quantity of HCl produced is proportional to the number of aldehyde groups presented in the ADA and it is determined by titration with NaOH 0.1M and methyl orange until reaching the red-to-yellow point. The degree of oxidation is determined with:

$$DO(\%) = \frac{198.M_{NaOH}\left(V_{sample} - V_{control}\right)}{m} * 100 \qquad (28)$$

where M_{NaOH} is the molecular weight of NaOH (40 g/mol), m is the mass of ADA (g) and V_{sample} and $V_{control}$ the volumes of NaOH 0.1M (mL) required to reach the red-to-yellow point for the

ADA-hydroxylamine hydrochloride mixture and a control with a mixture alginate-hydroxylamine hydrochloride respectively.

The evaluated conditions for the preparation of ADA are summarized in Table 5. Even if the molar ratio of sodium metaperiodate/sodium alginate was fixed at 0.32, it can be observed that a change in the concentration has a direct effect on the oxidation degree, obtaining a higher degree of oxidation (29.5% to 40.4%) when both concentrations of sodium alginate and sodium metaperiodate are multiplied by two at constant volume of ethanol and water. Indeed, a change in the total volume of each solution maintaining the same concentrations of sodium alginate and sodium metaperiodate has no reliable effect on the degree of oxidation.

Table 5: experimental conditions and obtained degree of oxidation for the different produced powder of ADA.

Alginate (g)	**$NaIO_4$ (g)**	**$V_{ethanol}$ (mL)**	**V_{H_2O} (mL)**	**Alginate (g/L)**	**$NaIO_4$ (mM)**	**Molar ratio ($NaIO_4$/Alginate)**	**DO %**
2	0.64	50	50	40	60	0.32	29.5
4	1.28	50	50	80	120	0.32	40.4
8	2.57	100	100	80	120	0.32	39.3

4.2.4. PolyVinyl Alcohol (PVA)

The selected polyvinyl alcohol (PVA) has a molecular weight between 146.000 and 186.000 g/mol and a degree of hydrolysis of 99% (Sigma-Aldrich). The protocol to prepare the PVA solution has been chosen following the recommendations in the literature [50]. Briefly, 10 g of PVA powder were dissolved in 100 mL of pure water through magnetic stirring at 90ºC during 6 hours. The obtained viscous and transparent mother solution with a concentration C_{PVA} = 100 g/L has been stored at 30ºC to guarantee a homogeneous solution [48]. Aqueous solutions at different concentration have been prepared by dilution of the appropriate volumes of mother solution and pure water by magnetic stirring overnight.

4.3. FTIR

The chemical groups of the different selected polymers have been first confirmed by Fourier Transformed InfraRed (FTIR) spectroscopy. As it is well known, FTIR spectroscopy detects the vibration characteristics of chemical functional groups in a sample. By comparing the wavelength of these vibrations with reference wavelength of databases it is possible to identify the chemical groups presented in the sample [51]. For the present case, selected polymer solutions have a very high amount of water varying in the range 90-98% of the total mass of the sample. If a FTIR spectra is recorded directly with these solutions, the contribution

of O-H linkages coming from the water will be so intense that the contribution of the chemical groups of the polymer chains will be masked. To avoid this drawback, polymeric films have been prepared by drying at room temperature a small amount of each of the polymer solutions before performing the FTIR analysis.

Experimental setup consists in a Bruker Equinox spectrometer with an attenuated total reflectance (ATR) cell operating in the wavelength range 600-4000 cm^{-1}. The light beam is reflected through a crystal on which the film sample was placed as schematized in Figure 13. It is important to remark that the infrared beam penetrate just in a thin layer in the surface of the film that is the region of sample where the measurement is performed. Even if the measurement has a short pathway through the sample, the multiple reflections allow to accumulate the specific frequencies absorbed by the sample, obtaining an intense signal just as it would be obtained in a classical transmission experiment. Before each sample measurement the background spectrum is recorded obtaining the spectrum of atmospheric components water and CO_2 and then is subtracted to subsequent sample measurements. Between each measurement, the crystal has been washed with ethanol and a background spectrum is recorded to confirm that there are no traces of ethanol before placing a new sample.

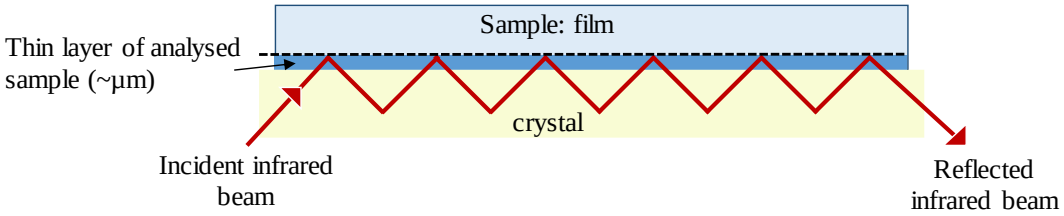

Figure 13: FTIR with attenuated total reflectance (ATR) experimental setup.

The obtained spectrums for the different polymers are presented in two figures (Figures 14 and 15) for a better comparison. Before analysing each of the spectrums individually, there is a common feature for all of them; an intense peak between 3300-3400 assigned to the O-H stretching from remaining water in film. The spectrums of sodium alginate and ADA (Figure 14) are almost identical, as the ADA was obtained by oxidation of sodium alginate. This finding suggests that the bands clearly observed represent chemical groups that were not modified during the oxidation. However, some small differences will be discussed in order to confirm the oxidation leading to the formation of two aldehyde groups. In any case is important to remember that the applied procedure is just a partial oxidation with a degree of oxidation of the obtained ADA of around 40% as previously determined by titration.

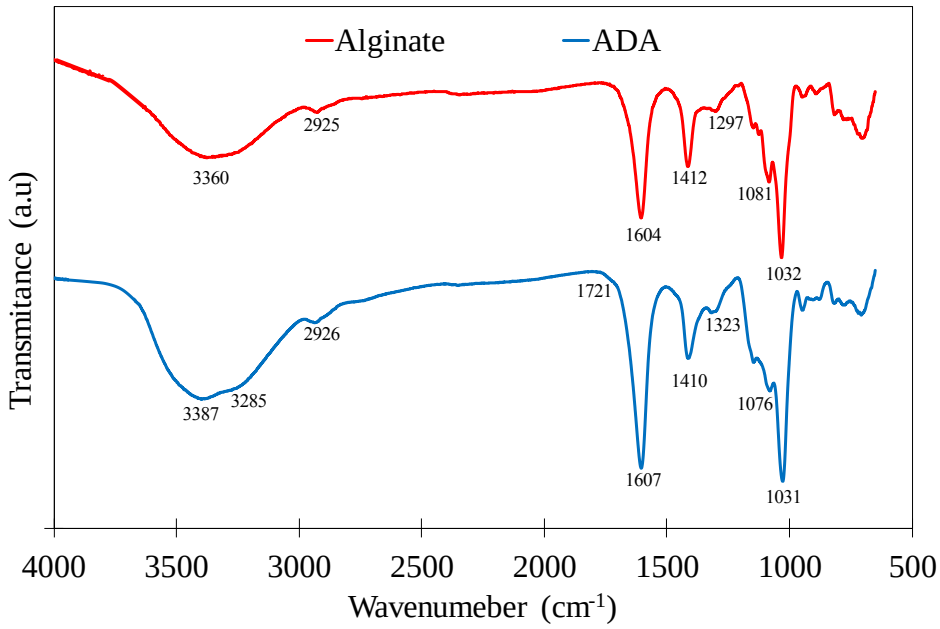

Figure 14: FTIR spectra of sodium alginate and ADA (obtained by oxidation of sodium alginate).

The band at 2925 and 2926 cm^{-1} (Figure 14) can be assigned to aliphatic C-H. The band at 1604 and 1607 cm^{-1} are assigned to carboxylic ester band confirming their carboxylate anion state found close to 1600 cm^{-1} by other authors [52]. The bands at 1410 and 1412 cm^{-1} due to C–OH deformation vibration with contribution of O–C–O symmetric stretching vibration of carboxylate group [53]. The bands at 1081 and 1076 cm^{-1} and more intense at 1031 and 1032 cm^{-1} may correspond to C–O and C–C stretching vibrations of pyranose ring. The band at 1297 and 1323 cm^{-1} are related to the chemical bonds C–C–H and O–C–H. The change of the position of this band in ADA (1297 cm^{-1}) with respect to the original sodium alginate (1323 cm^{-1}) is the first indication of the partial modification of the alginate monomer, opening the pyranose ring by breaking the C-C bond and exchanging two alcohols (C-OH) by two aldehydes (C=O). Other authors [40] proposed that the best way to confirm the oxidation of alginate into ADA can be a non-intense band close to 1735 cm^{-1}. In our case the intensity of this band is very low, but detectable at 1721 cm^{-1}.

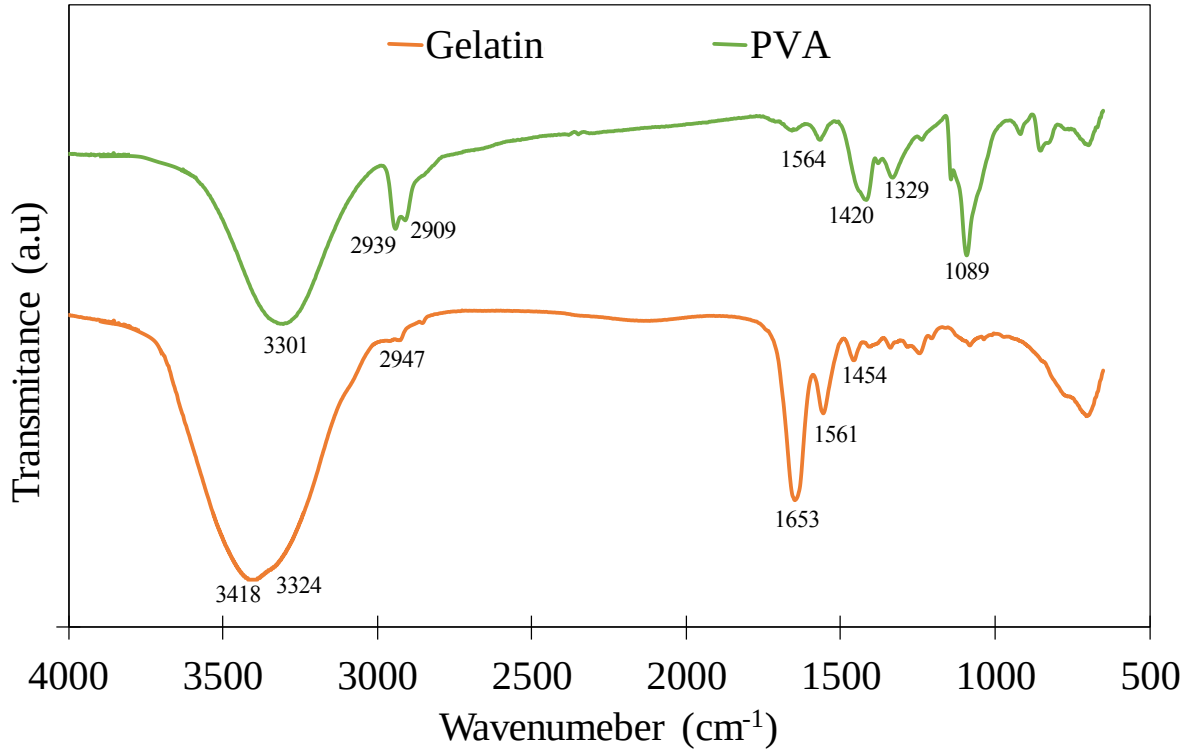

Figure 15: FTIR spectra of films of gelatin and PVA.

The spectra of gelatin and PVA are presented in Figure 15 where several low intensity peaks can be identified in the region 2900-3000 cm^{-1} indicative of aliphatic C-H of the gelatin backbone. However, the clearest peaks are found at 1653 cm^{-1} corresponding to carboxylic groups and at 1561 cm^{-1} assigned to a combination between N-H bending and C=N stretching, all of them presented in aminoacids [42]. The peaks for PVA at 2939 and 2909 cm^{-1} are due to the asymmetric stretching vibration of CH_2. The other peaks in the region 1600-1000 cm^{-1} are related to the carbonyl stretching (1564 cm^{-1}), the C-H bending vibration (1420 cm^{-1}), the C-H deformation vibration (1324 cm^{-1}) and the stretching of acetyl groups C-O (1089 cm^{-1}) [54–57].

4.4. Zeta potential

For the study of the interactions between polymer chains and MNPs, it is important to determine the charge of the polymer backbone which has also an effect on the dynamical behaviour of the polymer solutions as described theoretically in paragraph 2.3. One of the simplest ways to evaluate this electrostatic charge is the determination of the zeta potential in diluted aqueous solutions of the four studied polymers. For such purpose, polymeric aqueous solutions have been prepared in pure water with an adjusted concentration between 0.2 and 0.5 g/L to have an appropriate intensity of the diffused light in the ZetaSizer device. The results are summarized in the Table 6.

Table 6: zeta potential of diluted solutions of different polymers and polyelectrolytes.

Polymer	Concentration (g/L)	Zeta potential (mV)
Sodium alginate	0.2	-67±5
Gelatin	0.5	+12±1
ADA	0.5	-59±4
PVA	0.5	+2±5

From the obtained results we can confirm the polyelectrolyte behaviour of sodium alginate and ADA solutions with a strongly negative zeta potential coming from the carboxylic groups in the polymer backbone. For the case of gelatin, a weak polyelectrolyte with a weak positive charge but very close to the neutral behaviour is expected due to amino groups of amino acids. This positive charge is related with the type A gelatin showing an isoelectric point (pI) close to 5 due to the acid treatment during their production and therefore a positive charge at pH>pI in neutral conditions. The neutral nature of PVA is confirmed by a value of zeta potential close to zero.

4.5. Rheological study

A torque-controlled rheometer (MARS) with a cone-plate titanium geometry (diameter of 60 mm, angle of 1º, gap of 51.2 μm) has been used to carry out all the rotational shear rheology measurements. One best advantage of the cone and plate geometry is to apply constant shear stress and to measure constant shear rate over all the sample. Temperature control has been achieved by a Peltier device located under the lower plate of the geometry. As described in the paragraph 2.3 and 2.4 both the molar mass and the solution conformation are correlated with the viscosity of both neutral and polyelectrolyte polymer solution. In this chapter, an analysis of the concentration and shear rate dependence of the viscosity will be presented to investigate the different behaviours for each of the selected polymers and to relate them to their conformation and molecular weight.

Two kind of experimental protocols have been applied depending on the regime of concentration of the polymer solutions. For unentangled polymer solutions, the Newtonian viscosity has been determined by steady state shear flow measurements in a range of shear rates between 200 and 500 s^{-1}. Each viscosity measurement has been done by triplicate and the result shown corresponds with a mean over the three calculated values. For entangled polymer solutions, the shear rate dependence of the viscosity has been studied by steady state shear flow measurements between 0.1 and 2000 s^{-1}.

4.5.1. Concentration dependence of the viscosity: sodium alginate and PVA

The evolution of the zero-shear specific viscosity (η_{sp}) as function of the concentration is presented in Figure 16 to identify the different regimes of concentration for sodium alginate aqueous solutions. η_{sp} of a polymer solution is defined as $(\eta_0-\eta_s)/\eta_s$ where η_0 is the viscosity of the solution extrapolated at low shear rates from stationary flow curves and η_s the viscosity of the solvent. For the lower studied concentrations, the exponent of the concentration dependence of the viscosity found experimentally is 0.53 very close to the theoretical value for a polyelectrolyte solution in semi-dilute regime ($\eta \sim c^{1/2}$, equation 22). The explanation is that all the concentrations studied are above the overlap concentration that is commonly very low for polyelectrolytes due to their stiffness and electrostatic repulsive interactions between chains and monomers. In the same range of concentrations but in the presence of salt, the expanded conformation of sodium alginate is partially lost, and the chains are contracted due to the screening of the electrostatic repulsion between monomers decreasing the volume occupied by a sodium alginate coil. This change is translated into a decrease of the zero-shear specific viscosity. The exponent obtained experimentally for the viscosity is 1.21 being very close to the theoretical one for polyelectrolyte semi-dilute solutions with added salt ($\eta \sim c^{5/4}$, Table 3).

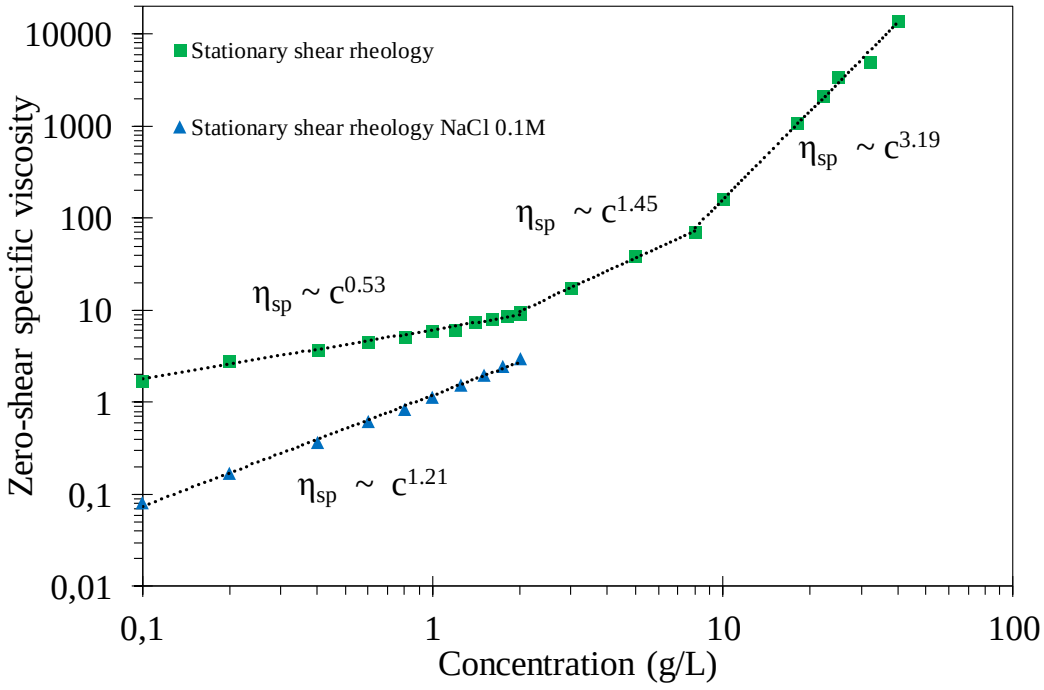

Figure 16: zero-shear specific viscosity of alginate solutions in pure water as function of the concentration at 25ºC.

Increasing the sodium alginate concentration, the size of the blobs become smaller until the concentration in which the size of the blob and the persistence length are equivalent leading to an entangled solution in the concentrated regime (c**= 2 g/L). The characteristic exponent

found experimentally for the concentrated regime is 1.45 also very close to the theoretical value for a polyelectrolyte solution ($\eta \sim c^{3/2}$, equation 24). However, above a concentration of 8 g/L a new change in the concentration dependence of the viscosity is observed. As noted in the theoretical discussion (paragraph 2.4), the electrostatic repulsions between chains become negligible when the density of entanglements between chains are very high and the behaviour of a very concentrated polyelectrolyte solution can be described by the laws of a neutral polymer. The characteristic exponent of 3.19 found experimentally for sodium alginate concentrations higher than 8 g/L is in good agreement with the one for a neutral polymer in the concentrated regime ($\eta \sim c^{15/4}$, Table 2).

The evolution of the zero-shear specific viscosity as function of the concentration is presented in Figure 17 for PVA solutions. For the lower studied concentrations, the exponent found experimentally is 1.08 very close to the theoretical value for neutral polymers in the dilute regime ($\eta \sim c^{1}$, equations 1 and 2). Increasing the PVA concentration, the chains become to be closer to each other from the overlap concentration (c* = 5g/L) defining the beginning of the semi-diluted regime. In these conditions the polymer can be divided in blobs as schematized in the Figure 4. The value of the exponent found experimentally in the semi-dilute regime (1.66) is between the theoretical value for a good solvent ($\eta \sim c^{5/4}$, Table 1) and for θ-solvent ($\eta \sim c^{2}$, Table 1). Above the crossover concentration (c** = 30 g/l), the characteristic exponent found experimentally for the viscosity (4.09) is very close to the theoretical value for a concentrated solution of a neutral polymer in good solvent ($\eta \sim c^{15/4}$, Table 2).

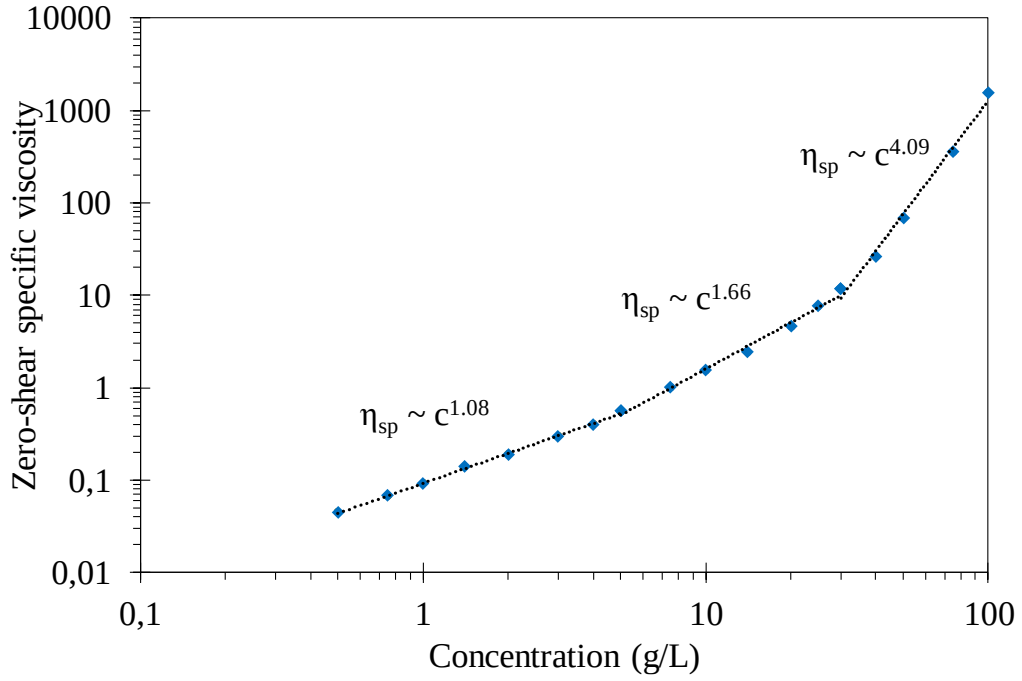

Figure 17: zero-shear specific viscosity of PVA solutions in pure water as function of the concentration at 30°C.

4.5.2. Diluted regime: viscosity average molecular weight

Polymer molecules in the diluted regime are isolated and interact only with the solvent molecules simplifying their description through the determination of the intrinsic viscosity [η]. The intrinsic viscosity depends on the concentration and size of the dissolved macromolecules, as well as on the solvent quality and temperature. For these conditions, the specific viscosity (η_{sp}) of a solution can be described via the Taylor expansion:

$$\eta_{sp} = B_1.\phi + B_2.\phi^2 + B_3.\phi^3 + \cdots \quad (29)$$

where ϕ represents the volume fraction of polymer in the solution and B_i are the virial coefficients. In diluted regime, Taylor expansion can be simplified to first order polynomial models; the Huggins and Kraemer equations:

$$\frac{\eta_{sp}}{C} = [\eta] + k_H[\eta]^2 C \quad (30)$$

$$\frac{\ln(\eta_{rel})}{C} = [\eta] + k_K[\eta]^2 C \quad (31)$$

where C is the concentration of polymer, η_{rel} is the relative viscosity (η/η_0), η_{sp} the specific viscosity and k_H and k_K are the Huggins and Kraemer coefficient respectively. k_H and k_K are considered adequate criteria to evaluate the quality of the solvent [58]. Experimental results indicate that the higher the affinity between polymer and solvent, the lower is the k_H value. At the same time, negative values for k_K are typically an indication of good solvent and positive values indicate poor ones. Moreover, the intrinsic viscosity [η] can be determined by extrapolation to zero concentration of the fitted of experimental concentration dependence of the viscosity of diluted polymer solutions. The obtained intrinsic viscosity [η] is a measure of a solute contribution to the viscosity and can be related to the polymer viscosity average molecular weight (M_v) by the Mark-Houwink equation:

$$[\eta] = KM_V^{\alpha} \quad (32)$$

The values of the Mark-Houwink parameters (α and K) depend on the polymer-solvent system and they can be found in the bibliography determined by complementary techniques such as chromatography or dynamic light scattering (DLS). Experimental conditions and the Mark-Houwink parameters summarized in Table 7 have been carefully selected based on previous results on the literature [59]. For sodium alginate and ADA, the solutions have been prepared in NaCl 0.1M to screen the negative electrostatic charges in carboxylic groups to avoid the electrostatic repulsions that could lead to interactions between chains and therefore a non-linear variation of the reduced viscosity with the concentration. For the case of gelatin it is not necessary to add salt since the electrostatic repulsion are not relevant, but the selected

temperature was 37.4ºC to ensure a good solubility in individual coils avoiding the formation of triple helices.

Table 7: experimental conditions for the rheological measurements and Mark-Houwink parameters for the four studied polymers.

Polymer	C (g/L)	Solvent	Temp. (ºC)	α	K	Ref
Sodium alginate	0.1-2	NaCl 0.1M	25.0	0.963	$1.228.10^{-4}$	[60]
ADA	0.5-8	NaCl 0.1M	25.0	0.685	$1.125.10^{-4}$	[61]
Gelatine	2-10	Pure water	37.4	0.820	$9.290.10^{-3}$	[62]
PVA	0.5-5	Pure water	30.0	0.640	$5.140.\ 10^{-4}$	[63]

The results of sodium alginate are presented in Figure 18 as an example of the data treatment to determine the intrinsic viscosity [η] and the viscosity average molecular weight (M_v). The experimental data have been fitted by equations 30 and 31. The intrinsic viscosity [η], Huggins (k_H) and Kraemer (k_K) coefficients have been obtained by the y-intercept and the slopes respectively.

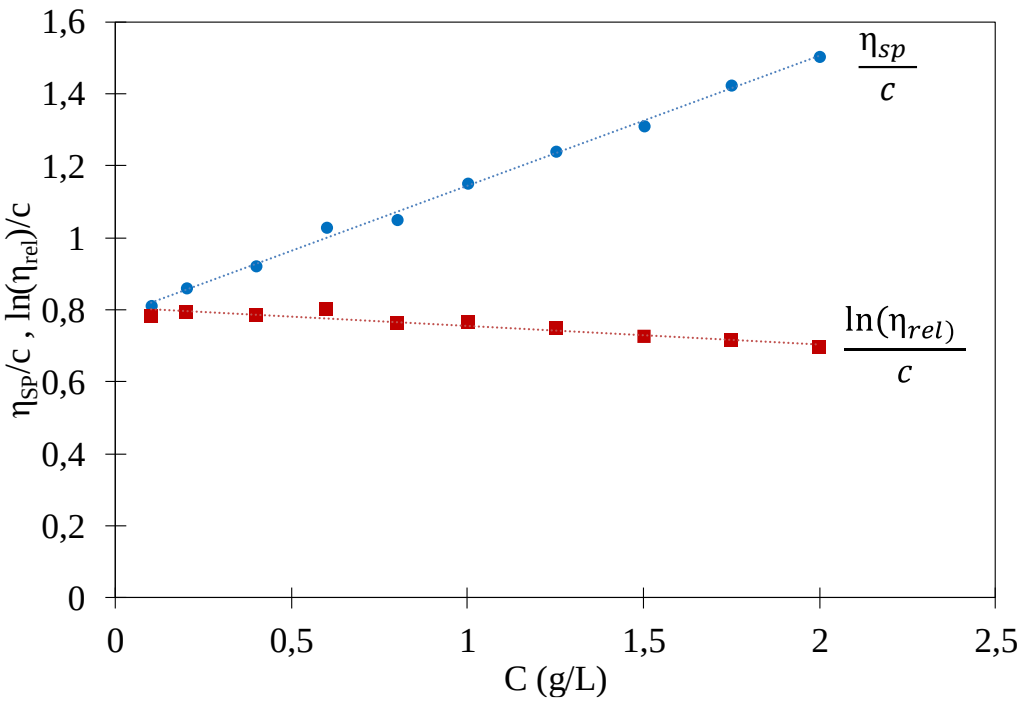

Figure 18: representation to determine the intrinsic viscosity of sodium alginate based on Huggins and Kraemer equations.

The value of M_v has been then deduced using the Mark-Houwink equation (equation 32) and parameters of Table 7. The results obtained for the four studied polymers are summarized in the Table 8. The values of k_H for sodium alginate, gelatin and PVA close to 0.5 suggest a polymer-solvent system close to θ-conditions, while the lower value for ADA indicates good solvent conditions. In addition, the bigger negative value of k_K for ADA confirms the good solvent conditions while for sodium alginate, PVA and gelatin it is close to zero.

The differences in the intrinsic viscosity for the four different polymers can be also related with their chain stiffness and their conformation in solution. The main parameters influencing the conformation of a polymer in the diluted regime are molar mass, solvent quality, temperature, branching and chemical structure [59]. The highest intrinsic viscosity is obtained for sodium alginate confirming the highest chain stiffness even with the addition of salt to screen the electrostatic repulsions. A decrease in the intrinsic viscosity is observed for ADA in comparison to the original sodium alginate. This is explained not only by the decrease of the molecular weight due to the chain scission during the oxidation that will be discussed later but also to the rupture of the C-C bond between carbons 2 and 3 during the oxidation decreasing the chain stiffness. Moreover, the intrinsic viscosity of PVA and, especially, gelatin is much lower suggesting a more compact conformation of the coils than the other studied polymers.

The value of the M_v obtained for sodium alginate is in the classical range of molecular weights found in the literature (5.10^3-3.10^6 g/mol) [64]. We have also confirmed a moderate decrease of this molecular weight during the oxidation to ADA due to the chain scission that it is not very important. For the case of gelatin, the obtained value of M_v is in a good agreement with the values for a pig skin type A gelatin [65]. While for PVA, the obtained value is slightly lower than the qualitative information provided by the manufacturer ($1.46.10^5$-$1.86.\ 10^5$ g/mol).

Table 8: results of viscosity average molecular weight of different biopolymers.

Polymer	$[\eta]_H$ (L/g)	k_H	$[\eta]_K$ (L/g)	k_K	$\lvert[\eta]\rvert$ (L/g)	M_v (g/mol)
Sodium alginate	0.787	0.58	0.815	-0.09	0.801	$9.98x10^4$
ADA	0.219	0.22	0.212	-0.17	0.216	$6.20x10^4$
Gelatin	0.045	0.48	0.045	-0.06	0.045	$5.20x10^5$
PVA	0.088	0.49	0.088	-0.07	0.088	$1.14\ x10^5$

4.5.3. Rheological behaviour as function of shear rate

Polymer solutions are usually non-Newtonian fluids when the concentration is increased, meaning a shear rate dependence of the viscosity of the polymer solutions. The study of this rheological behaviour is a highly recognized methodology in several stages of the manufacturing and processing of polymers at industrial scale [66]. Likewise, it plays a key-role in the elaboration of nanocomposites at a laboratory scale coming from the deduction of important microstructural information that results crucial in the mixing protocol and the particle-polymer interactions.

Sodium alginate

The results of the shear rate dependence of the viscosity are presented in Figure 19 for a set of representative concentrations above the crossover concentration (c** = 2 g/L) for sodium alginate aqueous solution. A Newtonian plateau characterized by the zero-shear viscosity is observed at low shear rates. At a certain critical shear rate, the shear-thinning behaviour begins due to the disentanglement and alignment of alginate chains in the direction of the applied shear rate. For the present study we have chosen the Cross equation to fit the data. It is the best empirical model to describe the evolution of the shear viscosity for concentrated polymer solutions as function of the shear rate:

$$\eta_a = \eta_\infty + \frac{\eta_0 - \eta_\infty}{1 + \left(\dot{\gamma}/\dot{\gamma}_c\right)^{1-n}} \qquad (33)$$

where η_0 and η_∞ are limiting viscosities at zero and infinite shear rates respectively. The parameter n is a rate constant characteristic of the flow behavior in the shear-thinning region. The typical values lie in the range 1 < n < 0.2; a value of 1 is representative of a Newtonian behaviour and as the value becomes smaller the shear thinning behaviour will become more important. The infinite shear rate viscosity η_∞ was not obtained experimentally. It was fixed to 10^{-3} Pa s. As seen in Figure 19, the Cross model fits accurately the experimental results for all the studied concentrations except perhaps for 40 g/L at shear rate higher than 600 s^{-1}. However, a fitting without considering these experimental points change the adjusted parameters less than 10%. The results are summarized in Table 9.

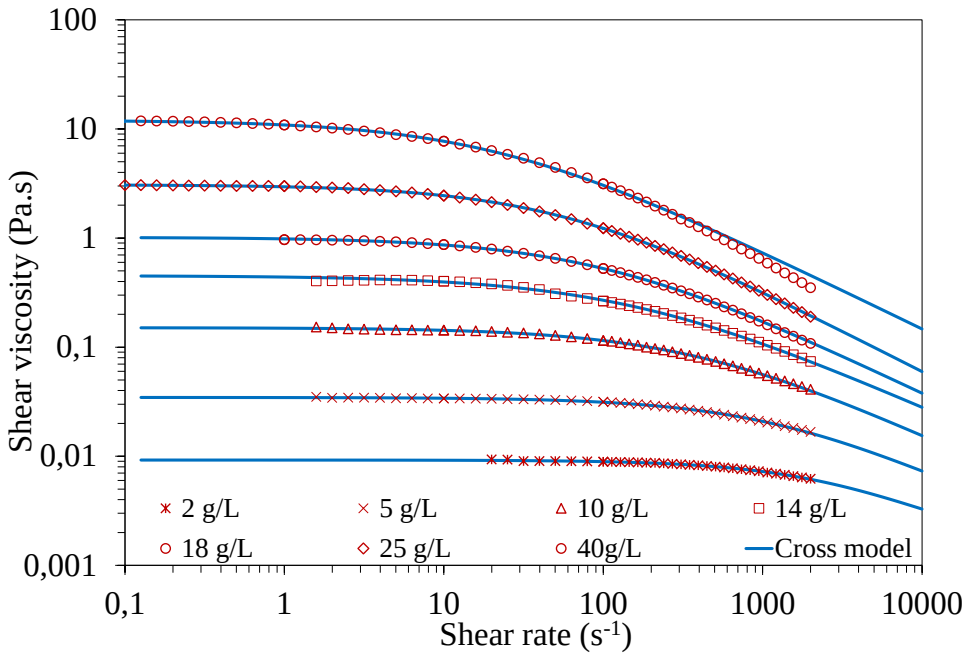

Figure 19: evolution of the shear viscosity as function of the shear rate for sodium alginate aqueous solutions at different concentrations fitted with the Cross model at 25ºC.

Table 9: Cross fitting parameters for the flow curves for sodium alginate solutions at 25ºC inside the concentrated regime.

C_{alg} (g/L)	η_0 (Pa.s)	n	$1/\dot{\gamma}_c$ (s)
2	0.009	0.19	3.10^{-4}
3	0.016	0.27	4.10^{-4}
5	0.035	0.24	6.10^{-4}
8	0.063	0.20	8.10^{-4}
10	0.15	0.23	0.002
14	0.4	0.29	0.004
18	0.97	0.26	0.009
22	1.85	0.29	0.013
25	3.14	0.25	0.019
32	4.45	0.25	0.021
40	12.06	0.28	0.045

These values of η_0 have been used in Figure 16. The inverse of the critical shear rate ($1/\dot{\gamma}_c$) can be defined as a critical relaxation time (τ_c). The concentration dependence of this critical relaxation time (Figure 20) shows two regimes clearly differentiated by the same critical concentration of 8 g/L found with the concentration dependence of the zero-shear specific viscosity (Figure 16). However, the exponents obtained for the relaxation time in Figure 20 do are not close to the theoretical values ($\tau \sim c^0$ equation 23 and $\tau \sim c^{3/2}$ Table 2). Dou and Colby have already observed such a discrepancy [67]. These authors have suggested the existence of dipolar interactions between monomers through counterions, which are not included in the theoretical model.

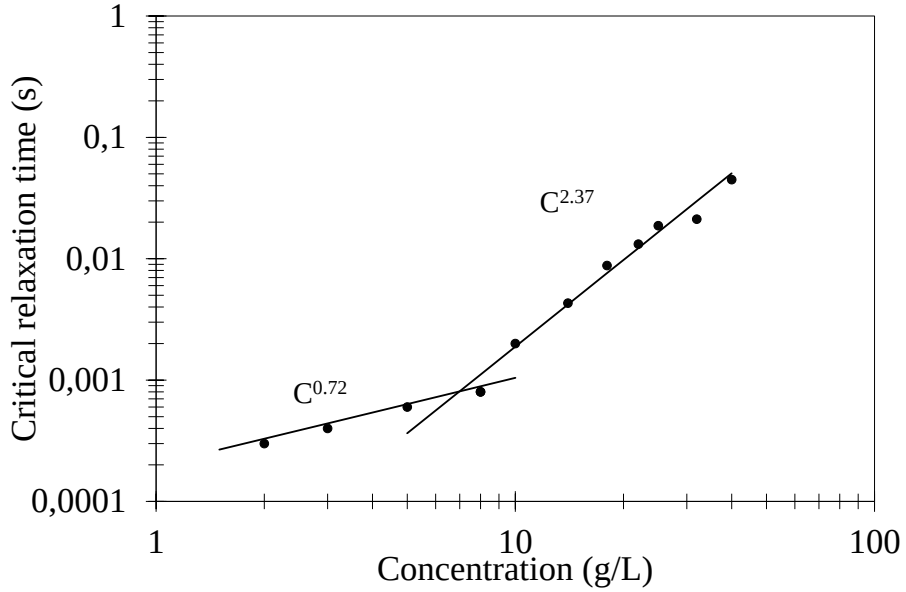

Figure 20: concentration-dependence of the critical relaxation exponent obtained from the fitting to Cross model from experimental data for aqueous solutions of sodium alginate.

Gelatin

The results of the viscosity measurements of gelatin salt-free aqueous solutions with concentrations 18, 25 and 50 g/L at 40ºC are presented in Figure 21. For all concentrations, a Newtonian behaviour is observed, in contrast to other polymer solutions and in agreement with previously reported work [68–70]. The values of the Newtonian viscosities are directly obtained from the slope. This Newtonian behaviour could be explained by the compact conformation of the coils and high density of segments which reduce the importance of the entanglement mechanism at 40ºC.

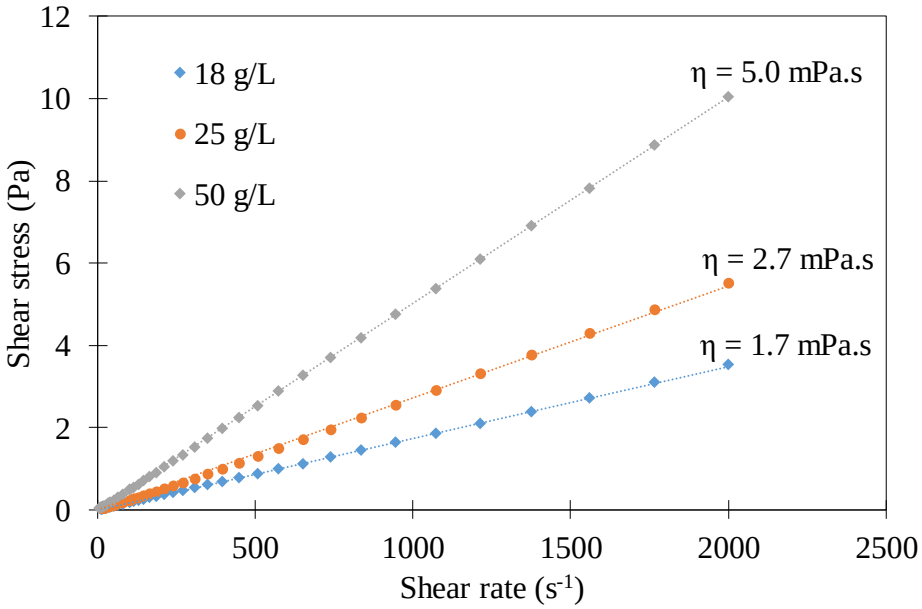

Figure 21: evolution of the shear stress as function of shear rate for gelatin salt-free aqueous solutions at 40ºC for different concentrations.

ADA

ADA solutions have been prepared in phosphate buffer solution (PBS) for a range of concentration between 5 and 50 g/L at 25ºC accordingly with the protocols recommended for the elaboration of gelatin-ADA crosslinked hydrogels [42]. A Newtonian behaviour is observed for concentrations below 30 g/L (Figure 22). The Newtonian viscosities, directly indicated in the Figure 22, have been determined from the slope of the flow curves in the range of shear rate between 200 and 500 s^{-1}. For the highest concentration of 50 g/L the effect of the solvent has been tested using pure water and PBS respectively. For both cases a low shear thinning behaviour is observed slightly more important for pure water (Figure 23). The decrease of the shear-thinning behaviour in PBS is related to the screening of the electrostatic charges of the ADA polyelectrolyte decreasing the electrostatic repulsions and therefore the chain stiffness tending to a more compact conformation of the chains. In any case, it is important to remark

that the oxidation of sodium alginate into ADA has a drastic effect on the conformation of the chains in solution by a decrease of both the molar mass and the chain stiffness leading to much more compact coils that occupy less volume in solution compared to sodium alginate.

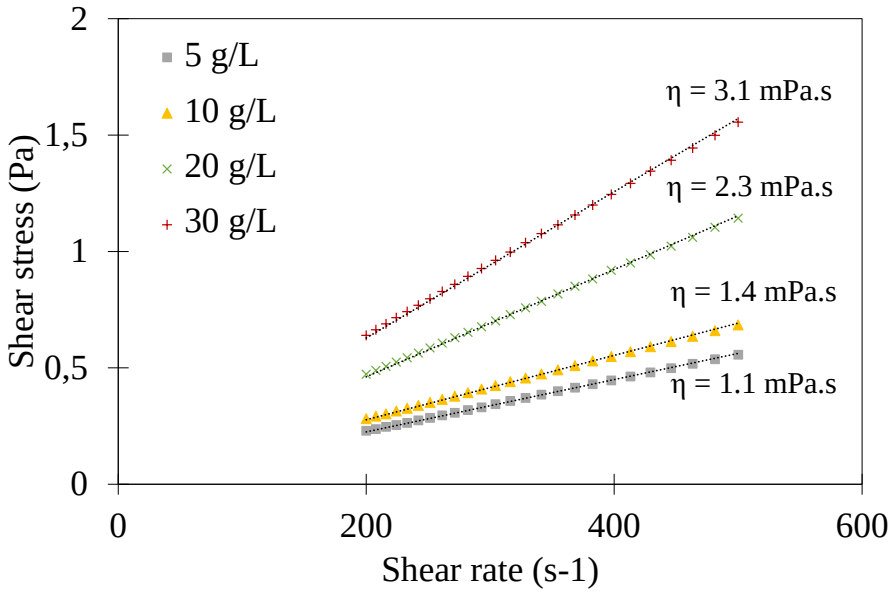

Figure 22: evolution of the shear stress as function of the shear rate for ADA phosphate buffer solutions at 25ºC for different concentrations.

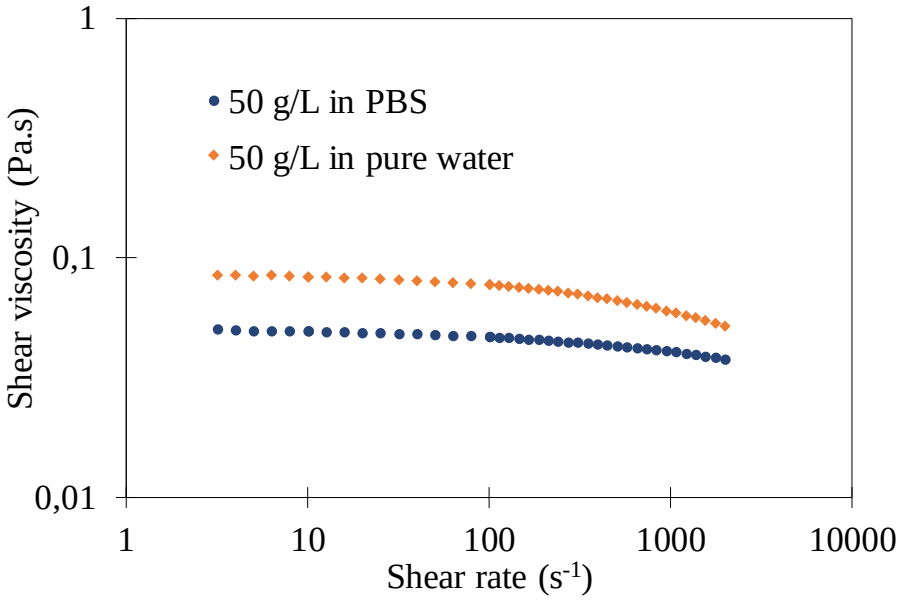

Figure 23: evolution of the shear viscosity as function of the shear rate for ADA phosphate buffer and pure water solutions at 25ºC.

PVA

The study of the shear rate dependence of the viscosity of PVA is focused on the concentrated regime identified previously in which entanglement and interactions between polymer chains are important. Therefore, the results of the shear rate dependence of the viscosity for concentrations higher than the crossover concentration c** of 30 g/L are presented

in Figure 24 observing a shear-thinning behaviour due to the disentanglement and alignment of PVA chains in the direction of the applied shear rate. The results have been fitted successfully with the Cross model as show in Figure 24 and the fitting parameters are given in Table 10.

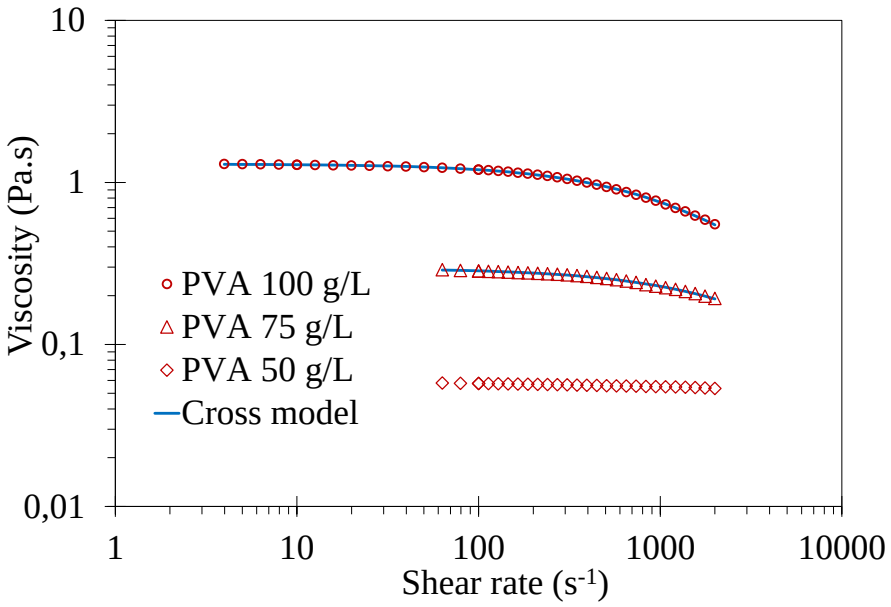

Figure 24: evolution of the shear viscosity as function of the shear rate for PVA aqueous solutions at different concentrations fitted with the Cross model at 30ºC.

Table 10: Cross fitting parameters for the flow curves for PVA solutions at 30ºC in the concentrated regime.

C_{PVA} (g/L)	η_0 (Pa.s)	n	$1/\dot{\gamma}_c$(s)
50	0.06	-	-
75	0.30	0.07	0.0003
100	1.30	0.10	0.0007

4.6. Conclusions

The elaboration and study of aqueous polymer solutions of different natures is the first step for the selection of a polymer matrix with the most suitable properties for the elaboration of nanocomposites. It has been developed an experimental methodology to prepare such solutions in a reproducible way allowing to control precisely their properties. Then, polymer films were prepared in order to perform a compositional analysis by FTIR spectroscopy to identify the main chemical groups of the polymer chains that can serve as base for the subsequent characterization of nanocomposites. The measurement of the zeta potential in diluted polymer solutions allow to confirm the anionic polyelectrolyte behaviour of sodium alginate and Alginate diAldehyde (ADA), a soft cationic polyelectrolyte behaviour of gelatin and a neutral behaviour of Poly(VinylAlcohol) (PVA). These different behaviours are very important not only for the interpretation of the polymer conformation in solution but also for the possible particle-polymer interactions in the subsequent elaboration of nanocomposites.

Then, a complete rheological flow study has been performed in order to define the three regimes of concentration: diluted, semi-diluted and concentrated. The intrinsic viscosity [η] has been determined by the Huggins and Kraemer methods in the diluted regime deducing the viscosity average molecular weight by the Mark-Houwink equation. The low value of [η] for gelatin and PVA have suggested a compact coil conformation in aqueous solution. On the contrary, the higher value of [η] for sodium alginate have confirmed the chain rigidity and strong electrostatic repulsion between monomers that lead to an expanded conformation in aqueous solution. However, [η] decreases when the sodium alginate is oxidized to ADA, explained by the chain scission and rupture of C-C bonds between carbons 2 and 3. Steady state flow measurements have been carried out in PVA and sodium alginate aqueous solutions in the concentrated regime finding a shear-thinning behaviour related with the entanglement/disentanglement of polymer chains.

This complete study allows to understand better the microstructure of polymer aqueous solutions of different natures. Even if no important differences have been found between the molecular weight of the polymers, the differences in the chain stiffness and interactions between monomers lead to different conformations changing dramatically their properties. The potential application of the four studied polymer solutions for the elaboration of nanocomposites requires a moderate viscosity with entanglements between the chains that allow to develop a network in which MNPs are stable. For this reason, ADA and gelatin solutions have been discarded for the elaboration of nanocomposites due to their compact conformation and low viscosity even at high concentrations leading to sodium alginate and PVA as main candidates.

5. Multiscale viscoelastic investigation of sodium alginate aqueous solutions

The viscoelastic properties of polymer aqueous networks either in sol state or crosslinked hydrogels are related to their supramolecular assembly. It has been obtained some information about the microstructure of the polymer solutions from the shear viscosity obtained by macrorheological measurements in the different polymers. However, a more complete knowledge of these properties at different scales can be of decisive importance not only from a fundamental point of view but also for their application for the elaboration of nanocomposites. In this context, we propose a global strategy with the objective of studying the viscoelastic properties of the main selected polymer of this work (sodium alginate) at different concentrations and over a wide range of frequencies from the characteristics of the individual

polymer chains to the polymeric network by combining complementary macroscopic shear oscillatory rheology (Hz), diffusing-wave spectroscopy (DWS) and dynamic light scattering (DLS) based microrheology (kHz-MHz) and Brillouin spectroscopy (GHz) as schematically shown in Figure 25. Additional Small-Angle X-ray Scattering (SAXS) experiments are also performed to directly probe the structural properties.

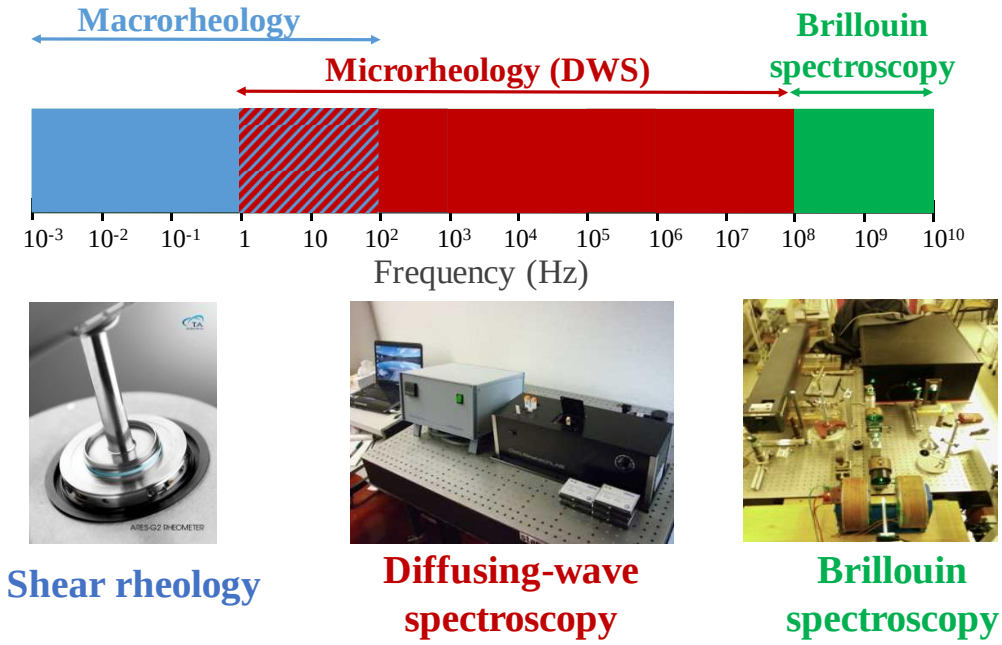

Figure 25: experimental techniques and their frequency range for the multi-scale viscoelastic investigation.

5.1. Macrorheology

Frequency sweeps have been performed between 0.01 Hz and 100 Hz with a fixed strain of 1% within the linear viscoelastic domain of the material and constant temperature of 25.0±0.1ºC using the rheological experimental setup described in the paragraph 4.5.

5.2. DWS-based microrheology

Microrheological measurements based on diffusing-wave spectroscopy (DWS) have been performed using a laboratory-made setup (Figure 26) in collaboration with the École Supérieure de Physique et de Chimie Industrielles de la ville de Paris (ESPCI). The coherent source is a Spectra-Physics Cyan CDRH laser, operated at λ = 488 nm with an output power of 50 mW. The laser beam is expanded to approximately 1 cm at the sample. The diffused light is collected by a photon counter system and analysed to obtain the intensity autocorrelation function. Sodium alginate samples for DWS measurements were prepared in cuvettes for fluorescence spectroscopy (path length L = 4 mm). Spherical microparticles of polystyrene (diameter of 500 nm) covered with alkyl-OH surface (Micromod Partikeltechnologie GmbH) have been dispersed in the sodium alginate solutions with a concentration of 1 % w/w to be used of centres

of scattering. No aggregation or precipitation have been observed macroscopically for all the dispersions tested in this work.

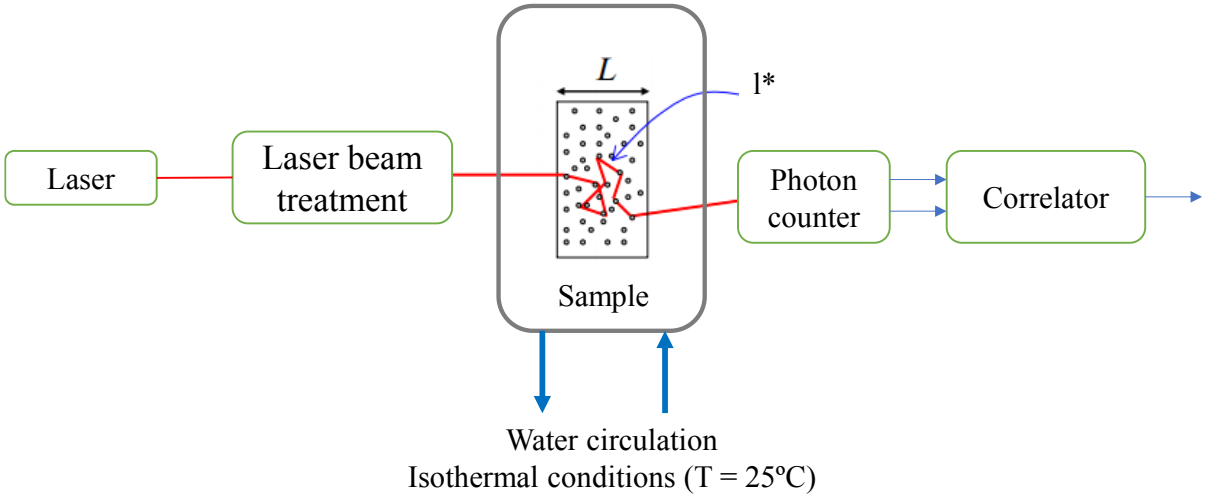

Figure 26: DWS schematic experimental setup.

The obtained intensity autocorrelation function $g^{(2)}(t)$ has been converted into the field autocorrelation function $g^{(1)}(t)$ by the Sieger relation, $g^{(2)}(t) = \beta\,[1 + g^{(1)}(t)]^2$. The results of the normalized field autocorrelation function $g^{(1)}(t)$ are presented in Figure 27 for sodium alginate aqueous solutions with the different concentrations and pure water.

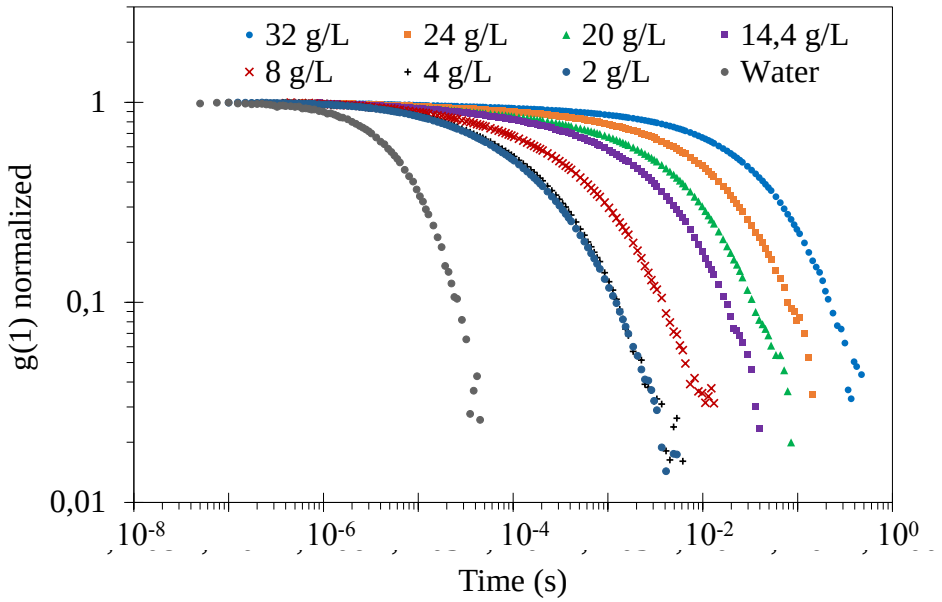

Figure 27: time evolution of the normalized field autocorrelation function for sodium alginate aqueous solutions with different concentrations at 25.0±0.1ºC determined by DWS.

From the time evolution of the field autocorrelation function, the mean square displacement (MSD = $\langle \Delta r^2(t) \rangle$) have been calculated by solving numerically the following equation [47]:

$$g^{(1)}(t) = \left[\frac{L}{l^*} + \frac{4}{3}\right] \Big/ \left\{\left[\frac{z_0}{l^*} + \frac{2}{3}\right] \times \left\{sinh\left[\frac{z_0}{l^*}\sqrt{k_0^2\langle\Delta r^2(t)\rangle}\right] + \frac{2}{3}\sqrt{k_0^2\langle\Delta r^2(t)\rangle}\, cosh\left[\frac{z_0}{l^*}\sqrt{k_0^2\langle\Delta r^2(t)\rangle}\right]\right\} \Big/ \left\{\left(1 + \frac{4}{9}k_0^2\langle\Delta r^2(t)\rangle\right) sinh\left[\frac{L}{l^*}\sqrt{k_0^2\langle\Delta r^2(t)\rangle}\right] + \frac{2}{3}\sqrt{k_0^2\langle\Delta r^2(t)\rangle}\, cosh\left[\frac{L}{l^*}\sqrt{k_0^2\langle\Delta r^2(t)\rangle}\right]\right\} \quad (34)$$

where L is the sample thickness, l* is the sample transport mean free path of scattered light, k_0 is the wave factor ($k_0=2\pi/\lambda$), z_0 is the distance that the light must travel through the sample before becoming randomized, $z_0 = l^*$. The only unknown parameter (L/l*) has been obtained for each sample by comparison with the previously determined value of L/l* and the intensity of the diffused wave for water ($L/l^*(H_2O) = 26.3$, I_{H_2O}= 31.8 kHz). The general tendency for the performed experiments is that the values of L/l* decrease as the concentration of sodium alginate is increased taking values between 30 and 12.

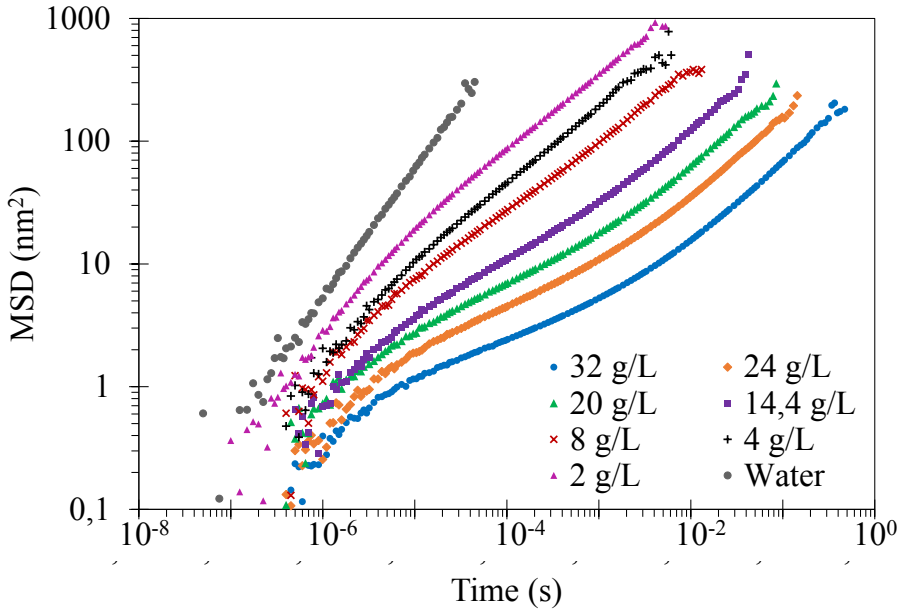

Figure 28: time evolution of the mean square displacement for sodium alginate aqueous solutions with different concentrations at 25.0±0.1ºC determined by DWS.

The results of the MSD corresponding to Figure 27 are given in Figure 28. The frequency dependence of the complex shear modulus can be then obtained from the generalized Stokes-Einstein equation:

$$\tilde{G}(s) = \frac{k_B T}{\pi R s \langle\Delta\tilde{r}^2(s)\rangle} \quad (35)$$

where $\tilde{G}(s)$ is the viscoelastic spectrum as a function of Laplace frequency, k_B is the Boltzmann constant, T is the absolute temperature and $\langle\Delta\tilde{r}^2(s)\rangle$ is the Laplace transform of the mean

square displacement $\langle \Delta r^2(t) \rangle$. This equation can be expressed in the Fourier frequency domain to obtain the complex viscoelastic modulus G*(ω):

$$G^*(\omega) = \frac{k_B T}{\pi R i \omega \mathcal{F}\langle r^2(t) \rangle} \quad (36)$$

where $\mathcal{F}\langle r^2(t) \rangle$ is the Fourier transform of the mean square displacement. Assuming a local power law form for the mean square displacement, G*(ω) can be written as a function of the experimentally measured mean square displacement $\langle \Delta r^2(t) \rangle$:

$$G^*(\omega) = \frac{k_B T}{\pi R \langle \Delta r^2(1/\omega) \rangle \Gamma[1 + \alpha(\omega)]} \quad (37)$$

The elastic G' and loss G" moduli are then deduced:

$$G'(\omega) = G^*(\omega) \cos\left[\frac{\pi \alpha(\omega)}{2}\right] \quad (38)$$

$$G"(\omega) = G^*(\omega) \sin\left[\frac{\pi \alpha(\omega)}{2}\right] \quad (39)$$

where t = 1/ω, α(t) = ∂[ln$\langle \Delta r^2(t) \rangle$]/ ∂[ln t] is the slope of $\langle \Delta r^2(t) \rangle$ plotted against the time in logarithmic scales. Γ is the gamma function which serves as conversion factor of the transform. DWS-based microrheology allows then to determine both G' and G" in the frequency range between 1 and 10^5 Hz in complement to macrorheological measurements.

5.3. DLS-based microrheology

Dynamic light scattering measurements have been performed with an ALV CGS-3 goniometry system equipped with a cuvette rotation/translation unit (CRTU) and a He–Ne laser (22 mW at λ = 632.8 nm). The system measures the time-averaged autocorrelation function of the scattered light intensity at a scattering amplitude vector defined as q = ((4πn/λ sin (θ/2)), where n is the refractive index and θ the scattering angle. Sodium alginate solutions for DLS measurements were prepared in test tubes (10 mm in diameter). Filtered mother solution of sodium alginate was mixed with filtered pure water and an appropriate quantity of spherical microparticles of polystyrene (diameter of 500 nm) covered with alkyl-OH surface. Syringe filters of 0.80 μm and 0.10 μm have been used respectively for alginate solutions and pure water. The concentration of microparticles has been fixed to 0.005% w/w, high enough to obtain a much higher scattered intensity in comparison with the scattered intensity coming from the polymer chains but low enough to avoid multi-scattering. This concentration of microparticles has experimentally been determined considering the relation of the scattered intensity for microparticle aqueous dispersion ($I_{\mu p}$) and sodium alginate aqueous solution for a concentration of 8 g/L (I_{alg}), obtaining a value $I_{\mu p}$/ I_{alg} = 30.

As for DWS, the obtained intensity autocorrelation function $g^{(2)}(t)$ has been converted into the field autocorrelation function $g^{(1)}(t)$ by the Sieger relation, $g^{(2)}(t) = \beta\,[1 + g^{(1)}(t)]^2$. The results of the time evolution of the field autocorrelation function for different sodium alginate concentrations are shown in Figure 29.

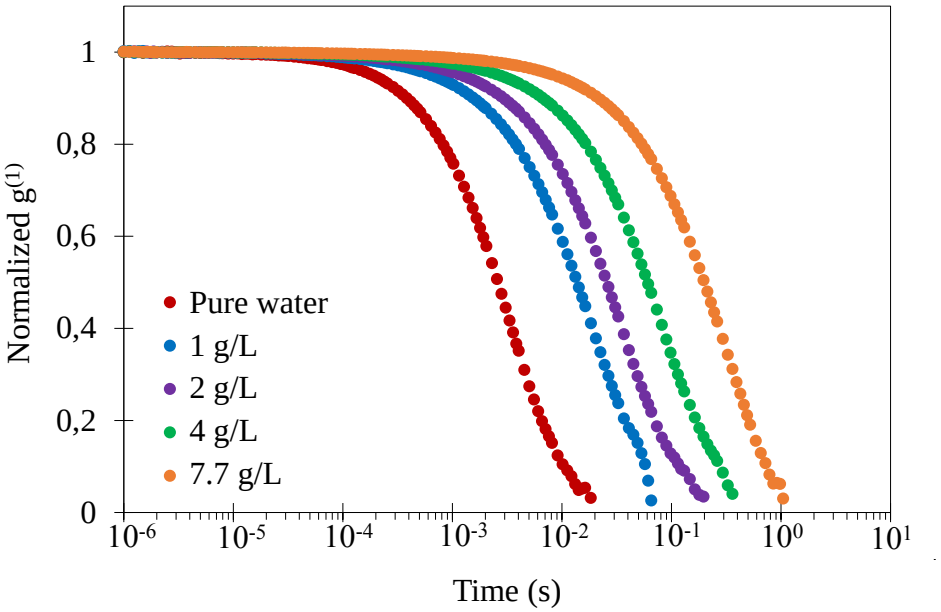

Figure 29: time evolution of the normalized field autocorrelation function for sodium alginate aqueous solutions with different concentrations at 25°C determined by DLS.

The mean square displacement $\langle \Delta r^2\,(t)\rangle$ has been calculated by the following equation valid for low concentrated aqueous solutions of sodium alginate.

$$g_1(q,t) = exp\left[-\frac{< \Delta r^2(t) > \,.q^2}{6}\right] \qquad (40)$$

As shown in Figure 30, the mean square displacement varies linearly with time in the whole studied time range for pure water and a more restricted range at long times for sodium alginate solutions. This time dependence is the signature of a Newtonian behaviour as expected by the Einstein-Stokes equation:

$$< \Delta r^2(t) \geq 6.D.t \qquad (41)$$

where D is the translational coefficient of diffusion:

$$D = \frac{k_B T}{6\pi.\eta.R} \qquad (42)$$

D could be determined from the slope of the linear fitting of experimental data of Figure 30 and then the viscosity of the sample directly shown in the Figure 30 is deduced knowing the radius of the spherical microparticles (250 nm) and the temperature (25.0±0.1°C).

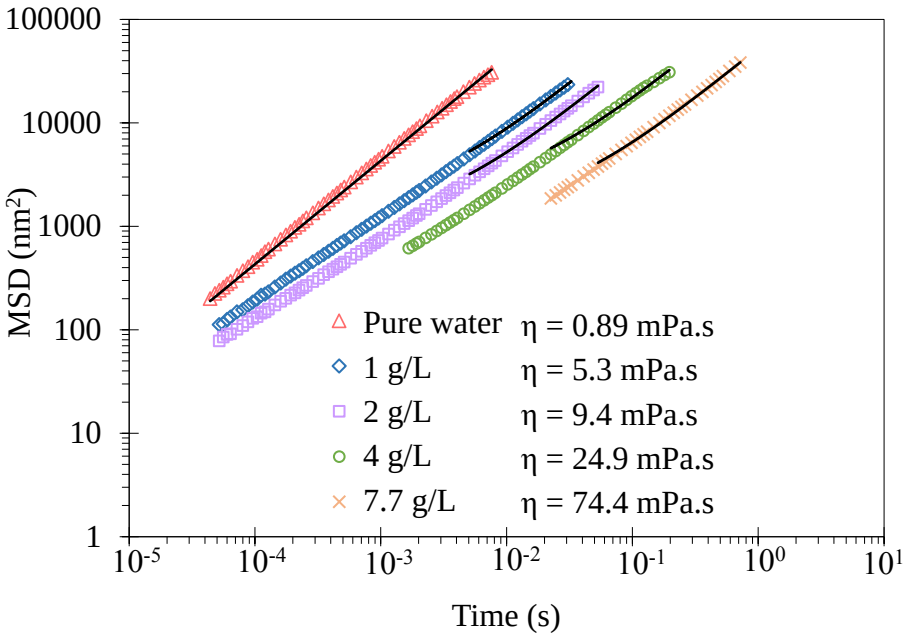

Figure 30: time-evolution of the mean square displacement for sodium alginate aqueous solutions with different concentrations at 25ºC determined by DLS. Solid lines correspond to a linear fitting of experimental data (symbols).

5.4. Brillouin spectroscopy

The longitudinal sound velocity V_L has been measured locally in sodium alginate solutions by the Brillouin light scattering technique in the backscattering geometry (Figure 31) in collaboration with the Laboratoire des Sciences des Procédés et des Matériaux (LSPM). The experimental setup (Figure 32) is composed mainly by an incident light of a longitudinal mode laser at a wavelength λ_L = 532 nm (Coherent Verdi), a 2x3-pass tandem Fabry-Perot interferometer and a photodetector in addition to a set of optical fixtures to filter and to focalise the light. The intensity of the incident light in the sample has been maintained constant around 100 mW for all the measurements. The back-scattered light has been recorded in the Stokes and anti-Stokes region.

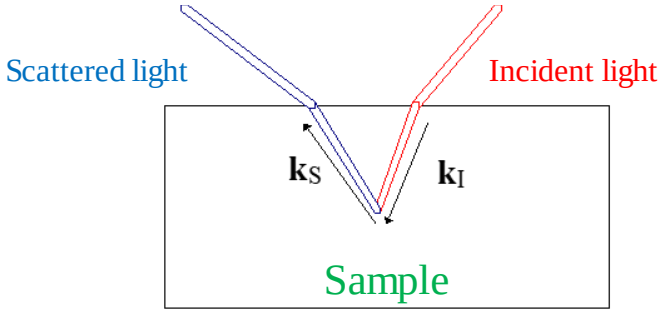

Figure 31: coupling between the light and a wave for a bulk transparent material (backscattering geometry).

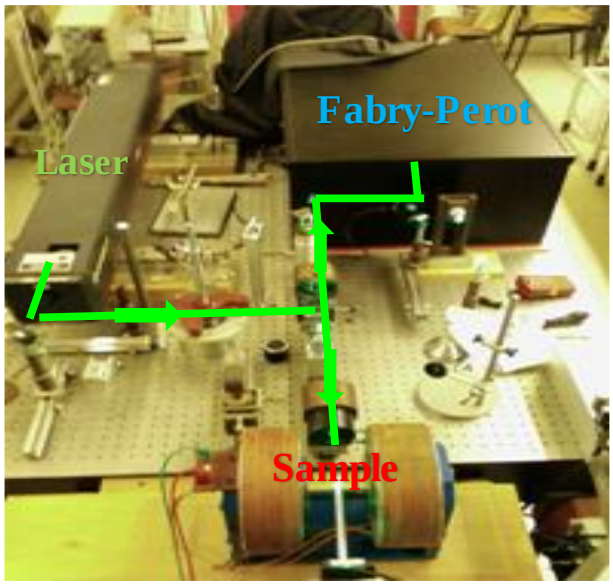

Figure 32: Brillouin spectroscopy experimental setup. © LPSM

The amplitude of the wave vector k of the scattered bulk acoustic wave is defined by:

$$k = \frac{4.\pi.n}{\lambda_L} \tag{43}$$

where n is the refractive index of the sample. For a sodium alginate aqueous solution n increases linearly with the concentration and is close to that of water (n = 1.331) (for the sodium alginate concentration of 30 g/L, n = 1.338) [72].

The obtained results consist in the accumulated counts as a function of the frequency shift (f) that are represented by the intensity (a.u.) of the scattered light as function of the frequency shift. A raw accumulation of the scattered light shows a high intensity peak at zero frequency shift that corresponds with the Rayleigh scattering. This signal has been used before the measurement to calibrate the position of the detector and the Fabry-Perot interferometer. Subsequently, during the measurements, the signal between -5 and 5 GHz was not recorded as it is not related to the properties of interest and to not saturate the photodetector. Thus, the analysis is focused on the analysis of the two characteristic peaks of the sample that appear in the Stokes and anti-Stokes region with a negative and positive frequency shift. These peaks are fitted to determine the frequency shift (f_B) and the full width at half maximum (Γ_B) as observed in Figure 33 for a sodium alginate aqueous solution with concentration of 20 g/L. Each of these two peaks represent a convoluted signal as a result of the addition of the instrumental and the sample contribution. To determine the instrumental contribution, it has been performed an experiment using a polished metal part (high refractive material) founding that is well reproduced by a Gaussian distribution with 0 frequency shift and a linewidth of σ = 314 MHz. Thus, to obtain the characteristic linewidth of the sample the measured peaks presented in

Figure 33 have to be deconvoluted into a Gaussian peak with linewidth σ_d = 314 MHz and the peak containing the characteristic linewidth and frequency shift of the material.

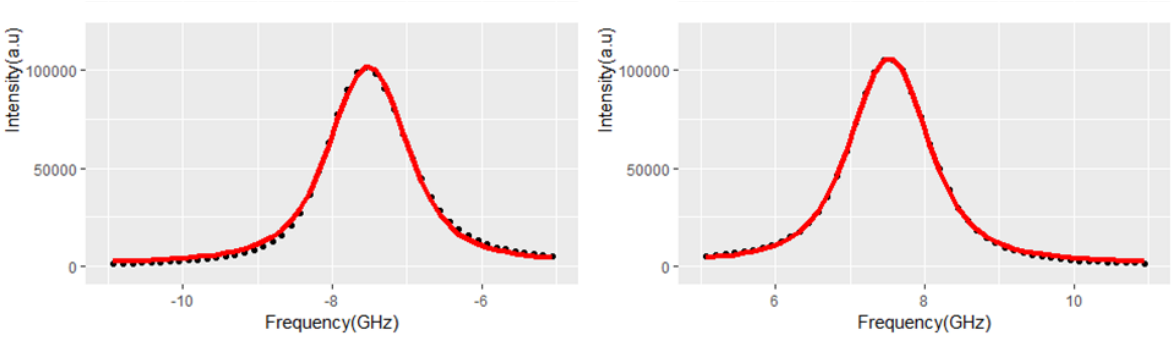

Figure 33: intensity as function of the frequency shift in the Stokes (right) and anti-Stokes (left) region for a sodium alginate aqueous solution of 20 g/L. Red line corresponds to the fitting with a Voigt distribution with fixed Gaussian linewidth σ = 314MHz and adjusted Lorentzian linewidth $\gamma = \gamma_M$.

The most accurate fitting of this experimentally obtained peaks has been achieved by a Voigt profile that is given by a convolution of a Lorentz distribution and a Gaussian distribution with two parameters, σ (Gaussian linewidth) and γ (Lorentzian linewidth). After different fittings of the obtained peaks for the sodium alginate solutions at different concentrations, it has been found systematically that the Gaussian linewidth of the Voigt profile (σ) obtained to fit the experimental data is always very close to the device linewidth, σ_d = 314 MHz, simplifying the mathematical calculation by setting $\sigma = \sigma_d$ = 314 MHz and leaving as unique adjusted parameters the Lorentzian linewidth (γ) that corresponds to the characteristic linewidth of the material, $\gamma = \gamma_m$ and the position of the peak that corresponds with the frequency shift (f_B).

The experimental frequency shift (f_B) and the full width at half maximum ($\Gamma_B = 2.\ \gamma_m$) are then used to determine the sound velocity (v_L) and the dynamical longitudinal viscosity η_L respectively according to the following equations:

$$v_L = \frac{f_B \lambda_L}{2n} \tag{44}$$

$$\eta_L = \frac{\rho \Gamma_B}{k^2} \tag{45}$$

where ρ is the volumetric mass of the sample in kg/m^3. In the range of studied concentrations between 5 g/L and 30 g/L the volumetric mass of sodium alginate aqueous solutions increases linearly with the concentration from 1002 to 1013 kg/m^3 [73]. The longitudinal storage modulus E' and the longitudinal loss modulus E'' of sodium alginate solutions can be finally determined by:

$$E' = \rho v_L^2 \tag{46}$$

$$E'' = 2\pi f_B \eta_L \tag{47}$$

5.5. Combined results

5.5.1. Viscosity and longitudinal loss modulus as a function of frequency

The viscous behaviour of sodium alginate aqueous solutions analysed through the frequency-dependence of the dynamic viscosity (η'=G"/ω) is presented in Figure 34. They are calculated from the values of G"(ω) obtained by DWS-based microrheology by the equation 39 and the results of shear macrorheology. It can be clearly observed a good continuity between the two sets of experimental data allowing a wide range of investigated frequencies (10^{-2}-10^{5} Hz). The experimental data has been fitted with a modified version of the Cross model replacing in equation 33 the shear rate by the frequency. The results are given in Table 11.

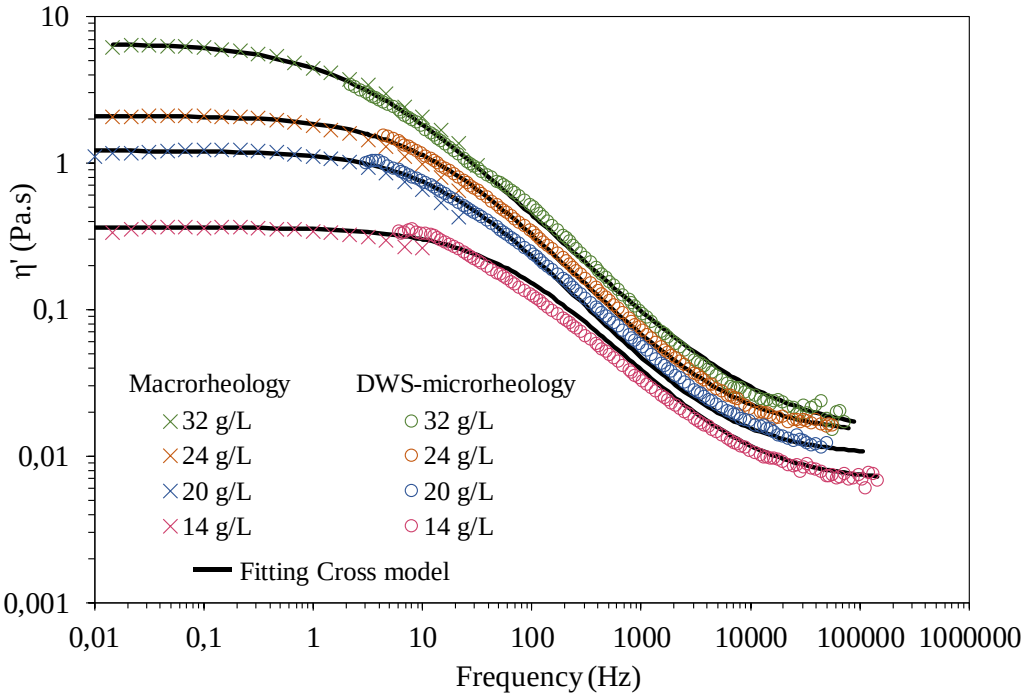

Figure 34: evolution of the dynamic viscosity η' as function of the frequency of sodium alginate aqueous solutions for different concentrations combining shear macrorheology (MR) and diffusive wave spectroscopy (DWS).

Table 11: parameter of Cross fitting for the evolution of n' as function of the frequency for combined results of MR and DWS.

C_{alg} (g/L)	η'_0 (Pa.s)	η'_∞ (Pa.s)	n	$1/f_c$ (s)
14	0.36	0.0067	0.16	0.016
20	1.21	0.0100	0.16	0.058
24	2.10	0.0140	0.17	0.085
32	6.60	0.0140	0.26	0.377

In addition, the longitudinal viscous modulus (E") has been obtained from Brillouin spectroscopy as described previously (equation 47) from the width of the Brillouin peak for

very high frequency (GHz). The observed experimental linear concentration dependence of E" (Figure 35) can be described by the addition of the contribution of water and the one of sodium alginate polymer by using a simple mixing law [74]:

$$E'' = E''_{water}.x_w + E''_{alginate}.(1 - x_w) \quad (48)$$

where x_w is the weight fraction of water and E''_{water} and $E''_{alginate}$ are the intrinsic longitudinal loss modulus of water and sodium alginate respectively. A Brillouin experiment with pure water leads to the value E''_{water}= 0.0325 GPa. We can then deduce the intrinsic longitudinal loss modulus of sodium alginate with the slope in Figure 35 obtaining $E''_{alginate}$= 0.329 GPa.

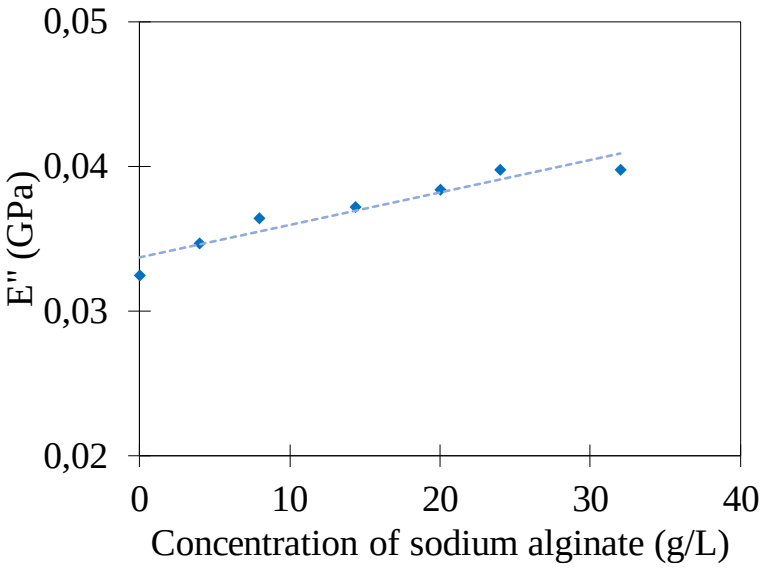

Figure 35: evolution of the longitudinal viscous modulus of aqueous solutions of sodium alginate as function of the concentration at extremely high frequencies (GHz)determined by Brillouin spectroscopy.

5.5.2. Shear elastic modulus and longitudinal elastic modulus as a function of frequency

Sodium alginate aqueous solutions begin to show a relevant shear elasticity in the concentrated regime when the density of entanglement points increases and the distance between them decreases. The combination of shear macrorheology (MR) and diffusive-wave spectroscopy (DWS) microrheology allows to perform a continuous study of the elastic modulus (G') over a wide frequency range between 10^{-2}-10^{5} Hz as shown in Figure 36 for the different sodium alginate concentrations.

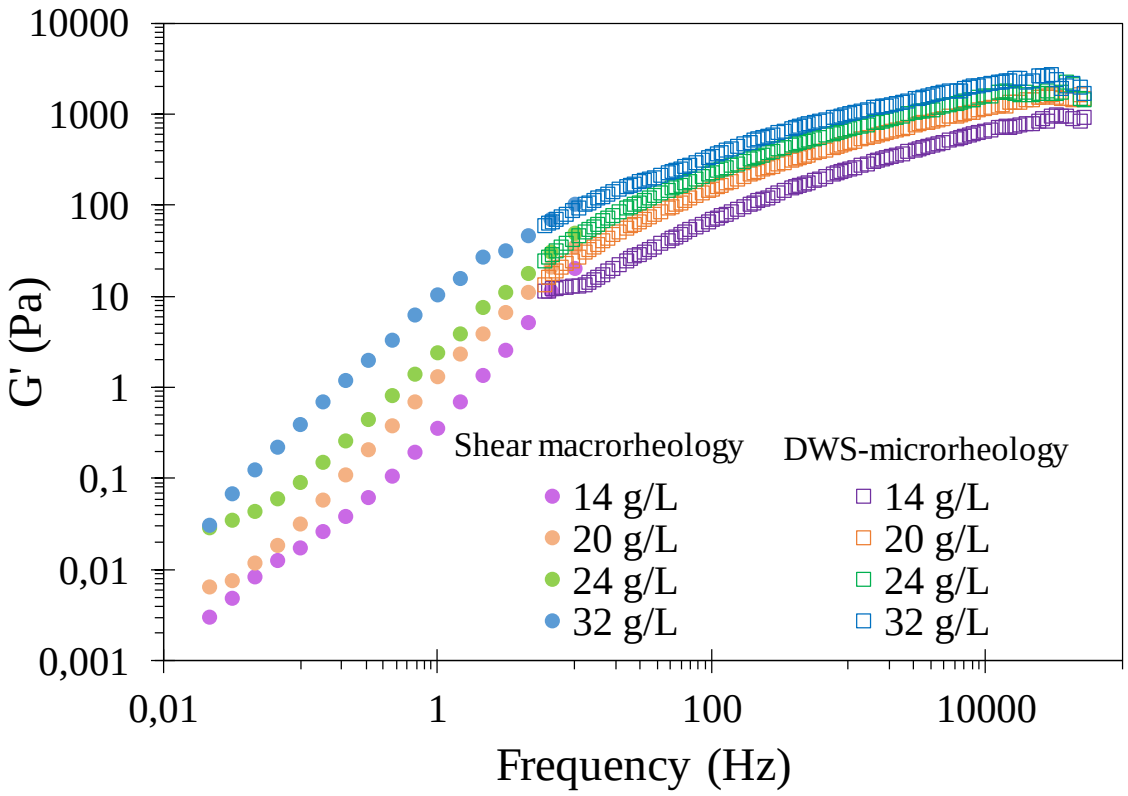

Figure 36: evolution of the elastic moduli as function of the frequency of sodium alginate aqueous solutions for different concentrations by combining shear macrorheology (MR) and diffusive wave spectroscopy (DWS).

In addition, the elastic longitudinal modulus (E') has been obtained from Brillouin spectroscopy as described previously (equation 46) from the frequency shift of the Brillouin peak for very high frequency (GHz). The observed experimental linear concentration dependence of E' (Figure 37) can be described as for E'' by using a mixing law [74]:

$$E' = E'_{water}.x_w + E'_{alginate}.(1 - x_w) \quad (49)$$

where x_w is the weight fraction of water and E'_{water} and $E'_{alginate}$ are the intrinsic longitudinal elastic modulus of water and sodium alginate respectively. A Brillouin experiment with pure water leads to the value E'_{water}= 2.21 GPa. We can then deduce the intrinsic longitudinal elastic modulus of sodium alginate with the slope in Figure 37 obtaining $E'_{alginate}$= 4.98 GPa.

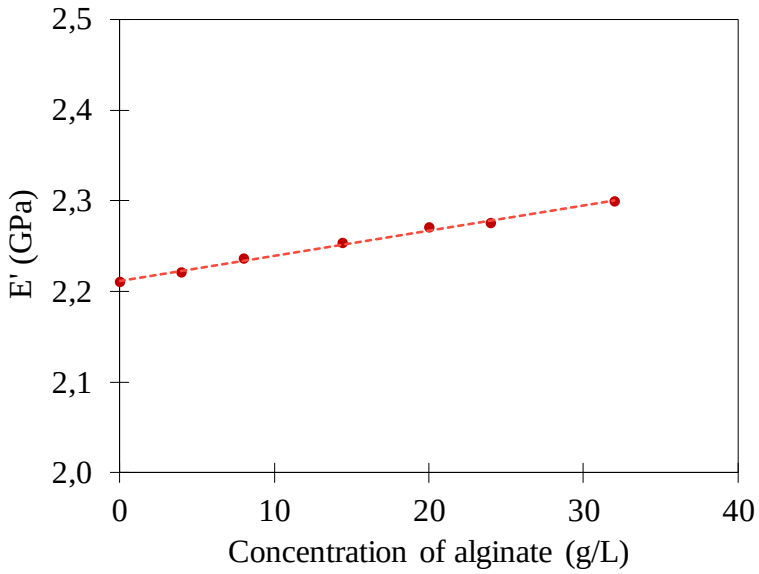

Figure 37: evolution of the longitudinal elastic modulus of aqueous solutions of sodium alginate as function of the concentration at extremely high frequencies (GHz) determined by Brillouin spectroscopy.

5.5.3. Zero shear viscosity

Different complementary experimental methods have been used to investigate the zero-shear viscosity of sodium alginate solutions as described below for the different concentration regimes:

- Semi-dilute regime (0.1-2 g/L): (1) Newtonian viscosity determined by shear rheology and (2) slope of the mean square displacement determined by DLS-microrheology for the alginate concentrations 1 and 2 g/L (Figure 30).
- Concentrated regime dominated by electrostatic repulsions (2-8 g/L): (1) first Newtonian shear viscosity (η_0) obtained from the fitting of steady shear flow measurements with Cross model (Table 9) and (2) slope of the mean square displacement at long times determined by DLS-microrheology for the alginate concentrations 4 and 8 g/L (Figure 30).
- Concentrated regime dominated by entanglements (8-40 g/L): (1) first Newtonian shear viscosity (η_0) obtained from the fitting of steady shear flow measurements with the Cross model (Table 9) and (2) first Newtonian shear viscosity (η_0) obtained from the fitting of the frequency-dependence of the dynamic viscosity (η') with the Cross model combining oscillatory macrorheology and DWS-based microrheology.

The values of the zero-shear specific viscosity are presented in Figure 38 showing a good agreement between all the methodologies.

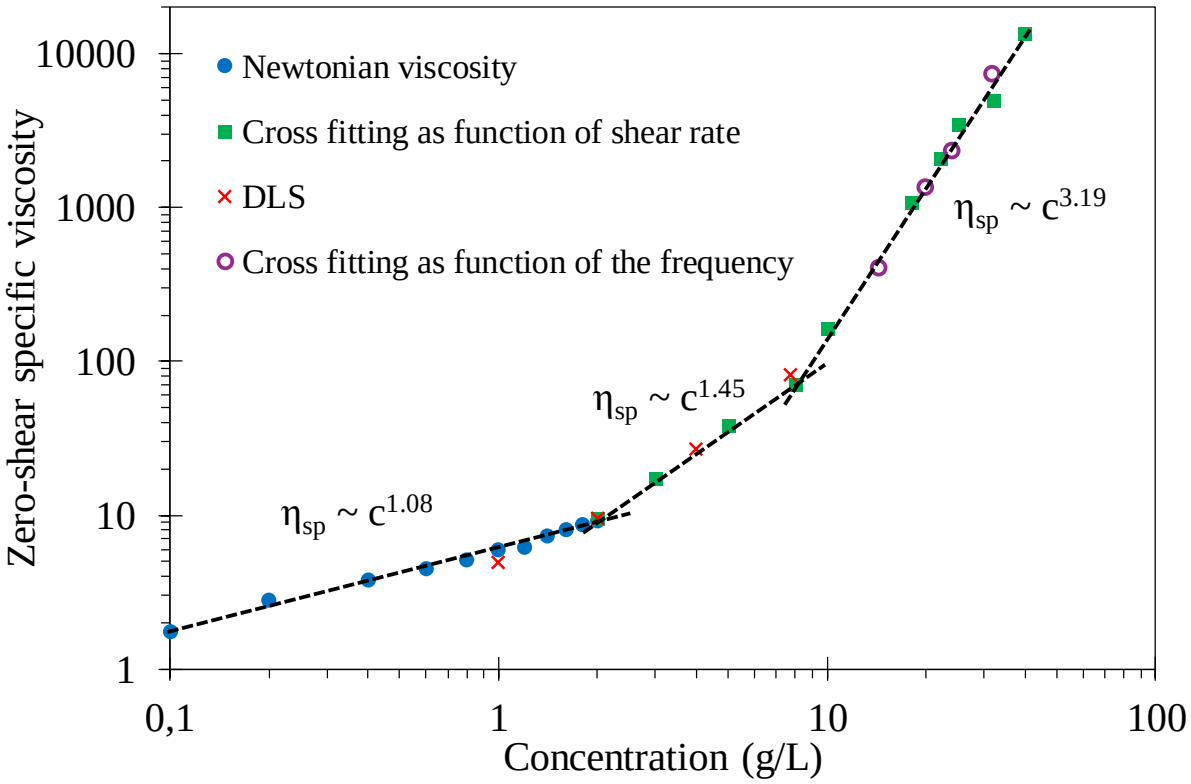

Figure 38: zero-shear specific viscosity as function of the sodium alginate concentration determined by different techniques and methodologies.

5.5.4. Determination of the persistence length (L_p) of sodium alginate

The determination of the viscoelastic properties of sodium alginate aqueous solutions in a wide range of frequencies between 10^{-2} and 10^{5} Hz opens the possibility to determine the persistence length of sodium alginate depending on the different power laws describing the evolution of the complex modulus ($G^* \sim \omega^n$). Theoretically, for concentrated solutions, the complex modulus (G*) follows a power law frequency dependence of $n < 1/2$ at low frequencies. When the frequency increases the single chain viscoelasticity starts to be measured showing a regime of $n = 5/9$ (Zimm-Rouse mode). Finally, at very high frequencies, the length scale decreases and the chain rigidity start to control the viscoelasticity showing a regime of $n = 3/4$ (bending mode) [75]. The persistence length of the polymer can be determined from the frequency (ω_c) at the transition between the Zimm-Rouse and bending mode by application of the following equation:

$$\omega_C = \frac{k_B T}{8\eta_S L_P^3} \qquad (50)$$

where k_BT is the thermal energy of the system and η_s the viscosity of the solvent (water). In order to determine this critical frequency (ω_c), the data was fitted with power law equations to identify the transition between the previously mentioned Rouse-Zimm and bending modes. An

example of this determination is presented in Figure 39 for an aqueous solution of sodium alginate with a concentration of 8 g/L.

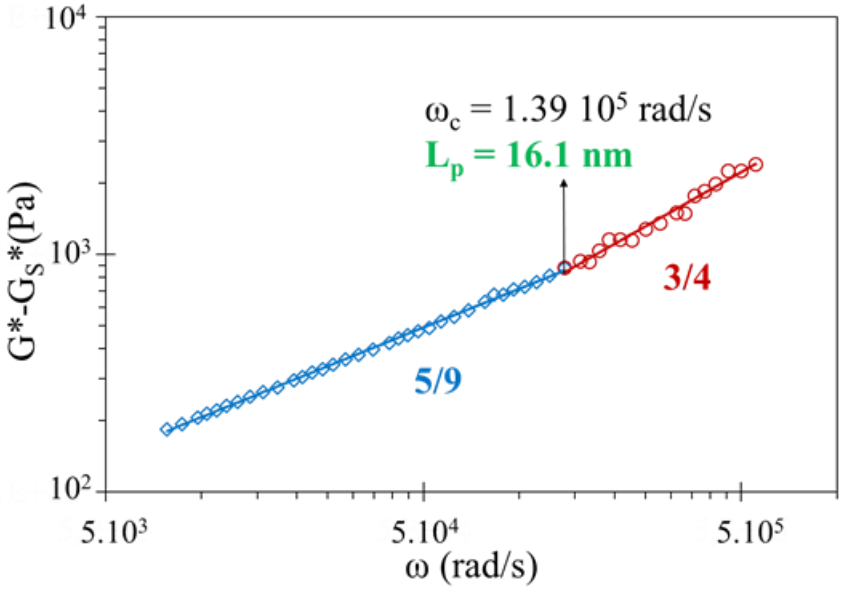

Figure 39: determination of the critical frequency (ω_c) for an aqueous solution of sodium alginate with a concentration of 8 g/L from the frequency dependence of the complex modulus (G*).

The values of the persistence length for the different concentrations of sodium alginate are collected in the Table 12. The value of the critical frequency (ω_c) increases with the concentration while the value of the persistence length decreases. For higher alginate concentrations the critical frequency is too high to be identified properly with the available results.

Table 12: persistence length of sodium alginate chains for aqueous solutions at different concentration.

C_{Alg} (g/L)	ω_c (rad/s)*10^4	L_p (nm)
2	6.25	21.0
4	8.93	18.6
8	13.9	16.1
14	19.2	14.4

To explain the experimentally observed concentration dependence of L_p, we can use the Odjik Skolnick Fixman relation (equations 51, 52 and 53). This model considers that the electrostatic charges along the chain tend to increase the local rigidity of the sodium alginate. For the present case, even if solutions were always prepared in pure water without addition of any salt, the effect of the proper Na^+ counterions can have an important effect on the ionic strength of the medium and then in the local rigidity. Thus, the increase of the sodium alginate concentration induces an increase of the concentration of counterions screening the electrostatic repulsion and therefore decreasing the electrostatic contribution to the persistence length ($L_{p,e}$). This tendency is in a good agreement with the experimental results obtained showing a decrease

of the persistence length as function of the alginate concentration. However, the decrease of L_p calculated with equation 51 is much smaller than the differences obtained experimentally.

$$L_p = L_{p,e} + L_{p,0} \quad (51)$$

$$L_{p,e} = \frac{\left(\frac{l_B}{b}\right)^2}{4l_b}\kappa^{-2} \quad (52)$$

$$\kappa^{-1} = \frac{1}{\sqrt{4\pi l_B C_f}} \quad (53)$$

where $L_{p,e}$ nd $L_{p,0}$ are the electrostatic and intrinsic contributions to L_p respectively, $l_B$is the Bjerrum length (0.71 nm in water), κ^{-1} is the Debye-Huckel screening length, b is the distance between charges and C_f is the ionic concentration of the solution.

The bigger differences of L_p determined experimentally can be explained by the change in the density of entanglements in the network as it was explained for other polyelectrolytes [76]. As schematized in the Figure 40, when the value of L_p is bigger than the mesh size (ξ_c) we are properly determining L_p from the critical frequency (ω_c). However, when L_p is smaller than the mesh size this determination is no longer possible due to the presence of entanglements.

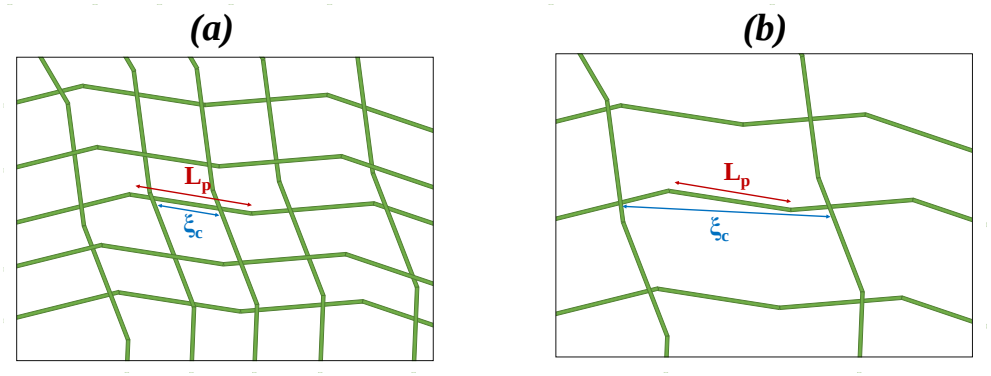

Figure 40: schematic representation of an entangled alginate solution with: (a) $L_p > \xi_c$ and (b) $L_p < \xi_c$.

5.6. Small-Angle X-ray Scattering (SAXS)

SAXS experiments were performed on ID02 high brilliance beamline at ESRF (European Synchrotron Radiation Facility, Grenoble, France; local contact: Frederic Pignon). An incident monochromatized X-ray beam with a wavelength $\lambda = 0.995$ Å was used. Scattered intensities were recorded on a two-dimensional CCD detector at sample-to-detector distances varied between 0.75 and 8 m leading to scattering vectors in the range 2.10^{-3} nm^{-1} < q < 3.5 nm^{-1}. The scattering intensity distribution as a function of scattering vector was obtained by radial integration of 2D scattering pattern. For measurements at constant temperature (25 ± 1ºC), capillary cell (diameter of ~2 mm) was filled with sodium alginate aqueous solutions at different concentrations (4 g/L, 8 g/L, 14 g/L, 20 g/L, 24 g/L and 32 g/L) in addition to a measurement

of pure water. For each concentration the experiments have been done in quintuplicate and the presented results are the average over them after the subtraction of the water background.

The evolution of the scattered intensity as function of the wave vector q has been normalized by the sodium alginate concentration and presented in the Figure 41. We can observe an overlapping at high q values for all the concentrations from which we have obtained the fractal dimension (d_f) from the slope according to equation 54. From the literature we know that there are two limit cases. For strong polyelectrolytes, the value of d_f is expected to be 1 which means a rod like conformation while, for neutral polymers with random coil conformation, a value of d_f = 5/3 is obtained considering exclude volume effects.

$$\frac{I}{c} \sim q^{-d_f} \tag{54}$$

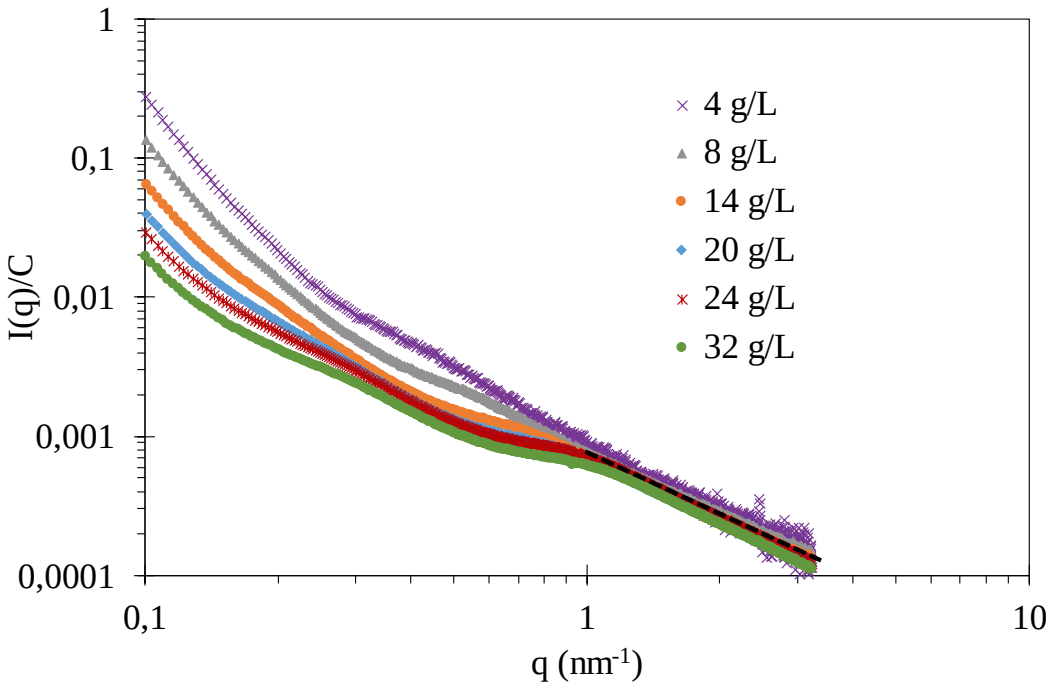

Figure 41: normalized scattering intensities I/c as function of q for alginate aqueous solutions at different concentrations.

As seen in Table 13, the values of d_f calculated for each concentration are close to 5/3 meaning that in the studied, the negative charge of sodium alginate are screened with a predominant of entanglements showing the behaviour of the concentrated regime of a neutral polymer. This is in good agreement with the characteristic exponent determined in Figure 16 for concentrations higher than 8 g/L.

Table 13: fractal dimension (d_f) and mesh size (ξ_c) as function f the alginate concentrations.

C_{Alg} (g/L)	d_f	ξ_c (nm)
4	1.58	-
8	1.43	11.90
14	1.44	8.84
20	1.48	7.45
24	1.51	6.61
32	1.53	5.98

The q-dependence of the structure factor S(q) defined as I(q)*q is shown in the Figure 42. From this representation it is possible to clearly identify a peak from which a characteristic distance (ξ) of the network could be defined ($q_{max} = 2\pi/\xi$) with ξ corresponding to the mesh size (ξ_c) or distance between entanglement of the sodium alginate chains. As expected, this distance becomes shorter as the concentration of sodium alginate is increased. following a power law concentration-dependence with an exponent 0.51 (Figure 43). This value is close to the theoretical value predicted for a polyelectrolyte solution in the concentrated regime ($\xi_c \sim c^{-1/2}$, equation 20). For the lowest alginate concentration (4 g/L) this peak cannot be detected. By comparing the values of ξ_c with the previously determined persistence length (L_p), it can be confirmed that at least for alginate concentrations higher than 8 g/L we are in the case (a) of the Figure 40 with $L_p > \xi_c$. It is also in good agreement with the behaviour of a concentrated solution dominated by entanglements found for concentrations higher than 8 g/L by the representation of the zero-shear viscosity in Figure 16.

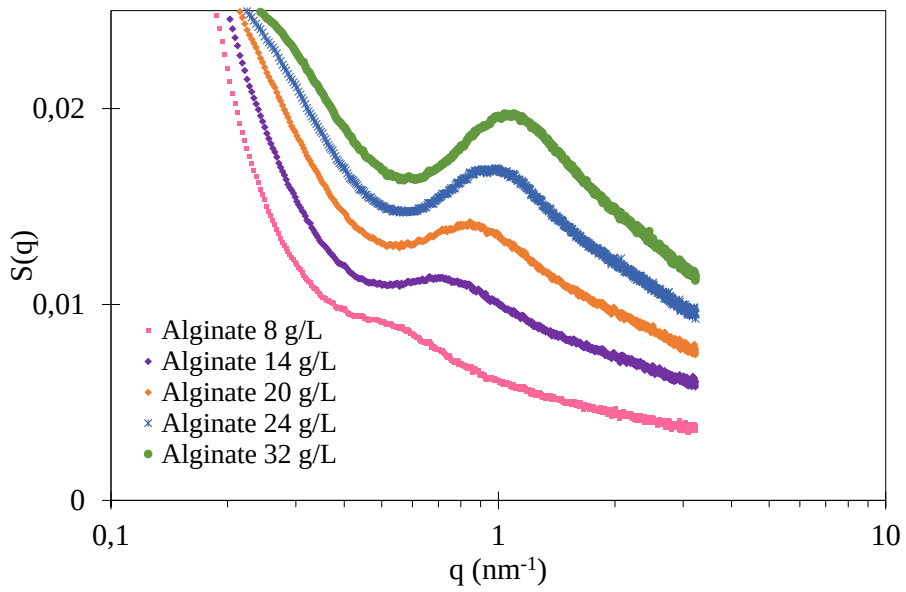

Figure 42: structure factor as function of the vector q in aqueous solutions of sodium alginate at different concentrations obtained by SAXS.

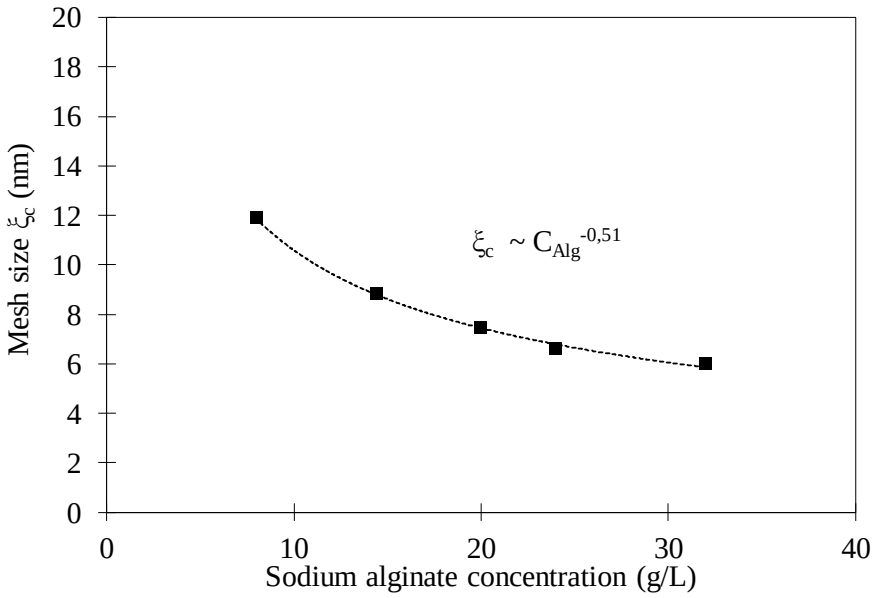

Figure 43: concentration-dependence of the mesh size of sodium alginate solutions determined by SAXS.

5.7. Conclusions

The multi-scale study performed in the aqueous solutions of sodium alginate, selected as main candidate for the elaboration of nanocomposites, has made possible to extend the characterization of its microstructure. A complete viscoelastic characterization of these materials has been obtained over seven frequencies decades by a combination of the results from macrorheology and microrheology. The persistence length of the alginate chains have been determined as function of the concentration from the measurements of DWS by identification of the characteristic frequency corresponding with the transition between a behaviour following Bending mode and Zimm-Rouse mode. The concentration dependence of the viscosity and the compressibility modulus in the GHz domain have been also determined from spectra obtained by Brillouin scattering. Complementary Small-Angle X-ray Scattering (SAXS) experiments are also performed to directly probe the structural properties. The evolution of the scattered intensity as function of the wave vector q shows at high-q values a power law behaviour with an exponent suggesting a polyelectrolyte random coil conformation due to charge screening if we compare with theoretical values from statistical approach of polymer physics for a wide range of concentrations (4-32 g/L). Moreover, the structure factor S(q) shows clearly peaks from which the mesh size of the entangled solution can be deduced.

As conclusion of this study, it can be confirmed that the characteristic size (mesh size and persistence length) of the entangled aqueous solutions of sodium alginate is in the same order of magnitude than the previously determined size of MNPs (~10 nm).

6. References

[1] L. Bedian, A.M. Villalba-Rodríguez, G. Hernández-Vargas, R. Parra-Saldivar, H.M.N. Iqbal, Bio-based materials with novel characteristics for tissue engineering applications – A review, Int. J. Biol. Macromol. 98 (2017) 837–846. https://doi.org/10.1016/j.ijbiomac.2017.02.048.

[2] N. Kalai Selvan, T.S. Shanmugarajan, V.N.V.A. Uppuluri, Hydrogel based scaffolding polymeric biomaterials: Approaches towards skin tissue regeneration, J. Drug Deliv. Sci. Technol. 55 (2020) 101456. https://doi.org/10.1016/j.jddst.2019.101456.

[3] S.H. Aswathy, U. Narendrakumar, I. Manjubala, Commercial hydrogels for biomedical applications, Heliyon. 6 (2020) e03719. https://doi.org/10.1016/j.heliyon.2020.e03719.

[4] B. Sharma, P. Malik, P. Jain, Biopolymer reinforced nanocomposites: A comprehensive review, Mater. Today Commun. 16 (2018) 353–363. https://doi.org/10.1016/j.mtcomm.2018.07.004.

[5] C.D. Spicer, Hydrogel scaffolds for tissue engineering: the importance of polymer choice, Polym. Chem. 11 (2020) 184–219. https://doi.org/10.1039/C9PY01021A.

[6] Z. Zhang, O. Ortiz, R. Goyal, J. Kohn, Chapter 23 - Biodegradable Polymers, in: R. Lanza, R. Langer, J. Vacanti (Eds.), Princ. Tissue Eng. Fourth Ed., Academic Press, Boston, 2014: pp. 441–473. https://doi.org/10.1016/B978-0-12-398358-9.00023-9.

[7] M.C. Hacker, J. Krieghoff, A.G. Mikos, Chapter 33 - Synthetic Polymers, in: A. Atala, R. Lanza, A.G. Mikos, R. Nerem (Eds.), Princ. Regen. Med. Third Ed., Academic Press, Boston, 2019: pp. 559–590. https://doi.org/10.1016/B978-0-12-809880-6.00033-3.

[8] W.E. Hennink, C.F. van Nostrum, Novel crosslinking methods to design hydrogels, Adv. Drug Deliv. Rev. 64 (2012) 223–236. https://doi.org/10.1016/j.addr.2012.09.009.

[9] N. Reddy, R. Reddy, Q. Jiang, Crosslinking biopolymers for biomedical applications, Trends Biotechnol. 33 (2015) 362–369. https://doi.org/10.1016/j.tibtech.2015.03.008.

[10] P.-G. de Gennes, P.P.-G. Gennes, Scaling Concepts in Polymer Physics, Cornell University Press, 1979.

[11] M. Rubinstein, R.H. Colby, Polymer Physics, OUP Oxford, 2003.

[12] Qicong. Ying, Benjamin. Chu, Overlap concentration of macromolecules in solution, Macromolecules. 20 (1987) 362–366. https://doi.org/10.1021/ma00168a023.

[13] Polymer Solutions: An Introduction to Physical Properties | Wiley, Wiley.Com. (n.d.).

[14] R.C. Ball, Scaling in Polymer Physics, in: R. Pynn, A. Skjeltorp (Eds.), Scaling Phenom. Disord. Syst., Springer US, Boston, MA, 1991: pp. 483–490. https://doi.org/10.1007/978-1-4757-1402-9_42.

[15] P.-G. de Gennes, P.P.-G. Gennes, Scaling Concepts in Polymer Physics, Cornell University Press, 1979.

[16] G. Strobl, ed., Polymer Solutions, in: Phys. Polym. Concepts Underst. Their Struct. Behav., Springer, Berlin, Heidelberg, 2007: pp. 69–104. https://doi.org/10.1007/978-3-540-68411-4_3.

[17] A.V. Dobrynin, M. Rubinstein, Theory of polyelectrolytes in solutions and at surfaces, Prog. Polym. Sci. 30 (2005) 1049–1118. https://doi.org/10.1016/j.progpolymsci.2005.07.006.

[18] R.M. Fuoss, Viscosity function for polyelectrolytes, J. Polym. Sci. 3 (1948) 603–604. https://doi.org/10.1002/pol.1948.120030414.

[19] A.V. Dobrynin, R.H. Colby, M. Rubinstein, Scaling Theory of Polyelectrolyte Solutions, Macromolecules. 28 (1995) 1859–1871. https://doi.org/10.1021/ma00110a021.

[20] T. Odijk, On the ionic-strength dependence of the intrinsic viscosity of DNA, Biopolymers. 18 (1979) 3111–3113. https://doi.org/10.1002/bip.1979.360181215.

[21] J. Skolnick, M. Fixman, Electrostatic Persistence Length of a Wormlike Polyelectrolyte, Macromolecules. 10 (1977) 944–948. https://doi.org/10.1021/ma60059a011.

[22] F. Oosawa, Polyelectrolytes, New York, 1971.

[23] G.S. Manning, Limiting Laws and Counterion Condensation in Polyelectrolyte Solutions I. Colligative Properties, J. Chem. Phys. 51 (1969) 924–933. https://doi.org/10.1063/1.1672157.

[24] M. Muthukumar, Theory of viscoelastic properties of polyelectrolyte solutions, Polymer. 42 (2001) 5921–5923. https://doi.org/10.1016/S0032-3861(00)00907-1.

[25] S. Van Vlierberghe, P. Dubruel, E. Schacht, Biopolymer-Based Hydrogels As Scaffolds for Tissue Engineering Applications: A Review, Biomacromolecules. 12 (2011) 1387–1408. https://doi.org/10.1021/bm200083n.

[26] J.L. Drury, D.J. Mooney, Hydrogels for tissue engineering: scaffold design variables and applications, Biomaterials. 24 (2003) 4337–4351. https://doi.org/10.1016/S0142-9612(03)00340-5.

[27] G.A. Martău, M. Mihai, D.C. Vodnar, The Use of Chitosan, Alginate, and Pectin in the Biomedical and Food Sector—Biocompatibility, Bioadhesiveness, and Biodegradability, Polymers. 11 (2019) 1837. https://doi.org/10.3390/polym11111837.

[28] L. Pereira, J. Cotas, Introductory Chapter: Alginates - A General Overview, Alginates - Recent Uses This Nat. Polym. (2020). https://doi.org/10.5772/intechopen.88381.

[29] K.I. Draget, C. Taylor, Chemical, physical and biological properties of alginates and their biomedical implications, Food Hydrocoll. 25 (2011) 251–256. https://doi.org/10.1016/j.foodhyd.2009.10.007.

[30] J. Aamodt, D. Grainger, Extracellular Matrix-based Biomaterial Scaffolds and the Host Response, Biomaterials. 86 (2016). https://doi.org/10.1016/j.biomaterials.2016.02.003.

[31] O. Aarstad, E.B. Heggset, I.S. Pedersen, S.H. Bjørnøy, K. Syverud, B.L. Strand, Mechanical Properties of Composite Hydrogels of Alginate and Cellulose Nanofibrils, Polymers. 9 (2017) 378. https://doi.org/10.3390/polym9080378.

[32] G.C. Porter, D.R. Schwass, G.R. Tompkins, S.K.R. Bobbala, N.J. Medlicott, C.J. Meledandri, AgNP/Alginate Nanocomposite hydrogel for antimicrobial and antibiofilm applications, Carbohydr. Polym. 251 (2021) 117017. https://doi.org/10.1016/j.carbpol.2020.117017.

[33] V. Spiridonov, I. Panova, Y. Antonova, L. Makarova, S. Zezin, A. Yaroslavov, Magnetosensitive Water-Soluble Nanocomposite Based on Sodium Alginate and Fe2O3 Nanoparticles, Macromol. Symp. 389 (2020) 1900082. https://doi.org/10.1002/masy.201900082.

[34] A. Dodero, L. Pianella, S. Vicini, M. Alloisio, M. Ottonelli, M. Castellano, Alginate-based hydrogels prepared via ionic gelation: An experimental design approach to predict

the crosslinking degree, Eur. Polym. J. 118 (2019) 586–594. https://doi.org/10.1016/j.eurpolymj.2019.06.028.

[35] S. Kommareddy, D. Shenoy, M. Amiji, Gelatin Nanoparticles and Their Biofunctionalization, in: Nanotechnologies Life Sci. Vol 1 Biofunctionalization Nanomater., 2007. https://doi.org/10.1002/9783527610419.ntls0011.

[36] P. Harris, V. Normand, I.T. Norton, GELATIN, in: B. Caballero (Ed.), Encycl. Food Sci. Nutr. Second Ed., Academic Press, Oxford, 2003: pp. 2865–2871. https://doi.org/10.1016/B0-12-227055-X/00551-4.

[37] S. Thakur, P.P. Govender, M.A. Mamo, S. Tamulevicius, V.K. Thakur, Recent progress in gelatin hydrogel nanocomposites for water purification and beyond, Vacuum. 146 (2017) 396–408. https://doi.org/10.1016/j.vacuum.2017.05.032.

[38] A. Bakravi, Y. Ahamadian, H. Hashemi, H. Namazi, Synthesis of gelatin-based biodegradable hydrogel nanocomposite and their application as drug delivery agent, Adv. Polym. Technol. 37 (2018) 2625–2635. https://doi.org/10.1002/adv.21938.

[39] B. Balakrishnan, S. Lesieur, D. Labarre, A. Jayakrishnan, Periodate oxidation of sodium alginate in water and in ethanol–water mixture: a comparative study, Carbohydr. Res. 340 (2005) 1425–1429. https://doi.org/10.1016/j.carres.2005.02.028.

[40] Z. Emami, M. Ehsani, M. Zandi, R. Foudazi, Controlling alginate oxidation conditions for making alginate-gelatin hydrogels, Carbohydr. Polym. 198 (2018) 509–517. https://doi.org/10.1016/j.carbpol.2018.06.080.

[41] C.G. Gomez, M. Rinaudo, M.A. Villar, Oxidation of sodium alginate and characterization of the oxidized derivatives, Carbohydr. Polym. 67 (2007) 296–304. https://doi.org/10.1016/j.carbpol.2006.05.025.

[42] B. Sarker, D. G. Papageorgiou, R. Silva, T. Zehnder, F. Gul-E-Noor, M. Bertmer, J. Kaschta, K. Chrissafis, R. Detsch, A. R. Boccaccini, Fabrication of alginate–gelatin crosslinked hydrogel microcapsules and evaluation of the microstructure and physico-chemical properties, J. Mater. Chem. B. 2 (2014) 1470–1482. https://doi.org/10.1039/C3TB21509A.

[43] W. Ding, J. Zhou, Y. Zeng, Y. Wang, B. Shi, Preparation of oxidized sodium alginate with different molecular weights and its application for crosslinking collagen fiber, Carbohydr. Polym. 157 (2017) 1650–1656. https://doi.org/10.1016/j.carbpol.2016.11.045.

[44] K. Deshmukh, M. Basheer Ahamed, R.R. Deshmukh, S.K. Khadheer Pasha, P.R. Bhagat, K. Chidambaram, 3 - Biopolymer Composites With High Dielectric Performance: Interface Engineering, in: K.K. Sadasivuni, D. Ponnamma, J. Kim, J.-J. Cabibihan, M.A. AlMaadeed (Eds.), Biopolym. Compos. Electron., Elsevier, 2017: pp. 27–128. https://doi.org/10.1016/B978-0-12-809261-3.00003-6.

[45] A. Barui, 3 - Synthetic polymeric gel, in: K. Pal, I. Banerjee (Eds.), Polym. Gels, Woodhead Publishing, 2018: pp. 55–90. https://doi.org/10.1016/B978-0-08-102179-8.00003-X.

[46] N.B. Halima, Poly(vinyl alcohol): review of its promising applications and insights into biodegradation, RSC Adv. 6 (2016) 39823–39832. https://doi.org/10.1039/C6RA05742J.

[47] T. Narita, K. Mayumi, G. Ducouret, P. Hébraud, Viscoelastic Properties of Poly(vinyl alcohol) Hydrogels Having Permanent and Transient Cross-Links Studied by

Microrheology, Classical Rheometry, and Dynamic Light Scattering, Macromolecules. 46 (2013) 4174–4183. https://doi.org/10.1021/ma400600f.

[48] M. Bercea, S. Morariu, D. Rusu, In situ gelation of aqueous solutions of entangled poly(vinyl alcohol), Soft Matter. 9 (2013) 1244–1253. https://doi.org/10.1039/C2SM26094H.

[49] M. Hu, X. Gu, Y. Hu, Y. Deng, C. Wang, PVA/Carbon Dot Nanocomposite Hydrogels for Simple Introduction of Ag Nanoparticles with Enhanced Antibacterial Activity, Macromol. Mater. Eng. 301 (2016) 1352–1362. https://doi.org/10.1002/mame.201600248.

[50] C.M. Hassan, N.A. Peppas, Structure and Morphology of Freeze/Thawed PVA Hydrogels, Macromolecules. 33 (2000) 2472–2479. https://doi.org/10.1021/ma9907587.

[51] Infrared and Raman Characteristic Group Frequencies: Tables and Charts, 3rd Edition | Wiley, Wiley.Com. (n.d.). https://www.wiley.com/en-us/Infrared+and+Raman+Characteristic+Group+Frequencies%3A+Tables+and+Charts%2C+3rd+Edition-p-9780470093078 (accessed March 2, 2021).

[52] D. Leal, B. Matsuhiro, M. Rossi, F. Caruso, FT-IR spectra of alginic acid block fractions in three species of brown seaweeds, Carbohydr. Res. 343 (2008) 308–316. https://doi.org/10.1016/j.carres.2007.10.016.

[53] E. Gómez-Ordóñez, P. Rupérez, FTIR-ATR spectroscopy as a tool for polysaccharide identification in edible brown and red seaweeds, Food Hydrocoll. 25 (2011) 1514–1520. https://doi.org/10.1016/j.foodhyd.2011.02.009.

[54] A. Kharazmi, N. Faraji, R. Hussin, E. Saion, W.M. Mat Yunus, K. Behzad, Structural, optical, opto-thermal and thermal properties of ZnS–PVA nanofluids synthesized through a radiolytic approach, Beilstein J. Nanotechnol. 6 (2015) 529–536. https://doi.org/10.3762/bjnano.6.55.

[55] J. Lee, T. Isobe, M. Senna, Preparation of Ultrafine Fe3O4Particles by Precipitation in the Presence of PVA at High pH, J. Colloid Interface Sci. 177 (1996) 490–494. https://doi.org/10.1006/jcis.1996.0062.

[56] N.V. Bhat, M.M. Nate, M.B. Kurup, V.A. Bambole, S. Sabharwal, Effect of γ-radiation on the structure and morphology of polyvinyl alcohol films, Nucl. Instrum. Methods Phys. Res. Sect. B Beam Interact. Mater. At. 237 (2005) 585–592. https://doi.org/10.1016/j.nimb.2005.04.058.

[57] I. Omkaram, R.P. Sreekanth Chakradhar, J. Lakshmana Rao, EPR, optical, infrared and Raman studies of VO2+ ions in polyvinylalcohol films, Phys. B Condens. Matter. 388 (2007) 318–325. https://doi.org/10.1016/j.physb.2006.06.134.

[58] D. Marani, J. Hjelm, M. Wandel, Use of Intrinsic Viscosity for evaluation of polymer-solvent affinity, in: Nord. Rheol. Soc. Annu. Trans., Nordic Rheology Society; 1997, 2013. https://orbit.dtu.dk/en/publications/use-of-intrinsic-viscosity-for-evaluation-of-polymer-solvent-affi (accessed March 25, 2021).

[59] W.-M. Kulicke, C. Clasen, Viscosimetry of Polymers and Polyelectrolytes, Springer-Verlag, Berlin Heidelberg, 2004. https://doi.org/10.1007/978-3-662-10796-6.

[60] M. Mancini, M. Moresi, F. Sappino, Rheological behaviour of aqueous dispersions of algal sodium alginates, J. Food Eng. 28 (1996) 283–295. https://doi.org/10.1016/0260-8774(95)00068-2.

[61] I.M.N. Vold, K.A. Kristiansen, B.E. Christensen, A study of the chain stiffness and extension of alginates, in vitro epimerized alginates, and periodate-oxidized alginates using size-exclusion chromatography combined with light scattering and viscosity detectors, Biomacromolecules. 7 (2006) 2136–2146. https://doi.org/10.1021/bm060099n.

[62] M.A. Masuelli, M.G. Sansone, Hydrodynamic Properties of Gelatin - Studies from Intrinsic Viscosity Measurements, Prod. Appl. Biopolym. (2012). https://doi.org/10.5772/34401.

[63] Mark-Houwink Parameters for Polymers, (n.d.). http://www.ampolymer.com/Mark-Houwink.html (accessed March 30, 2021).

[64] M. Masuelli, C. Illanes, Review of the characterization of sodium alginate by intrinsic viscosity measurements. Comparative analysis between conventional and single point methods, 1 (2014) 1–11.

[65] K. Nishinari, M. Djabourov, S.B. Ross-Murphy, eds., Helical structures from neutral biopolymers, in: Phys. Gels Biol. Synth. Polym., Cambridge University Press, Cambridge, 2013: pp. 182–221. https://doi.org/10.1017/CBO9781139024136.008.

[66] J. Vlachopoulos, N. Polychronopoulos, Basic Concepts in Polymer Melt Rheology and Their Importance in Processing, in: Appl. Polym. Rheol., John Wiley & Sons, Ltd, 2011: pp. 1–27. https://doi.org/10.1002/9781118140611.ch1.

[67] S. Dou, R.H. Colby, Charge density effects in salt-free polyelectrolyte solution rheology, J. Polym. Sci. Part B Polym. Phys. 44 (2006) 2001–2013. https://doi.org/10.1002/polb.20853.

[68] M.L. Olivares, M.B. Peirotti, J.A. Deiber, Analysis of gelatin chain aggregation in dilute aqueous solutions through viscosity data, Food Hydrocoll. 20 (2006) 1039–1049. https://doi.org/10.1016/j.foodhyd.2005.10.019.

[69] R. Wulansari, J.R. Mitchell, J.M.V. Blanshard, J.L. Paterson, Why are gelatin solutions Newtonian?, Food Hydrocoll. 12 (1998) 245–249. https://doi.org/10.1016/S0268-005X(98)00038-1.

[70] Y. Li, R. Cheng, Viscometric study of gelatin in dilute aqueous solutions, J. Polym. Sci. Part B Polym. Phys. 44 (2006) 1804–1812. https://doi.org/10.1002/polb.20847.

[71] C. Galindo-Gonzalez, S. Gantz, L. Ourry, F. Mammeri, S. Ammar-Merah, A. Ponton, Elaboration and Rheological Investigation of Magnetic Sensitive Nanocomposite Biopolymer Networks, Macromolecules. 47 (2014) 3136–3144. https://doi.org/10.1021/ma402655g.

[72] M. Choi, M. Humar, S. Kim, S.-H. Yun, Step-Index Optical Fiber Made of Biocompatible Hydrogels, Adv. Mater. 27 (2015) 4081–4086. https://doi.org/10.1002/adma.201501603.

[73] P. Del Gaudio, P. Colombo, G. Colombo, P. Russo, F. Sonvico, Mechanisms of formation and disintegration of alginate beads obtained by prilling, Int. J. Pharm. 302 (2005) 1–9. https://doi.org/10.1016/j.ijpharm.2005.05.041.

[74] M. Bailey, M. Alunni-Cardinali, N. Correa, S. Caponi, T. Holsgrove, H. Barr, N. Stone, C.P. Winlove, D. Fioretto, F. Palombo, Viscoelastic properties of biopolymer hydrogels determined by Brillouin spectroscopy: A probe of tissue micromechanics, Sci. Adv. 6 (2020) eabc1937. https://doi.org/10.1126/sciadv.abc1937.

[75] N. Willenbacher, C. Oelschlaeger, M. Schopferer, P. Fischer, F. Cardinaux, F. Scheffold, Broad Bandwidth Optical and Mechanical Rheometry of Wormlike Micelle Solutions, Phys. Rev. Lett. 99 (2007). https://doi.org/10.1103/PhysRevLett.99.068302.

[76] T. Saint-Martin, Rheological study of a new semi-rigid giant polysaccharide for the mechanical reinforcement of hydrogels, Theses, Université Pierre et Marie Curie - Paris VI, 2017

Chapter III: polymer hydrogels

1. Introduction

Hydrogels are three-dimensional (3D), insoluble, crosslinked polymer networks that are able to retain a large amount of water in their swollen state [1] due to their hydrophilic functional groups along the polymer backbone and their resistance to dissolution. The combination of a polymer network with the presence of water inside the pores allows the free diffusion of some solute molecules through a material with mechanical integrity leading to a lot of interesting properties, such as absorption capacity, swelling behaviour, stability and degradation, bioactivity, permeability, mechanical properties, optical and surface properties that make them excellent candidates in a wide range of applications, being particularly noteworthy their uses for the elaboration of biomedical devices for cell culture, tissue engineering and drug delivery.

Depending on the nature of the crosslinking, two main types of hydrogels are usually defined. In the one hand, physical hydrogels, are crosslinked by various strong/weak intermolecular interactions between the polymer chains; such as hydrogen bonds, electrostatic interactions, hydrophobic interactions, crystallization, etc. In the other hand, chemical gels are covalently crosslinked either by the formation of branched macromolecules during the polymerization or by the covalent crosslinking of previously formed macromolecules. The main difference between both types is that irreversible chemical hydrogels are more stable due to the covalent links, while reversible physical gels can be easily modified by external stimuli due to the reversible nature of the physical interactions.

In this context, the purpose of this chapter is to develop different methodologies to prepare hydrogels from the previously studied polymer solutions. Based on the literature [1–9], two methods have been chosen to elaborate calcium alginate hydrogels and PVA hydrogels. A complete study of sol-gel transition, viscoelasticity and swelling properties of the totally gelled samples has been performed to optimize the conditions of the development of nanocomposite hydrogels.

2. Elaboration of polymer hydrogels

The two chosen strategies for the elaboration of hydrogels from the selected polymer solutions studied in the chapter II are presented below.

2.1. Ionic crosslinking of sodium alginate with calcium cations

The gelation of sodium alginate in the presence of high amounts of water has been a main topic of investigation during the last decades due to the interesting properties of the formed hydrogels. The most common method to prepare those hydrogels is the ionic crosslinking with bivalent cations giving rise to aligned ribbon-like assemblies with cavities in which bivalent cations are located in the known as egg-box structure [10]. The affinity of the carboxylic groups for the alkaline earth metals changes by the following order: Mg ≪ Ca < Sr < Ba. Based on the steric configuration and the displacement of sodium ions (Na^+) from the original sodium alginate it has been found that, despite some specific applications, the more suitable ionic crosslinking for biomedical applications is achieved with calcium cations (Ca^{2+}) [11–13]. Thus, calcium alginate hydrogels have been elaborated through the ionic crosslinking mechanism schematized in Figure 1 consisting in the binding of Ca^{2+} cations between two available carboxylate groups of the sodium alginate chains showing preference for guluronic monomers.

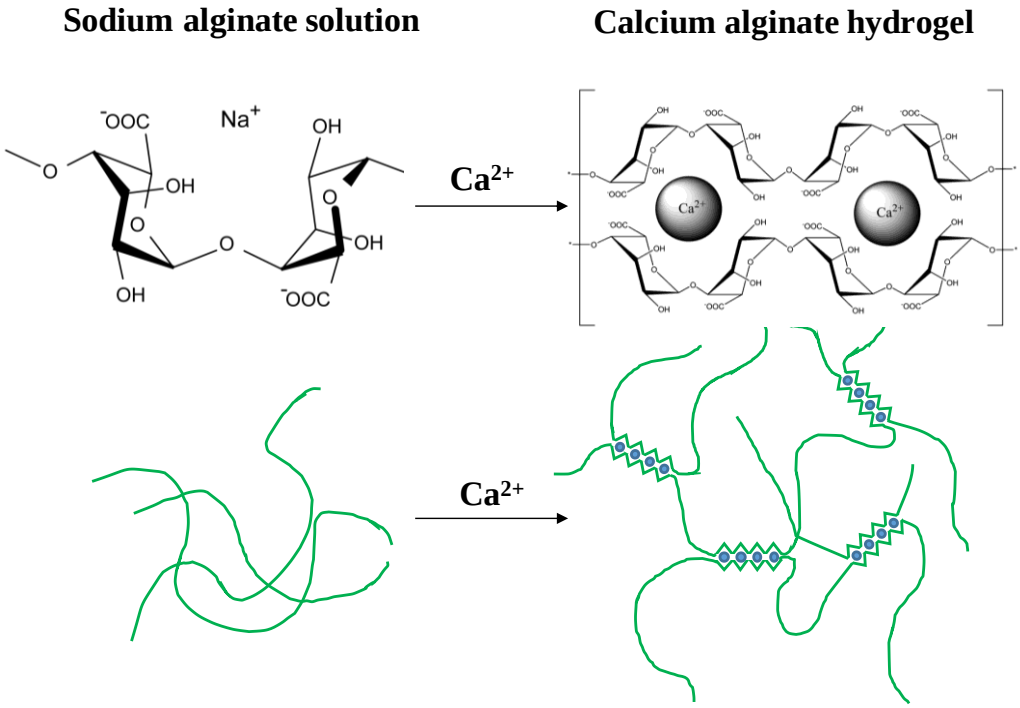

Figure 1: schematic crosslinking of the alginate chains and calcium cations in egg-box model.

The addition of calcium can be achieved by external or internal method. In external gelation method, the sodium alginate solution is directly mixed with an aqueous solution of a soluble source of calcium. This methodology is very appropriate for the elaboration of calcium

alginate microbeads introducing the sodium alginate solution drop by drop in an aqueous solution of calcium chloride ($CaCl_2$) [14]. However, it is no appropriate to obtain a homogeneous macroscopic hydrogel due to the extremely fast gelation which occurs on the surface of the hydrogel hindering the diffusion of calcium to its core. In the internal method schematized in Figure 2, a source of calcium is dispersed in an aqueous solution of sodium alginate. This calcium will not interact with the carboxylate groups of the sodium alginate chains because it is not in its cationic form (Ca^{2+}). Thus, it can be homogeneously dispersed in the sodium alginate solution resulting in a pre-gel system. Then, the release of calcium cations (Ca^{2+}) is induced by a decrease of pH by adding glucono-delta-lactone (GDL) to initiate the ionic crosslinking in a controlled manner. In this study, we have selected two different internal methods based on the formation of a complex of calcium chloride in Ethylenediaminetetraacetic Acid ($CaCl_2$-EDTA) [15] and the calcium carbonate ($CaCO_3$) insoluble salt [16] respectively.

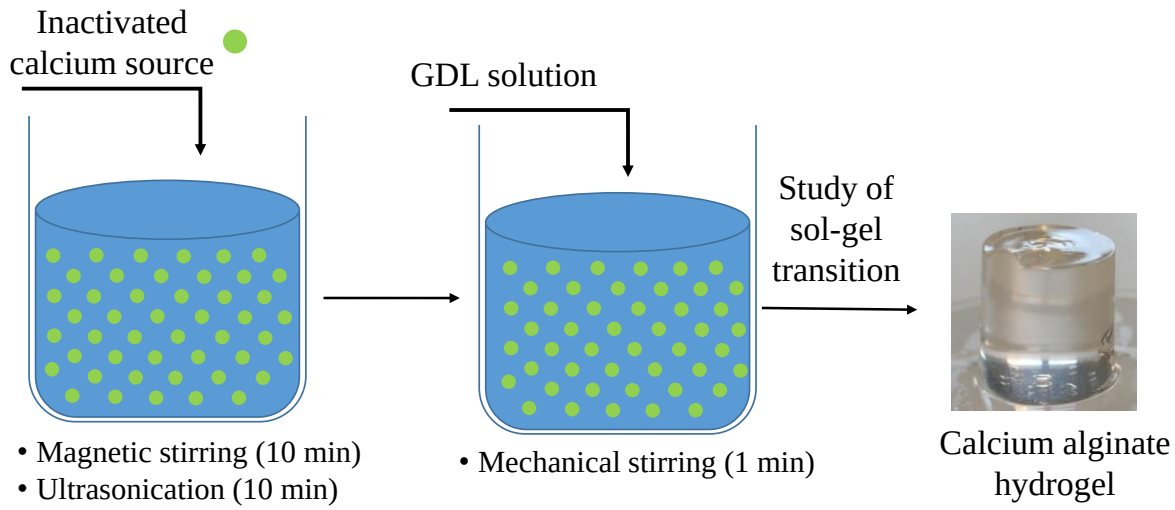

Figure 2: schematic representation of the experimental protocol to elaborate calcium alginate hydrogels by an internal method: (a) dispersion of the calcium source to prepare the pre-gel system, (b) addition of GDL to decrease the pH to induce the release of Ca^{2+} and (c) resultant homogenous macroscopic calcium alginate hydrogel.

2.1.1. Source of calcium: $CaCl_2$-EDTA complex solution

In this case calcium chloride ($CaCl_2$, Sigma-Aldrich) has been mixed with the chelating agent Ethylenediaminetetraacetic Acid (EDTA, Sigma-Aldrich) and NaOH (aq) to adjust the pH forming a $CaCl_2$-EDTA aqueous complex solution that presents a pH-dependent stability constant. This complex solution has been prepared in principle at pH = 9 to ensure a high stability constant and introduced in aqueous solution of sodium alginate under continuous mechanical stirring to achieve a homogeneous distribution of the source of calcium. The gelation has then been initiated by decreasing the pH with the addition of a freshly prepared D-glucono-delta-lactone (GDL, Alfa Aesar) aqueous solution which is slowly hydrolyzed to

gluconic acid in water as described in the literature [17]. The gelation kinetics are controlled by the slowly release of Ca^{2+} from the complex due to the decrease of its stability constant induced by the decrease of the pH.

2.1.2. Source of calcium: $CaCO_3$ salt

For the second source of calcium, we take the advantage of the pH dependent solubility of calcium carbonate ($CaCO_3$, Sigma-Aldrich) in water. The $CaCO_3$ powder has been directly dispersed in an aqueous solution of sodium alginate by sonication and vortex at neutral pH for which its solubility is almost negligible. The solubilisation of the dispersed $CaCO_3$ has then induced by the addition of freshly prepared GDL solution. The gelation kinetics are controlled by the slowly solubilisation of $CaCO_3$ that is a surface-controlled process due to the micronic size of $CaCO_3$ particles much bigger than molecular size of the $CaCl_2$-EDTA complex.

2.2. PVA hydrogels

The elaboration of poly (vinyl alcohol) (PVA) hydrogels has been motivated by the crosslinking process without adding any crosslinking agent [18]. PVA hydrogels have been prepared by placing a volume of as prepared PVA aqueous solutions with a concentration of 100 g/L in a Petri dish and submitting them to repeated freezing–thawing cycles which included a freezing step (16h at -22ºC) followed by a thawing step (8h at 25ºC). As schematized in Figure 3 the sol-gel transition takes place due to the formation of crystalline regions.

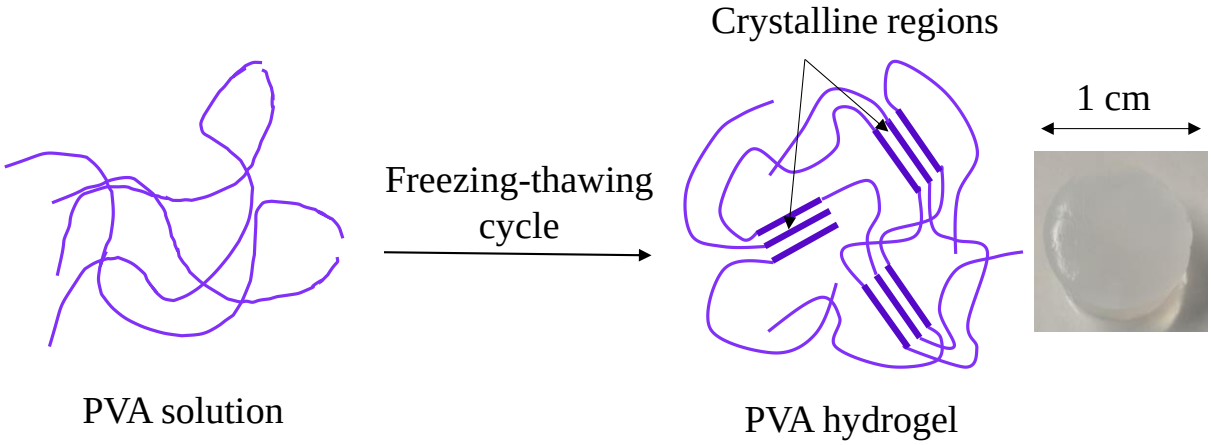

Figure 3: schematic crosslinking of the PVA by the formation of crystalline regions.

3. Study of the sol-gel transition of calcium alginate hydrogels

3.1. Introduction

When a polymer is crosslinked, either by physical or chemical crosslinking, a sol-gel transition occurs over time, and an infinite three-dimensional (3D) polymer network is formed at the gelation time (t_g) where the divergence of mechanical properties such as viscosity or equilibrium modulus associated to critical exponents is observed. Rheology is then a powerful tool to investigate the sol-gel transition both for physical [19] and chemical gelation [20].

3.2. Experimental

The simplest approach to investigate the sol-gel transition is the measurement of the time-evolution of the elastic (G') and viscous (G") moduli for a constant frequency and fixed strain amplitude in the linear viscoelastic domain. The gel point is then defined by the transition between a liquid-like behaviour (G"(t)>G'(t)) to a solid-like behaviour (G"(t)<G'(t)). Nevertheless, it has been reported that this crossover time of both moduli is frequency-dependent [21] and the gel point should be independent of the chosen experimental conditions. A different approach is based on the fact that a material undergoing a sol-gel transition shows an intermediate state between solid and liquid named as critical gel. Based on experimental studies, Winter and Chambon [22] have proposed a mechanical definition of the critical gel based on the experimental finding of a power law time dependence of the shear modulus G(t):

$$G(t) = S.t^{-\Delta} \text{ for } \lambda_0 < t < \infty \quad (1)$$

where S is named the gel stiffness, Δ is the relaxation exponent and λ_0 is a critical relaxation time above which the power law is observed.

It can be demonstrated by using the classical equations of the viscoelasticity that the distribution of the relaxation times of the critical gel is also described by a power law meaning a continuous distribution of relaxation times and properties of self-similarity. The determination of shear modulus as function of time by creep experiment (measurement of shear stress as a function of time under applied constant shear strain) is not appropriate for samples for which the gelation process cannot be quenched at different times. In this case oscillatory measurements are more useful taking into account the frequency dependence of elastic (G') and viscous (G") moduli obtained by Fourier transform of equation 1:

$$G' = \frac{\pi.S.\omega^{\Delta}}{2.\Gamma(\Delta).sin\left(\frac{\Delta.\pi}{2}\right)} \quad (2)$$

$$G'' = \frac{\pi . S . \omega^{\Delta}}{2 . \Gamma(\Delta) . cos\left(\frac{\Delta . \pi}{2}\right)} \quad (3)$$

where Γ is the Legendre function and ω is the angular frequency.

In consequence, at the gel point G' and G" have a power law frequency dependence with the same exponent (Δ) and the ratio of both moduli is independent of the frequency:

$$\tan \delta = \frac{G''}{G'} = \tan\left(\frac{\Delta . \pi}{2}\right) \quad (4)$$

Therefore, the plot of G"/G' as a function of time for the different frequencies allows to define the gel time (t_g) from the intersection point of all the curves. The relaxation exponent (Δ) and the gel stiffness can be then deduced using equations 2-4 The theoretical values of Δ are between 0 and 1. The case of Δ = 0 corresponds to the limiting behaviour of a Hookean solid (the relaxation modulus is a constant); while the restriction of Δ to values less than unity is necessary to assure a diverging zero-shear viscosity at the gel point.

This experimental study of the sol-gel transition is known as time-resolved mechanical spectroscopy (TRMS). It has been performed with a torque controlled rheometer MARS II (Thermo Fischer Scientific) fitted with a cone and plate geometry (diameter of 60 mm and angle of 1°). Temperature has been kept constant at 25±0.1 ºC by using a Peltier system located in the lower plate with a solvent trap to reduce the evaporation of sample during the measurements. The pre-gel system has been loaded on the plate just after the addition of GDL and oscillatory measurements have been performed by successive frequency sweeps between 0.2 and 3 Hz at constant stress amplitude of 1 Pa within the linear viscoelastic domain (LVD). The TRMS experiment protocol requires that the time-evolution of the rheological properties of the samples remain negligible compared to the period (t_{exp}) of each frequency sweep. This hypothesis can experimentally be checked in terms of a mutation number N_{mu} which quantifies the change of a dynamical rheological property during an experiment, and the Deborah number, N_{De} [23]. For a gelation experiment Winter *et al*. [24] found that a sample can be considered quasi-stable if $N_{mu} < 0.15$.

3.3. Source of calcium: $CaCl_2$-EDTA complex solution

3.3.1. TRMS study

An example of the time-evolution of G"/G' at different frequencies from a TRMS experiment just after the addition of GDL is presented in Figure 4 including the time-evolution of the elastic modulus G'(t) for a fixed frequency f = 1Hz in the insert. Even if the evolution of G'(t) do not allow to define unambiguously the gel point, it allows to certainly understand the

different steps taking place after the addition of GDL to induce the Ca^{2+} release and the ionic crosslinking of the sodium alginate chains. During the first step, G'(t) remains nearly constant until an induction time (t_i) for which the pH reaches a low enough value to induce the Ca^{2+} release accordingly with the decrease of the chelating stability constant of the $CaCl_2$-EDTA complex (pH ~ 5 [25]). More precisely, the induction time (t_i) is defined as the time required to have enough Ca^{2+} to create the first ionic crosslinks between alginate chains that are detected by the onset of G'(t). In a second step, the continuous release of Ca^{2+} from the complex induces electrostatic interactions of carboxylate groups of first guluronate and then manuronate sequences of the sodium alginate leading to aligned ribbon-like assemblies with cavities in which Ca^{2+} cations are located in the well-known egg-box structure [10]. This progressive formation of junction zones induces a sharp increase of G'(t) characteristic of a sol-gel transition that is studied in more detail defining the gelation time (t_g), the gel stiffness (S) and the relaxation exponent (Δ) by the crossover point of G"/G' at different frequencies as firstly proposed by Winter and according to the equations 2, 3 and 4. The transition between a liquid behaviour (G"/G' decreases with the frequency) and solid behaviour (G"/G' increases with the frequency) can be also observed in this plot. At longer times, G'(t) tends to a plateau from which is defined the value G'_∞, as preliminary characterization of the totally gelled state.

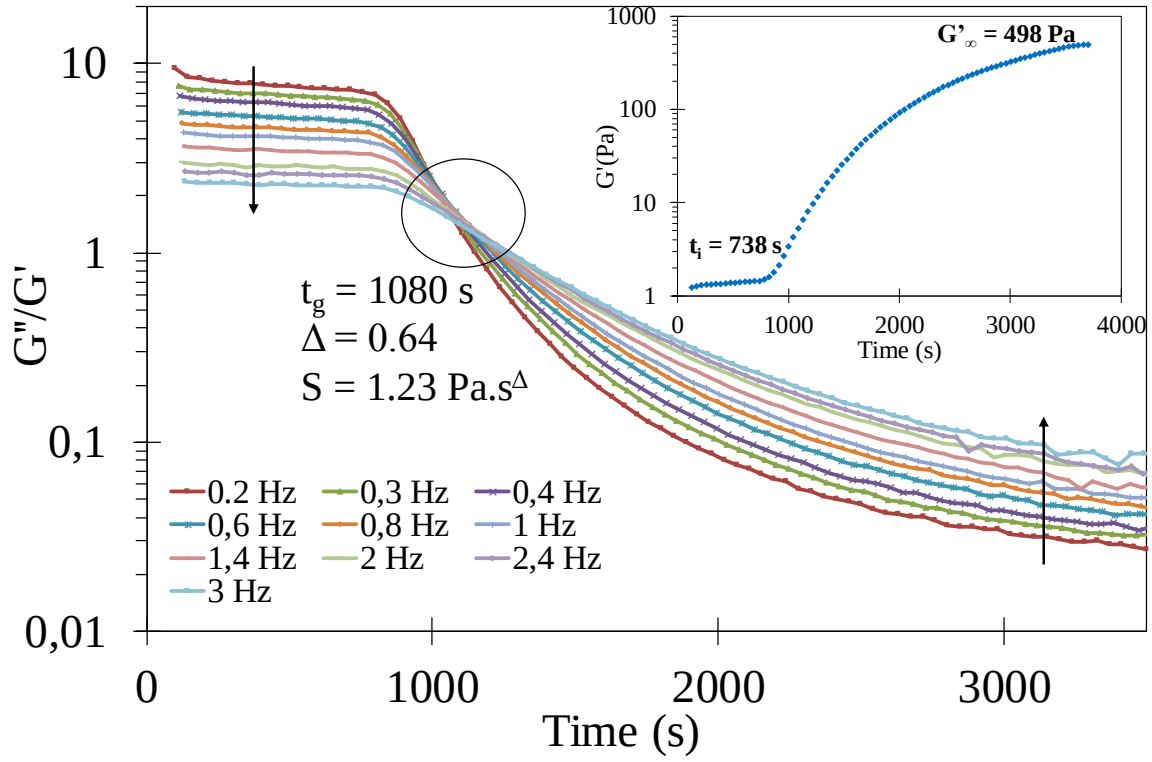

Figure 4: TRMS for the sol-gel transition of calcium alginate hydrogel with $CaCl_2$-EDTA as source of calcium, C_{alg} = 18 g/L, R_{Ca}=0.5, EDTA/$CaCl_2$ = 1 and GDL/$CaCl_2$ = 1.8. Time-evolution of the elastic modulus (G') for f = 1Hz in the insert.

All the determined parameters from Figure 4 can depend on several experimental conditions selected for the elaboration of the calcium alginate hydrogel with the $CaCl_2$-EDTA complex. A preliminary study of the effect of the several experimental conditions on the sol-gel transition has been performed to fix them and to let only the molar ratio between added calcium and carboxylate groups ($R_{Ca} = [Ca^{2+}]/[COO^-]$) as open control parameter. The different experimental conditions to be analysed are divided in the two following subchapters:

3.3.2. Effect of the alginate concentration (C_{Alg})

The results from the analysis of three independent TRMS experiments for sodium alginate concentrations of 10, 18 and 25 g/L with the other experimental conditions fixed to constant values are presented in the Table 1. The gel strength (S) increases as function of the sodium alginate concentration in good agreement with the relation between S and the total mass of alginate in solution found by Liu *et al.* [26]. The values of Δ remain practically independent of C_{Alg}. The value of Δ defines the viscoelastic behaviour at the critical gel point being $\Delta = 0.5$ a limiting value between more solid-like than liquid-like (G'>G") critical gels ($0<\Delta<0.5$) and more liquid-like than solid -like (G<G") critical gels ($1>\Delta>0.5$). Typically, Δ and S are inversely related values, and when S increases is accompanied by a Δ decrease following some relations for certain conditions found on the literature [27]. However, experimentally it was not always observed this tendency. The observed increase of S not accompanied by a Δ decrease as function of C_{Alg} has been explained by several authors based on the change of the crosslinking degree at the critical gel point for calcium alginate hydrogels prepared by an internal method [26,28]. The crosslinking degree can be defined as the proportion between calcium crosslinked carboxylates and total carboxylates in the alginate chains. It has been observed experimentally that the crosslinking degree at the gel point decreases as the sodium alginate concentration is increased. Therefore, the observed increase of S as function of C_{Alg} should be related with this increase in the crosslinking degree leading to denser junction points while the value of Δ remains constant.

Moreover, the change on the kinetics identified by the variation of the characteristic times t_i and t_g shown in the Figure 5 can also influence the characteristics at the gel point. It is observed a linear variation of t_i with the alginate concentration that should be related with the different amounts of GDL added (proportionally to the sodium alginate concentration). The gelation time (t_g) follows also a linear decrease as function of C_{alg}. However, the variation indicated by the slope in the Figure 5 is more important fo t_g suggesting other mechanism controlling the kinetics in addition to the amount of GDL. Concerning the properties of the

totally gelled samples, G'_∞ increases when the alginate concentration is increased from 10 g/L to 18 g/L but it does not change when the concentration of alginate is increased from 18 g/L to 25 g/L. This can be explained by a more restricted diffusion of Ca^{2+} as the crosslinking mechanism progresses for C_{Alg} = 25 g/L.

Table 1: TRMS results for calcium alginate hydrogels with $CaCl_2$-EDTA with different C_{Alg} and fixed R_{Ca} = 0.5, [EDTA]/[Ca^{2+}] = 1, [GDL]/[Ca^{2+}] = 1.8 and pH = 9.

C_{Alg} (g/L)	t_i (s)	G'_∞ (Pa)	t_g (s)	Δ	S (Pa.s^{Δ})
10	1071±20	127±20	1460±40	0.58±0.04	0.30±0.09
18	743±20	498±50	1080±40	0.64±0.04	1.23±0.38
25	605±20	525±50	820±40	0.60±0.05	3.92±1.23

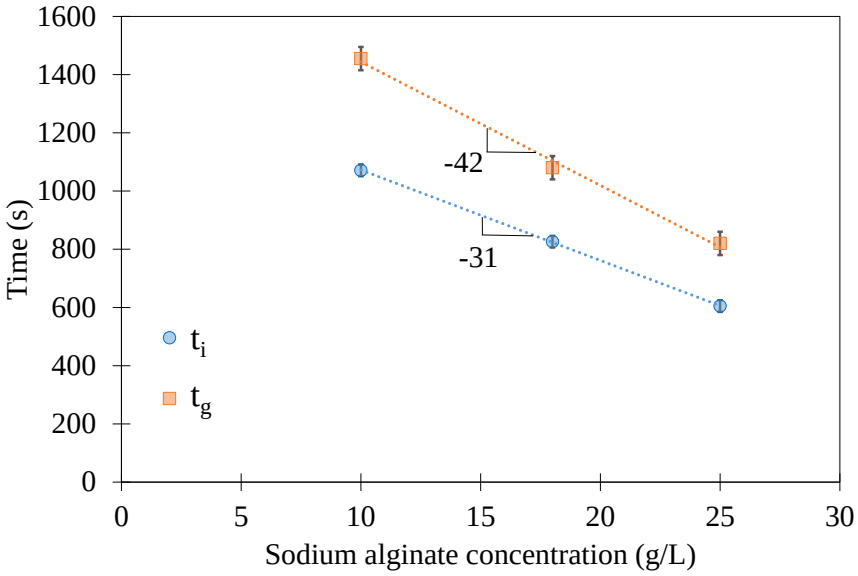

Figure 5: variation of the characteristic times t_i and t_g for alginate gels prepared with different sodium alginate concentrations.

The study of the effect of the alginate concentration on the sol-gel transition by TRMS leads to an optimal C_{Alg} = 18 g/L. In the one hand, the selection of a higher (C_{Alg} = 25 g/L) leads to a slightly hard critical gel but without observing an increase of the elastic modulus at long times (G'_∞) probably due to the limitations of diffusion of Ca^{2+} through the more concentrated network in the advanced steps of the gelation. In the other hand the lower concentration (C_{Alg} = 10 g/L) leads to weak elastic modulus at long times (G'_∞).

3.3.2. Effect of the parameters of the complex solution

There are two parameters in the elaboration of the complex solution that could be used to modify the Ca^{2+} release, the ratio [EDTA]/[Ca^{2+}] and the pH. The recommended value according to the literature [15] for the molar ratio is [EDTA]/[Ca^{2+}] = 1 considering the

formation of a complex in between one molecule of $CaCl_2$ and EDTA. To confirm that, an experiment was carried out with a molar ratio [EDTA]/[Ca^{2+}] = 0.8 observing an increase of the viscosity when the complex solution and the sodium alginate solution were mixed demonstrating that it is necessary at least an equimolecular proportion EDTA:$CaCl_2$ to have a totally insolube source of calcium. Then, two independent TRMS studies of the sol-gel transition have been performed with two values of ratio ([EDTA]/[Ca^{2+}] = 1 and 1.2) fixing all the other conditions. The results of the analysis are collected in the Table 2. The increase of the ratio leads to a softer critical gel (lower S and higher Δ) that can be ascribed to a slow down of the kinetics of Ca^{2+} released observed by an important increase of t_g and t_i. In addition, the value of G'_∞ strongly decrease with the increase of [EDTA]/[Ca^{2+}] concluding that an increase of this ratio decreases the rate of Ca^{2+} release but also imply a non-desired decrease of the final mechanical properties of the totally gelled sample.

Table 2: TRMS results for calcium alginate hydrogels with $CaCl_2$-EDTA with two molar ratios [EDTA]/[Ca^{2+}] and fixed C_{Alg} = 18 g/L, R_{Ca} = 0.5, [GDL]/[Ca^{2+}] = 1.65 and pH=9.

[EDTA]/[Ca^{2+}]	t_i (s)	G'_∞ (Pa)	t_g (s)	Δ	S (Pa.s^{Δ})
1	738±20	498±50	1010±40	0.65±0.05	0.86±0.29
1.2	2217±20	170±20	2700±100	0.70±0.08	0.61±0.37

Concerning the pH of the complex solution, a value of pH = 9 is initially selected since it is enough to ensure a high stability chelation constant of the $CaCl_2$-EDTA complex accordingly to previous experiences in the laboratory MSC. However, to evaluate the effect of pH, the results of independent TRMS experiments performed at three different pH (12, 9 and 7) fixing all the previously defined parameters are presented in the Table 3. The main observed effect is an increase of the induction time as function of the increase of the pH.

Table 3: TRMS results for calcium alginate hydrogels with $CaCl_2$-EDTA with different pH of the complex solution and fixed C_{Alg} = 18 g/L, R_{Ca} = 0.4, [EDTA]/[Ca^{2+}] = 1 and [GDL]/[Ca^{2+}] = 2.

pH	t_i (s)	G'_∞ (Pa)	t_g (s)	Δ	S (Pa.s^{Δ})
7	857±20	620±50	1100±30	0.72±0.04	0.50±0.14
9	951±20	600±50	1220±30	0.70±0.03	0.59±0.14
12	1547±20	322±30	1900±30	0.72±0.02	0.53±0.09

As conclusion, the modulation of the kinetics of Ca^{2+} release by the selection of the ratios [EDTA]/[Ca^{2+}] or the pH of the complex solution show to be not appropriate in the present study. In the first case, because even if it succeeds to slow down the Ca^{2+} release it indirectly

induces a non-desired decrease of the elastic modulus of the gelled samples (G'_∞). In the second case, because the pH has only an effect on the induction time but not on the rate of release of Ca^{2+}. In view of these, we decide to fix the ratio [EDTA]/[Ca^{2+}] = 1 and pH = 7 for the following studies of calcium alginate hydrogels.

3.3.4. Conclusions

As conclusion, the experimental conditions for the elaboration of calcium alginate hydrogels with the $CaCl_2$-EDTA complex solution have been fixed to the selected values shown in the Table 4. In addition to the previously studied parameters, the amount of GDL added has been selected stoichiometrically equivalent to the quantity of calcium in the complex solution, [GDL]/[Ca] = 2. Therefore, the value of R_{Ca} will remain as the only modifiable parameter to modulate the structure and mechanical properties for the following studies in calcium alginate hydrogels prepared with $CaCl_2$-EDTA.

Table 4: selected conditions for the elaboration of calcium alginate hydrogels with EDTA-$CaCl_2$ as source of calcium.

$CaCl_2$-EDTA complex	
C_{Alg} (g/L)	18
[EDTA]/[Ca^{2+}]	1
pH	7
[GDL]/[Ca]	2
R_{Ca}	variable

3.4. Source of calcium: $CaCO_3$ salt

The time evolution of G”/G’ at different frequencies from a TRMS experiment with the $CaCO_3$ salt just after the addition of GDL is very similar to the one obtained for the $CaCl_2$-EDTA complex (Figure 5). The addition of $CaCO_3$ powder in the aqueous solution of sodium alginate leads to a pH = 9 that blocks the solubilisation of more $CaCO_3$. Then, by the addition of GDL, calcium is gradually released by the dissolution of solid microparticles of $CaCO_3$ due to the counterbalance of the OH^- formed in the dissolution of $CaCO_3$ by the H^+ coming from the hydrolysis of GDL. The use of $CaCO_3$ as source of calcium presents the advantage of requiring less quantity of chemical products than with the $CaCl_2$-EDTA complex solution. Thus, considering the same criteria as previously to select C_{Alg} = 18 g/L and [GDL]/[Ca] = 2, the experimental conditions are fixed to the values shown in Table 5 leaving, as well as for the previous source of calcium, R_{Ca} as the only modulated parameter.

Table 5: selected conditions for the elaboration of calcium alginate hydrogels with $CaCO_3$ as calcium source.

$CaCO_3$ salt	
C_{Alg} (g/L)	18
pH	-
[GDL]/[Ca]	2
R_{Ca}	variable

3.5. Sol-gel transition of the calcium alginate hydrogels with the selected experimental conditions

The values of the molar ratios R_{Ca} have been fixed to 0.2, 0.3 and 0.4 for the elaboration of calcium hydrogels. Values of R_{Ca} lower than 0.2 lead to extremely soft hydrogels while values higher than 0.4 have shown to not increase the mechanical properties of the totally gelled hydrogels. This suggests that the crosslinking density of the hydrogels reaches a limit below the stoichiometric value $R_{Ca} = 0.5$ either by the limited diffusion of Ca^{2+} when the hydrogel is already formed or by the difficult access to some of the carboxylate groups of mannuronic monomers to form ionic crosslinks.

The results from the analysis of independent TRMS experiments are presented in the Tables 6 and 7 for the $CaCl_2$-EDTA complex solution and the $CaCO_3$ salt respectively with different R_{Ca}. In both cases t_g decreases as R_{Ca} is increased explained by the bigger amounts of insoluble calcium dispersed in the pre-gel system as R_{Ca} is increased and the selection of a fixed ratio [GDL]/[Ca] = 2. Moreover, it can be clearly observed that for a R_{Ca} fixed value, the $CaCO_3$ salt leads to faster sol-gel transition compared to the $CaCl_2$-EDTA complex solution with a decrease of the gelation time (t_g) and the absence of measurable induction time (t_i). These differences can be explained by the different source of calcium and their associated mechanism of Ca^{2+} release.

In the one hand, Ca^{2+} is gradually released by the dissolution of solid microparticles of $CaCO_3$ by the effect of the H^+ resultant from the hydrolysis of GDL according to:

$$CaCO_3(s) \rightarrow Ca^{2+} + CO_3^{2-}$$

$$CO_3^{2-} + H_2O \rightarrow HCO_3^- + OH^-$$

In the other hand, the Ca^{2+} is gradually released from the $CaCl_2$-EDTA complex due the pH dependent chelating stability constant (K_f (pH = 7) = $1.7.10^7$, K_f (pH = 4) = $1.3.10^2$) of the $CaCl_2$-EDTA complex leading to:

$$Ca - EDTA \overset{K_f}{\leftrightarrow} Ca^{2+} + EDTA^{2-}$$

$$K_f = \frac{[Ca - EDTA]}{[Ca^{2+}] * [EDTA^{2-}]}$$

The time-evolution of the pH for $CaCl_2$-EDTA and $CaCO_3$ after the addition of GDL (Figure 6) shows different evolution depending on the source of calcium. For the case of $CaCO_3$ salt, the pH decreases rapidly to a value close to 7 and remain constant at this value indicating that the Ca^{2+} release begins practically immediately when the GDL is added since the H^+ liberated from the hydrolysis of GDL are quickly counterbalance by the OH^- due to the dissolution of $CaCO_3$. For the $CaCl_2$-EDTA complex a slow decrease of the pH is observed reaching a value around pH = 4.5. The release of Ca^{2+} from the complex should imply the formation of $EDTA^{2-}$. $EDTA^{2-}$ is a conjugate base that should counterbalance the H^+ released from the hydrolysis of GDL in a similar way than CO_3^{2-}during the solubilisation of the $CaCO_3$ salt. Therefore, the fact that the pH continues to decrease could be an indication that the Ca^{2+} release from the complex solution is a much slower mechanism than from the $CaCO_3$ salt confirming that the results obtained in the rheological measurements are related with the different rate of Ca^{2+}release between both sources of calcium.

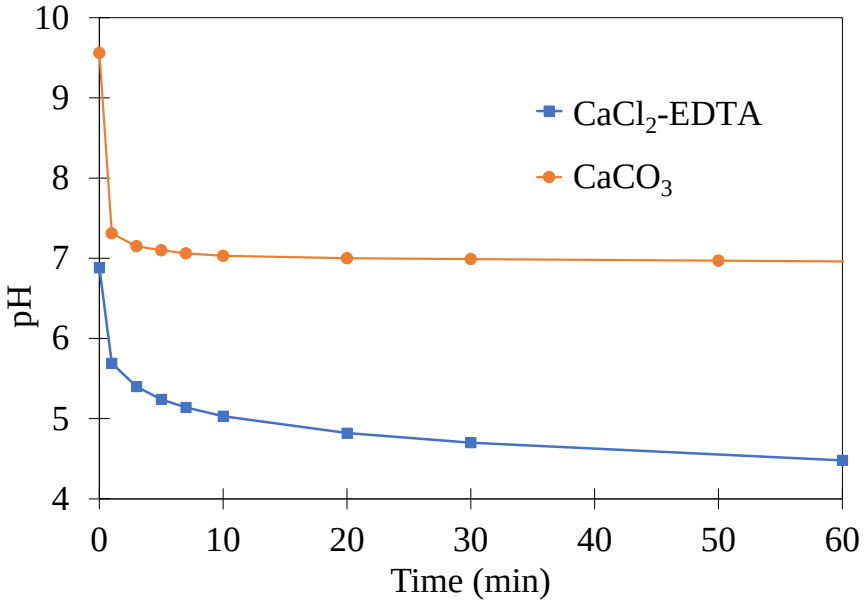

Figure 6: time-evolution of the pH just after addition of GDL in calcium alginate hydrogels with R_{Ca}=0.4 prepared with the two alternative sources of calcium.

The source of calcium has also an effect on the properties of the critical gel. For all studied R_{Ca}, the $CaCl_2$-EDTA complex leads to softer critical gels (with lower S and higher Δ) and weaker elastic properties at long time (G'_∞) than the $CaCO_3$ salt. Many theoretical models have been proposed to describe a universal behaviour of crosslinking polymers at the gel point. For example, the Rouse limit without hydrodynamic interactions gives Δ = 0.66, the Zimm limit

with hydrodynamic interactions gives $\Delta = 1$ and the percolation model gives $\Delta = 0.71$. It was found experimentally that the gelation induced by chemical crosslinking seems to be well described by these theoretical values which are predicted to be independent of physico-chemical conditions [29,30] while for physical gelation, this universality is not always observed due to the transient nature of the physical crosslinking [26,28,31]. For example, values of Δ between 0.66 and 0.76 depending on the sodium alginate concentration [26] using $CaCl_2$ or values between 0.56 and 0.69 [32,33] depending on the molecular structure of the sodium alginate using $CaCl_2$-EDTA complex.

Table 6: TRMS study during the sol-gel transition of calcium alginate hydrogels elaborated with $CaCl_2$-EDTA complex solution with the optimized experimental conditions and different R_{Ca}.

R_{Ca}	t_i (s)	G'_∞ (Pa)	t_g (s)	Δ	S (Pa.s$^\Delta$)
0.2	1918±20	370±40	2500±20	0.74±0.02	0.35±0.07
0.3	1189±20	540±50	1530±20	0.73±0.02	0.42±0.06
0.4	857±20	620±50	1085±20	0.73±0.02	0.40±0.05

Table 7: TRMS study during the sol-gel transition of calcium alginate hydrogels elaborated with $CaCO_3$ salt with the optimized experimental conditions and different R_{Ca}.

R_{Ca}	G'_∞ (Pa)	t_g (s)	Δ	S (Pa.s$^\Delta$)
0.2	880±50	780±10	0.68±0.01	0.54±0.05
0.3	1220±100	435±5	0.65±0.01	0.68±0.06
0.4	1580±100	380±10	0.59±0.01	1.56±0.14

Our experimental results (Tables 6 and 7) show that the hydrogels prepared with the complex have a constant value independent of R_{Ca} of $\Delta = 0.73$ close to the one predicted by the percolation theory ($\Delta = 0.71$). However, the value of Δ for the $CaCO_3$ salt seems to decrease as R_{Ca} is increased. This change of Δ could be explained by a hierarchical gelation due to the inhomogeneities of the sample at the microscopic level considering that the calcium is initially in the form of microparticles of $CaCO_3$. Then, when the Ca^{2+} is released a gradient of Ca^{2+} concentration appears from the microparticles. These Ca^{2+} gradients can be the responsible of the loss of random crosslinking process and a more favourable gelation of the alginate chains close to the $CaCO_3$ microparticles. The effect of these gradients become more important for the faster gelation that could explain that the difference between experimental values of Δ and the one of percolation theory ($\Delta = 0.71$) increase when R_{Ca} is increased (t_g decrease).

Concerning G'_{∞}, the values increase as the molar ratio is increased for both sources of calcium but with higher values for $CaCO_3$ salt. This is in good agreement with the behaviour at tg (lower values of Δ and higher values of S).

3.6. Conclusions

The study of the sol-gel transition of calcium alginate hydrogels by an internal method with either the $CaCl_2$-EDTA complex solution or the $CaCO_3$ salt has been performed by TRMS applying the methodology proposed by Winter *et al*. Firstly, some parameters of the experimental protocols have been studied to fix them leaving R_{Ca} ($[Ca^{2+}]/[COO^-]$) as the control parameter to modulate the properties of the hydrogels in the following studies. The chosen source of calcium has a clear effect on the kinetics of the sol-gel transition obtaining higher gelation times (t_g) for the complex than for $CaCO_3$ due to the different rates of Ca^{2+} release as demonstrated with the time-evolution of the pH. In both cases t_g also decreases as R_{Ca} is increased. Moreover, the structure of the critical gel (hydrogel at t_g) depends also on the source of calcium. In the one hand, for the complex solution, the critical gel shows a universal relaxation exponent independent of R_{Ca} close to the value predicted by the percolation theory ($\Delta = 0.71$). In the other hand, for $CaCO_3$ salt, the critical gel shows a slight decrease of Δ as R_{Ca} is increased. These two different behaviours can be explained by a more homogeneous distribution of the Ca^{2+} released for the complex solution than for the $CaCO_3$ leading in the first case to a completely random gelation while for the second a hierarchical gelation can be induced by local gradients of Ca^{2+} concentrations.

4. Study of totally gelled samples

4.1. Introduction

Further to the study of sol-gel transition of hydrogels presented in the previous paragraph, the final gelled state of hydrogels when the crosslinking mechanism is totally accomplished has been studied for both sources of calcium ($CaCO_3$ and $CaCl_2$-EDTA) and three values of R_{Ca} (0.2, 0.3, 0.4). In addition, PVA hydrogels are investigated with different numbers of freezing/thawing cycles (N_c).

4.2. Experimental

40 g of pre-gel systems have been prepared following the protocol described in the paragraph 2.1 with the selected conditions. For the case of alginate, the pre-gel system has been placed in a sealed petri dish with a diameter of 10 cm just after adding GDL solution and left for 16 hours at 25ºC. The PVA solution has been also loaded on a petri dish with a diameter of

10 cm, sealed, and subjected to one, two or three freezing/thawing cycles accordingly with the protocol described in the paragraph 2.2. For both cases solid hydrogels have been obtained (Figure 7a) and cylindrical disks with a diameter of 20 mm and a variable height between 5-7 mm have been prepared with a cutter tool punch (Figure 7b) to perform the experiments as explained above.

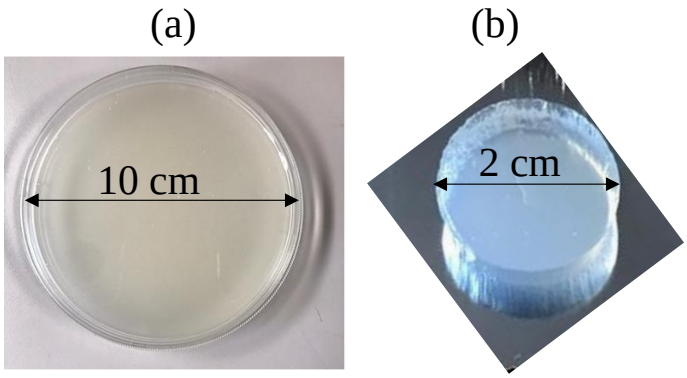

Figure 7: elaboration of hydrogel samples: (a) 40 g of totally gelled sample prepared in petri dish and (b) cylindrical disk cut from a with a cutter tool punch.

4.2.1. Uniaxial compression test

Uniaxial compression tests have been performed using the normal force sensor of the MARS II rheometer with a plate and plate geometry of 20 mm of diameter. The prepared cylindrical disks (Figure 7b) have been placed on the lower plate and a small compressive pre-load of 0.02N has been applied by the upper plate. Strain has been varied between 0 and 40% for all the measurements with a test speed of 1.8 $mm.min^{-1}$ and the value of stress has been recorded every 0.5% of strain. Temperature has been controlled on the lower plate by water flow at 25.0 ± 0.1°C. Measurements have been performed by triplicate for three different hydrogel disks and average values have been calculated for the shown experimental data.

4.2.2. Swelling

Hydrogels can extensively swell in water media depending on the characteristic of their polymer network. To study this phenomenon, the prepared cylindrical disks (Figure 7b) have been individually introduced in plastic cups filled with 20 mL of pure water and weighted at different times after gentle surface wiping using absorbent paper. The swelling degree after each measurement has been calculated using the following equation:

$$Q(\%) = \frac{W_s(t) - W_0}{W_0} * 100\% \qquad (5)$$

where $W_s(t)$ is the weight of a swollen disk at time t and W_0 is the initial weight of the as-prepared disk just before its immersion in water. Measurements have been performed by triplicate for three different hydrogel disks and average values have been calculated for the shown experimental data.

After the equilibrium swelling degree (Q_e) is achieved, uniaxial compression tests have been performed for the swollen samples following the same protocol described in 4.2.1. section.

4.3. Alginate hydrogels

4.3.1. Uniaxial compression

The stress-strain curves of uniaxial compression measurements for calcium alginate hydrogels elaborated with the $CaCO_3$ salt and the three R_{Ca} are presented in Figure 9. It can first be observed a linear region at low strain (see insert of Figure 9) from which the compressive Young modulus (E) can be deduced from the slope. Followed, the increase of the stress-strain relation should correspond to a strain hardening effect due to the limit of deformability of the gel network. The curves for the calcium alginate hydrogels elaborated with $CaCl_2$-EDTA show a similar evolution and they are not shown here for brevity.

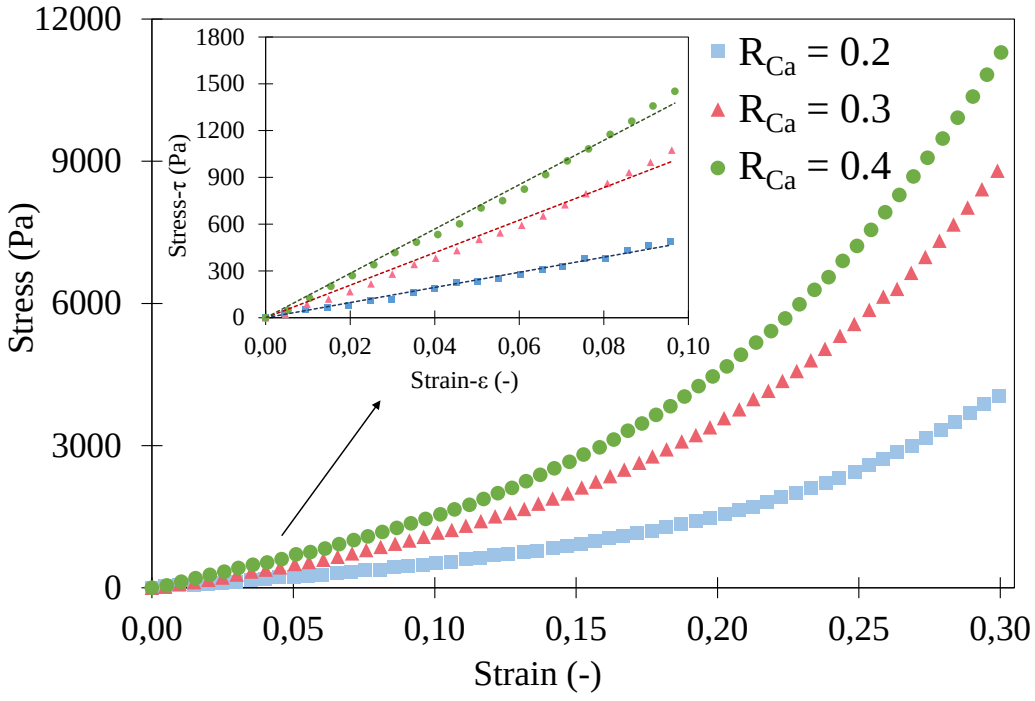

Figure 9: stress-strain curves for calcium alginate hydrogel disks prepared with $CaCO_3$ salt at different R_{Ca}. Linear region of the stress-strain dependence in the insert.

The values of the determined Young modulus for the six studied hydrogels are shown in Figure 10 observing clearly higher values for the calcium alginate hydrogels prepared with the $CaCO_3$ salt than for the $CaCl_2$-EDTA complex. As expected, the increase of the value of R_{Ca}

leads also to an increase of E due to the higher crosslinking degree with a linear increase for calcium alginate hydrogels prepared with the $CaCO_3$ salt. This behaviour of the totally gelled hydrogels is in a good agreement with the values of G'_∞ determined previously by TRMS study (Table 6 and 7). These results confirm that hydrogels elaborated with the $CaCO_3$ salt have higher crosslinking degree and stronger mechanical properties than those elaborated with the $CaCl_2$-EDTA complex.

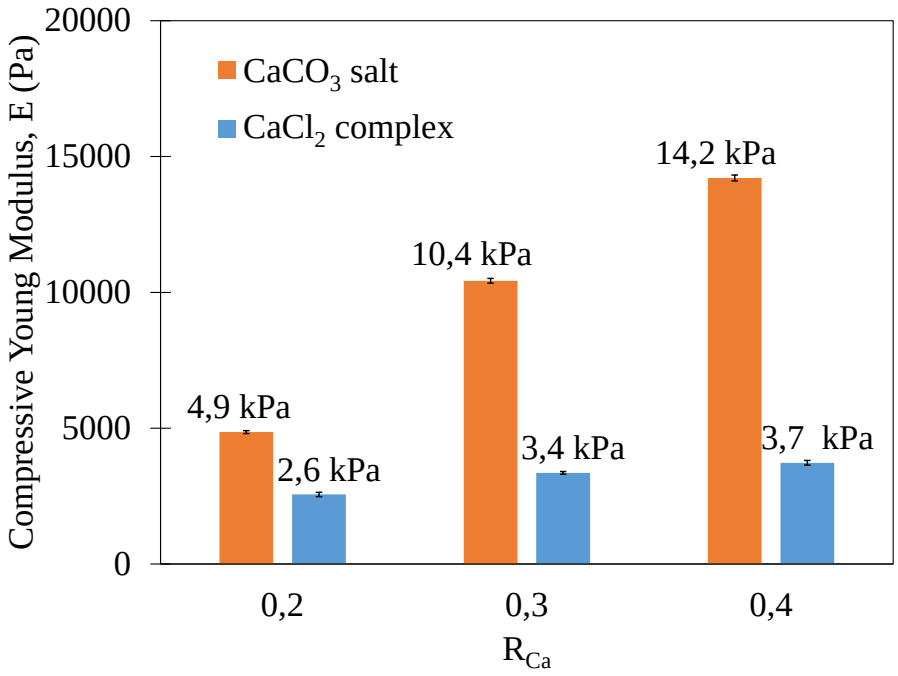

Figure 10: comparison of the compressive Young modulus of calcium alginate hydrogels determined from the linear region of the stress-strain curves for the two sources of calcium and different R_{Ca}.

4.3.2. Swelling

The degree of swelling as function of time is shown in Figure 11 for calcium alginate hydrogels elaborated with the $CaCO_3$ salt with different R_{Ca}. The hydrogels elaborated with the $CaCl_2$-EDTA complex show to have not enough mechanical integrity to perform such type of analysis being impossible to manipulate after 1 hour of immersion in pure water because they are too soft. For the studied hydrogels, the degree of swelling is fast during the first three hours and then slow down to reach equilibrium swelling states (Q_e). Two kinetic models are commonly used in the literature [34] for the modelling of absorption kinetics:

- Pseudo first-order model: $Q(t) = Q_e.(1 - e^{-k_1.t})$ (6)
- Pseudo second-order model: $Q(t) = Q_e.\frac{k_2.t}{1+k_2.t}$ (7)

where k_1 and k_2 are the pseudo first-order and second-order constants respectively.

Taking into account that a significant number of experimental points (at least 50%, Figure 11) are close to equilibrium, it was shown [34] that a fitting with two open parameters (Q_e and k) may introduce errors. Consequently, Q_e are fixed to experimental values and the constant k is the only open parameters for the adjustment. Using the equations 6 and 7 the best fit is obtained with the first-order model (Figure 11) and the results are summarized in Table 8.

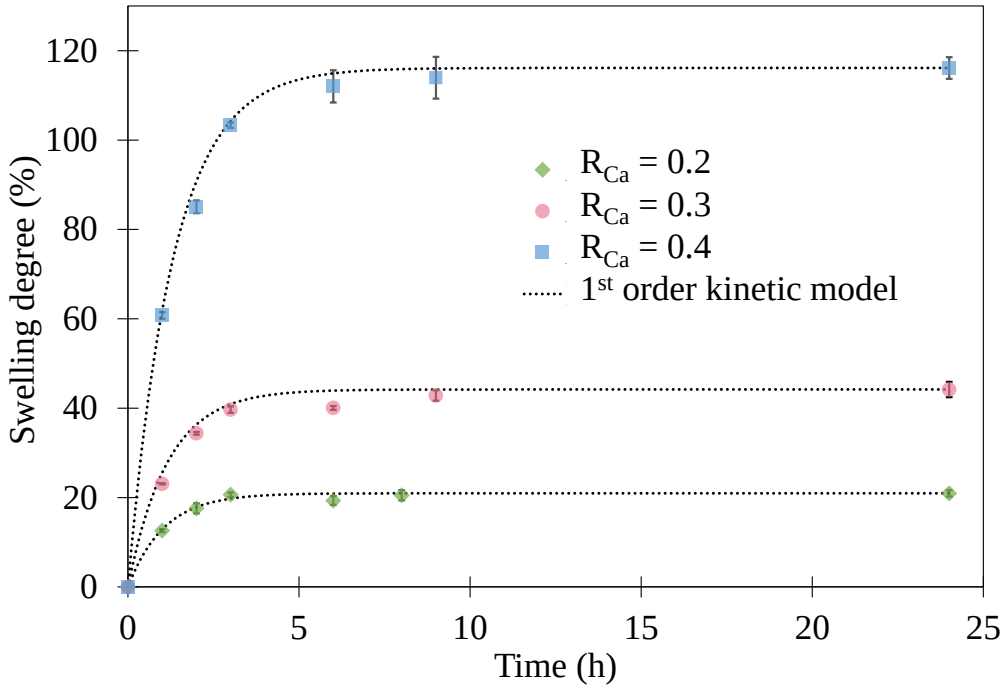

Figure 11: time-evolution of the swelling degree (Q) for calcium alginate hydrogels elaborated with the $CaCO_3$ salt with different R_{Ca}.

Table 8: first order model parameters for the fitting of the swelling degree as function of time for calcium alginate hydrogels elaborated with the $CaCO_3$ salt with different R_{Ca}.

Sample	Q_e (%)	k (h^{-1})	Q_e*k (%.h^{-1})
R_{Ca} = 0.2	116.1	0.76	88.2
R_{Ca} = 0.3	44.2	0.86	38.0
R_{Ca} = 0.4	20.9	0.95	19.9

By the immersion of the calcium alginate hydrogels in water, the diffusion of water into the network takes place driven by the high hydrophilicity of alginate. This swelling is governed by the balance between the stretching produced by the volume expansion and the elastic contraction produced by the chains of alginate. Hydrogels with lower R_{Ca} show a higher swelling degree at equilibrium. This finding could be explained due to the lower crosslinking degree allowing a less restricted movement of the alginate chains that can be easily stretched to increase the size of the pores. This will provide a higher space for solvent absorption for lower values of R_{Ca}. The rate constant k (h^{-1}) can be defined as the proportionality factor which

explains the relationship between the rate of water absorption and the distance to the swelling equilibrium (Q_e). Then, the factor Q_e*k (%.h^{-1}) is used for a preliminary comparison of the absolute rates of water absorption observing a faster absorption of water for the hydrogels with lower R_{Ca} explained as previously by the lower degree of crosslinking of the network. These results are in good agreement with the lower values of the compressive Young modulus as R_{Ca} is decreased (Figure 9).

4.3.3. Uniaxial compression of swollen disks

The compression tests performed on the swollen hydrogels at their equilibrium swelling degree (Q_e) shows important enhancements of the swollen compressive young modulus (E_{sw}) in comparison to the as-prepared hydrogels as schematized in the Figure 12. This increase of the compressive Young modulus is related with the quantity of absorbed water that penetrates in the pores of the hydrogel elongating the alginate chains and stiffening the network. The factor of increase of the Young modulus (E_{sw}/E) is correlated with the amount of water absorbed during the swelling. The lower is the R_{Ca}, the higher are the swelling degree and the factor E_{sw}/E confirming that bigger amounts of absorbed water lead to more incompressible hydrogels.

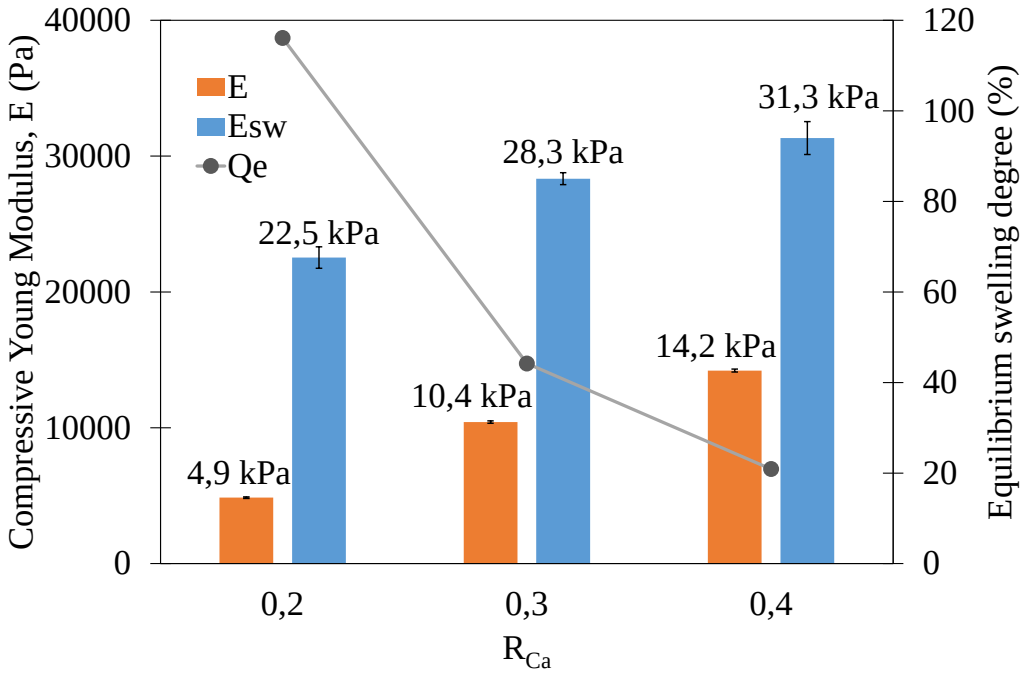

Figure 12: equilibrium swelling degree (Q_e) and compressive Young modulus of swollen in comparison to as-prepared calcium alginate hydrogels with different R_{Ca}.

4.4. PVA hydrogels

4.4.1. Compression

The stress-strain curves for PVA hydrogels with different crosslinking degrees achieved by different number of freezing/thawing cycles (N_c) are presented in Figure 13. The behaviour is very similar to the one for calcium alginate hydrogels with a linear region from which the compressive Young modulus is determined from the slope followed by an increase of the stress-strain relation. The higher values of N_c leads to more resistant to compression samples due to the higher crosslinking degree as expected.

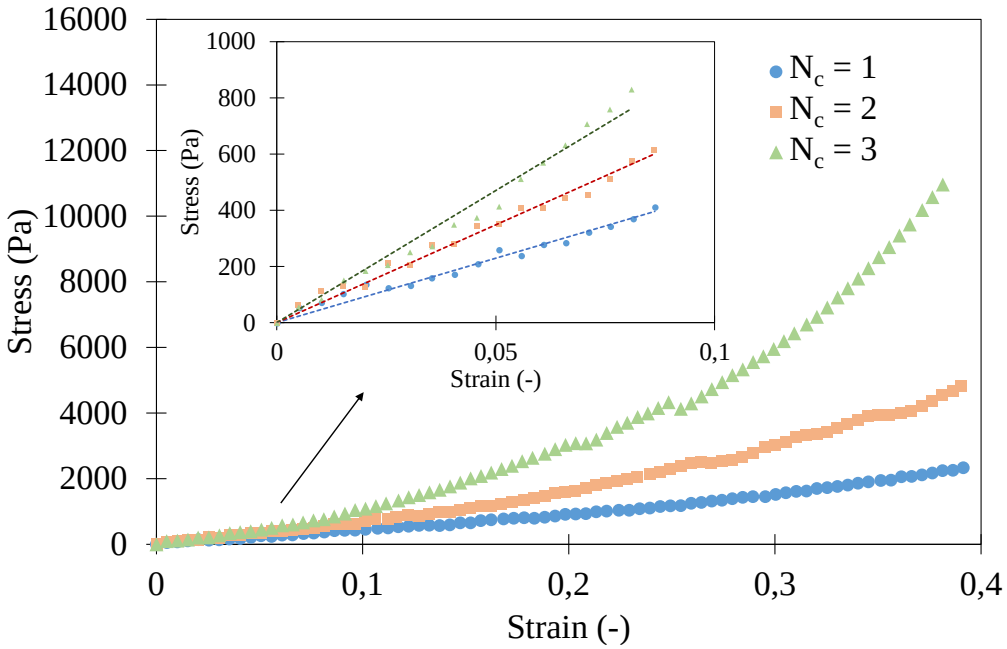

Figure 13: stress-strain curves for PVA hydrogel (100 g/L) subjected to different number of freezing/thawing cycles (N_c). Linear region of the stress-strain dependence in the insert.

4.4.2. Swelling

The degree of swelling as function of time for PVA hydrogels is shown in Figure 14 for different N_c**.** For PVA hydrogels the evolution of the degree of swelling is slow in comparison with calcium alginate hydrogels probably due to the higher polymer concentration (C_{PVA} = 100 g/L) and to the lower hydrophilicity of PVA in comparison with sodium alginate as deduced by the more compact polymer conformation defined in the Chapter II. Experimental data are fitted as the same manner as the ones of calcium alginate hydrogels. The results are summarized in Table 9. The observed decrease of the equilibrium swelling (Q_e) and the rate of water absorption estimated by $k*Q_e$ as Nc is increased can be explained as for calcium alginate hydrogels by an increase of the crosslinking degree related to the formation of microcrystalline structures

promoted by the freezing/thawing cycles in PVA [35]. Moreover, this variation is in a good agreement with previous study [36].

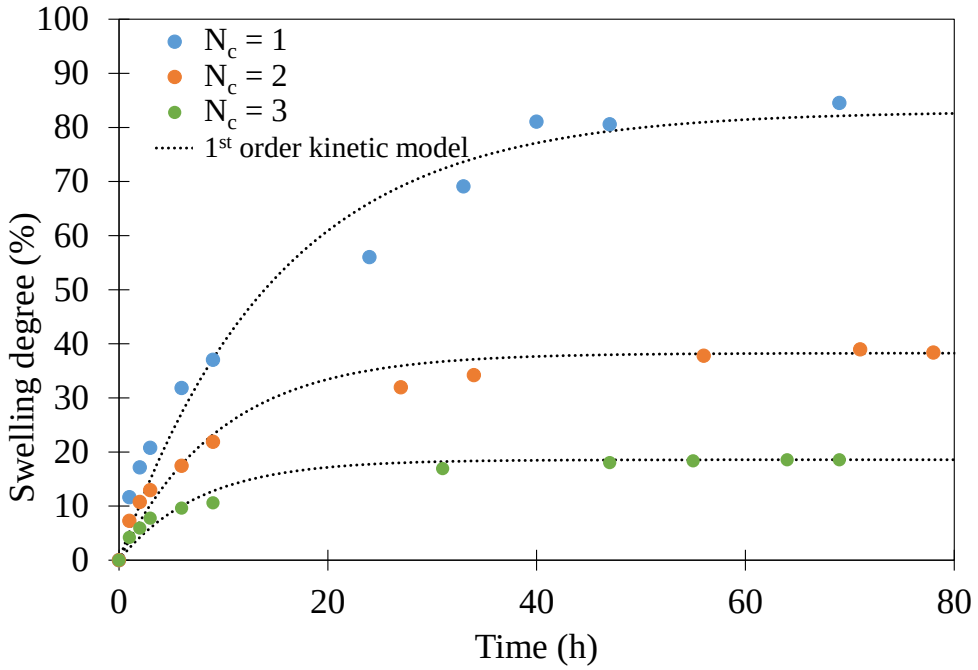

Figure 14: time-evolution of the swelling degree (Q) for PVA hydrogels subjected to different number of freezing/thawing cycles (N_c).

Table 9: first order model parameters for the fitting of the swelling degree as function of time for PVA hydrogels subjected to different number of freezing/thawing cycles (N_c).

Sample	Q_e (%)	k (h^{-1})	Q_e*k (%.h^{-1})
N_c = 1	83.0	0.066	5.5
N_c = 2	38.3	0.104	4.0
N_c = 3	18.6	0.129	2.4

4.4.3. Uniaxial compression of swollen disks

The uniaxial compression tests performed on the swollen hydrogels at their equilibrium swelling degree (Q_e) shows important modifications of the swollen compressive young modulus (E_{sw}) as compared in the Figure 15. For the PVA hydrogels with N_c = 1, the compressive Young modulus decreases after the swelling, while for PVA hydrogels with N_c = 3, it increases. An intermediate behaviour is found for N_c = 2. This can be explained by two mechanism identified by Hassan *et al*. when PVA hydrogels are immersed in water. Firstly, the decrease of the degree of physical crosslinking after absorption of water and secondly, the dissolution of the PVA chains that did not participate in the crystallite formation process. Both effects are more important when N_c is lower. Then, for PVA hydrogel with N_c = 1, the more important decrease

of the crosslinking degree and the dissolution of a fraction of PVA chains leads to the decrease of the compressive Young modulus. At medium $N_c = 2$, the crosslinking degree is now higher and even if some free PVA chains are dissolved this effect is compensated by the water absorption having no noticeable effect on the compressive Young modulus. At $N_c = 3$, both mechanisms should be almost negligible since the net effect of the swelling is an increase of the modulus and the crystalline regions formed during the freezing/thawing become more and more stable as N_c is increased. According to the changes of the compressive Young modulus after swelling, three cycles of freezing/thawing seems to be necessary to have stable PVA hydrogels in water without PVA dissolution in the liquid phase and with stable crystalline regions.

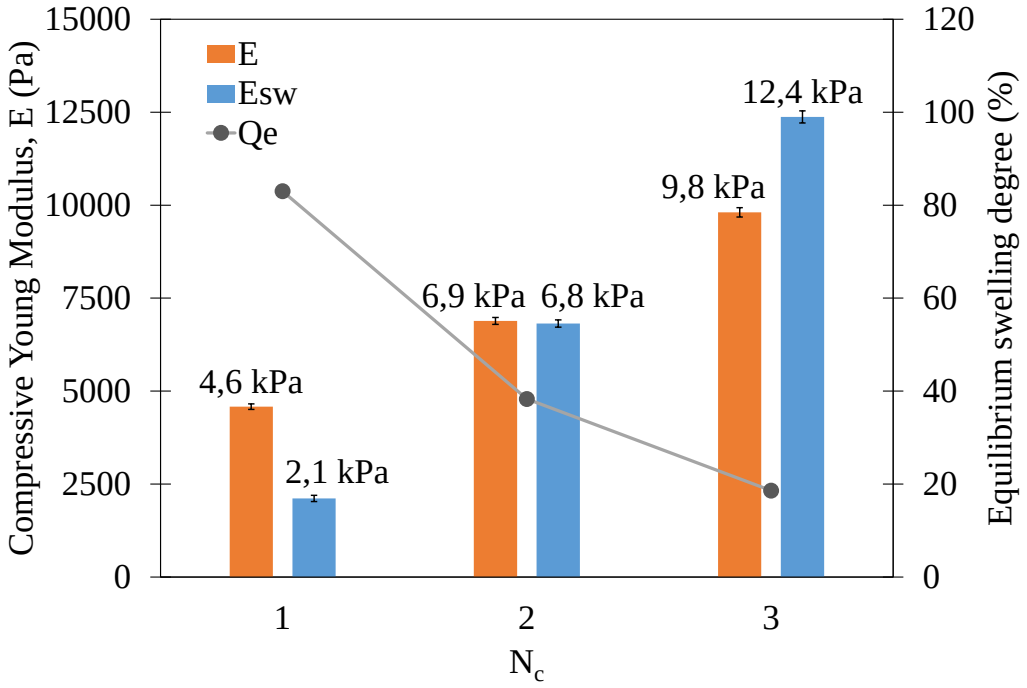

Figure 15: equilibrium swelling degree (Q_e) and compressive Young modulus of swollen in comparison to as-prepared PVA hydrogels with different number of thawing/freezing cycles (N_c).

4.5. Conclusions

The mechanical and structural study of the elaborated hydrogels modulated either by the amount of calcium added (R_{Ca}) for calcium alginate hydrogels or by the number of freezing/thawing cycles (N_c) for PVA hydrogels allow to correlate their stiffness and porosity to the crosslinking degree. The elastic shear moduli at gelled state (G'_∞) deduced from the study of the sol-gel transition seems to be a good qualitative estimation of the stiffness of the totally gelled hydrogels. More quantitative information is obtained by the determination of the compressive Young modulus (E) and the study of the swelling of totally gelled hydrogels.

5. Conclusions

Three methodologies have been studied for the elaboration of hydrogels including the ionic crosslinking of sodium alginate with two different sources of calcium ($CaCl_2$-EDTA complex solution and $CaCO_3$ salt) and the freezing/thawing method for PVA solutions. The study of the sol-gel transition of calcium alginate hydrogels has been performed by time-resolved mechanical spectroscopy (TRMS). It has been shown that the kinetics of the sol-gel transition (gelation time t_g) and the properties of hydrogels at t_g can be modulated by the molar ratio between added calcium and carboxylate groups ($R_{Ca} = [Ca^{2+}]/[COO^-]$) and the source of calcium. The elastic constant at gelled state (G'_∞) from the study of the sol-gel transition seems to be a good estimation of the stiffness of the totally gelled hydrogels. However, the determination of the compressive Young modulus (E) and the study of the swelling for the totally gelled hydrogels give a more quantitative information of their structure and mechanical properties allowing to correlate their stiffness and porosity to the variation of the crosslinking degree depending on either the amount of calcium added (R_{Ca}) for calcium alginate hydrogels or the number of freezing/thawing cycles (N_c) for PVA hydrogels. These results of complete study of hydrogels will be used for the development of magnetic nanocomposite hydrogels (chapter V).

6. References

[1] K. Varaprasad, G.M. Raghavendra, T. Jayaramudu, M.M. Yallapu, R. Sadiku, A mini review on hydrogels classification and recent developments in miscellaneous applications, Mater. Sci. Eng. C. 79 (2017) 958–971. https://doi.org/10.1016/j.msec.2017.05.096.

[2] N. Kalai Selvan, T.S. Shanmugarajan, V.N.V.A. Uppuluri, Hydrogel based scaffolding polymeric biomaterials: Approaches towards skin tissue regeneration, J. Drug Deliv. Sci. Technol. 55 (2020) 101456. https://doi.org/10.1016/j.jddst.2019.101456.

[3] N. Reddy, R. Reddy, Q. Jiang, Crosslinking biopolymers for biomedical applications, Trends Biotechnol. 33 (2015) 362–369. https://doi.org/10.1016/j.tibtech.2015.03.008.

[4] M. Djabourov, K. Nishinari, S.B. Ross-Murphy, Physical Gels from Biological and Synthetic Polymers, Cambridge University Press, Cambridge, 2013. https://doi.org/10.1017/CBO9781139024136.

[5] M. Mahinroosta, Z. Jomeh Farsangi, A. Allahverdi, Z. Shakoori, Hydrogels as intelligent materials: A brief review of synthesis, properties and applications, Mater. Today Chem. 8 (2018) 42–55. https://doi.org/10.1016/j.mtchem.2018.02.004.

[6] A.K. Gaharwar, N.A. Peppas, A. Khademhosseini, Nanocomposite hydrogels for biomedical applications, Biotechnol. Bioeng. 111 (2014) 441–453. https://doi.org/10.1002/bit.25160.

[7] F. Wahid, X.-J. Zhao, S.-R. Jia, H. Bai, C. Zhong, Nanocomposite hydrogels as multifunctional systems for biomedical applications: Current state and perspectives, Compos. Part B Eng. 200 (2020) 108208. https://doi.org/10.1016/j.compositesb.2020.108208.

[8] O. Okay, General Properties of Hydrogels, in: G. Gerlach, K.-F. Arndt (Eds.), Hydrogel Sens. Actuators Eng. Technol., Springer, Berlin, Heidelberg, 2010: pp. 1–14. https://doi.org/10.1007/978-3-540-75645-3_1.

[9] Q. Chai, Y. Jiao, X. Yu, Hydrogels for Biomedical Applications: Their Characteristics and the Mechanisms behind Them, Gels. 3 (2017) 6. https://doi.org/10.3390/gels3010006.

[10] G.T. Grant, E.R. Morris, D.A. Rees, P.J.C. Smith, D. Thom, Biological interactions between polysaccharides and divalent cations: The egg-box model, FEBS Lett. 32 (1973) 195–198. https://doi.org/10.1016/0014-5793(73)80770-7.

[11] C.K. Kuo, P.X. Ma, Ionically crosslinked alginate hydrogels as scaffolds for tissue engineering: Part 1. Structure, gelation rate and mechanical properties, Biomaterials. 22 (2001) 511–521. https://doi.org/10.1016/S0142-9612(00)00201-5.

[12] T. Andersen, P. Auk-Emblem, M. Dornish, 3D Cell Culture in Alginate Hydrogels, Microarrays. 4 (2015) 133–161. https://doi.org/10.3390/microarrays4020133.

[13] K.Y. Lee, D.J. Mooney, Alginate: Properties and biomedical applications, Prog. Polym. Sci. 37 (2012) 106–126. https://doi.org/10.1016/j.progpolymsci.2011.06.003.

[14] O. Khanna, J.C. Larson, M.L. Moya, E.C. Opara, E.M. Brey, Generation of Alginate Microspheres for Biomedical Applications, J. Vis. Exp. JoVE. (2012). https://doi.org/10.3791/3388.

[15] X. Liu, L. Qian, T. Shu, Z. Tong, Rheology characterization of sol–gel transition in aqueous alginate solutions induced by calcium cations through in situ release, Polymer. 44 (2003) 407–412. https://doi.org/10.1016/S0032-3861(02)00771-1.

[16] I. Fernández Farrés, I.T. Norton, Formation kinetics and rheology of alginate fluid gels produced by in-situ calcium release, Food Hydrocoll. 40 (2014) 76–84. https://doi.org/10.1016/j.foodhyd.2014.02.005.

[17] Y. Pocker, Edmond. Green, Hydrolysis of D-glucono-.delta.-lactone. I. General acid-base catalysis, solvent deuterium isotope effects, and transition state characterization, J. Am. Chem. Soc. 95 (1973) 113–119. https://doi.org/10.1021/ja00782a019.

[18] E.A. Kamoun, X. Chen, M.S. Mohy Eldin, E.-R.S. Kenawy, Crosslinked poly(vinyl alcohol) hydrogels for wound dressing applications: A review of remarkably blended polymers, Arab. J. Chem. 8 (2015) 1–14. https://doi.org/10.1016/j.arabjc.2014.07.005.

[19] S.B. Ross-Murphy, Biopolymer gelation- exponents and critical exponents, Polym. Bull. 58 (2007) 119–126. https://doi.org/10.1007/s00289-006-0596-1.

[20] H.H. Winter, The Critical Gel, in: R. Borsali, R. Pecora (Eds.), Struct. Dyn. Polym. Colloidal Syst., Springer Netherlands, Dordrecht, 2002: pp. 439–470. https://doi.org/10.1007/978-94-010-0442-8_14.

[21] H.H. Winter, Can the gel point of a cross-linking polymer be detected by the G′ – G″ crossover?, Polym. Eng. Sci. 27 (1987) 1698–1702. https://doi.org/10.1002/pen.760272209.

[22] H.H. Winter, F. Chambon, Analysis of Linear Viscoelasticity of a Crosslinking Polymer at the Gel Point, J. Rheol. 30 (1986) 367–382. https://doi.org/10.1122/1.549853.

[23] M. Mours, H.H. Winter, Time-resolved rheometry, Rheol. Acta. 33 (1994) 385–397. https://doi.org/10.1007/BF00366581.

[24] H.H. Winter, P. Morganelli, F. Chambon, Stoichiometry effects on rheology of model polyurethanes at the gel point, Macromolecules. 21 (1988) 532–535. https://doi.org/10.1021/ma00180a048.

[25] K. Yamamoto, Y. Yuguchi, B.T. Stokke, P. Sikorski, D.C. Bassett, Local Structure of Ca2+ Alginate Hydrogels Gelled via Competitive Ligand Exchange and Measured by Small Angle X-Ray Scattering, Gels. 5 (2019). https://doi.org/10.3390/gels5010003.

[26] S. Liu, H. Li, B. Tang, S. Bi, L. Li, Scaling law and microstructure of alginate hydrogel, Carbohydr. Polym. 135 (2016) 101–109. https://doi.org/10.1016/j.carbpol.2015.08.086.

[27] A. Izuka, H.H. Winter, T. Hashimoto, Self-Similar Relaxation Behavior at the Gel Point of a Blend of a Cross-Linking Poly(ε-caprolactone) Diol with a Poly(styrene-co-acrylonitrile), Macromolecules. 30 (1997) 6158–6165. https://doi.org/10.1021/ma961620g.

[28] Lu, X. Liu, Z. Tong, Q. Gao, Critical Exponents and Self-Similarity for Sol-Gel Transition in Aqueous Alginate Systems Induced by in Situ Release of Calcium Cations, J. Phys. Chem. B. 110 (2006) 25013–25020. https://doi.org/10.1021/jp060155e.

[29] M. Takahashi, K. Yokoyama, T. Masuda, T. Takigawa, Dynamic viscoelasticity and critical exponents in sol-gel transition of an end-linking polymer, J. Chem. Phys. 101 (1994) 798–804. https://doi.org/10.1063/1.468135.

[30] D. Adolf, J.E. Martin, J.P. Wilcoxon, Evolution of structure and viscoelasticity in an epoxy near the sol-gel transition, Macromolecules. 23 (1990) 527–531. https://doi.org/10.1021/ma00204a028.

[31] L. Dai, X. Liu, Z. Tong, Critical behavior at sol–gel transition in gellan gum aqueous solutions with KCl and CaCl2 of different concentrations, Carbohydr. Polym. 81 (2010) 207–212. https://doi.org/10.1016/j.carbpol.2010.02.013.

[32] X. Liu, L. Qian, T. Shu, Z. Tong, Rheology characterization of sol–gel transition in aqueous alginate solutions induced by calcium cations through in situ release, Polymer. 44 (2003) 407–412. https://doi.org/10.1016/S0032-3861(02)00771-1.

[33] Lu, X. Liu, Z. Tong, Q. Gao, Critical Exponents and Self-Similarity for Sol-Gel Transition in Aqueous Alginate Systems Induced by in Situ Release of Calcium Cations, J. Phys. Chem. B. 110 (2006) 25013–25020. https://doi.org/10.1021/jp060155e.

[34] J.-P. Simonin, On the comparison of pseudo-first order and pseudo-second order rate laws in the modeling of adsorption kinetics, J. Chem. Eng. (2016). https://doi.org/10.1016/j.cej.2016.04.079.

[35] M. Bercea, S. Morariu, D. Rusu, In situ gelation of aqueous solutions of entangled poly(vinyl alcohol), Soft Matter. 9 (2013) 1244–1253. https://doi.org/10.1039/C2SM26094H.

[36] C.M. Hassan, N.A. Peppas, Structure and Morphology of Freeze/Thawed PVA Hydrogels, Macromolecules. 33 (2000) 2472–2479. https://doi.org/10.1021/ma9907587.

Chapter IV: magnetic nanocomposite solutions

1. Introduction

One main step on the elaboration of magnetic nanocomposites is the dispersion of previously synthetized maghemite MNPs in aqueous polymeric solutions to obtain nanomaterials which combine the biocompatibility and viscoelastic behaviour of polymeric solutions with some of the outstanding properties of metal oxide nanoparticles. Some examples found in the literature are the elaboration of TiO_2/PVA [1], ZnO/sodium alginate [2] or ZnO, CuO or TiO_2/silk fibroin [3] metal oxide/polymer nanocomposites. Rheological and structural properties of the polymeric solution are generally modified by the addition of particle fillers. For the case of nanoparticles, the agglomeration and their dispersion in polymer matrix give more complexity to predict its characteristics [3]. In addition, the volume fraction of nanoparticles to induce a significant difference on these rheological properties could be quite high.

In this chapter it is then first proposed a strategy for the dispersion of MNPs with different electrostatic interactions in an entangled polymeric matrix in order to obtain different microstructures with volume fractions as low as 1% v/v. Secondly, the mechanical properties of the elaborated nanocomposite solutions without and with an applied magnetic field are investigated. The outline of this chapter is the following. After a description of the elaboration of polymer/MNPs nanocomposites, the results of their rheological and structural study are discussed focused on the different interactions between the polymeric matrix and the MNPs surface leading to different microstructures and magnetic effects on the rheological properties. The main part of the study is carried out in a magneto-opto-rheological cell developed in the laboratory MSC that allows at the same time to characterize the rheological and structural properties by *in-situ* optical observation during the application of magnetic field.

2. Elaboration of nanocomposites

A key point to design composite materials is to get a better understanding of the interactions between the fillers and the polymer matrix and the link with the global properties.

To answer this open question, we have elaborated nanocomposites by combining two different polymer matrices and iron oxide (γ-Fe_2O_3) magnetic nanoparticles (MNPs) functionalized with organic ligands of different characteristics (Figure 1). As presented in the Chapter I, negatively charged citrated-MNPs and positively charged APPA-MNPs have been prepared either by adsorption of citrate ions or by grafting of APPA double ligand respectively. For the polymer matrix, sodium alginate that is a negatively charged polyelectrolyte in aqueous solution, and polyvinyl alcohol (PVA) that is a neutral polymer in aqueous solution have been chosen according to the results presented in chapter II.

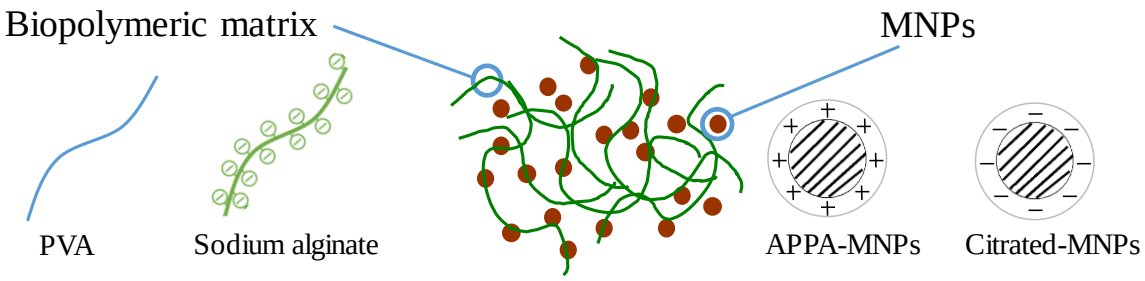

Figure 1: schematic representation of the different alternatives proposed for the elaboration of nanocomposite solutions with different MNPs-polymer interactions.

The concentration of polymer was selected to obtain an entangled solution with a mesh size in the range of size of the MNPs. For the case of the aqueous solutions of sodium alginate, it was deduced from the mesh size (ξ) by SAXS (see Chapter II Table 13) and concentrations of sodium alginate of 10 and 18 g/L were selected (ξ ~ 8-10 nm). For the case of PVA, this information is not available. Then, it was decided to choose a concentration of PVA to have similar zero shear viscosity and shear-thinning behaviour than the sodium alginate aqueous solution of 18 g/L (~1 Pa.s) to facilitate the comparison of the two polymer matrices. According to this criterion, a concentration of PVA of 100 g/L was selected. For the volume fraction of MNPs (Φ_{MNPs}), two criteria were applied: having enough concentration of MNPs to clearly observe a magnetic effect on the rheological and structural properties and obtaining a macroscopically homogeneous mixture characterized by a dark colour. Based on these conditions, it was selected a range of Φ_{MNPs} between 0.5 and 1%. The homogeneous dispersions of MNPs have been introduced in the polymer solutions and carefully mixed by mechanical agitation at 200 rpm during at least 10 minutes at isothermal conditions (25ºC for sodium alginate and 30ºC for PVA) until homogeneous nanocomposite samples have been obtained.

3. Magneto-opto-rheology

3.1. Experimental methodology

The measurements have been performed with an improved version of the magneto-opto-rheological device developed in the MSC laboratory [4] schematically represented in the Figure 2. It consists in a modification of a torque controlled rheometer MARS II (Thermo Fischer Scientific) including a magnetic part and an *in-situ* optical observation system. The selected geometry was a cone and plate cell (diameter of 60 mm and angle of 1°) made of a non-magnetic material, titanium for the cone and glass for the plate. A solvent trap was used to reduce the water evaporation of the samples. The temperature was controlled in the lower plate with a home-made Peltier system.

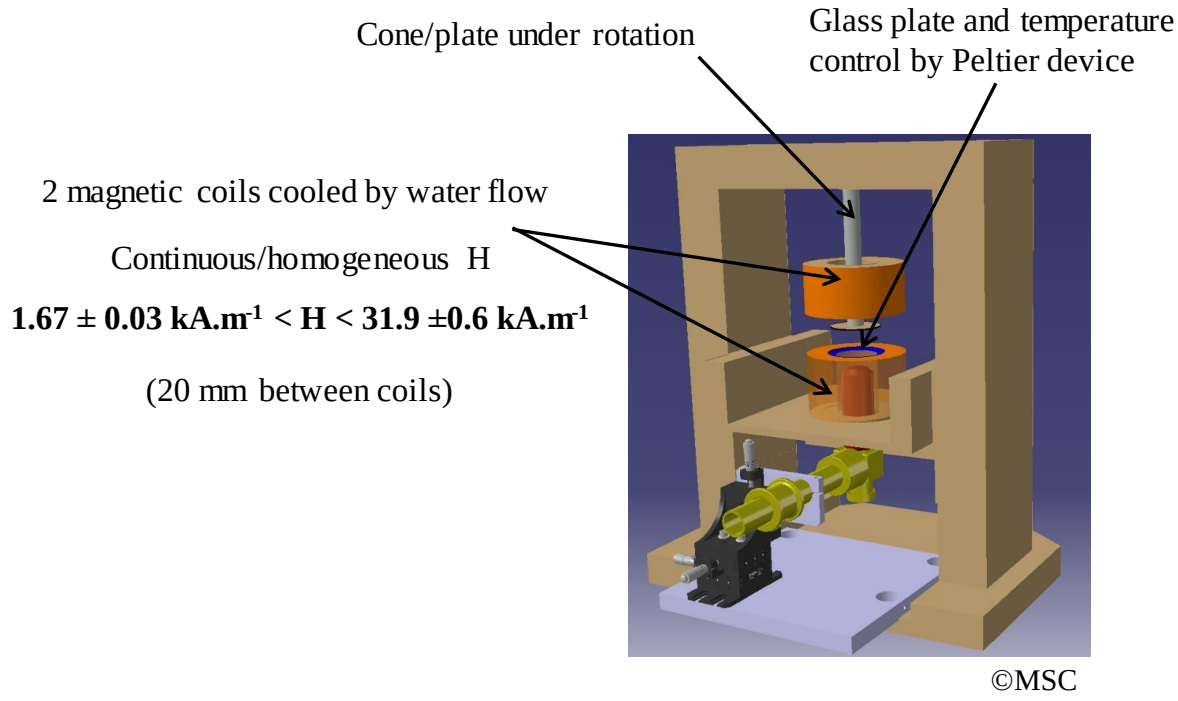

Figure 2: magneto-opto-rheological device [4].

The magnetic part that allows to apply a continuous and homogeneous magnetic field over all the sample in the direction normal to the shear, consists in a pair of Helmholtz coils. The overheating of the magnetic coils by Joule effect was prevented with a flow of cold water. The evaluation of this magnetic system has been performed and presented in a previous paper demonstrating the homogeneity of the magnetic field applied over all the sample and the efficiency of the cooling system [4]. The range of applied magnetic fields can be varied between 0 and 31.9 kA/m in the current geometrical conditions.

The *in-situ* optical observation system consists in a microscope objective (40x) connected to a CCD camera and a light source. The glass plate, on which is placed the sample, allows the

observation during the rheological measurements and it was provided with a laboratory-made Peltier system linked to a PID device to maintain the desired isothermal conditions. The scale of the obtained images was calibrated using polystyrene microparticles with a diameter of 10 µm. This optical observation system allows to obtain a direct visualization of the micronic structures of nanocomposites during the rheological measurements. From these online measurements, some selected images were recorded and analysed with a processing software developed in the MSC laboratory. This software is based on the application of a Laplacian filter and a segmentation of the image in a binary system with two types of pixels, black and white. The black pixels represent the microstructure of aggregated MNPs. To define these microstructures, two different functions were applied to plot the contour of these objects, with different degree of details, from which the different morphological parameters will be extracted. The first one is a function which defines precisely the object pixel by pixel. The second one is traced by a rotated rectangle that can hold inside the object (Figure 3).

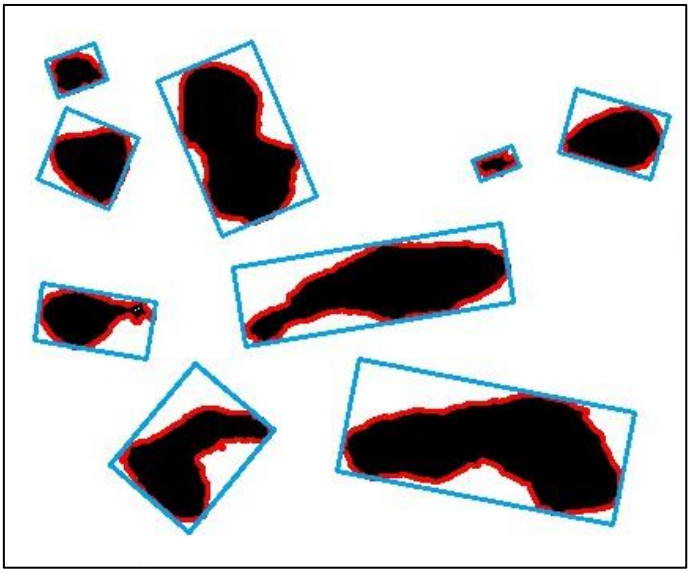

Figure 3: different methods to define the objects in image processing: precise contour (red), and rotated rectangle (blue).

Once the microstructure presented in the images is defined, the following relevant parameters have been chosen for a precise characterization of the morphology of the microstructures:

- Area: defined with a precise contour (Figure 3 - red).
- Ratio: relation of width to height of bounding rectangle of the object (Figure 3 - blue). A number equal or higher than 1.
- Angle of orientation: represents the orientation of the bounding rectangle (Figure 3 - blue) varying between 0° and 180°.

The analysis of microstructures by *in-situ* optical observation during the rheological measurements was possible in the cases of micronic structure formed with enough contrast to be clearly analysed in the obtained images. These images can be recorded during all the duration of the rheological measurements having a direct probe of the magneto- and shear- induced microstructural modifications in the materials responsible of the change of the viscoelastic properties. However, when this analysis was not possible, a glass capillary was filled with the nanocomposite sample and placed between two magnets (Figure 4). The microstructure was observed in an optical microscope.

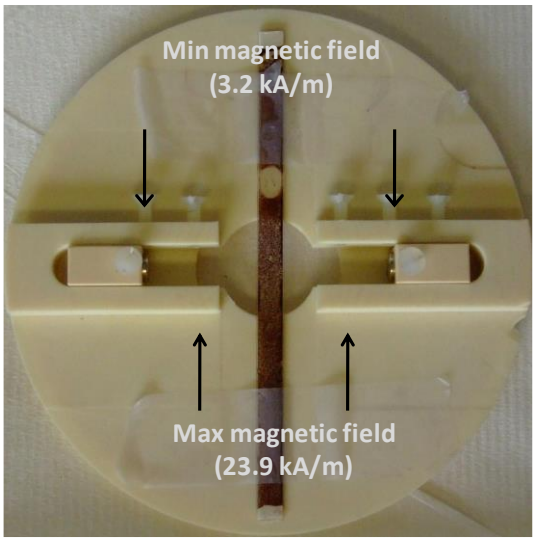

Figure 4: optical observation device.

Both, flow and oscillatory shear rheological measurements were carried out. Firstly, the steady-state flow curves, were obtained by increasing the shear rate between 0.01 and 2000 s^{-1}. The duration of each step was varied in order to measure the stationary value of the shear rate. Moreover, for oscillatory measurements, the strain amplitude was first varied between 0.01 and 100 at constant frequency of 1 Hz to identify the linear viscoelastic domain (LVD). Then, frequency sweep between 0.01 and 100 Hz were performed at a constant strain amplitude selected individually for each studied nanocomposite in the LVD. For all the cases the measurements were carried out under application of magnetic field of different intensities. Before starting the rheological measurement, the field was switched off and a rest time of 10 minutes at zero stress has been established after loading the sample on the plate of the geometry. It has been demonstrated that this time is long enough to ensure an equilibrium state of the reorganization of the microstructure induced by the applied magnetic field.

3.2. Sodium alginate + APPA-MNPs

3.2.1. Introduction

The first studied nanocomposite is sodium alginate solution with a concentration C_{alg} = 10 g/L and APPA-MNPs with volume fraction Φ_{MNPs} = 0.7%. Firstly, the magnetic sensitive microstructure was studied by the magneto-opto-rheological device described in paragraph 3.1. in order to investigate the time evolution of the microstructural changes under applied magnetic field without any applied shear stress. Then flow and viscoelastic measurements coupled with optical observation during the application of different magnetic fields are presented respectively.

3.2.2. Optical observation under applied magnetic field without shear stress

As observed in Figure 5, micronic structures are clearly observed before (Figure 5a) and after (Figure 5b) the application of a magnetic field of 19.6 kA/m. Without magnetic field, the aggregated microstructures could be explained by attractive interactions between negatively charged carboxylate groups of sodium alginate chains and positively charged amino groups on the surface of APPA-MNPs. Then, by application of the homogenous magnetic field, more differentiated microstructures are observed due to the particle-polymer electrostatic interactions and particle-particle magnetic interactions preventing the rotation of individual MNPs to align their magnetization in the direction of external magnetic field [5]. These microstructures tend to orientate in the direction of the applied magnetic field perpendicular to the image. This kind of magnetic-field dependent reorganization in the microscopic level has been previously observed in other polymer – MNPs systems [6].

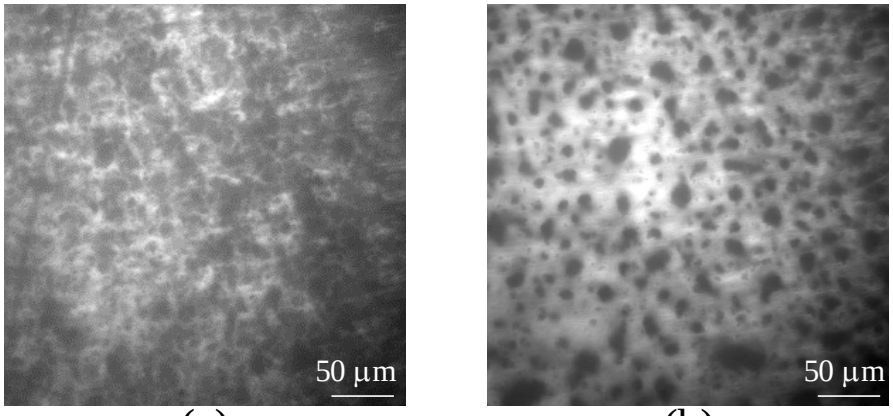

Figure 5: images obtained by in-situ optical observation for the nanocomposite sodium alginate (10 g/L) + APPA-MNPs (Φ_{MNPs} = 0.7%): (a) without magnetic field; (b) 10 minutes after the application of a magnetic field of 19.6 kA/m.

In order to study the formation of this magneto-induced microstructures, three sets of images have been analysed, as described in the experimental protocol, following the application of magnetic fields of different values (13.9, 19.6 and 25.6 kA/m) during 10 minutes in order to determine the area, ratio and angle of orientation considering all the aggregates except those smaller than 50 μm^2 or located on the borders of the images. The ratio and angle of orientation have been found independent of the time and the three values of the magnetic field. This result seems reasonable considering that the orientation of the microstructure in the direction of the applied magnetic field is not observable since it is perpendicularly to the plane of the image. However, the case is rather different for the area of microstructures for which it can be observed an effect of the time after the application of the magnetic field. The best way to analyse this modification is the evolution of the total area of microstructures presented in the recorded images as function of time. The initial state of the nanocomposite consists in a biphasic system at the microscale composed of a microstructure of aggregated MNPs and trapped sodium alginate chains dispersed in a continuous phase of aqueous solution of sodium alginate. When the magnetic field is applied, the first observed phenomena is a fast orientation of this microstructure in the direction of the field in a few seconds, too fast to be detected at the time-scale of the images taken. However, for the three studied values of magnetic field, the results show a slow increase of the total area during some minutes following the application of the field and then tends to an equilibrium in about 10 minutes (Figure 6). This could be explained by the presence of some MNPs individually dispersed in the continuous phase that do not respond immediately to the application of the field. When the magnetic field is applied, these free MNPs are attracted to form part of the microstructure increasing the size of the aggregates during some minutes.

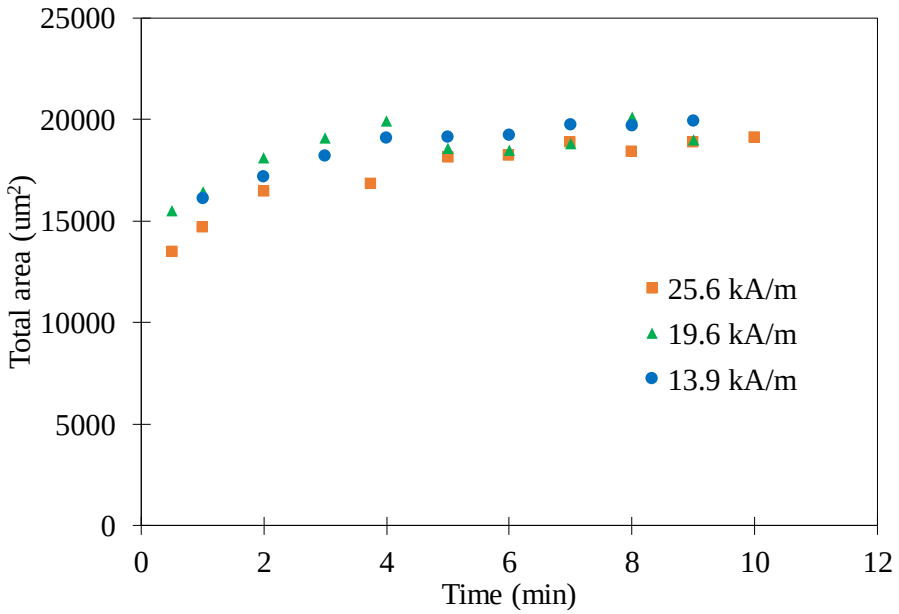

Figure 6: time-evolution of the total area of microstructures per image as function of time for different applied magnetic fields for the nanocomposites sodium alginate (10 g/L) + APPA-MNPs (Φ_{MNPs} = 0.7%).

Another way to underline this effect is the organization of the microstructures in three ranges of area namely small (<200 µm^2), medium (200-500 µm^2) and large (>500 µm^2). If we analyse the time evolution for the different applied magnetic fields, a global increase of the three range of microstructures can be observed during 4 minutes; and then, nearly constant values for longer times as evidenced in Figure 7 for a magnetic field of 19.6 kA/m. Anyhow. the small variations observed can be explained by the relatively small fraction of free MNPs before the application of the magnetic field and an extremely fast response of the forming the microstructure.

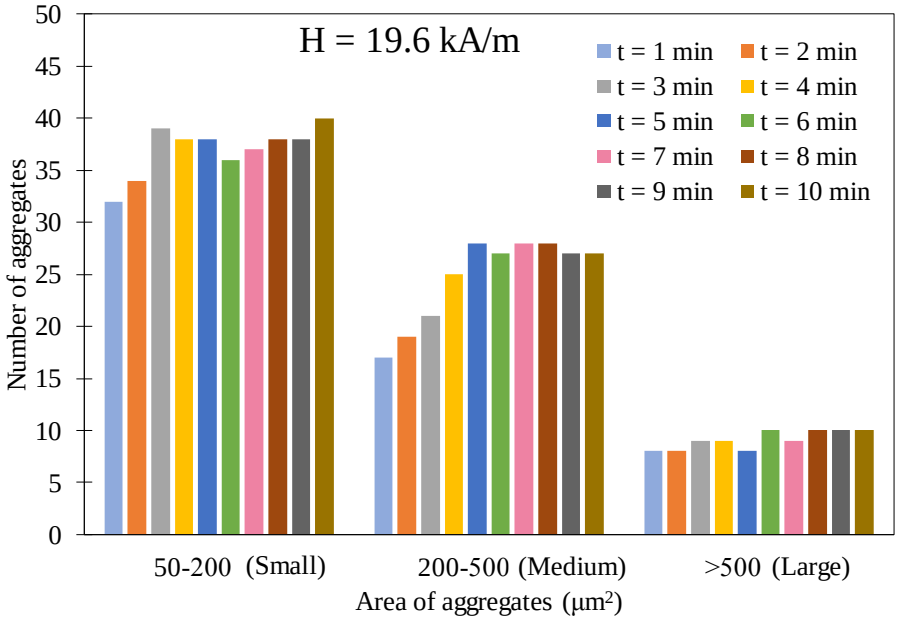

Figure 7: time-evolution of the number of microstructures in each range of sizes after application of a magnetic field of 19.6 kA/m for the nanocomposites sodium alginate (10 g/L) + APPA-MNPs (Φ_{MNPs} = 0.7%).

3.2.3. Shear flow measurements

The steady-state flow curves without magnetic field and for different values of magnetic field are shown in Figure 8. The existence of a microstructure without the application of magnetic field is evidenced by comparison of the curve with and without APPA-MNPs and zero magnetic field. We can observe firstly an increase of the shear viscosity at low shear rates (< 1 s^{-1}) without magnetic field when APPA-MNPs are introduced in the sodium alginate solutions. This can be explained by attractive interactions between negatively charged carboxylate groups (COO^-) of sodium alginate chains and positively charged amino groups (NH_3^+) of APPA-MNPs leading to the microstructures observed previously (see Figure 5a). Since these electrostatic interactions are uniform in all the directions it is expected that the nanocomposite shows isotropic mechanical properties slightly higher in comparison with those of the individual polymeric matrix as it has been found for other similar nanocomposites [7]. By application of the magnetic field, the increase of the shear viscosity becomes more pronounced as a result of the reorganization of the microstructures perpendicularly to the shear as evidenced with the representation of the magneto-viscous effect (MVE = $(\eta_H - \eta_{H=0})/\eta_{H=0}$) in the Figure 9. The strength of the field-induced arrangements (and thus the intensity of the MVE) would be determined by the strength of the magnetic interactions between different particle/polymer aggregates and the resistance of the elongated aggregates to be inclined by hydrodynamic forces. Thus, this effect decreases as function of the shear rate until a superposition of all the curves for shear rates higher than 100s^{-1} where the shear effect prevails the magnetic effect.

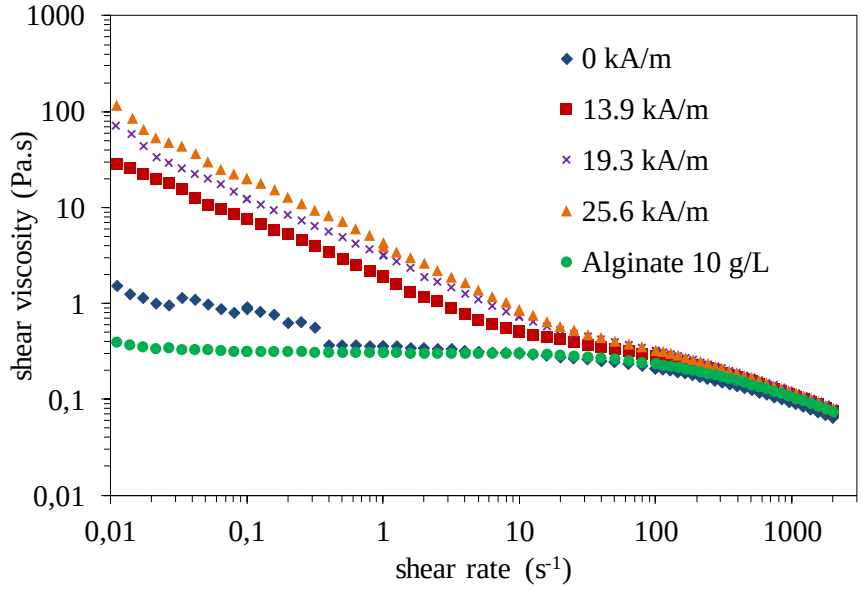

Figure 8: evolution of the viscosity as function of the shear rate during the application of different values of magnetic field for the nanocomposites sodium alginate (10 g/L) + APPA-MNPs (Φ_{MNPs} = 0.7%).

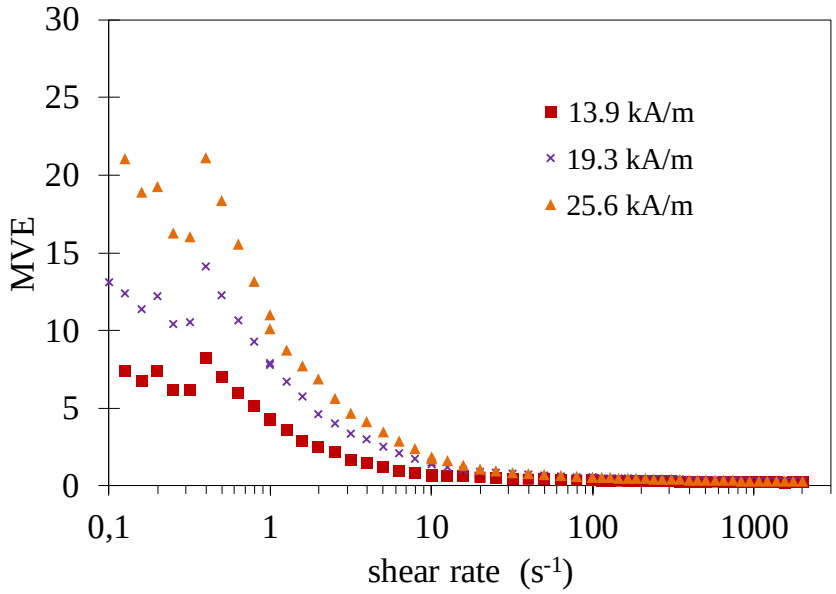

Figure 9: variation of the magneto-viscous effect (MVE) as function of the shear rate during the application of different values of magnetic field for the nanocomposites sodium alginate (10 g/L) + APPA-MNPs (Φ_{MNPs} = 0.7%).

The associated change of the mean area of microstructures under shear rate obtained by the analysis of images obtained by *in-situ* optical observation are presented in Figure 10. Three regions can be differentiated under applied magnetic field delimited by two critical shear rates (γ_c) presented in Table 1, corresponding to the onset of the reorientation of the microstructure in direction of the shear rate (γ_{c1}) and the maximum reorientation (γ_{c2}) before breaking of the microstructure. We observe an expected increase of these critical shear rates as function of the applied magnetic field associated with a more resistant to deformation microstructure as the magnetic field is increased.

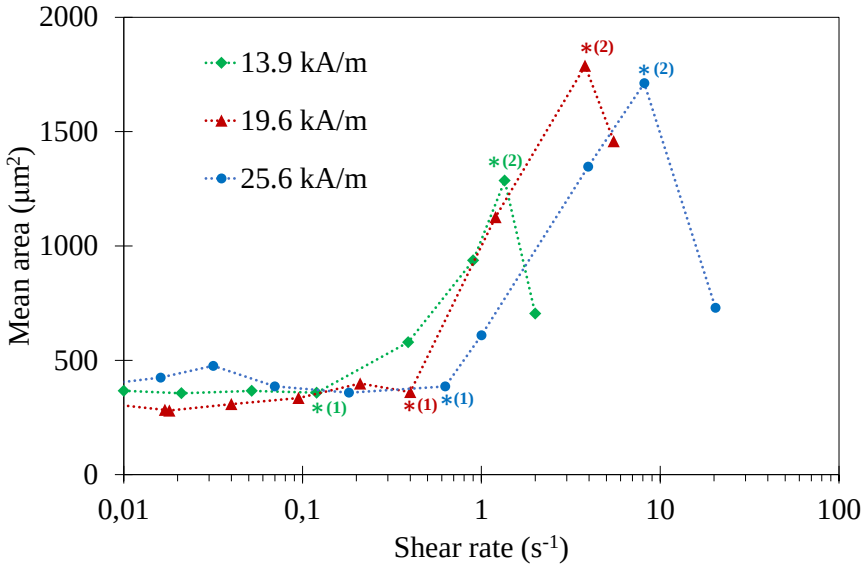

Figure 10: evolution of the mean area of the microstructure as function of the shear rate. *(1): critical shear rate - onset of deformation, *(2): critical shear rate - onset of breaking.

Table 1: critical shear rates for the different applied magnetic fields.

Magnetic field (kA/m)	$\dot{\gamma}_{C\,1}$ **(s^{-1})**	$\dot{\gamma}_{C\,2}$ **(s^{-1})**
13.9	0.18	1.35
19.6	0.40	3.80
25.6	0.63	8.15

A correlated analysis between rheological and optical results can be performed. At low shear rates ($\dot{\gamma} < \dot{\gamma}_{c1}$), the magneto-induced reorganization of the microstructure is associated to a yield stress (values in Table 2). The microstructure of the nanocomposite is elongated in the direction of the magnetic field showing an anisotropic behavior with maximal mechanical properties in the direction of the applied shear rate with the corresponding enhancement of the viscosity. The yield stress is found to be proportional to the square of the magnetic field (Figure 11). This result is in good agreement with the one found for concentrated magnetorheological fluids [8]. In order to link this increase of viscosity as function of the applied magnetic field observed macroscopically with microstructural modifications, we have analyzed the images corresponding to a shear rate of 0.1 s^{-1}. As observed in Figure 12, the microstructure is denser as the magnetic field increases as confirmed by the calculated total area of microstructures shown in the Table 2.

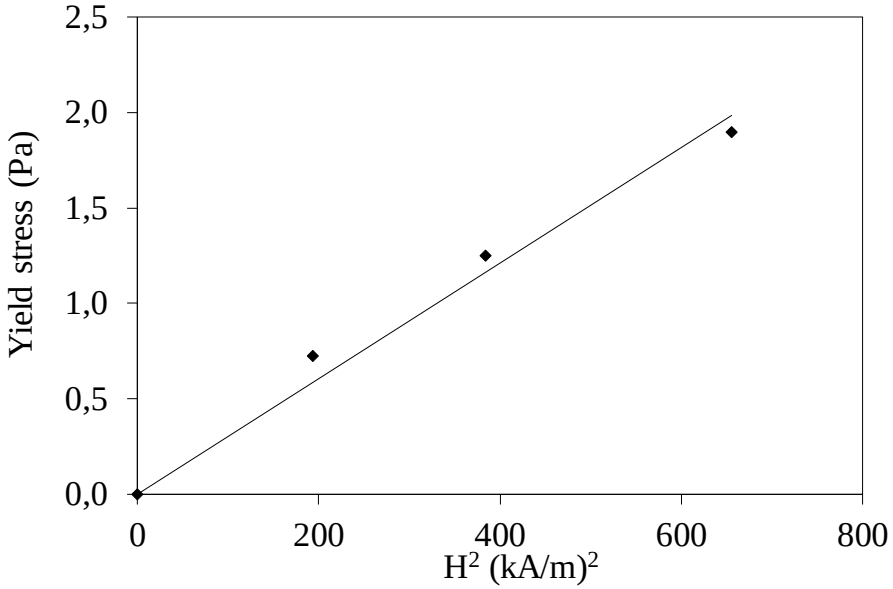

Figure 11: linear variation of the yield stress with the square of the magnetic field.

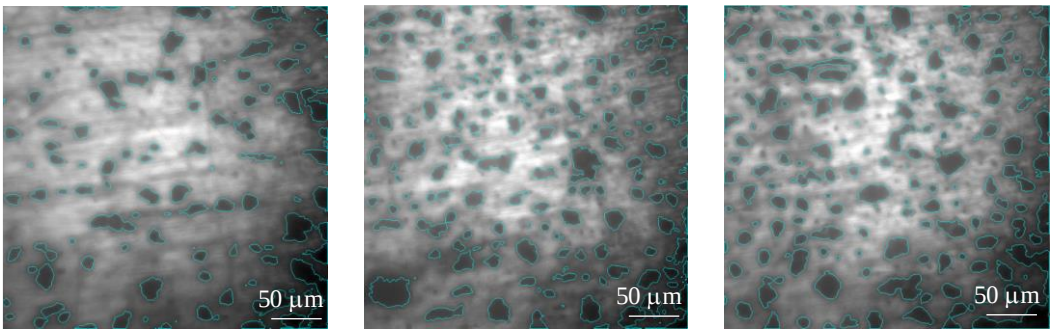

(a) (b) (c)

Figure 12: images analysed at low shear rate (0.1 s^{-1}) and during the application of magnetic field of: (a) 13.9 kA/m; (b) 19.6 kA/m; (c) 25.6 kA/m.

Table 2: results of the rheological and microstructural analysis at low shear rate for the different applied magnetic fields.

H (kA/m)	η ($\dot{\gamma}$ = 0.1 s^{-1}) (Pa.s)	Yield stress (Pa)	Total area (mm^2)
0.0	0.88	0	-
13.9	7.66	0.72	25.8
19.6	12.39	1.25	39.5
25.6	19.97	1.90	45.6

For shear rate ($\dot{\gamma}_{c1} < \dot{\gamma} < \dot{\gamma}_{c2}$), the applied shear begins to deform the magneto induced microstructure (Figure 13) in a direction perpendicular to the one of the magnetic forces as evidenced by the decrease of the magnetoviscous effect as the shear rate is increased. As shown in Figures 14 and 15 respectively, the % of microstructures with an elongated shape (ratio>2) and the % of structures oriented with an angle close to 90º in the direction of the applied shear rate increase confirming the elongation in the direction of the magnetic field, and then, the progressive orientation in the shear direction.

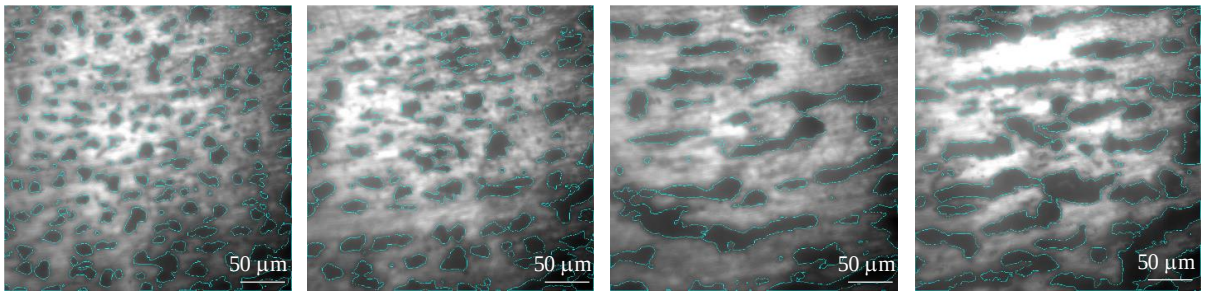

(a) (b) (c) (d)

Figure 13: processed images during the application of a magnetic field of 25.6 kA/m in the region of medium shear rates: (a) 0.12 s^{-1}; (b) 0.39 s-1; (c) 0.9 s^{-1}; (d) 1.35 s^{-1}.

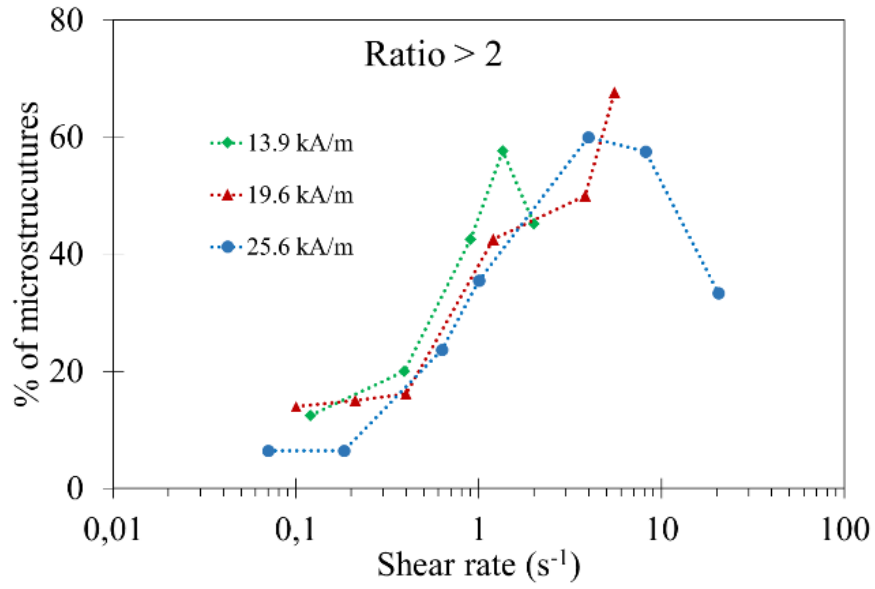

Figure 14: evolution of the percentage of microstructures with elongated shape (ratio > 2) as function of the shear rate during the application of magnetic field.

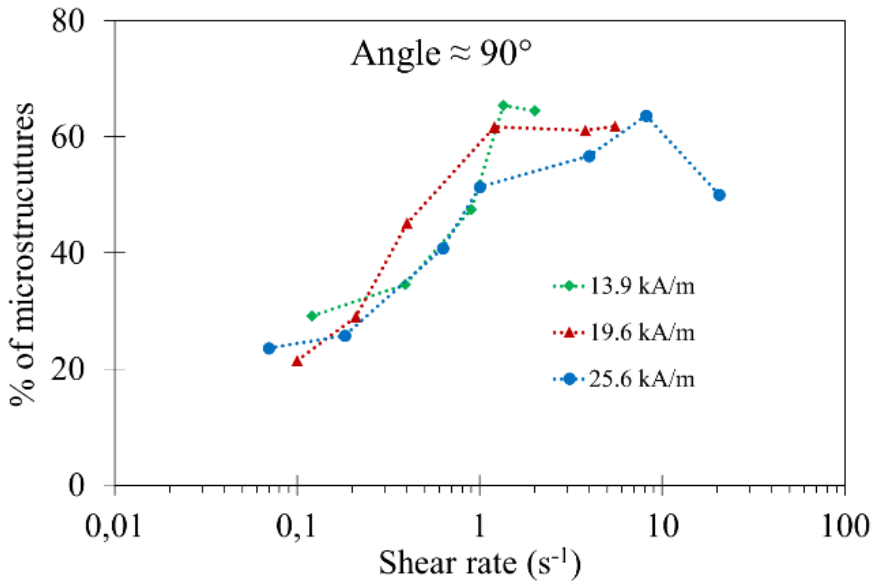

Figure 15: evolution of the percentage of microstructures with an angle of orientation close to 90° as function of the shear rate during the application of magnetic field.

The percentage of microstructures in three groups of area in the range of shear rates $\dot{\gamma}_{c1} < \dot{\gamma} < \dot{\gamma}_{c2}$ for a magnetic field of 13.9 kA/m is plotted in the form of histograms in Figure 16. It can be observed a decrease of the % of small microstructures and an increase of bigger ones as function of the shear rate due to the orientation of the magnetically elongated microstructures in the direction of the shear rate. Moreover, this detailed analysis suggests that the orientation of the microstructure in the directions of the shear depends on their size. The % of small microstructures rapidly decrease after $\dot{\gamma}_{c1}$ while the % of medium microstructures remains constant until $\dot{\gamma} = 0.90 s^{-1}$. Similar tendencies are observed for the other applied magnetic fields.

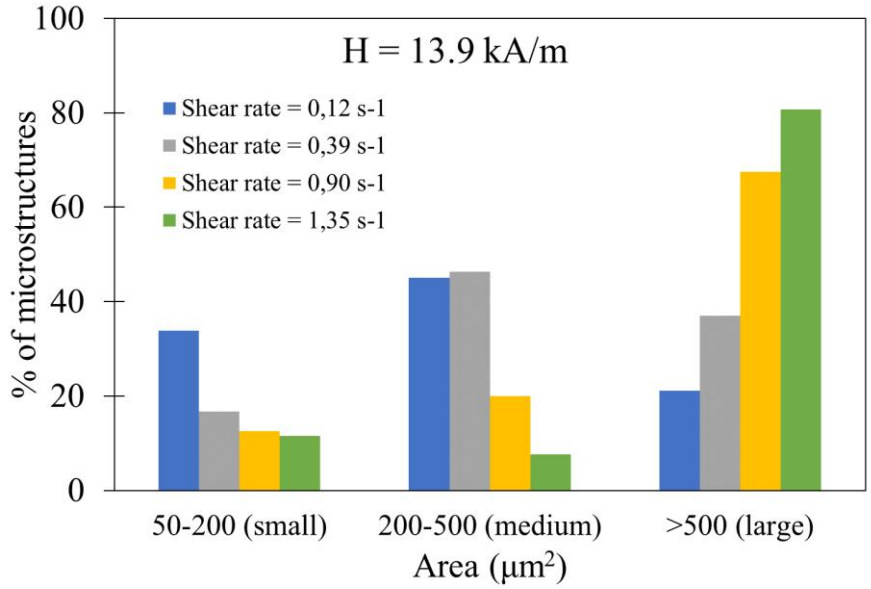

Figure 16: evolution of the % of microstructures in each range of sizes as function of the shear rate inside the region of medium shear rates during the application of a magnetic field of 13.9 kA/m.

At high shear rate ($\dot{\gamma} > \dot{\gamma}_{c2}$), the effect of the shear becomes predominant and the image analysis becomes difficult due to high speed of rotation. The shear rate tends to break all microstructures and the shear viscosity does not depend on the applied magnetic field any more as confirmed by the superposition of the steady shear flow curves for $\dot{\gamma} > 100\ s^{-1}$ (Figures 8 and 9). Similar trends were reported in [9] for the evolution of the viscosity as function of the shear rate during the application of magnetic field for a crosslinked PVA hydrogel with MNPs.

3.2.4. Shear viscoelastic measurements

As shown in Figures 17 and 18, an increase of the elastic (G') and loss (G") moduli are observed in the linear viscoelastic domain (LVD) as a function of an increase of the applied magnetic field. Beyond the limit of the LVD, G' and G" decrease progressively as the strain is increased before reaching a constant value independent of the applied magnetic field. These macroscopic changes are related with the strain-dependent alignment and breakage of the microstructures as confirmed by image analysis described below.

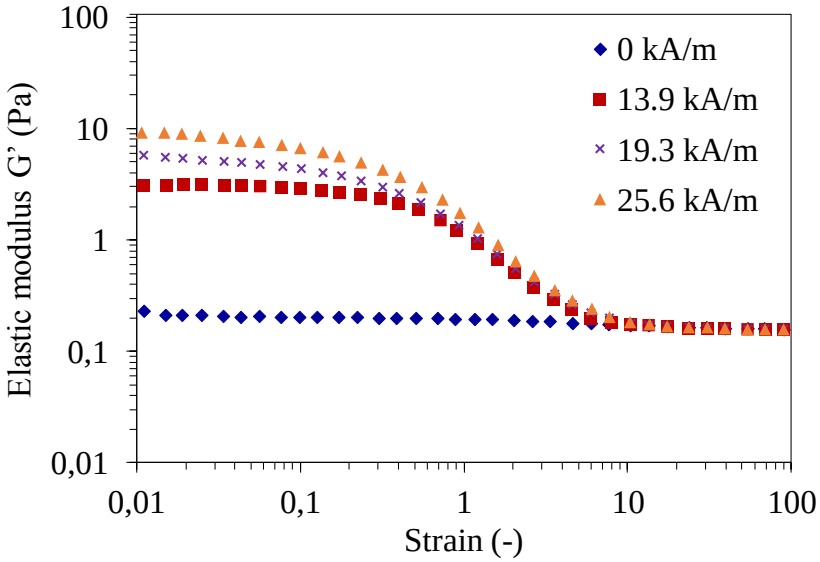

Figure 17: evolution of the elastic moduli as function of the strain without and with applied magnetic field of different values for the nanocomposites sodium alginate (10 g/L) + APPA-MNPs (Φ_{MNPs} = 0.7%).

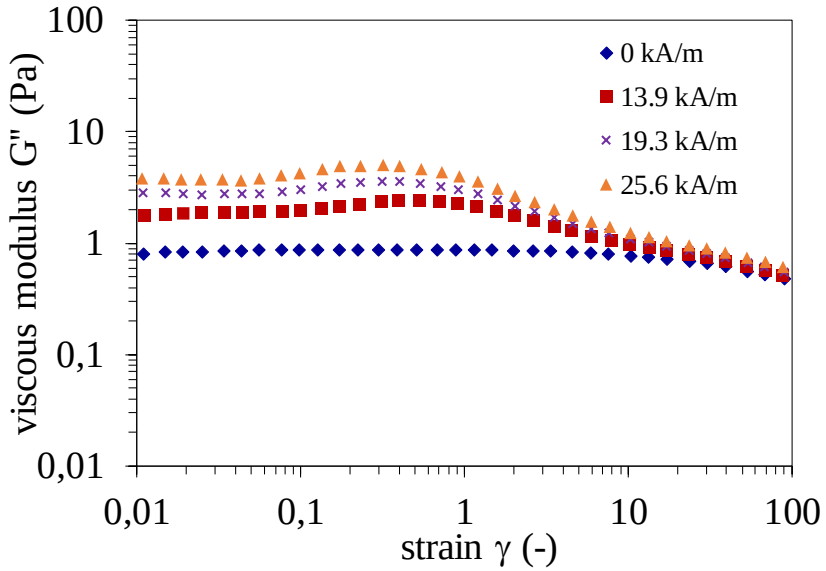

Figure 18: evolution of the viscous moduli as function of the strain without and with applied magnetic field of different values for the nanocomposites sodium alginate (10 g/L) + APPA-MNPs (Φ_{MNPs} = 0.7%).

As for the results of steady-state flow curves, we have analysed viscoelastic data in terms of magnetic field and strain dependence of microstructures. The variation of mean area as function of the strain for three applied magnetic fields in Figure 19 can be qualitatively divided in three regions. The mean area is rather constant for strain between 0.01 and 0.1 associated to constant values of G' and G" in the LVD. Then the mean area increases for strains between 0.1 and 4. This increase takes place close to the critical strain that defines the limit of the LVD and corresponding to the peak observed in the evolution of G". Finally, the decrease of the mean area is related to the decrease of G' and G" (Figures 17 and 18) associated to the breaking of the microstructure of the sample. This behaviour can be observed qualitatively in the selected images presented in Figure 20 for a magnetic field of 19.6 kA/m. The analysis of the

microstructures is in good agreement with the previous analysis for steady-state flow measurements confirming the progressive deformation and break up of microstructures elongated in the direction of the applied magnetic field.

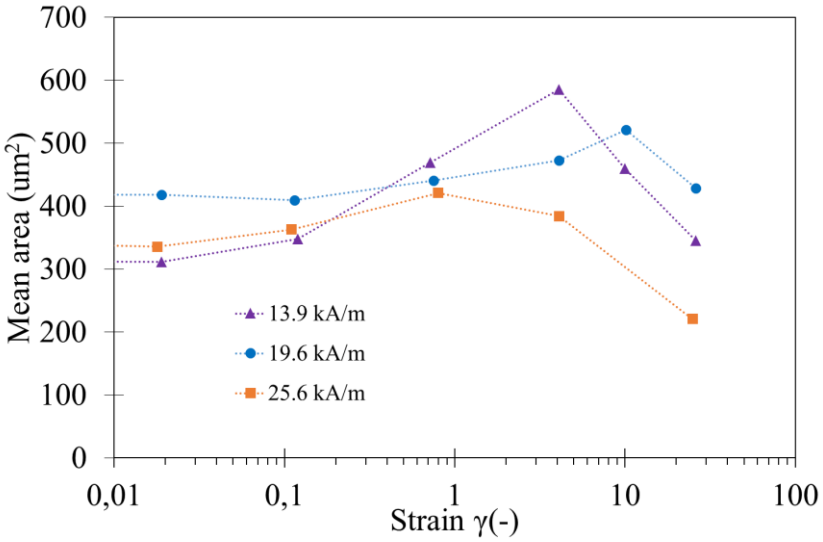

Figure 19: evolution of the mean area as function of the strain during the application of a magnetic field.

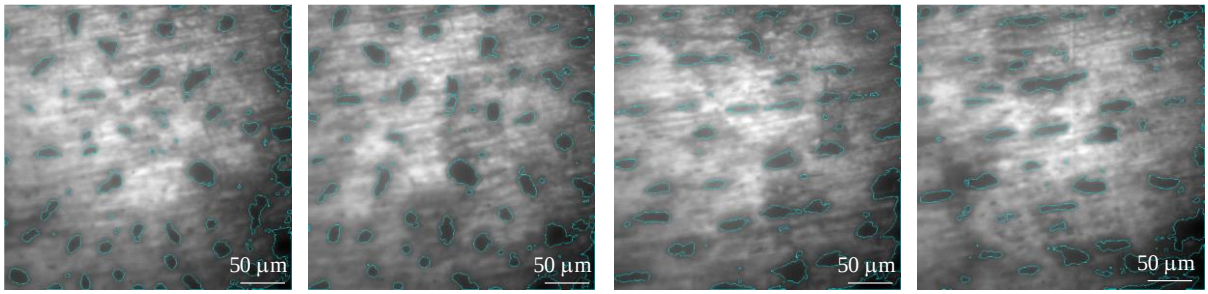

(a) (b) (c) (d)

Figure 20: images analysed during the application of a magnetic field of 19.6 kA/m at different strains: (a) in the LVD,) γ = 0.11; (b) in the limit of the LVD, γ = 0.75 and(c) out of the LVD, γ = 4 and (d) γ = 10.

Due to a lower number of analysed images than the ones for flow curves, it is not possible to precisely define critical strains in Figure 19 (as critical shear rates in Figure 10). However, the increase of G' and G'' in the LVD as a function of the applied magnetic field can be related to an increase of the number and size of microstructures accordingly with the results summarized in Table 3.

Table 3: results of the macroscopic and microscopic analysis at low strain for the different magnetic fields applied.

Magnetic field (kA/m)	G'(Pa)at γ = 0.01	G''(Pa) at γ = 0.01	Total area (mm^2)
0.0	0.2	0.8	-
13.9	3.1	1.8	18.1
19.6	5.7	2.9	21.3
25.6	9.3	3.8	25.2

The frequency dependence of G' and G" in the LVD ($\gamma = 0.05$) clearly shows (Figures 21 and 22) a fluid to solid transition at low frequencies when the magnetic field is applied. Indeed, G' is nearly constant as for a gel or rubber material. This solid-like behaviour can be explained by the built up of denser microstructures with an increase of magnetic field as observed in Figure 23 and confirmed by the values summarized in the Table 4.

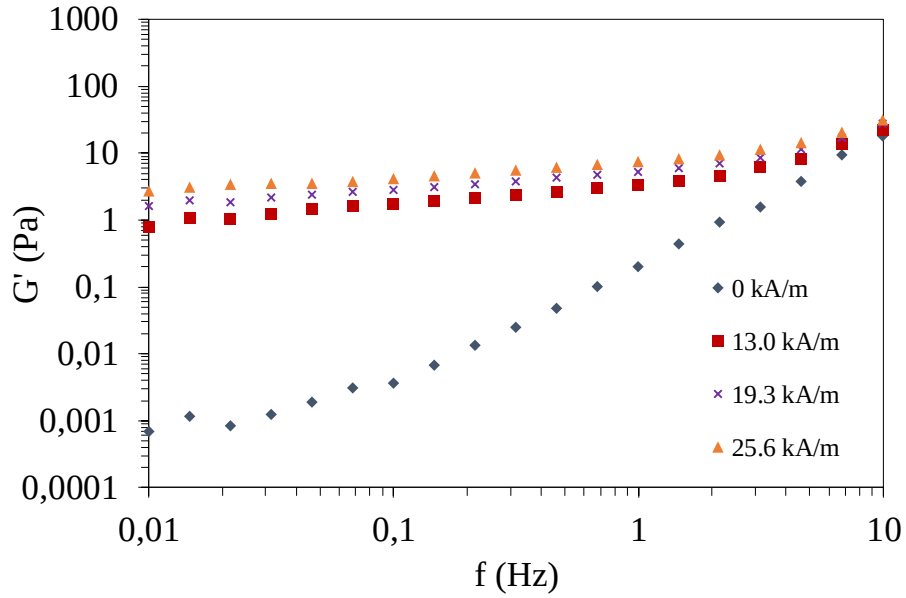

Figure 21: evolution of the elastic moduli as function of frequency without and with applied magnetic field of different values for the nanocomposites sodium alginate (10 g/L) + APPA-MNPs (Φ_{MNPs} = 0.7%).

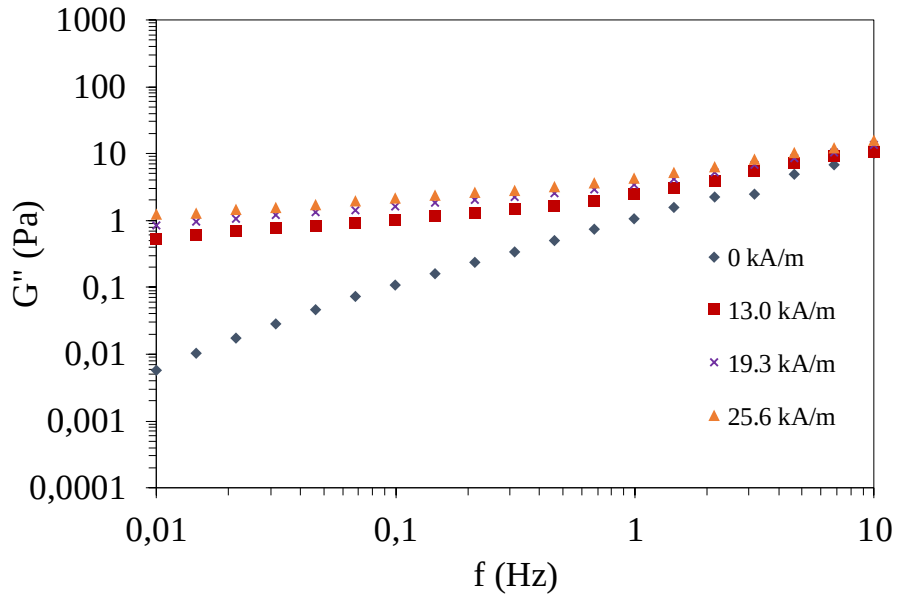

Figure 22: evolution of the viscous moduli as function of frequency without and with applied magnetic field of different values for the nanocomposites sodium alginate (10 g/L) + APPA-MNPs (Φ_{MNPs} = 0.7%).

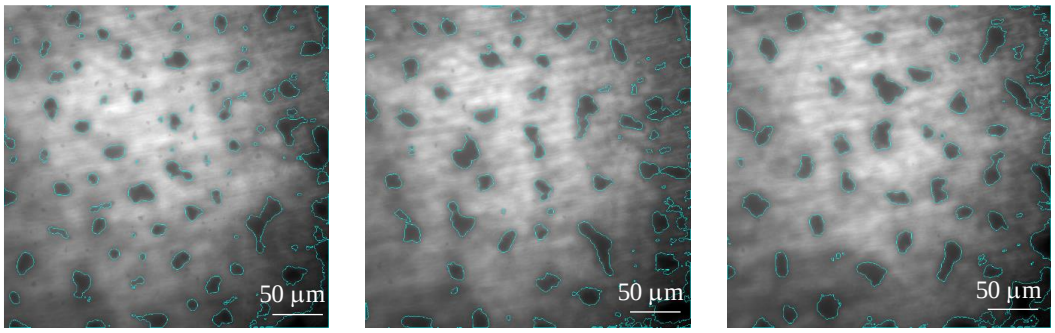

(a) (b) (c)

Figure 23: images analysed at frequency f = 0.1 Hz during the application of magnetic field of: (a) 13.9 kA/m; (b) 19.6 kA/m; (c) 25.6 kA/m.

Table 4: results of the rheological and microstructural analysis at f = 0. 01 Hz for the different applied magnetic fields.

H (kA/m)	G' (Pa) at f = 0.1 Hz	G" (Pa) at f = 0.1 Hz	Total area (mm^2)
0.0	0.003	0.07	-
13.9	0.77	0.54	21.8
19.6	1.61	0.85	21.6
25.6	2.69	1.25	23.9

Similar behaviour with a low frequency plateau that becomes better defined as the concentration of nanofillers is increased has also been observed in other polymer nanocomposites including layered nanocomposites [10], nanofiber nanocomposites [11] or nanotube nanocomposites [12] confirming a typical behaviour for nanocomposites with elongated microstructures.

3.2.5. Conclusions

Novel magnetic sensitive composites have been elaborated by introduction of APPA-MNPs functionalized with a double ligand bearing an amine function in aqueous solution of sodium alginate. The formation of an interesting microstructure of aggregates evidenced by *in-situ* optical observation was related with the attractive electrostatic interactions between the negatively charged sodium alginate chain (carboxylate groups, COO^-) and positively charged APPA-MNPs (amino groups, NH_3^+). Shear flow and viscoelastic properties at constant temperature of these nanocomposites have been investigated under applied magnetic field with a magneto-opto-rheology device specifically designed for such purpose in the MSC laboratory. An enhancement of the viscosity at low shear rate and viscoelastic moduli in the linear viscoelastic domain (LVD) have been clearly evidenced and associated to microstructures observed optically *in-situ* for the first time. A clear correlation between rheological properties and microstructures depending on both magnetic field and shear rate has been established due

to a systematic analysis of images with a software developed in the MSC laboratory. Magneto-induced microstructures of a few hundred microns in size growth without applied shear during a few minutes after the application of magnetic field. Under shear, shear thinning behaviour and strain dependence of elastic and loss moduli can be explained by a competition between the orientation of microstructures in the direction of the magnetic field and alignment until breaking of microstructures in the perpendicular shear rate direction. Critical shear rates for alignment and breaking have been estimated from flow curves and correlated to image analysis (area, ratio and angle of orientation of microstructures). A fluid-solid transition has been clearly evidenced on the frequency dependence of viscoelastic moduli in the LVD associated to the formation of denser microstructures as the applied magnetic field was increased.

3.3. Sodium alginate + citrated-MNPs

3.3.1. Introduction

The second studied nanocomposite is sodium alginate aqueous solutions with citrated-MNPs. The higher productivity of the synthesis protocol of citrated-MNPs allows to prepare bigger amounts of nanocomposite. Thus, for this case, two concentrations of sodium alginate (C_{alg} = 10 g/L and C_{alg} = 18 g/L) and two volume fractions of citrated-MNPs (Φ_{MNPs}=0.7% and Φ_{MNPs}=1%) have been studied.

3.3.2. Optical observation under applied magnetic field without shear stress

No microstructures were found in such type of nanocomposites with the *in-situ* optical observation setup of the magneto-opto-rheological device probably due to their smaller size. However, a capillary filled with the nanocomposite and using the home-made device placed on an optical microscope (Figure 4) allow to obtain the images presented in the Figure 24 without and with the application of a continuous magnetic field. Without magnetic field a microstructure composed of spherical droplets of demixion is observed. By application of a weak magnetic field the droplets were deformed leading to a microstructure of highly elongated spheroid structures oriented in the direction of the applied field. The deformation of the droplets is completely reversible: when the magnetic field is switched off, the droplets recover their spherical initial shape. The image for H = 0 was analysed with imageJ software determining the size of 200 droplets obtaining a mean size of 3.3 ± 0.6 μm. The microdroplet size distribution is shown in Figure 25 obtaining a good fitting with a log-normal distribution.

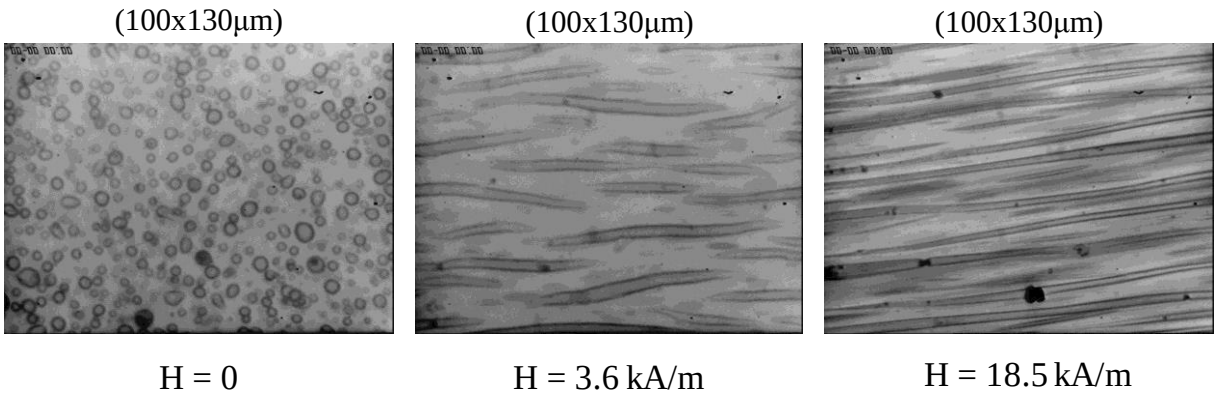

Figure 24: optical observation for the nanocomposites sodium alginate 18 g/L + citrated-MNPs Φ_{MNPs} = 1%. with and without the application of a magnetic field.

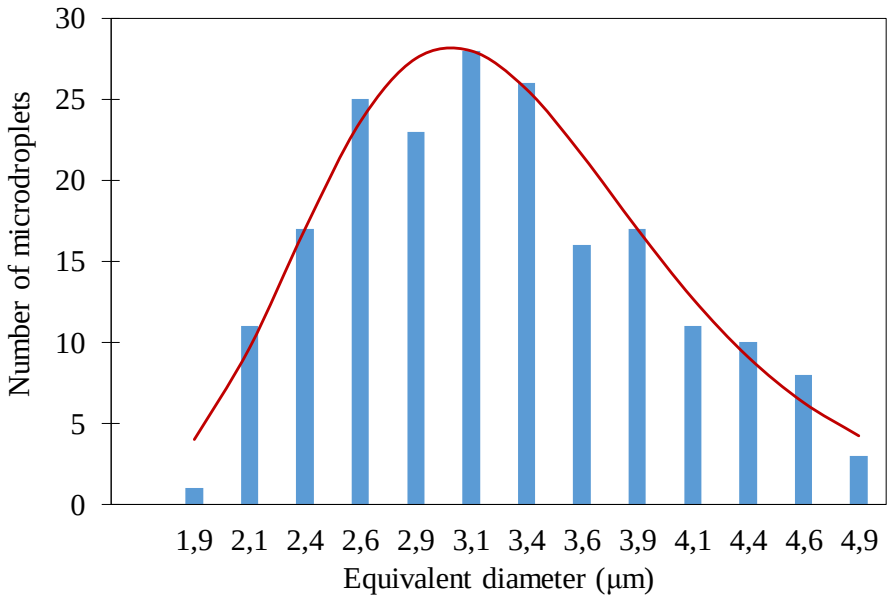

Figure 25: microdroplet size distribution fitted with a log-normal distribution for the nanocomposites sodium alginate (18 g/L) + citrated-MNPs (Φ_{MNPs} = 1%) without the application of a magnetic field.

It is important to remark that this microstructure of droplets of demixion was not found in aqueous dispersions of citrated-MNPs evidencing that the formation of droplets in the nanocomposite has its origin in colloidal forces other than magnetic forces. These droplets of demixion have been already observed in sodium alginate aqueous solutions containing citrated-MNPs and their formation was attributed to an increase in the ionic strength when the dispersion of citrated-MNPs is added to the sodium alginate solution [13]. The volume fraction of MNPs within the droplets has been experimentally obtained in a previous work and found to be Φ_{MNPs} = 13% v/v [13]. This value is considerably smaller than the maximum packing volume fraction for monodisperse spheres (Φ = 64%) and, consequently, is clear that the droplets should consist in both MNPs and sodium alginate polymer chains.

3.3.3. Shear flow measurements

The results of the steady-state flow curves during the application of different magnetic fields are presented in Figure 25 for C_{alg} = 10 g/L and Φ_{MNPs}=0.7% (identical conditions than previous nanocomposites sodium alginate + APPA-MNPs). By application of low magnetic field values, it can be noticed a very slight increase of the shear viscosity at low shear rates that becomes more important for the higher magnetic fields (19.6 and 25.6 kA/m). If we compare these curves with the previously presented results for nanocomposites sodium alginate + APPA-MNPs (Figure 8), the magneto-induced increase of viscosity at low shear rates is much less important for the present case. This can be explained by the lower magnetization of citrated-MNPs than APPA-MNPs as demonstrated in the chapter I. In addition, the attractive electrostatic interaction between APPA-MNPs and negatively charged sodium alginate chains can contribute to have a strong magnetoviscous effect, while this contribution is not expected from repulsive electrostatic interactions between negatively charged citrated-MNPs and negatively charged sodium alginate chains.

The effect of an increase of first sodium alginate concentration and then volume fraction of citrated-MNPs is show on Figures 27 and 28 respectively. An important increase of the magnetoviscous effect is observed when the alginate concentration is increased from 10 to 18 g/L. However, no significant effect is observed when Φ_{MNPs} is increased from 0.7% to 1% for the same alginate concentration (Figure 28).

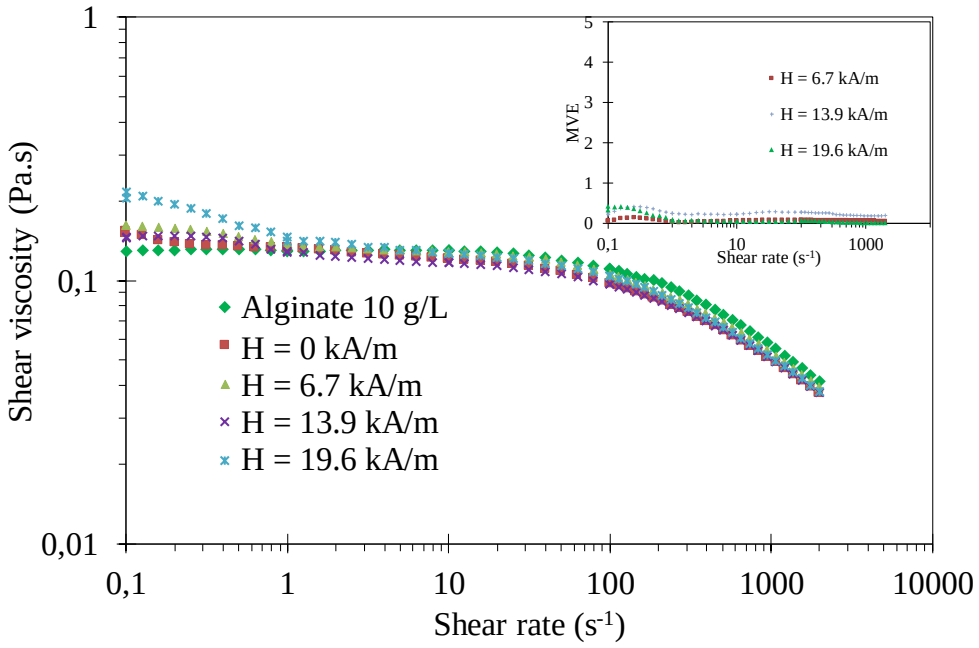

Figure 26: evolution of the viscosity as function of the shear rate during the application of different values of magnetic field for the nanocomposites sodium alginate (10 g/L) + citrated-MNPs (Φ_{MNPs} = 0.7%). The shear rate dependence of the magnetoviscous effect is shown in the insert.

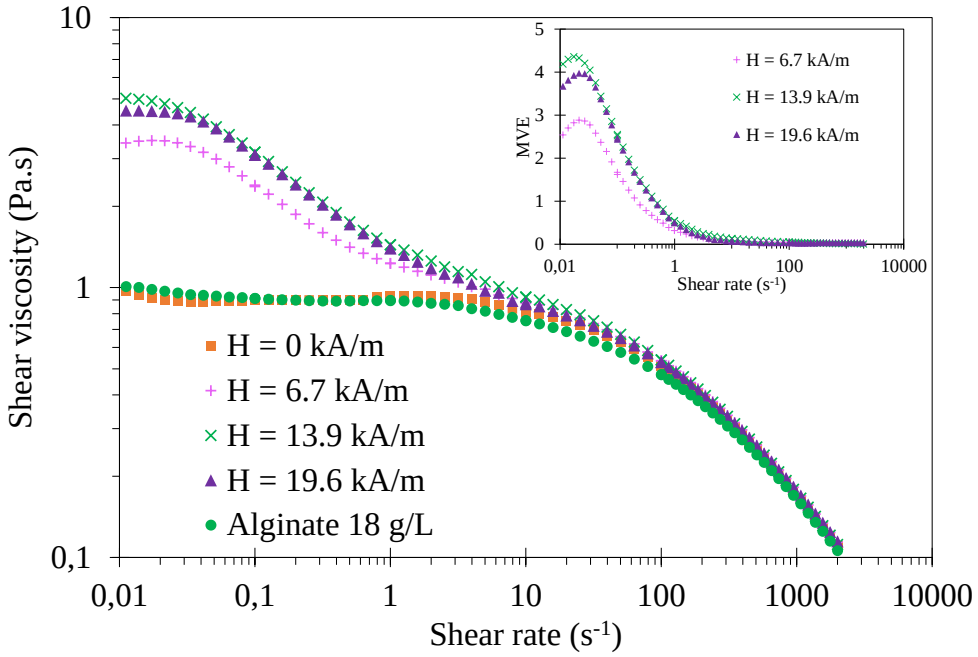

Figure 27: evolution of the viscosity as function of the shear rate during the application of different values of magnetic field for the nanocomposites sodium alginate (18 g/L) + citrated-MNPs (Φ_{MNPs} = 0.7%). The shear rate dependence of the magnetoviscous effect is shown in the insert.

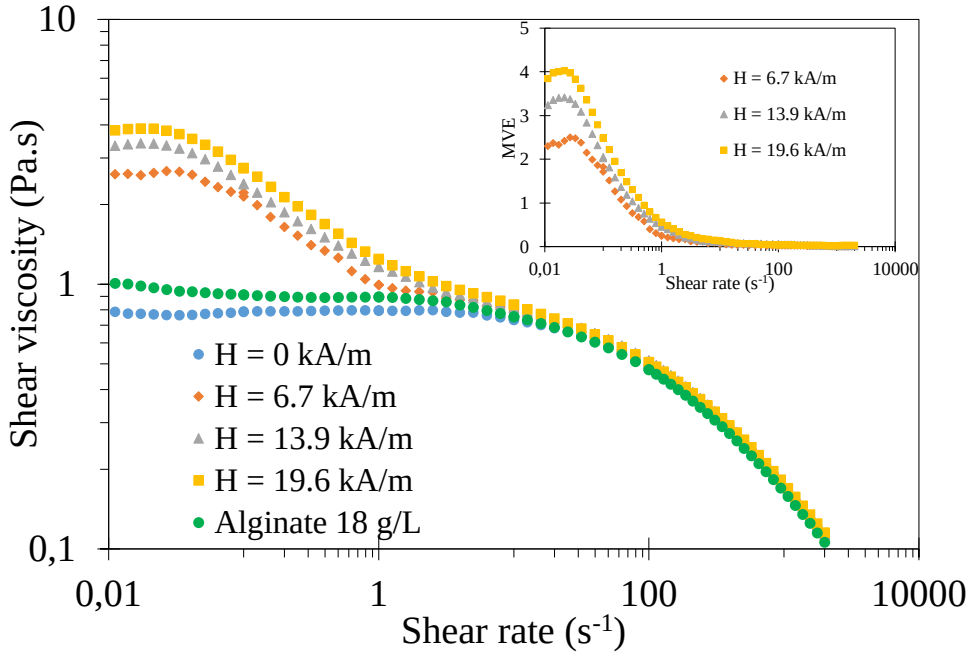

Figure 28: evolution of the viscosity as function of the shear rate during the application of different values of magnetic field for the nanocomposites sodium alginate (18 g/L) + citrated-MNPs (Φ_{MNPs} = 1%). The shear rate dependence of the magnetoviscous effect is shown in the insert.

In absence of applied magnetic field, the nanocomposite can be considered a suspension constituted by drop-like aggregates dispersed in a sodium alginate solution, in agreement with microscopic observations shown in Figure 24. The viscosity of such suspension can be determined by the Batchelor equation [14]:

$$\eta_s = (1 + 2.5\Phi + 6.2\Phi^2)\eta_0 \qquad (1)$$

where η_s is the viscosity of the suspension, η_0 the viscosity of the solution without aggregates and Φ the volume fraction of spherical droplets.

However, it is impossible to get the viscosity of the sodium alginate solution since an unknown fraction of the polymer chains should be trapped inside the droplets. For the studied experimental conditions (alginate concentration and volume fraction of MNPs), the viscosity does not strongly change by the addition of citrated-MNPs in the absence of applied magnetic field presumably due to two opposite effects: (1) decrease of η_0 due to the sodium alginate chains trapped in the droplets, (2) increase of η_s due to the effect of the droplets accordingly with the Batchelor equation. For Φ_{MNPs} = 0.7% η_0 and η_s could be in the same order while for Φ_{MNPs} = 1% the number of sodium alginate chains inside the droplets could increase leading to a decrease of η_0 higher than the increase of η_s and consequently the observed decrease of shear viscosity at low shear rates (Figure 28). Under the application of magnetic field, the viscosity at low shear rates is strongly increased leading to a Newtonian plateau followed by a shear-thinning behavior in two steps that could be explained to the orientation of the droplets of demixtion and the breaking up of the microstructure respectively.

3.3.4. Shear viscoelastic measurements

From the results of the viscous modulus (G") as function of the strain for a fixed frequency of 1 Hz presented in Figure 29, it can be confirmed a very similar viscous behaviour for both Φ_{MNPs} with a slight increase of G" in the LVD as function of the applied magnetic field. Likewise, the application of the field induces an increase of the elastic modulus (G') in the LVD for both nanocomposites (Figure 30). However, for this case, Φ_{MNPs} has an important effect, observing a much more important increase for the higher volume fraction of Φ_{MNPs} = 1% than for Φ_{MNPs} = 0.7%.

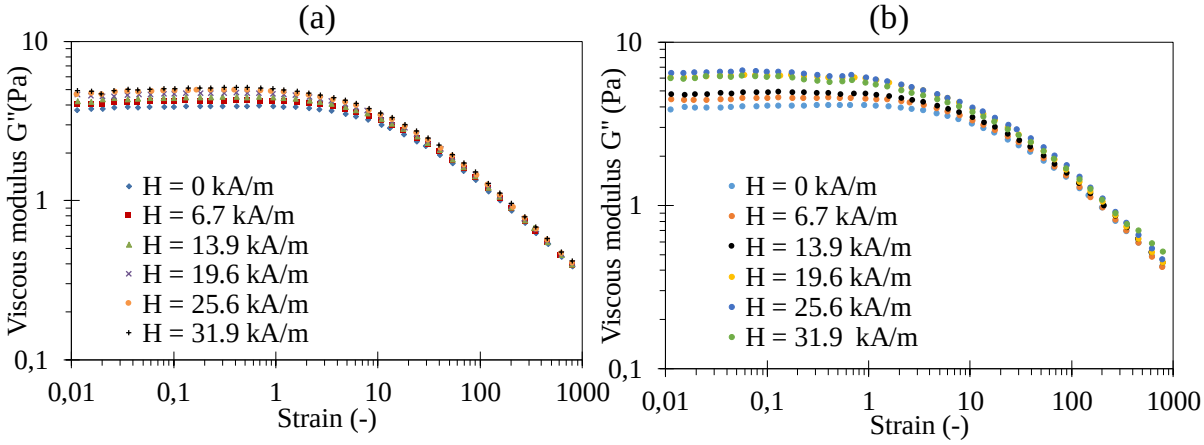

Figure 29: evolution of the viscous modulus as function of the strain during the application of different magnetic fields for the nanocomposites sodium alginate (18 g/L) + citrated-MNPs (a) Φ_{MNPs} = 0.7% and (b) Φ_{MNPs} = 1%.

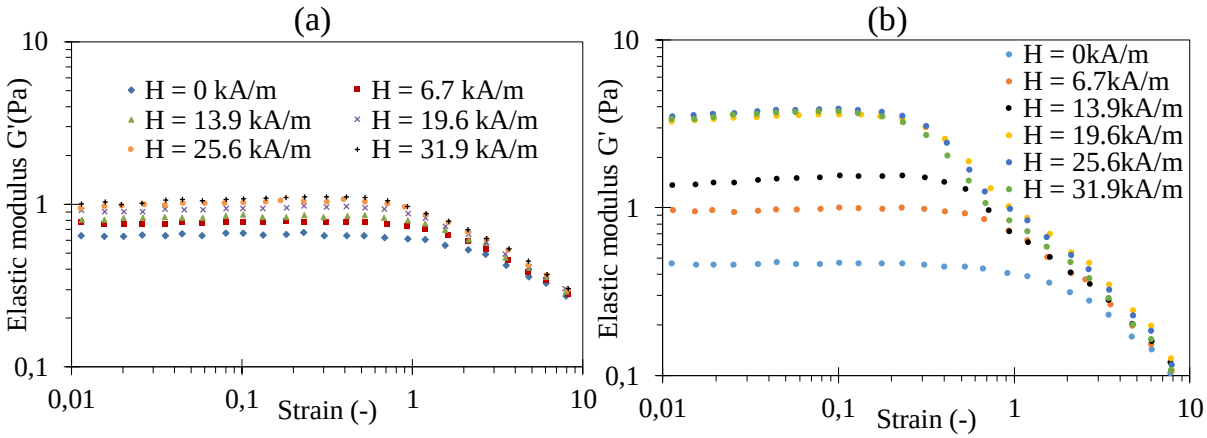

Figure 30: evolution of the elastic modulus as function of the strain during the application of different magnetic fields for the nanocomposites sodium alginate (18 g/L) + citrated-MNPs (a) Φ_{MNPs} = 0.7% and (b) Φ_{MNPs} = 1%.

As shown in Figure 31 and 32 for nanocomposites with C_{alg} = 18 g/L and Φ_{MNPs} = 1%., the frequency dependence of G' and G" in the linear viscoelastic domain (γ = 0.1) evidence clearly a fluid-solid transition at low frequencies when the magnetic field is increased with G'>G". This transition is attributed to the deformation of the spherical droplets of demixion under the application of the magnetic field (Figure 24). However, the increase of G' at low frequencies is less important by comparing the frequency evolution of G' (Figure 31) with the previous results obtained for sodium alginate + APPA-MNPs nanocomposites (Figure 21) highlighting the importance of the polymer-particle interactions. For the case of sodium alginate + APPA-MNPs, the attractive electrostatic forces between negatively charged sodium alginate chains and positively charged APPA-MNPs contribute to obtain a more interconnected microstructure that results in a more important effect of the magnetic field in the viscoelastic properties at low frequencies**.**

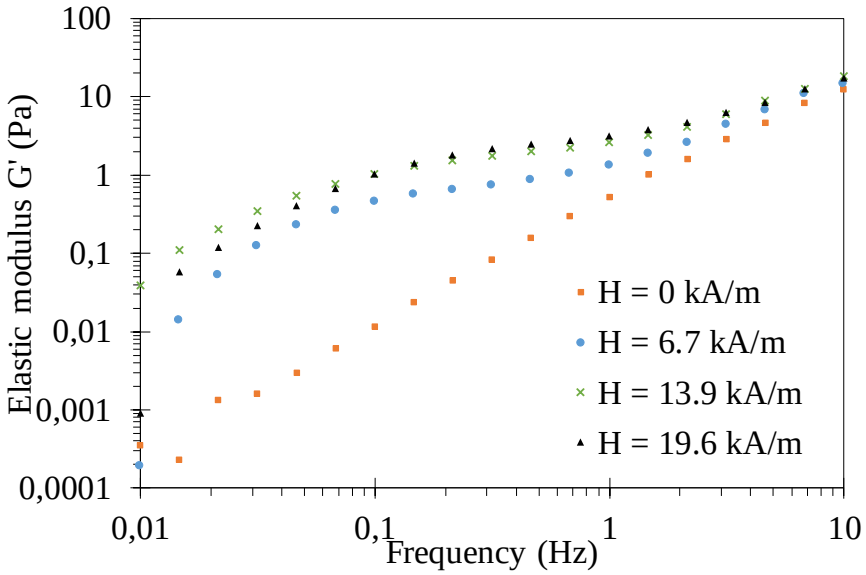

Figure 31: evolution of the elastic moduli as function of frequency without and with applied magnetic field of different values for the nanocomposites sodium alginate (18 g/L) + citrated-MNPs (Φ_{MNPs} = 1%).

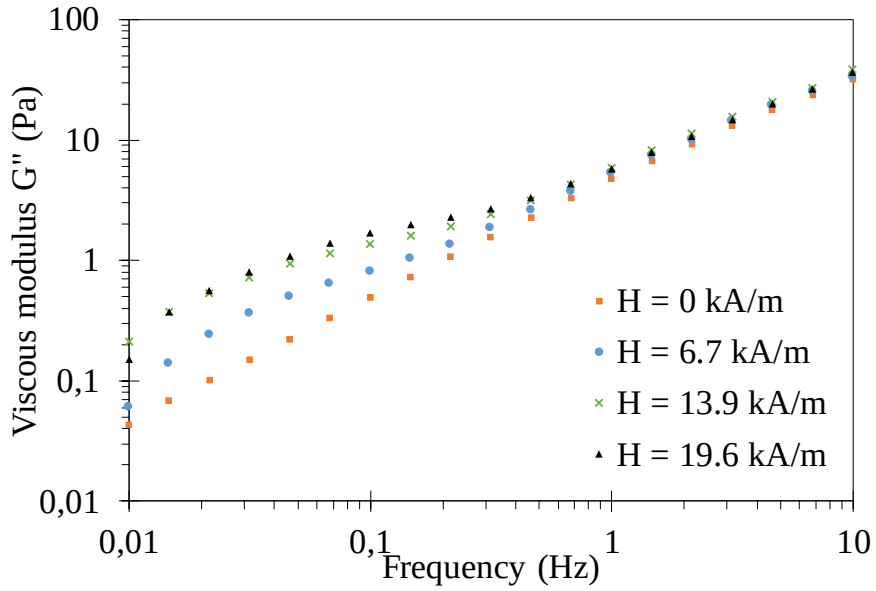

Figure 32: evolution of the viscous moduli as function of frequency without and with applied magnetic field of different values for the nanocomposites sodium alginate (18 g/L) + citrated-MNPs (Φ_{MNPs} = 1%).

3.3.5. Structural study by SAXS

SAXS experiments are performed on the SWING beamline (SOLEIL synchrotron, Saint-Aubin, France) with a photon energy of 12 keV and a sample-to-detector (Eiger 4M) distance of 6 m leading to the following q-ranges: $0.001 \leq q\ (Å^{-1}) \leq 0.19$. The studied samples are sodium alginate aqueous solution at 18 g/L, aqueous dispersions of citrated-MNPs with three volume fractions ((Φ_{MNPs} = 0.01, 0.1 and 1% v/v)) and nanocomposites with C_{Alg} = 18 g/L and three volume fractions ((Φ_{MNPs} = 0.01, 0.1 and 1% v/v)) in addition to a measurement of pure water. All of them were inserted into cylindrical quartz capillaries of 1.5 mm diameter that were sealed and left vertical in the field of gravity. Then, ten successive frames of 0.5 s each were recorded and compared to check the absence of beam damage. Each frame was first angularly averaged over all frames and the pure water spectrum was subtracted to obtain the presented results.

The results for citrated-MNPs shown in the Figure 33 show a good superposition when they are normalized by Φ_{MNPs} indicating a macroscopically homogeneous dispersion of MNPs. The characteristic exponent of -4.4 for the scaling law at high q-values it is close to -4, the characteristic value for spherical particles. The distinct peaks observed in the Kratky plot, $I(q)*q^2$ vs. q plot, are indicative of compact nanoparticles. The q-value at the maximum of the peak (q_{max}) represents the most probable interparticle distance ($d_p = 2.\pi/q_{max}$) [13]. This most probable distance is much larger than the size of an individual MNPs determined by TEM (8.1±1.4 nm) and it is found to be independent of the volume fraction (Φ_{MNPs}).

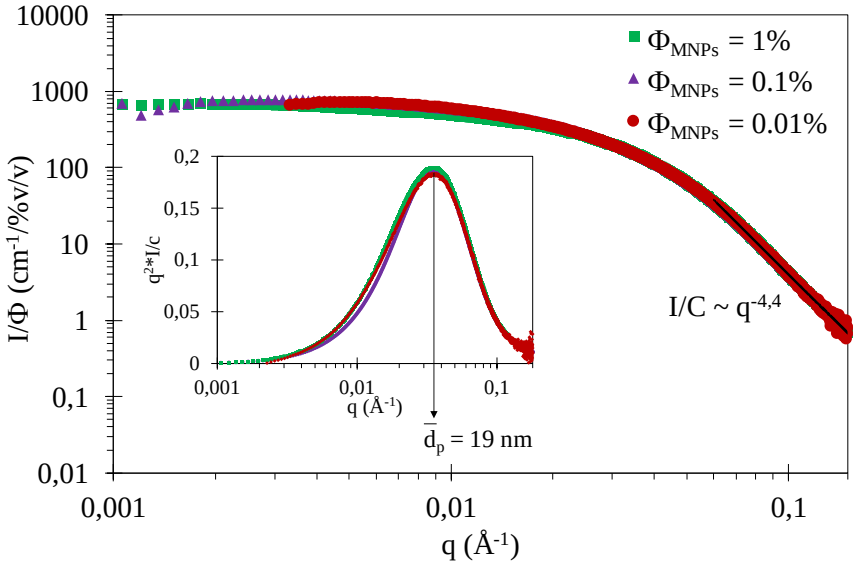

Figure 33: evolution of the scattered intensity normalized by Φ_{MNPs} as function of the vector q for citrated-MNPs in pure water at different volume fraction. The Kratky plot to determine the characteristic size is shown in the insert.

The results for nanocomposites sodium alginate (18 g/L) + citrated-MNPs at different volume fractions presented in the Figure 34 are similar to the ones of citrated-MNPs aqueous dispersions except at small q-values where an increase of the intensity is observed for nanocomposites and not in aqueous dispersions of citrated-MNPs. This could be related with an anisotropy due to the formation of droplets of demixion even if their sizes are bigger than the range of size related to the experimental q-range. These droplets of demixion shown in Figure 24 have a mean size of 3,3 µm while the lower q-limit of the experiment of $0.001 Å^{-1}$ corresponds with a size of 0.6 µm. However, this anisotropy is an indication that the formation of droplets of demixion takes place only in the presence of a sodium alginate and they are originated by colloidal forces other than magnetic forces. At intermediate q-values, the good superposition of all the curves indicates a macroscopically homogeneous dispersion of MNPs in the polymeric matrix in all the range of studied volume fractions (0.01 – 1 % v/v). At high q-values, the characteristic exponent of the scaling law depends on the volume fraction of MNPs. The refractive index of citrated-MNPs is much higher than the one of sodium alginate chains but, when Φ_{MNPs} = 0.01% the scattered light intensity from MNPs and sodium alginate are in the same order of magnitude. In these conditions the slope observed at high q-values corresponds with an intermediate value between that of sodium alginate (approximately -1.5 in chapter II Table 13) and that of citrated-MNPs (-4.4 in Figure 33). For the higher Φ_{MNPs}, the scattered intensity from the MNPs is much higher than the one coming from sodium alginate observing the characteristic exponent previously obtained for MNPs dispersions. The distinct peaks observed in the Kratky plot, $I(q)*q^2$ vs. q plot, are indicative of compact MNPs in the

nanocomposites. The distance between MNPs determined from the maximum of the peak ($d_p = 2.\pi/q_{max}$) remain the same in nanocomposites than in aqueous dispersions of MNPs.

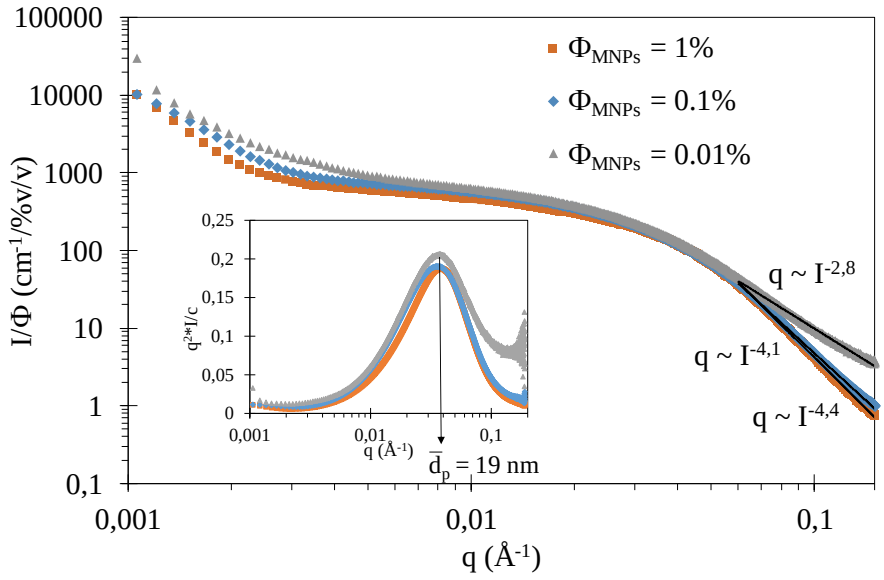

Figure 34: evolution of the scattered intensity normalized by Φ_{MNPs} as function of the vector q for the nanocomposites sodium alginate (18 g/) + citrated-MNPs with different Φ_{MNPs}. The Kratky plot to determine the characteristic size of is shown in the insert.

3.3.6. Conclusions

A second magnetic sensitive nanocomposite has been elaborated by introduction of negatively charged citrated-MNPs in aqueous solutions of sodium alginate. The formation of a microstructure of spherical droplets of demixion is evidenced by optical microscopy and it is attributed to an increase in the ionic strength when the dispersion of citrated-MNPs is added to the sodium alginate solution. Shear flow and viscoelastic properties at constant temperature of these composites have been investigated under applied magnetic field with the magneto-opto-rheology device showing an enhancement of the viscosity at low shear rate and the viscoelastic moduli in the linear viscoelastic domain (LVD). For such case, this behaviour is attributed to the deformation of the spherical droplets of demixion in the direction of the applied magnetic field perpendicular to the shear flow. The effect of both the concentration of sodium alginate (C_{Alg}) and the volume fraction of citrated-MNPs (Φ_{MNPs}) on the magnetoviscous effect have been evaluated obtaining that C_{Alg} = 18 g/L and Φ_{MNPs} = 1% are the most suitable concentrations for the elaboration of nanocomposites hydrogels with high magnetic sensitivity. Finally, SAXS measurements were performed. From the wave vector (q) dependence of the intensity, it was deduced a characteristic exponent representative of spherical MNPs at high q values while the formation of an anisotropy corresponding to the droplets of demixion is observed at low q

values. Moreover, from the Kraty plot (q^2*I vs q) it was deduced a most probable interparticle distance of 19 nm by the position of a peak.

3.4. PVA + citrated-MNPs

3.4.1. Introduction

The third studied nanocomposite is composed of a neutral polymer matrix of polyvinyl alcohol (PVA) and negatively charged citrated-MNPs. For such case it has been decided to use a higher polymer concentration (C_{PVA} = 100 g/L) to have an entangled solution with a shear thinning behaviour similar to a sodium alginate aqueous solution of 18 g/L. The volume fraction of MNPs chosen was Φ_{MNPs} = 0.5% since the dispersion of MNPs with a higher volume fraction in such concentrated PVA solution presents some difficulties leading to non-homogeneous mixtures.

3.4.2. Optical observation under applied magnetic field without shear stress

No microstructures have been found in such type of nanocomposites with the *in-situ* optical observation system installed in the magneto-opto-rheological device. We have then used the same home-made observation device (Figure 4) as for citrated-MNPs (paragraph 3.3.2) to obtain the images presented in Figure 35 without and with the application of a continuous magnetic field. Without magnetic field it is clearly observed a microstructure composed of spherical droplets of demixion very similar to those observed previously for sodium alginate + citrated-MNPs. Likewise, by application of a weak magnetic field (H = 6.7 kA/m) the droplets are deformed leading to a microstructure of highly elongated spheroid structures oriented in the direction of the applied field. The deformation of the droplets is completely reversible: when the magnetic field is switched off, the droplets recover their spherical shape. The image for H = 0 kA/m has been analysed with imageJ software determining the size of 200 droplets obtaining a mean size of 8.5 ± 4.3 μm. The higher mean and polydispersity of the droplet size distribution for PVA (Figure 36) than for sodium alginate nanocomposites could be attributed to the higher studied polymer concentration. The spheroid structures induced by application of magnetic field are also longer for the present case than for sodium alginate nanocomposites.

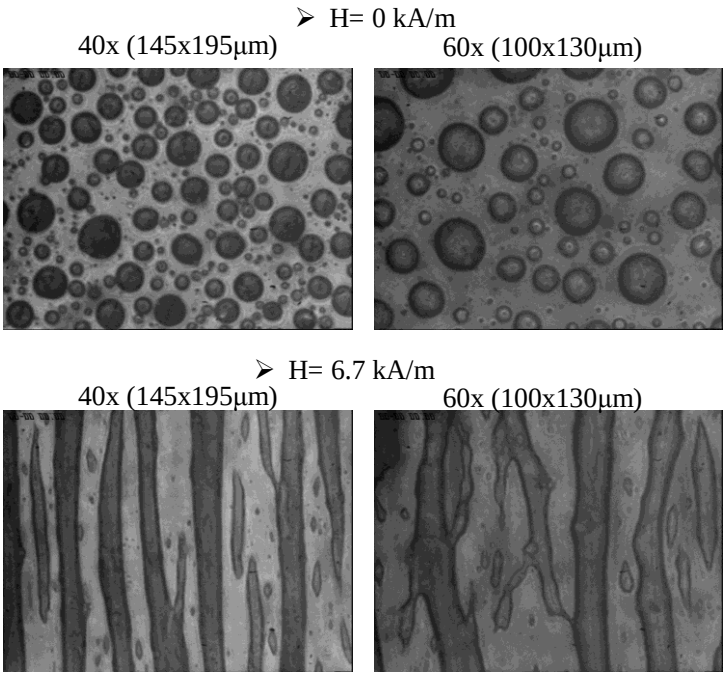

Figure 34: optical observation of nanocomposites of PVA (100 g/L) + citrated-MNPs (Φ_{MNPs} = 0.5%) with and without the application of a magnetic field.

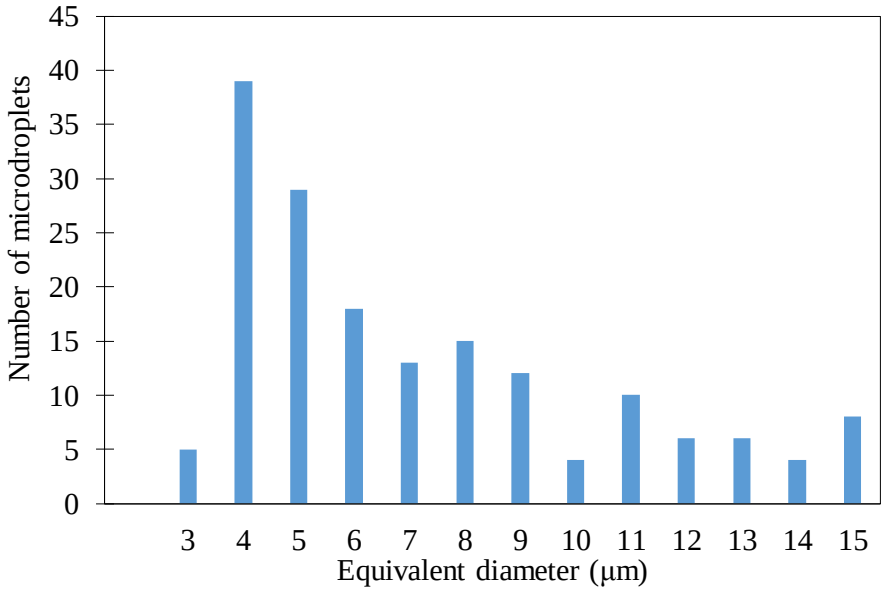

Figure 35: microdroplet size distribution for the nanocomposites of PVA (100 g/L) + citrated-MNPs (Φ_{MNPs} = 0.5%) without the application of a magnetic field.

3.4.3. Shear flow measurements

The steady-state flow curves without magnetic field and for different values of magnetic field are shown in Figure 37. It appears that the introduction of citrated-MNPs (H = 0 kA/m) increases the viscosity of PVA aqueous solution (PVA 100g/L) for shear rates lower than 100 s^{-1}. In case of sodium alginate, no difference was observed (Figure 27). By using the Batchelor equation (equation 1), we could expect that the increase of the suspension viscosity (η_s) is higher than the decrease of the solution viscosity (η_0) by the presence of PVA chains inside the

droplets. This could be explained by the bigger size of the droplets of demixion. Another possibility could be the presence of H bonds between hydroxyl groups of the citrated ions and PVA [15] and the H-bonds between PVA chains or PVA and water depending on the concentration of ions (citrate ions not adsorbed in the MNPs surface. By application of magnetic field, the increase of the shear viscosity becomes more pronounced as a result of the elongation of the droplets of demixion in the direction of the applied field perpendicularly to the shear. As well as for sodium alginate nanocomposites, this magnetoviscous effect decreases as function of the shear until a superposition of all the curves for shear rates higher than 100 s^{-1}probably due to the breaking of elongated droplets.

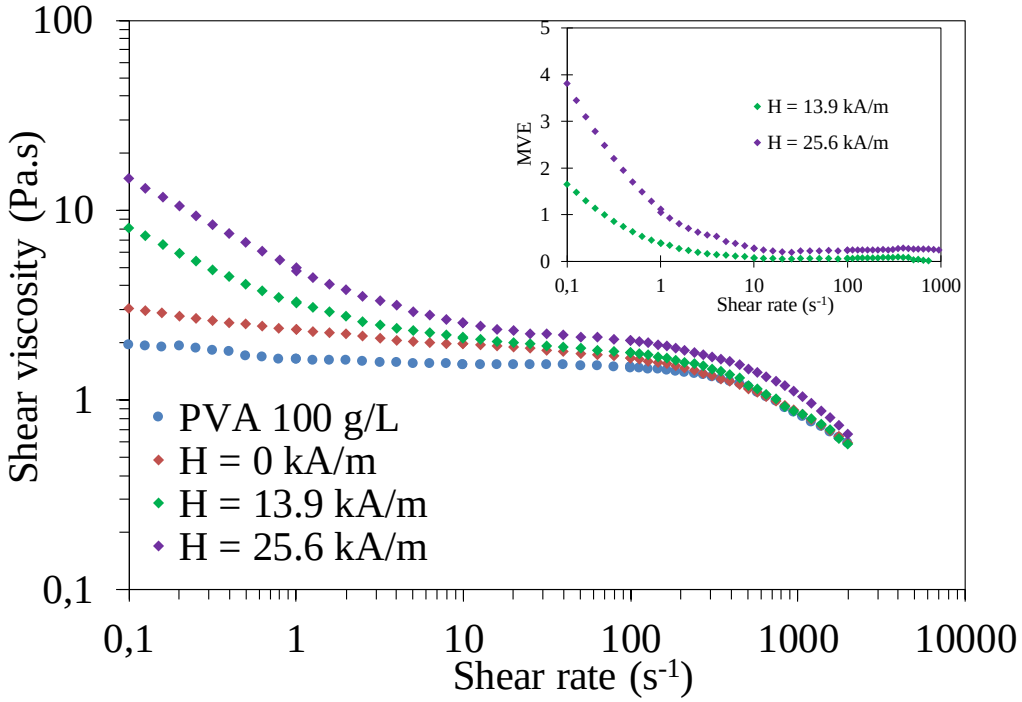

Figure 36: evolution of the viscosity as function of the shear rate during the application of different values of magnetic field for the nanocomposites PVA 100 g/L + citrated-MNPs Φ_{MNPs} = 0.5%. The shear rate dependence of the magnetoviscous effect is shown in the insert.

3.4.4. Conclusions

A third magnetic sensitive nanocomposite has been elaborated by introduction of negatively charged citrated-MNPs in aqueous solutions of neutral PVA. As in the sodium alginate solution, the formation of a microstructure of spherical droplets of demixion with a bigger diameter of 8.5 ± 4.3 μm is evidenced by optical microscopy. The viscosity of these composites at constant temperature has been investigated identifying a more important enhancement of the viscosity at low shear rate related with the bigger size of the droplets. The resultant magnetoviscous effect is comparable with this observed in sodium alginate

nanocomposites even if the volume fraction of citrated-MNPs is decreased to Φ_{MNPs} = 0.5% showing a promising magnetic sensitivity for the elaboration of nanocomposite hydrogels.

4. Conclusions

Three nanocomposite solutions have been prepared and studied by the introduction of maghemite MNPs either grafted with double ligands (APPA-MNPs) or stabilized by adsorption of citrate ions (citrated-MNPs) in a polyelectrolyte sodium alginate solution or in a neutral polymer PVA solution. The study of the flow, viscoelastic and structural properties of the different nanocomposites highlights the importance of the polymer-particle interactions and the relations between the microstructure and the magneto-induced enhancement of the viscoelastic properties. For the three studied nanocomposite, we have found that introduction of MNPs in polymer solutions (sodium alginate and PVA) lead to homogeneous nanocomposites on macroscopic scale while they are non-homogeneous on microscopic scale with the formation of spherical droplets of demixion for citrated-MNPs or aggregates between polymer chains and MNPs for APPA-MNPs. This could be explained by modification of ionic strength due to free citrated ions not absorbed on the surface of MNPs or by electrostatic attractions between the positively charged APPA-MNPs and negatively charged sodium alginate chains respectively.

The combined investigation of shear rheological measurements and optical observation allows to analyse flow and viscoelastic results under applied continuous magnetic field. In linear viscoelastic domains or low shear rates, spherical droplets of demixion are reversibly elongated or aggregates oriented in the direction of the applied magnetic field perpendicular to the shear flow inducing an enhancement of mechanical properties. When strains or shear rates are increased, these microstructures are progressively oriented in the direction of the shear before breaking as the shear rate effect predominates over the magnetic field. Taking into account that reversibility of field induced microstructure should be more favourable than dispersion of polydisperse aggregates in polymer solutions to develop nanocomposite hydrogels, citrated-MNPs are selected for the study of magnetic nanocomposite hydrogels.

5. References

[1] A. Shakouri, H. Ahmari, M. Hojjat, S.Z. Heris, Effect of TiO2 nanoparticle on rheological behavior of poly(vinyl alcohol) solution, J. Vinyl Addit. Technol. 23 (2017) 234–240. https://doi.org/10.1002/vnl.21502.

[2] W. Wu, T. Liu, H. He, X. Wu, X. Cao, J. Jin, Q. Sun, V.A.L. Roy, R.K.Y. Li, Rhelogical and antibacterial performance of sodium alginate/zinc oxide composite coating for

cellulosic paper, Colloids Surf. B Biointerfaces. 167 (2018) 538–543. https://doi.org/10.1016/j.colsurfb.2018.04.058.

[3] R. Yadav, R. Purwar, Influence of metal oxide nanoparticles on morphological, structural, rheological and conductive properties of mulberry silk fibroin nanocomposite solutions, Polym. Test. 93 (2021) 106916. https://doi.org/10.1016/j.polymertesting.2020.106916.

[4] C. Galindo-Gonzalez, A. Ponton, A. Bee, J. Chevalet, D. Talbot, R. Perzynski, E. Dubois, Investigation of water-based and oil-based ferrofluids with a new magnetorheological cell: effect of the microstructure, Rheol. Acta. 55 (2016) 67–81. https://doi.org/10.1007/s00397-015-0892-5.

[5] F. Ridi, M. Bonini, P. Baglioni, Magneto-responsive nanocomposites: Preparation and integration of magnetic nanoparticles into films, capsules, and gels, Adv. Colloid Interface Sci. 207 (2014) 3–13. https://doi.org/10.1016/j.cis.2013.09.006.

[6] S. Ghosh, I.K. Puri, Soft polymer magnetic nanocomposites: microstructure patterning by magnetophoretic transport and self-assembly, Soft Matter. 9 (2013) 2024–2029. https://doi.org/10.1039/C2SM27420E.

[7] G.A. Kloster, D. Muraca, O. Moscoso Londoño, M. Knobel, N.E. Marcovich, M.A. Mosiewicki, Structural analysis of magnetic nanocomposites based on chitosan, Polym. Test. 72 (2018) 202–213. https://doi.org/10.1016/j.polymertesting.2018.10.022.

[8] Y. Yang, L. Li, G. Chen, Static yield stress of ferrofluid-based magnetorheological fluids, Rheol. Acta. 48 (2009) 457–466. https://doi.org/10.1007/s00397-009-0346-z.

[9] Noorjahan, S. Pathak, K. Jain, R.P. Pant, Improved magneto-viscoelasticity of cross-linked PVA hydrogels using magnetic nanoparticles, Colloids Surf. Physicochem. Eng. Asp. 539 (2018) 273–279. https://doi.org/10.1016/j.colsurfa.2017.12.011.

[10] H. Eslami, M. Grmela, M. Bousmina, Linear and nonlinear rheology of polymer/layered silicate nanocomposites, J. Rheol. 54 (2010) 539–562. https://doi.org/10.1122/1.3372720.

[11] J. Xu, S. Chatterjee, K.W. Koelling, Y. Wang, S.E. Bechtel, Shear and extensional rheology of carbon nanofiber suspensions, Rheol. Acta. 44 (2005) 537–562. https://doi.org/10.1007/s00397-005-0436-5.

[12] F. Du, R.C. Scogna, W. Zhou, S. Brand, J.E. Fischer, K.I. Winey, Nanotube Networks in Polymer Nanocomposites: Rheology and Electrical Conductivity, Macromolecules. 37 (2004) 9048–9055. https://doi.org/10.1021/ma049164g.

[13] S. Roger, Y. Yip Cheung Sang, A. Bee, R. Perzynski, J. Meglio, A. Ponton, Structural and multi-scale rheophysical investigation of diphasic magneto-sensitive materials based on biopolymers, Eur. Phys. J. E Soft Matter. 38 (2015) 173. https://doi.org/10.1140/epje/i2015-15088-1.

[14] G.K. Batchelor, The effect of Brownian motion on the bulk stress in a suspension of spherical particles, J. Fluid Mech. 83 (1977) 97–117. https://doi.org/10.1017/S0022112077001062.

[15] M. Mousa, Y. Dong, The Role of Nanoparticle Shapes and Structures in Material Characterisation of Polyvinyl Alcohol (PVA) Bionanocomposite Films, Polymers. 12 (2020). https://doi.org/10.3390/polym12020264.

[16] B. Briscoe, P. Luckham, S. Zhu, The effects of hydrogen bonding upon the viscosity of aqueous poly(vinyl alcohol) solutions, Polymer. 41 (2000) 3851–3860. https://doi.org/10.1016/S0032-3861(99)00550-9.

Chapter V: magnetic nanocomposite hydrogels

1. Introduction

Hydrogels provide an excellent environment for cells due to their structural resemblance to the extracellular matrix [1] and good biocompatibility [2]. However, for a lot of biomedical applications their mechanical strength is too low [3]. A very useful and effective strategy to control and to improve the mechanical properties is to introduce magnetic nanoparticles (MNPs) in the hydrogels leading to a magnetic sensitivity that allows to modulate the mechanical properties. These magnetic sensitive composites materials show a rapid response time, high penetration and low invasiveness compared to other external stimuli-sensitive materials [4].

One of the key-points in the development of such materials is the state of MNPs dispersion, which is determined by the competition between particle-particle interactions and particle-polymer interactions [5]. The effect of these interactions between MNPs functionalized with different organic ligands and dispersed in the polymer solution were studied in the chapter IV selecting citrated-MNPs for the study of magnetic nanocomposites. Following, the crosslinking of those nanocomposite solutions has to be studied in order to elaborate the nanocomposite hydrogels [6]. The effect of different experimental parameters on the crosslinking of calcium alginate and PVA hydrogels has been studied in the Chapter III that allow to modulate the elaboration and final properties of the hydrogels without MNPs. However, the introduction of MNPs could affect the characteristic of the formed networks.

Thus, the aim of this chapter is to study the crosslinking of the nanocomposite solutions of chapter IV using the different crosslinking methodologies studied in the chapter III for the elaboration of calcium alginate and PVA nanocomposite hydrogels respectively. The sol-gel transition is firstly studied to evaluate the effect of the introduction of MNPs on the kinetics and properties of the formed networks. The effect of the application of the magnetic field on the sol-gel transition has been studied in two selected hydrogel nanocomposites. Finally, the mechanical properties of the totally gelled nanocomposites are evaluated by oscillatory shear rheology and uniaxial compression tests and swelling properties are also investigated.

2. Elaboration of nanocomposite hydrogels

Nanocomposite hydrogels have been elaborated based on the results obtained on nanocomposite solutions (Chapter IV) and on polymer hydrogels (Chapter III). In a general way, the experimental protocol consists in the elaboration of a pre-gel system in which citrated-MNPs have been carefully dispersed followed by the activation of the crosslinking mechanism either by the addition of GDL for calcium alginate or by the application of freezing/thawing cycles for PVA.

2.1. Calcium alginate nanocomposite hydrogels

For the elaboration of calcium alginate nanocomposite hydrogels, sodium alginate has been crosslinked with bivalent calcium either by the addition of a calcium carbonate ($CaCO_3$) salt or the ethylenediaminetetraacetic acid – calcium chloride (EDTA-$CaCl_2$) complex solution. For both cases an alginate concentration of 18 g/L and the three ratios $R_{ca} = [Ca^{2+}]/[COO^-]$ = 0.2, 0.3 and 0.4 has been selected accordingly with the conclusions of chapter III. The elaboration can be schematically divided in three steps (Figure 1). Firstly, the source of calcium is dispersed in the sodium alginate solution. Secondly, the citrated-MNPs were added in the form of a concentrated aqueous ferrofluid and dispersed by mechanical agitation. Finally, a freshly prepared Glucono-delta-lactone (GDL) solution with the ratio $([GDL])/[Ca^{2+}] = 2$ is added to induce the Ca^{2+} release and initiate the ionic crosslinking. Afterwards, the freshly prepared sample has been either loaded on the rheometer to study the sol-gel transition or placed in a sealed petri dish to obtain a totally gelled sample.

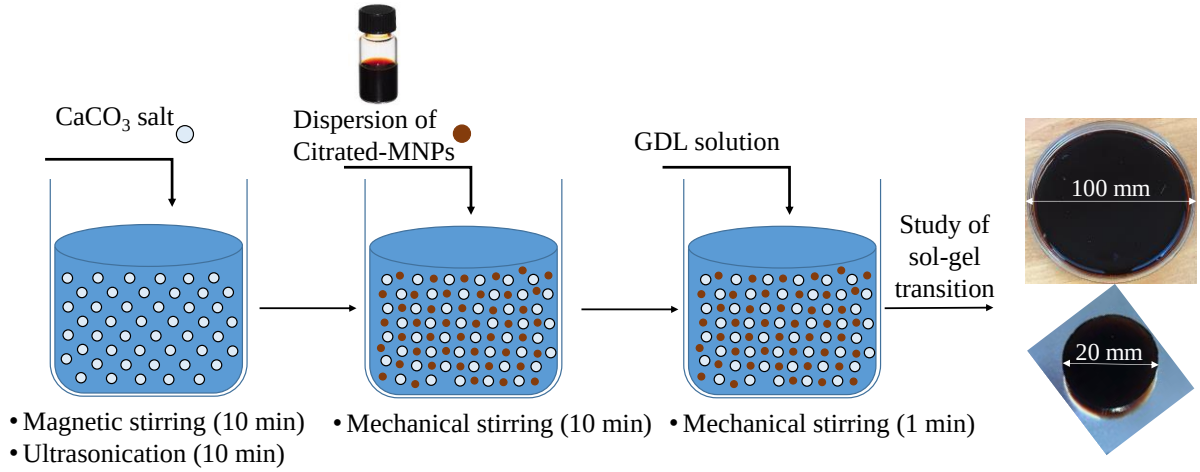

Figure 1: schematic representation of the elaboration of calcium alginate nanocomposite hydrogels.

2.2. PVA nanocomposite hydrogels

According to previous results, 40 g of PVA aqueous solutions (C_{PVA} = 100 g/L) containing citrated-MNPs (Φ_{MNPs} = 0.5 %) have been placed in a sealed petri dish after mixing

by mechanical stirring during 10 minutes (Figure 2). Then freezing (-22ºC during 16 h) and thawing (25ºC during 8 h) cycles have been performed three times successively. Consequently, only totally gelled state has been investigated.

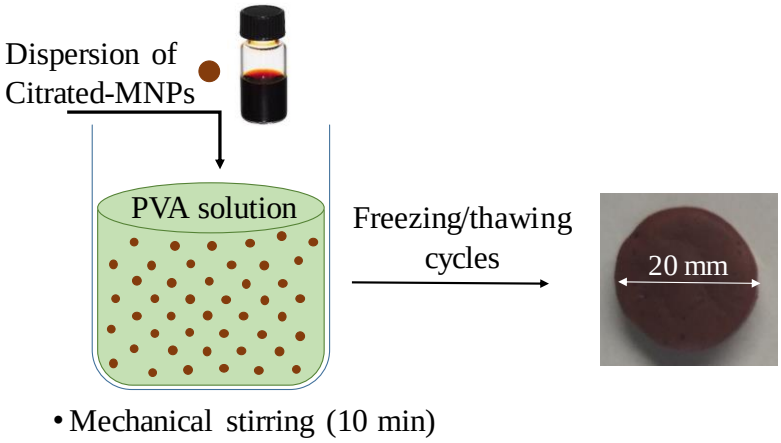

Figure 2: schematic representation of the elaboration of PVA nanocomposites hydrogels

3. Study of the sol-gel transition for calcium alginate nanocomposites

3.1. Experimental

The sol-gel transition has been investigated by time-resolved mechanical spectroscopy (TRMS) as previously described in chapter III. Firstly, citrated-MNPs have been introduced in different calcium alginate matrices to select the better experimental conditions. Then, the magneto-opto-rheological device has been used to study the effect of the application of a continuous magnetic field between 0 and 13.9 $kA.m^{-1}$ with specific selected experimental conditions. The Winter's method has been already validated for such types of systems consisting in crosslinking polymer with incorporated fillers of different nature [7,8] but to the best of our knowledge, it is the first time that it is used during the application of a magnetic field.

3.2. Effect of volume fraction of MNPs (Φ_{MNPs})

3.3.1. Introduction

Both sources of calcium are evaluated with a fixed molar ratio (R_{Ca} = 0.4) since the lower values of R_{Ca} were discarded in view of the observed longer gelation times. The selected volume fractions of citrated-MNPs are Φ_{MNPs} = 0.5% and Φ_{MNPs} = 1 %.

3.3.2. EDTA-$CaCl_2$ complex solution

The results of the analysis of the sol-gel transition by the methodology presented in the Chapter III paragraph 3.3.1. are summarized in Table 1. The clearest effect of the presence of

citrated-MNPs is the decrease of the gelation rate as Φ_{MNPs} is increased observed by an increase of the induction time (t_i), the G'-G" crossover time (t_c) and gelation time (t_g). The three characteristics times increase with similar tendencies whit the increase of Φ_{MNPs}. This could be explained by a decrease of the rate of Ca^{2+} release controlled by the pH dependent chelation stability of EDTA-$CaCl_2$ and the pH decrease induced by the progressive hydrolysis of GDL. To prove if the introduction of citrated-MNPs has a direct effect on the pH decrease, the time-evolution of the pH has been measured just after the addition of GDL (Figure 2) with and without MNPs. It is clearly observed that the presence of citrated-MNPs changes the pH decrease reaching in 3 hours to a pH = 5.5 while in their absence is reached pH = 4.6.

Table 1: results of the study of the sol-gel transition of nanocomposites with C_{alg} = 18 g/L with $CaCl_2$-EDTA complex solution R_{Ca} = 0.4 and different volume fraction of citrated-MNPs.

Φ_{MNPs} (%)	t_i (s)	t_c (s)	G'$_c$ (Pa)	G'$_\infty$ (Pa)	t_g (s)	Δ	S (Pa.s$^\Delta$)
0	857±20	1271±20	6.4±1.2	622±50	1085±20	0.73±0.02	0.40±0.05
0.5	2664±20	3511±20	9.0±0.5	596±50	3150±50	0.71±0.03	0.63±0.04
1	9140±50	12830±50	8.3±0.1	91±10	11220±50	0.72±0.01	0.55±0.02

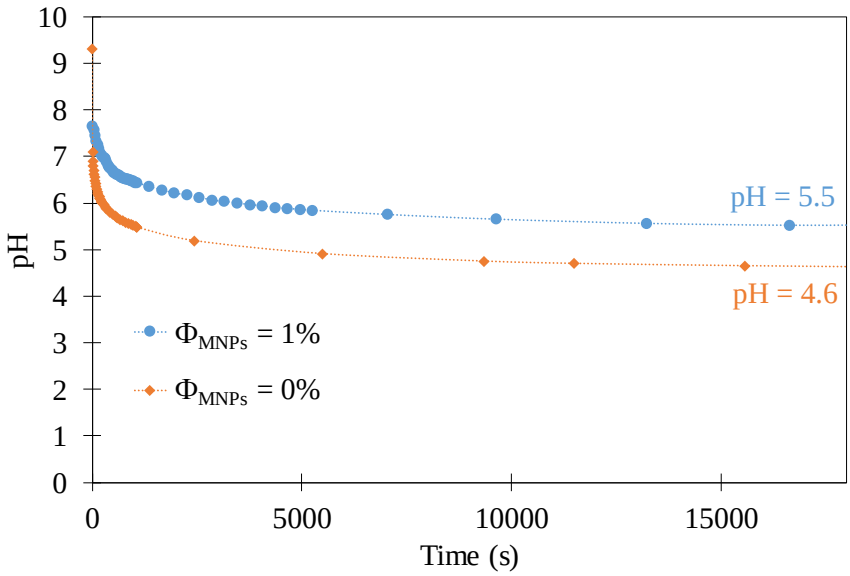

Figure 3: evolution of pH after addition of GDL in nanocomposite alginate hydrogels with Φ_{MNPs}=1% in comparison with alginate hydrogels.

The introduction of the MNPs has also a slight influence on the properties of the critical gel. The value of Δ remains practically constant in a value close to the one estimated by the percolation theory (Δ=0.71) maintaining the universality of Δ for all the calcium hydrogels prepared with the $CaCl_2$-EDTA complex independent of R_{Ca} (chapter III paragraph 3.5) and Φ_{MNPs}. The value of S is slightly higher for nanocomposites than for hydrogels. This could be explained by the presence of the microstructure of droplets of demixion that contributes to a

slightly increase of the viscoelastic properties at the gel point. The value of $G'_{\infty,}$ that is a first estimation of the mechanical properties of the gelled system, seems to be independent of the properties of the critical gel and it clearly decreases with the addition of MNPs experimenting a most important drop with the higher volume fraction Φ_{MNPs} = 1%. This decrease could be related with a decrease of the released Ca^{2+} due to the effect of citrated-MNPs on the pH drop.

3.3.3. $CaCO_3$ salt

The results of the TRMS analysis presented in Table 2 show that addition of citrated-MNPs slows down the kinetics of the sol-gel transition with the $CaCO_3$ salt as well as for the nanocomposite hydrogels with EDTA-$CaCl_2$ complex solution, but, with some differences. For example, the gelation time is multiplied by around 3 (Φ_{MNPs} = 0.5%) and 10 (Φ_{MNPs} = 1%) for the complex while the factors are 1.3 (Φ_{MNPs} = 0.5%) and 5 (Φ_{MNPs} = 1%) for the $CaCO_3$ salt. This decrease in the gelation rate could be related as previously to the effect of the citrate ions on the Ca^{2+} release even if, in this case, the effect cannot be confirmed with the measurement of the pH since the dissolution of $CaCO_3$ takes place at a constant pH = 7.

Table 2: results of the study of the sol-gel transition of nanocomposites with C_{alg} = 18 g/L with $CaCO_3$ salt R_{Ca} = 0.4 and different volume fraction of citrated-MNPs.

Φ_{MNPs} (%)	t_c (s)	G'_c (Pa)	G'_∞ (Pa)	t_g (s)	Δ	S ($Pa.s^{\Delta}$)
0	420±20	8.5±1.6	1215±100	380±10	0.59±0.01	1.56±0.14
0.5	530±20	8.6±1.4	1260±100	525±10	0.63±0.02	0.93±0.11
1	2030±20	8.5±0.5	345±30	1870±25	0.67±0.03	0.86±0.15

The nanocomposites have values of Δ and S characteristic of a softer critical gels than the calcium alginate hydrogel prepared with the same conditions showing values of Δ closer to the one estimated by the percolation theory as the kinetics of gelation are slower. This effect is in good agreement with the previously observed effect of R_{Ca} (chapter III paragraph 3.5) leading to softer critical gels for lower R_{Ca} corresponding with slower gelation rates. Likewise, the deviation of the values of Δ from the value estimated by with the percolation model could be explained by a not totally homogeneous release of the Ca^{2+} that is more important as the rate of Ca^{2+} release is faster. Thus, the introduction of citrated-MNPs slows down the rate of Ca^{2+} release leading to a more random gelation with a critical gel with a behaviour closer to that predicted by the percolation model. Moreover, the introduction of citrated-MNPs has also an effect in the values of G'_∞ that seems to change independently of the critical gel properties. The

value of G'_∞ is not affected with Φ_{MNPs} = 0.5 % while Φ_{MNPs} = 1 % leads to an important decrease.

3.3.4. Conclusions

The addition of citrated-MNPs to elaborate calcium alginate nanocomposite hydrogels by ionic crosslinking has a noticeable effect on the sol-gel transition for both sources of calcium ($CaCl_2$-EDTA complex solution and the $CaCO_3$ salt). These changes were analysed carefully since they should have important implications in the microstructure and characteristics of the network of the nanocomposite hydrogels. For the case of the $CaCl_2$-EDTA complex solution, the gelation rate is strongly slowed down by the effect of the citrated ions of the MNPs on the pH decrease and therefore on the rate of Ca^{2+} release. However, this change on the kinetics does not have an important effect on the parameters Δ and S of the critical gel but it shows and important decrease of the mechanical properties at long time (G'_∞) mainly for the highest Φ_{MNPs} = 1%. For the case of the $CaCO_3$ salt, a less important decrease of the gelation rate is observed, but, showing a clear effect on the critical gel properties identified by the change on the parameters Δ and S characteristic of softer gels in the presence of citrated-MNPs. These changes of Δ and S are explained by the formation of more homogeneous and random gel structure when the gelation rate is decreased by the effect of the introduction of the citrated-MNPs. The possibility to control the critical gel properties modulating the gelation rate makes more interesting to continue with the study of magnetic nanocomposites with the $CaCO_3$ salt under the application of magnetic field. In addition, the increase of the gelation times by the addition of citrated-MNPs lead to more appropriate gelation times with this option while they are unnecessary long when the $CaCl_2$-EDTA complex solution is used as source of calcium. These advantages together with the stronger mechanical properties of the obtained hydrogels and the chemical simplicity motivate to continue with the study of calcium alginate nanocomposite hydrogels elaborated with the $CaCO_3$ salt

3.4. Effect of an applied magnetic field

3.4.1. Experimental

As discussed in the Chapter IV, the application of a magnetic field modifies the viscoelastic properties of these kind of nanocomposites in sol state due to the elongation in the direction of the field of a microstructure composed of droplets of demixion (Chapter IV paragraph 3.3). Thus, the purpose of this study is to evaluate if this magneto-induced structural modification has some effect on the sol-gel transition and therefore on the obtained properties

of the nanocomposite hydrogels. After all the previous studies, the selected samples for this analysis are calcium alginate nanocomposite hydrogels prepared with the $CaCO_3$ salt at R_{Ca} = 0.4 and two volume fractions of MNPs (Φ_{MNPs} = 0.5% and Φ_{MNPs} = 1%). For the selected samples, three values of a continuous and homogenous magnetic field of 2.6, 6.7 and 13.9 kA/m have been applied perpendicularly to the shear stress during independent TRMS studies of the sol-gel transition.

3.4.2. Results

A preliminary analysis is performed by plotting the time evolution of the viscoelastic moduli G' and G" (Figure 4) at a fixed frequency (1 Hz). An enhancement of G' before crossover of both moduli (t_c) is clearly observed by the application of magnetic field that could be explained by the deformation of droplets of demixion along the direction of magnetic field as observed in nanocomposite solutions (Chapter IV paragraph 3.3). For $t > t_c$ we could expect that the deformation of droplets is hindered by the three-dimensional network of the hydrogel leading to not clear effects of the magnetic field on G' and G". The results for a magnetic field of 13.9 kA/m are not presented here since the magnetic effect is enough strong to change the material at the initial state into a viscoelastic solid hindering the observation of another sol-gel transition induced by the crosslinking with Ca^{2+}. For the other volume fraction, Φ_{MNPs} = 0.5 %, similar magnetic effects but considerably weaker due to lower content of MNPs have been found that are not shown here for brevity.

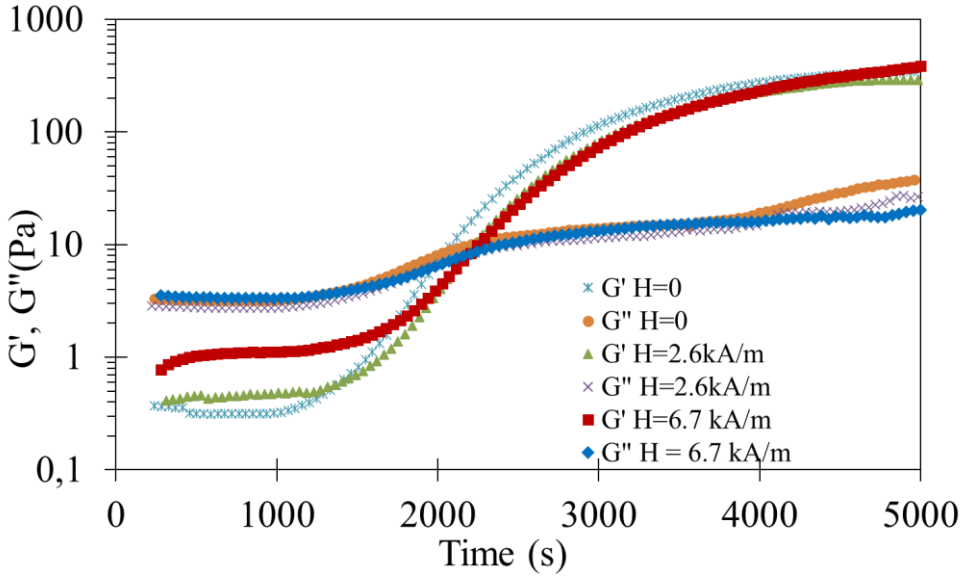

Figure 4: evolution of G' and G" as function of time for a f = 1 Hz for alginate nanocomposite hydrogels Φ_{MNPS}=1% during the application of magnetic field of different values.

The analyses of the TRMS experiment have been performed applying the methodology presented in the chapter III Figure 4. The different parameters obtained are presented in Table

3 for both volume fractions (Φ_{MNPs}=0.5% and Φ_{MNPs}=1%) and the different applied magnetic fields. In general lines the applied magnetic field has no clear effect of the parameters S and Δ of the critical gel even if the viscoelastic properties are enhanced before the gel point as it has been noted previously in Figure 4.

For a better understanding of the transformation before reaching the critical gel state, the evolution of G' and G" with the frequency are analysed at different times before the gel point. For such purpose it is defined the relative distance to the gel point, $\epsilon = (t_g-t)/t_g$. The evolution of G' ad G" with the frequency are represented in Figure 5 and 6 respectively for nanocomposites with R_{Ca}=0.4 and Φ_{MNPs} = 1% for the different ϵ between ϵ = 1 (initial sol-state) and ϵ = 0 (critical gel point). By fitting these curves to exponential laws ($G'\sim f^{\alpha}$ and $G''\sim f^{\beta}$), the apparent relaxation exponent of G' and G" are calculated as function of the distance to the gel point (ϵ). As presented in Figure 7, a decrease of both exponents which higher values for G' than for G" ($\alpha > \beta$) characteristic of a fluid viscoelastic behaviour is observed as function of the distance to the gel point where both achieve the same value $\alpha = \beta$ as physical characteristic defining the critical gel.

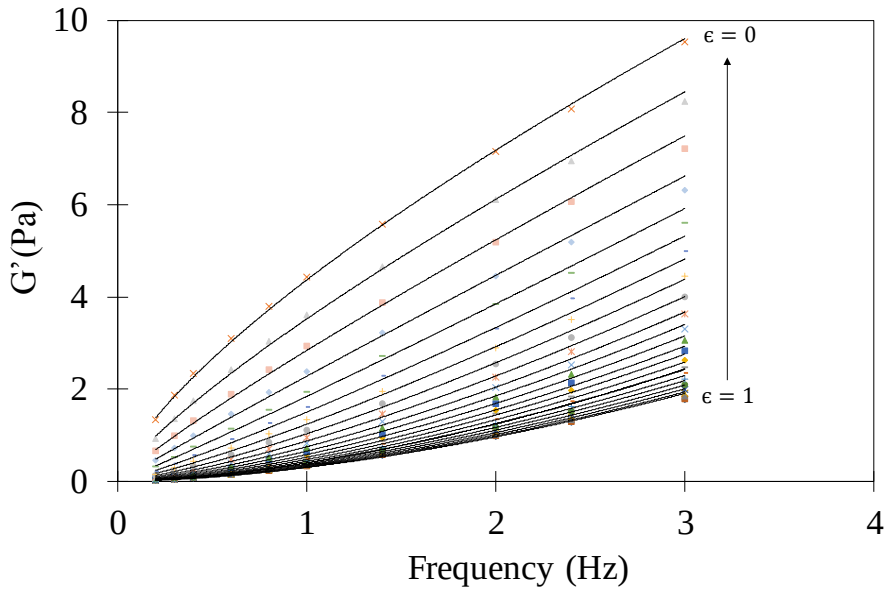

Figure 5: elastic modulus as function of the frequency at different relative distances to the gel point (ϵ) before the gel point for nanocomposite hydrogels with R_{Ca} = 0.4 and Φ_{MNPs} = 1%.

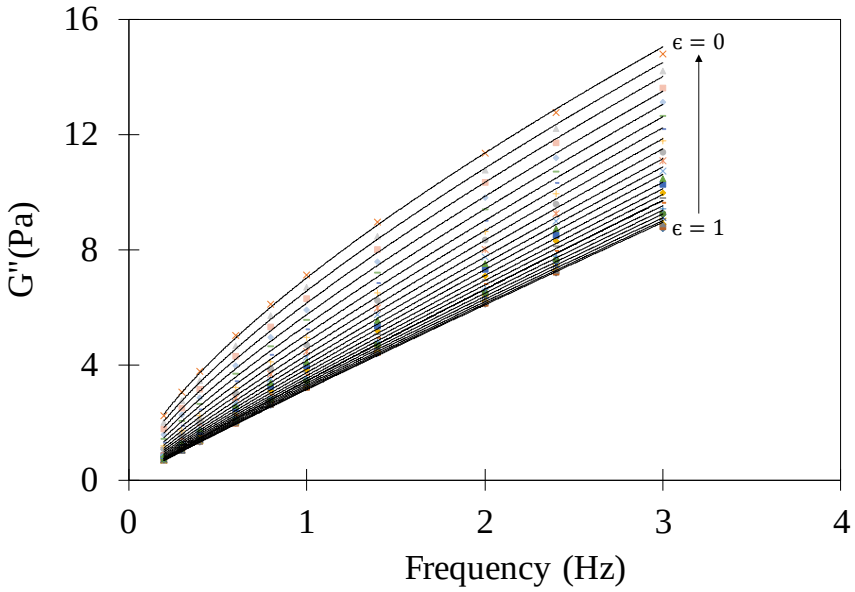

Figure 6: viscous modulus as function of the frequency at different relative distances to the gel point (ϵ) before the gel point for nanocomposite hydrogels with R_{Ca} = 0.4 and Φ_{MNPs} = 1%.

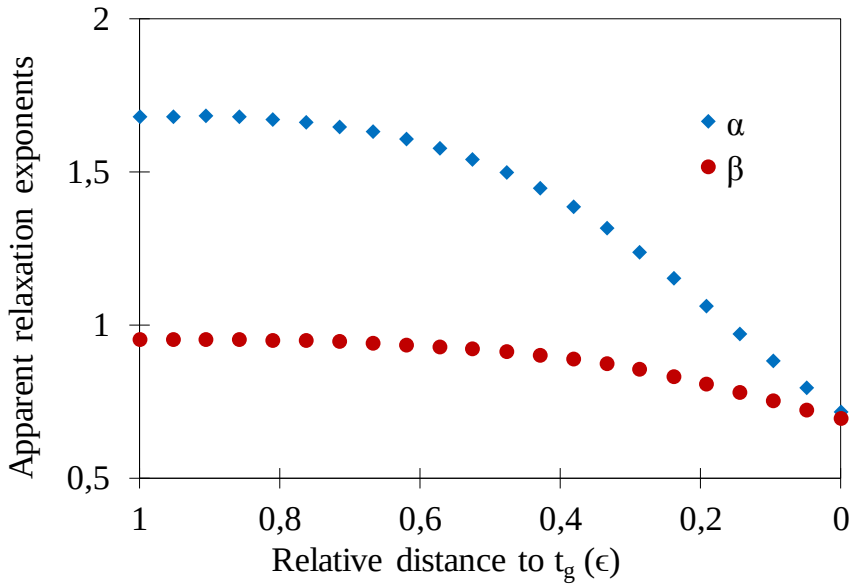

Figure 7: evolution of the apparent relaxation exponents determined from a power law fitting of G'(f) and G"(f) as function of the relative distance to the gel point (ϵ).

Considering the similar shape of the curves (Figures 5 and 6), a master curve could be built as proposed by Hodgson [7]. For this purpose, G′ and G″ are shifted vertically and horizontally by factors α_v and α_h depending on the relative distance to the gel point (ϵ). The parameters n and m are related to the critical exponent for the zero-shear viscosity (k) at $t<t_g$ and the critical exponent for the equilibrium modulus (z) at $t \geq t_g$. The critical exponent z is determined from the value of G' extrapolated to zero-frequency quenching the sol-gel transition by some authors [8]. For the present study we did not find a strategy for this determination of z since it is not possible to quench the sol-gel transition and the measurements of G' at lower frequencies require too long experimental time in comparison with the time-evolution of the

viscoelastic properties. Then, both z and k have been considered free parameters to obtain the better adjustment of the master curve.

$$\alpha_V = \left(\frac{\epsilon}{\epsilon_r}\right)^n \quad (1)$$

$$\alpha_h = \left(\frac{\epsilon}{\epsilon_r}\right)^m \quad (2)$$

$$n = -k \quad (3)$$

$$m = -(k + z) \quad (4)$$

where ϵ_r is the value of the relative distance to the gel point from which the master curve is built up. The good adjustment of the data, shown in Figure 8, confirms the self-similar structure of the nanocomposites leading to a master curve over at least 5 decades of frequency.

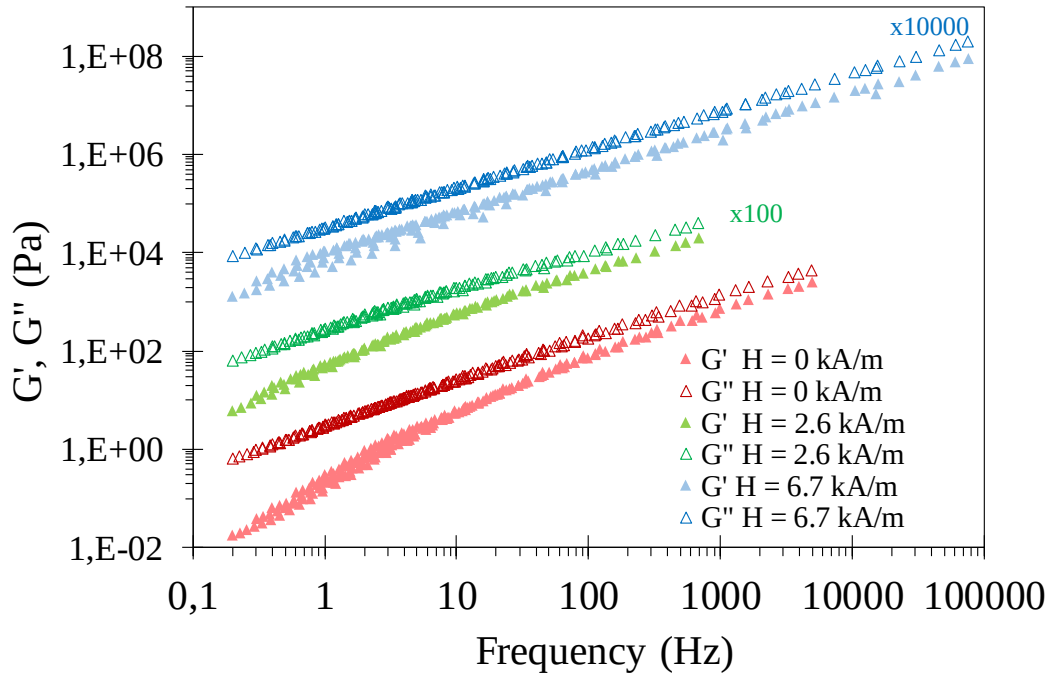

Figure 8: master curve of G' and G" of nanocomposites hydrogels with R_{Ca}=0.4 and Φ_{MNPs} = 1% merged from the shifting and superposition of data of G'(f) and G"(f) before the gel point (example in Figure 5 and 6) during the application of different magnetic field.

In addition, the adjustment with the shift factors (α_v, α_h) that depend on the physical parameters z and k allows to complete the characterization of the viscoelastic properties at the gel point. As well as the exponent Δ, the critical exponents z and k have been predicted based on different theoretical models [9]. For example, the Rouse limit without hydrodynamic interaction gives z = 2.7, and k = 1.35 and the Zimm limit with hydrodynamic interaction gives z = 2.7 and k = 0. The percolation model yields to z = 1.94, and k = 0.75. However, the universality of these exponents has been questioned by the several experimental values of k and z, for example for calcium alginate hydrogels [10]. The values of z and k adjusted to built the

master curves shown in Figure 8 are summarized in the Table 3. They are globally close to those proposed by the percolation model, z = 1.94 and k = 0.75. The main differences are found for the sample with the higher Φ_{MNPs} and H = 6.7 kA/m with higher values for both z and k. This discrepancy can be related with the clear increase of G' before the gel point observed in the Figure 4. In addition, postulating a symmetry of the divergence on both sides of the gel point leads to a relation between the critical exponents Δ, k, and z allowing to determine the value of the relaxation exponent by an alternative method than TRMS spectroscopy (Winter method). The values of Δ determined by this alternative methodology are slightly higher than the values determined by the Winter method.

$$\Delta = \frac{z}{k+z} \tag{5}$$

Table 3: results of the study of the sol-gel transition of nanocomposites with C_{alg} = 18 g/L with $CaCO_3$ salt R_{Ca} = 0.4 with two volume fractions of citrated-MNPs and during the application of different magnetic fields.

Φ_{MNPS}(%)	H (kA/m)	t_g (s)	Δ (Winter)	S (Pa.s$^{\Delta}$)	z	k	Δ
0.5	**0**	525±5	0.63±0.02	0.93±0.11	1.95	0.65	0.75
0.5	**2.6**	560±5	0.63±0.01	0.79±0.08	1.89	0.57	0.77
0.5	**6.7**	545±5	0.65±0.02	0.76±0.09	1.93	0.53	0.79
0.5	**13.9**	590±10	0.60±0.03	1.25±0.35	1.74	0.71	0.71
1	**0**	1870±25	0.67±0.03	0.86±0.15	1.89	0.55	0.78
1	**2.6**	1820±20	0.71±0.02	0.52±0.06	1.36	0.71	0.66
1	**6.7**	1850±50	0.72±0.02	0.52±0.10	2.80	1.00	0.74

3.4.3. Conclusions

The effect of an applied magnetic field on the sol-gel transition of calcium alginate nanocomposites hydrogels has been studied by time-resolved mechanical spectroscopy (TRMS) for first time with these concluding remarks: the application of a magnetic field allows to modulate the viscoelastic properties before the gel point. In particular an enhancement of the elastic modulus (G') is obtained (Figure 4) and a modification of the values of z and k to define the shift factors to build a master curve by merging the curves of G'(f) and G"(f) at different times before the gel point . However, these changes before the gel point have no effect on the kinetics of the sol-gel transition (t_g) and the parameters S and Δ of the critical gel since the characteristic of the sol-gel transition depends on the formed network and not on the magnetic-

sensitive microstructure since the droplets of demixtion are trapped in the hydrogel network. Therefore, it can be concluded that the applied magnetic field does not affect the mechanism of Ca^{2+} release that leads to the ionic crosslinking of the alginate chains that define the characteristics of the hydrogel network.

4. Characterization of totally gelled nanocomposites

4.1. Shear rheology

Oscillatory shear measurements were performed using MARS II rheometer with a plate and plate geometry of 20 mm of diameter. The gel disk was placed on the lower plate and the gap was selected manually to have a small compressive pre-load of 0.04N. Elastic G′ and loss G″ moduli were measured during the application of a sinusoidal strain sweep between 10^{-3} and 100 at a constant frequency (f = 1 Hz). Temperature was controlled on the lower plate by water circulation at 25.0± 0.1 °C. The viscoelastic properties as function of the strain amplitude have been investigated in order to identify the linear viscoelastic domain (LVD) of the calcium alginate and PVA nanocomposite hydrogels with fixed R_{Ca} = 0.4 and N_c = 3 respectively and two volume fractions of MNPs (Φ_{MNPs}=0.5% and Φ_{MNPs}=1%).

In the Figures 10 and 11 are presented the strain amplitude dependence of the elastic and viscous moduli in hydrogel and nanocomposite hydrogel disks. From these curves, critical strains (γ_c), mean values of the elastic modulus in the LVD (G'_{LVD}), strain at the peak of G" ($\gamma_{"}$) and maximum value of G" ($G"_{max}$) have been calculated and summarized in the Table 4. All the investigated samples have an elastic component (G') dominating over the viscous component (G") in the LVD confirming a solid viscoelastic gel network.

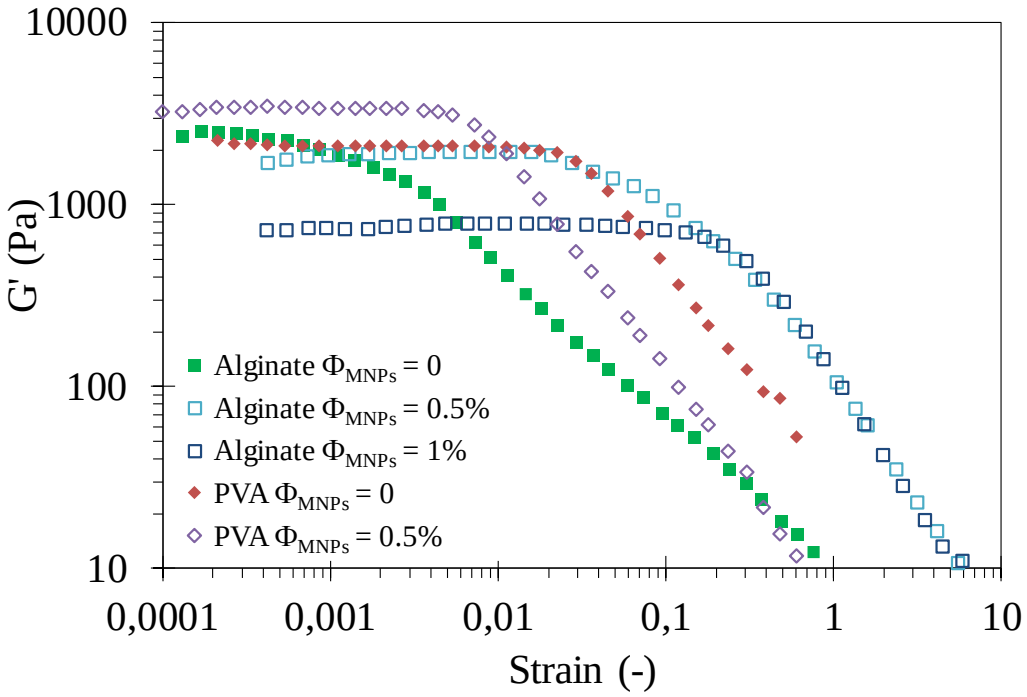

Figure 10: elastic modulus (G') as function of the strain amplitude for calcium alginate nanocomposite hydrogels with R_{Ca} = 0.4 and PVA nanocomposite hydroges with N_c = 3.

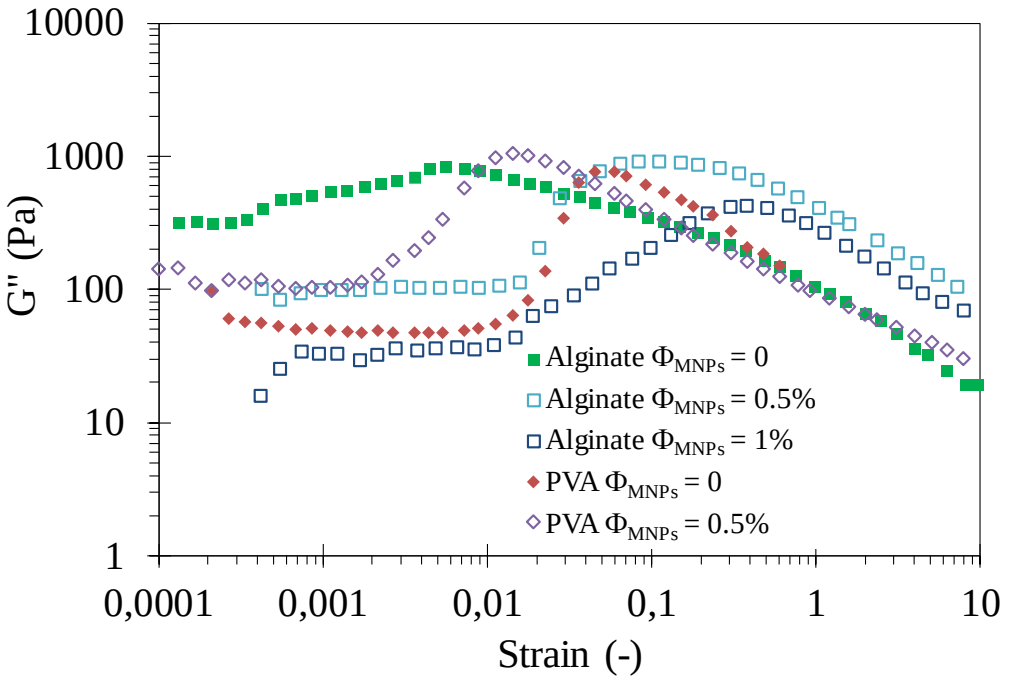

Figure 11: viscous moduli (G") as function of the strain amplitude for calcium alginate nanocomposite hydrogels with R_{Ca} = 0.4 and PVA nanocomposite hydrogel with N_c = 3.

For the case of calcium alginate, nanocomposite hydrogels show lower G'_{LVD} and G''_{max} and higher critical strains (γ_c and γ'') as Φ_{MNPs} is increased confirming the decrease of the mechanical properties observed in the previous study of the sol-gel transition (G'_∞ in Table 2). This is probably due to the electrostatic interactions between Ca^{2+} and the negatively charged citrate ions of the MNPs. The presence of a maximum peak for G" has also been observed in

other nanocomposites [11–13] and related with the energy dissipation due to the breakage of the gel like structure [12]. In the present case, the presence of a more important peak in G" in nanocomposites than in polymer hydrogels suggest that the presence of citrated-MNPs give rise to a microstructure that results in a higher resistance to the flow inside the sample in good agreement with the microstructure of droplets of demixion observed in nanocomposite solutions by optical microscopy (chapter IV Figure 23).

For the case of PVA, the introduction of citrated-MNPs shows a rather different effect with an increase of the viscoelastic moduli (G'_{LVD} and G''_{max}) and a decrease of the critical strains (γ_c and γ'') characteristic of a more rigid network. This is in good agreement with the results obtained for graphene oxide/PVA nanocomposites hydrogels [14]. This could be explained by the presence of a microstructure of droplets of demixion of bigger size (Chapter IV Figure 33). Other option is the same explanation that has been found for the enhancement of the viscosity in nanocomposites solutions due to the presence of H-bonds between hydroxyl groups of the citrated ions and the PVA chains [15].

Table 4: results of the analysis of strain sweep tests for calcium alginate nanocomposite hydrogels with R_{Ca} = 0.4 and PVA nanocomposite hydrogels with N_c = 3.

Sample	γ_c	G'_{LVD} (Pa)	γ''_{max}	G''_{max}(Pa)
Alginate Φ_{MNPs} = 0	0.0005	3940±200	0.006	835
Alginate Φ_{MNPs} = 0.5%	0.016	1853±100	0.08	920
Alginate Φ_{MNPs} = 1%	0.13	763±50	0.38	427
PVA Φ_{MNPs} = 0	0.023	2100±48	0.05	760
PVA Φ_{MNPs} = 0.5%	0.005	3328±74	0.014	1053

As conclusion, the addition of citrated-MNPs allows to modulate the viscoelastic properties of calcium alginate or PVA nanocomposites hydrogels. In the one hand, for alginate nanocomposites, the viscoelastic properties decrease by the addition of citrated-MNPs leading to more flexible networks. In the other hand, for PVA nanocomposites, the viscoelastic properties are enhanced by the addition of MNPs leading to more rigid networks.

4.2. Uniaxial compression

The stress-strain curves of uniaxial compression measurements (experimental protocol is described in chapter III paragraph 4.2.1) performed for identical samples than those studied by shear rheology are presented in Figure 12. The uniaxial compressive Young modulus (E) can be deduced as the slope by a linear fit. As observed in Figure 13, the previously studied viscoelastic properties and the compressive properties show similar trends. Adding citrated-

MNPs decreases the compressive Young modulus for alginate nanocomposites while for PVA nanocomposites, it increases in agreement respectively with the decrease or increase of the value of G'_{LVD} and G''_{max} determined by shear rheology. This correlation between shear and compression mechanical properties is usually obtained for such kind of nanocomposites [16,17].

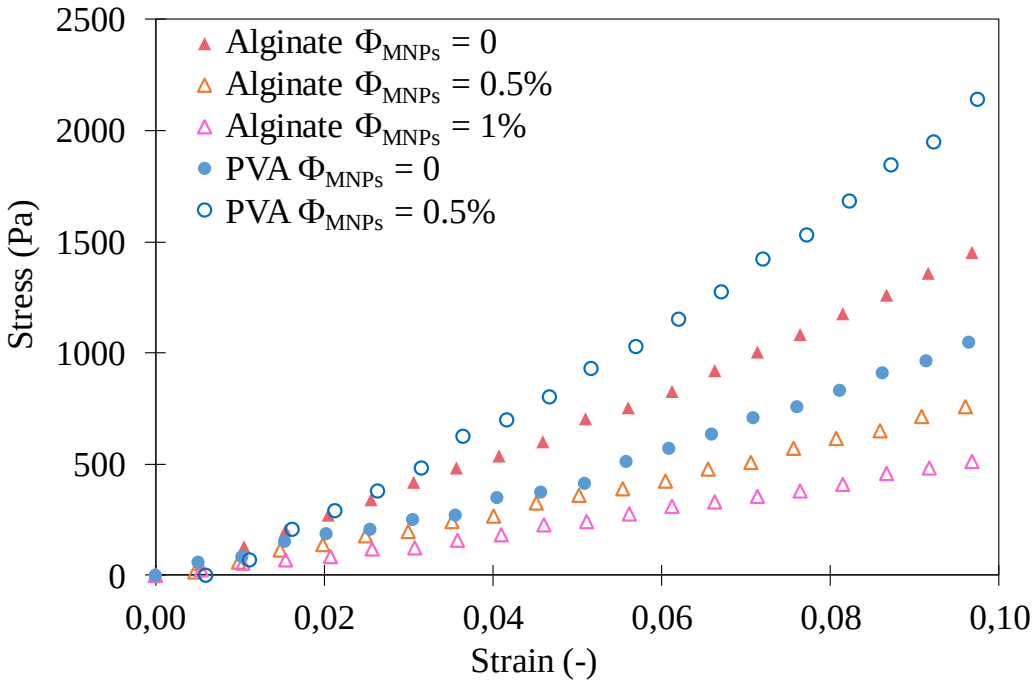

Figure 12: stress-strain curves for calcium alginate nanocomposite hydrogels with R_{Ca} = 0.4 and PVA nanocomposite hydrogel with N_c = 3.

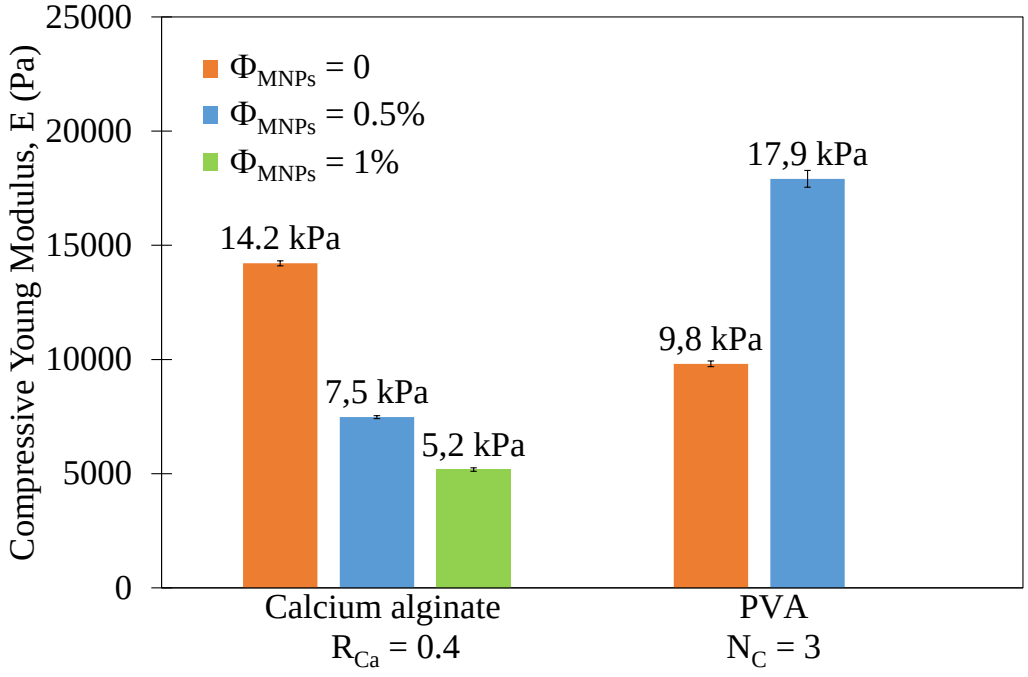

Figure 13: comparison of the compressive Young modulus calculated from the slope of the stress-strain curves in the linear region for nanocomposites and native hydrogels of alginate with R_{Ca} = 0.4 and PVA with N_c = 3.

4.3. Swelling

The time-evolution of the degree of swelling (experimental protocol in chapter III paragraph 4.2.2.) performed for identical samples than those studied by shear rheology and compression is presented in the Figures 14 and 15. For all studied samples, the degree of swelling increases fast during an initial step and it slows down to reach an equilibrium swelling state (Q_e). As well as for hydrogels in chapter III, the swelling kinetics are faster for calcium alginate nanocomposites (equilibrium achieved in ~ 3 hours) than for PVA nanocomposites (equilibrium achieved in ~ 12 hours) explained previously due to the higher hydrophilicity and the lower polymer concentration of the calcium alginate nanocomposite hydrogels. The experimental results are successfully adjusted by a first order model according to Chapter III – equation 4. By analyzing the effect of Φ_{MNPs} on the fit parameters shown in the Table 6, it is deduced an opposite effect of the addition of citrated-MNPs on the characteristics of the network for the two polymer matrices. For calcium alginate, the addition of citrated-MNPs leads to hydrogel networks with lower crosslinking degree as previously probed by the decrease of G'_{LVD} and E. In these conditions, the higher space for solvent adsorption and the weaker contraction forces against volume expansion explain the higher values of Q_e as well as higher values of absolute rate of water absorption estimated by $k*Q_e$. For PVA nanocomposites, the values of Q_e decrease in comparison with the PVA hydrogel confirming the contribution of citrated-MNPs to create a more rigid network with less space for solvent absorption in good agreement with the increases of G'_{LVD}, G''_{max} and E. Similar behaviour have been observed for other physically crosslinked nanocomposite hydrogels with TiO_2 [18] , clay [19] or graphen oxide [20] nanoparticles explained by the polymer-particle interactions such as the envisaged hydrogen bonds between hydroxyl groups of PVA and carboxylic groups of citrate ions in citrated-MNPs in the studied PVA nanocomposite hydrogels that prevent the water access.

Table 5: parameters from the adjustment of the swelling degree to a first order model for calcium alginate nanocomposite hydrogels with R_{Ca} = 0.4 and PVA nanocomposite hydrogels with N_c = 3.

Sample	Q_e(%)	k (h^{-1})	$k*Q_e$(%.h^{-1})
Alginate Φ_{MNPs} = 0	20.9	0.93	18.1
Alginate Φ_{MNPs} = 0.5%	41.7	1.21	50.5
Alginate Φ_{MNPs} = 1%	51.3	1.22	62.6
PVA Φ_{MNPs} = 0	18.4	0.131	2.4
PVA Φ_{MNPs} = 0.5%	4.8	0.503	2.4

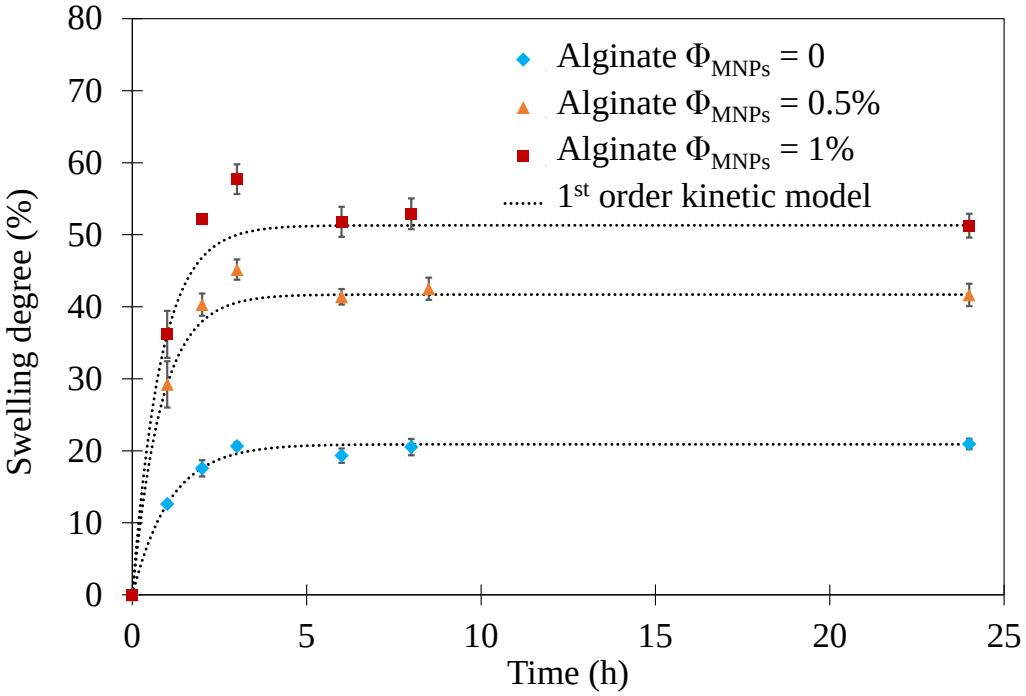

Figure 14: evolution of the swelling degree for calcium alginate nanocomposite hydrogels with R_{Ca} = 0.4 and different Φ_{MNPs}. The dashed lines correspond to the fitting of experimental data with the first-order kinetic model.

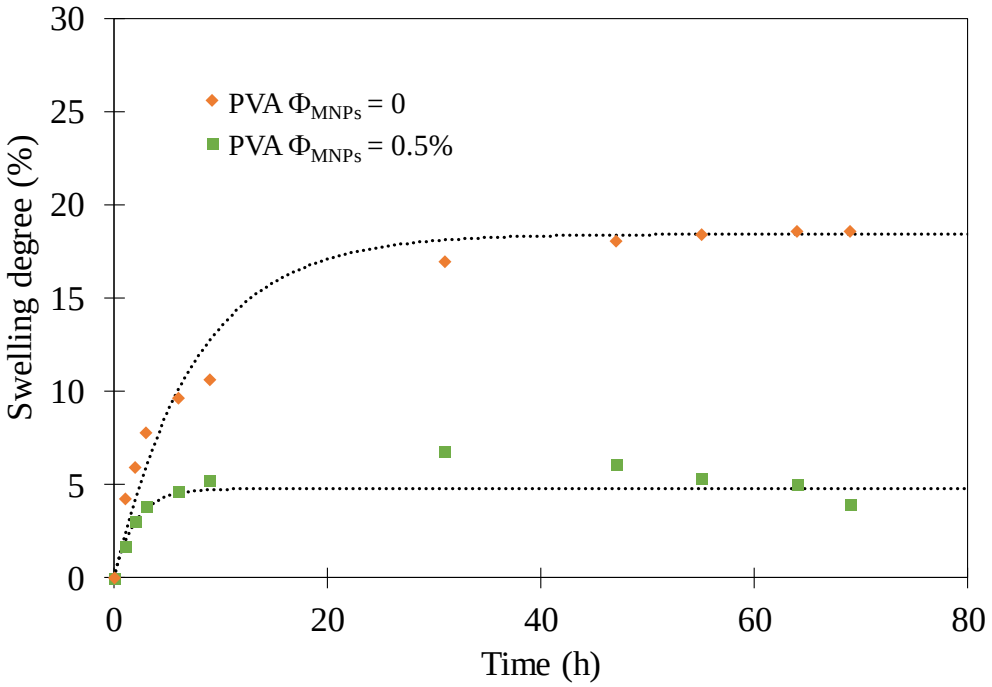

Figure 15: evolution of the swelling) for PVA nanocomposite hydrogels with N_c = 3. The dashed lines correspond to the fitting of experimental data with the first-order kinetic model.

4.4. Compression of swollen nanocomposites

The compressive properties of the nanocomposite hydrogels depend on their swelling state as it has been proved for polymer hydrogels in the chapter III. As well as for polymer hydrogels, nanocomposites show a significantly higher compressive Young modulus at the

swollen equilibrium (E_{sw}) than for as-prepared samples (E). The increase of the compressive modulus is correlated with the amount of absorbed water defined by the equilibrium swelling degree (Q_e). As it is shown in Figure 16, the higher Q_e leads to a more important increase of the compressive Young modulus in calcium alginate nanocomposite hydrogels while a smaller Q_e leads to a small increase of the modulus for PVA nanocomposites hydrogels.

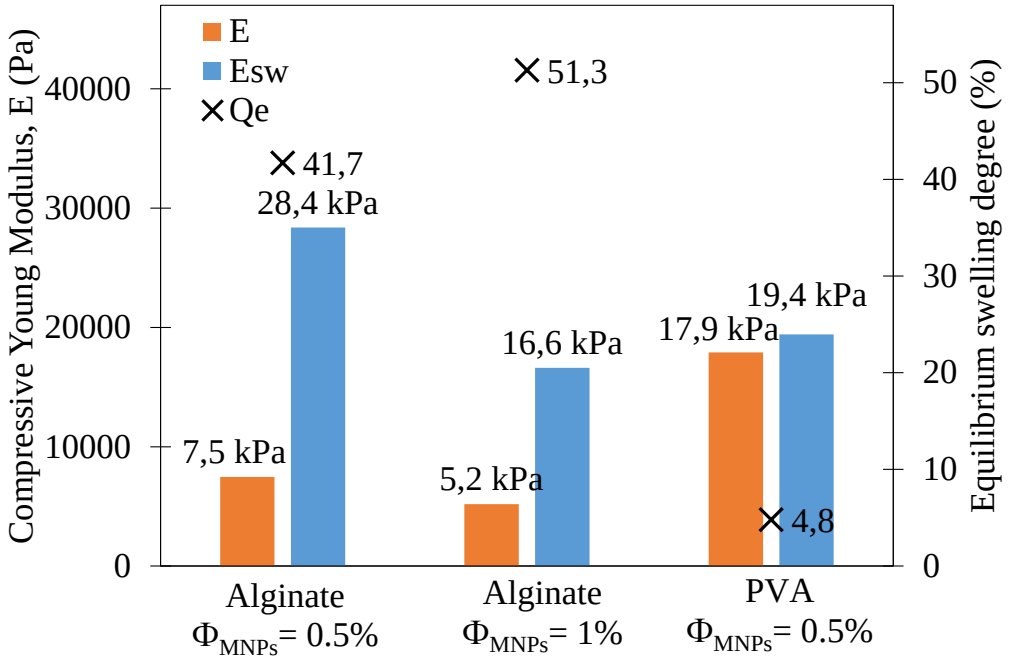

Figure 16: equilibrium swelling degree (Q_e) and compressive Young modulus of swollen in comparison to as-prepared calcium alginate (R_{Ca} = 0.) and PVA (N_c = 3) nanocomposite hydrogel.

4.5. Conclusions

The mechanical and structural study of the elaborated nanocomposite hydrogels allows to correlate the effect of the introduction of citrated-MNPs on the stiffness and porosity of the networks in comparison with the equivalent polymer hydrogels. The obtained results of shear viscoelastic properties, compressive Young modulus and swelling are all in good agreement showing an opposite effect of the introduction of citrated-MNPs in each of the studied polymer matrices. In the one hand, calcium alginate nanocomposite hydrogels show lower shear viscoelastic and compressive moduli and higher swelling capacity than the equivalent calcium alginate hydrogels confirming a lower crosslinking degree in good agreement with the previous study of the sol-gel transition. In the other hand, PVA nanocomposite hydrogels show higher shear viscoelastic and compressive moduli and lower swelling capacity in comparison with the equivalent PVA hydrogels confirming that polymer-particle interactions established by H-bonding increase the stiffness of the formed network.

5. Conclusions

The modulation of the final properties of the studied magnetic nanocomposite hydrogels has been obtained by the selection of different experimental parameters. The effect of the introduction of citrated-MNPs in calcium alginate hydrogels is firstly studied by time-resolved mechanical spectroscopy (TRMS) finding a noticeable slow down of the kinetics of the sol-gel transition for both sources of calcium ($CaCl_2$-EDTA complex solution and the $CaCO_3$ salt). In addition, softer critical gels and higher elastic modulus at long times (G'_∞) in the presence of citrated-MNPs leads to continue with the elaboration of magnetic nanocomposite with the $CaCO_3$ salt methodology. Then, the effect of an applied magnetic field on the sol-gel transition are studied by TRMS for first time finding that it allows to modulate the viscoelastic properties before the gel point but not the kinetics of the sol-gel transition and the parameters S and Δ of the critical gel since they depend on the characteristics of the formed network. Moreover, the mechanical and structural study of the previous calcium alginate and a new PVA nanocomposite hydrogel at the totally gelled state allow to correlate the effect of the introduction of citrated-MNPs on the final mechanical and structural properties of the networks. The obtained results of shear viscoelastic properties, compressive Young modulus and swelling are all in good agreement confirming a decrease of the stiffness and the crosslinking degree when citrated-MNPs are introduced in the calcium alginate matrix. In contrast, the introduction of citrated-MNPs in the PVA matrix leads to stiffer networks due the polymer-particle interactions due to H-bonding between PVA chains and citrated-MNPs.

6. References

[1] J. Rowley, G. Madlambayan, D. J. Mooney, Alginate Hydrogels As Synthetic Extracellular Matrix Materials, Biomaterials. 20 (1999) 45–53. https://doi.org/10.1016/S0142-9612(98)00107-0.

[2] A.D. Augst, H.J. Kong, D.J. Mooney, Alginate hydrogels as biomaterials, Macromol. Biosci. 6 (2006) 623–633. https://doi.org/10.1002/mabi.200600069.

[3] Q. Chai, Y. Jiao, X. Yu, Hydrogels for Biomedical Applications: Their Characteristics and the Mechanisms behind Them, Gels. 3 (2017) 6. https://doi.org/10.3390/gels3010006.

[4] X. Long, J. Ye, D. Zhao, S.-J. Zhang, Magnetogenetics: remote non-invasive magnetic activation of neuronal activity with a magnetoreceptor, Sci. Bull. 60 (2015). https://doi.org/10.1007/s11434-015-0902-0.

[5] W. Yu, J. Wang, W. You, Structure and linear viscoelasticity of polymer nanocomposites with agglomerated particles, Polymer. 98 (2016) 190–200. https://doi.org/10.1016/j.polymer.2016.06.028.

[6] N.S. Satarkar, D. Biswal, J.Z. Hilt, Hydrogel nanocomposites: a review of applications as remote controlled biomaterials, Soft Matter. 6 (2010) 2364–2371. https://doi.org/10.1039/B925218P.
[7] D.F. Hodgson, E.J. Amis, Dynamic viscoelastic characterization of sol-gel reactions, Macromolecules. 23 (1990) 2512–2519. https://doi.org/10.1021/ma00211a019.
[8] S. Liu, H. Li, B. Tang, S. Bi, L. Li, Scaling law and microstructure of alginate hydrogel, Carbohydr. Polym. 135 (2016) 101–109. https://doi.org/10.1016/j.carbpol.2015.08.086.
[9] H. Winter, M. Mours, Rheology of Polymers Near Liquid-Solid Transitions, in: Adv Polym Sci, 1997: pp. 165–234. https://doi.org/10.1007/3-540-68449-2_3.
[10] Lu, X. Liu, Z. Tong, Q. Gao, Critical Exponents and Self-Similarity for Sol-Gel Transition in Aqueous Alginate Systems Induced by in Situ Release of Calcium Cations, J. Phys. Chem. B. 110 (2006) 25013–25020. https://doi.org/10.1021/jp060155e.
[11] I. Marić, N.Š. Vujičić, A. Pustak, M. Gotić, T. Jurkin, One-step synthesis of poly(ethylene oxide)/gold nanocomposite hydrogels and suspensions using gamma-irradiation, Radiat. Phys. Chem. 170 (2020) 108657. https://doi.org/10.1016/j.radphyschem.2019.108657.
[12] T.C. dos Santos, R. Hernández, N. Rescignano, L. Boff, F.H. Reginatto, C.M.O. Simões, A.M. de Campos, C. Mijangos, Nanocomposite chitosan hydrogels based on PLGA nanoparticles as potential biomedical materials, Eur. Polym. J. 99 (2018) 456–463. https://doi.org/10.1016/j.eurpolymj.2017.12.039.
[13] G.C. Porter, D.R. Schwass, G.R. Tompkins, S.K.R. Bobbala, N.J. Medlicott, C.J. Meledandri, AgNP/Alginate Nanocomposite hydrogel for antimicrobial and antibiofilm applications, Carbohydr. Polym. 251 (2021) 117017. https://doi.org/10.1016/j.carbpol.2020.117017.
[14] Y. Lei, I. Boucenna, V. Thévenet, D. Dragoe, A. Ponton, Modulation of Viscoelastic and Absorption Properties of Poly(vinyl alcohol)-graphene Oxide Composites, ACS Appl. Polym. Mater. (2021). https://doi.org/10.1021/acsapm.1c00872.
[15] M. Mousa, Y. Dong, The Role of Nanoparticle Shapes and Structures in Material Characterisation of Polyvinyl Alcohol (PVA) Bionanocomposite Films, Polymers. 12 (2020). https://doi.org/10.3390/polym12020264.
[16] Z. Cai, J. Wu, M. Wu, R. Li, P. Wang, H. Zhang, Rheological characterization of novel carboxymethylated curdlan-silica hybrid hydrogels with tunable mechanical properties, Carbohydr. Polym. 230 (2020) 115578. https://doi.org/10.1016/j.carbpol.2019.115578.
[17] L. Yu, D. Wang, Y. Tan, J. Du, Z. Xiao, R. Wu, S. Xu, J. Huang, Super tough bentonite/SiO2-based dual nanocomposite hydrogels using silane as both an intercalator and a crosslinker, Appl. Clay Sci. 156 (2018) 53–60. https://doi.org/10.1016/j.clay.2018.01.026.
[18] L. Toledo, L. Racine, V. Pérez, J.P. Henríquez, R. Auzely-Velty, B.F. Urbano, Physical nanocomposite hydrogels filled with low concentrations of TiO2 nanoparticles: Swelling, networks parameters and cell retention studies, Mater. Sci. Eng. C. 92 (2018) 769–778. https://doi.org/10.1016/j.msec.2018.07.024.
[19] M.K. Jaiswal, J.R. Xavier, J.K. Carrow, P. Desai, D. Alge, A.K. Gaharwar, Mechanically Stiff Nanocomposite Hydrogels at Ultralow Nanoparticle Content, ACS Nano. 10 (2016) 246–256. https://doi.org/10.1021/acsnano.5b03918.
[20] Y. Huang, M. Zeng, J. Ren, J. Wang, L. Fan, Q. Xu, Preparation and swelling properties of graphene oxide/poly(acrylic acid-co-acrylamide) super-absorbent hydrogel nanocomposites, Colloids Surf. Physicochem. Eng. Asp. 401 (2012) 97–106. https://doi.org/10.1016/j.colsurfa.2012.03.031.

Chapter VI: biocompatibility of nanocomposites

1. Introduction

Tissue engineering is based on the manipulation of cells and their biochemical and biomechanical environments. For such purpose, one of the main topics is the use of a biocompatible hydrogel matrix to provide the mechanical stability in culture conditions and to enable the adherence of cells and their proliferation [1]. In addition, the introduction of MNPs with superparamagnetic properties allows to elaborate magneto-sensitive nanocomposites with mechanical and structural properties that can be controlled by the application of an external magnetic field. Some of the key properties of the proposed nanocomposites for these applications, such as the physicochemical structure, the porosity and the mechanical properties [1,2] have been already studied in the previous chapters. However, it seems mandatory to evaluate the interactions between the elaborated nanomaterials and biological entities in order to evaluate their biocompatibility.

Biocompatibility is the most commonly used term to describe appropriate biological requirements of a material used for biomedical applications [3] defined as the ability of an implant material to function *in vivo* without causing any adverse response. However, a classical first step to assess biocompatibility is to perform *in vitro* cytotoxicity tests since it is simpler and faster than *in vivo* animal testing. In the literature we can find numerous data on cytotoxicity of the materials used for the elaboration of nanocomposites, either MNPs [4] or polymers [5]. The results are quite variable depending in each specific case. For iron oxide MNPs, the biocompatibility strongly depends on the size, aggregation and functionalization. For the case of naturally occurring polymers, such as sodium alginate, the purity, and batch-to-batch reproducibility are critical factors.

In this context, the purpose of this chapter is the evaluation of the cytotoxicity of the elaborated nanocomposites to deduce some relations between their interactions with cells and the physico-chemical properties studied throughout this PhD. The outline of this chapter is the following. After the description of the methodologies required to perform cytotoxicity tests in a two-dimensional (2D) monolayer cell culture of mouse fibroblast NIH-3T3 cells, the different obtained results are presented and discussed following the order of the previous chapters: (1)

MNPs, (2) polymers, (3) nanocomposite solutions and (4) nanocomposite hydrogels. Finally, some conclusions are presented focused on the possible modifications of the different parameters studied for the elaboration of nanocomposites with improved biocompatibility.

2. *In vitro* cytotoxicity test

2.1. Experimental

2.1.1. Introduction

Cytotoxicity tests are performed in collaboration with the laboratory Biologie fonctionnelle et adaptative (BFA) (Université de Paris) on 2D monolayer cells using an experimental method that allows to measure the cellular metabolic activity. A general description of all the used protocols and procedures to perform these tests is presented below.

2.1.2. Sterile conditions

A set of laboratory procedures have been applied to avoid the contamination of the cell cultures with bacteria or microorganisms that are present in the air and in the human skin. The general rules applied following the guidelines of the experts of the BFA laboratory are listed below:

- Disposable gloves and clean laboratory coats must always be worn in cell culture laboratory and must not leave the laboratory.
- Work must only be carried out in a laminar flow tissue culture cabinet (work area) allowing to maintain an area free of particles, especially of possible contaminant agents that can access the cell culture.
- Work area must be properly disinfected before and after each use with 70% ethanol and ultraviolet (UV) light.
- Consumables including multi-well plates, Petri dishes, filters, syringes and pipettes must be always of sterile grade and only unpacked inside the work area.
- Cell-culture wastes are disposed in autoclave sterilized bottles, neutralized with bleach and threw in the appropriate containers.

2.1.3. Cell culture: NIH-3T3 fibroblasts

The mouse embryonic fibroblast cell line NIH-3T3 (from ATCC, CRL-1658) has been selected for all the viability tests presented in this chapter. This cell line is abundantly used in material biocompatibility testing [2,6], thus, obtained results are readily comparable to

published data in the literature. The cells are disposed on 2D monolayers on flat dishes optimized for cell attachment and growth in a 5% CO_2 incubator at 37°C. Cells require carbohydrates, salts, amino acids, vitamins, fatty acids and proteins to survive *in vitro*. The basal medium used to provide these nutrients is DMEM (Dulbecco's Modified Eagle Medium, GIBCO) containing phenol red and a bicarbonate-based buffering system that in combination with a 5% CO_2 atmosphere allow to maintain the optimum pH between 7.2 and 7.4 and, at the same time, acts as a pH indicator (yellow: acid, purple: basic). The medium is complemented with a 10% of fetal bovine serum (FBS) containing proteins and growth factors, 1% of GlutaMAX supplement (GIBCO) and 1% of non-essential amino acids NEAA (GIBCO) giving the complete medium. The medium added to the cells has been always tempered in a thermostatic bath at 37ºC prior to use.

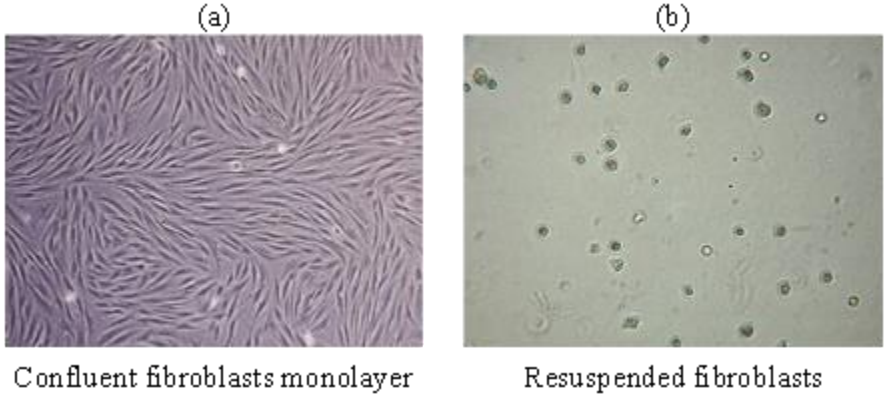

Figure 1: optical observation of fibroblast in different states.

Once the cells attach to the substrate of the flask, they start to divide and multiply to form a complete layer, commonly known as confluent layer (Figure 1a). Fibroblast cells become contact inhibited and stop growing or tend to form undesired multiple layers when they are close to the confluence. Thus, cells in culture should be ideally passaged when they are about 70-80% confluent. The passage of the cells (Figure 2) has been established every 3 days and it has been performed by adding 0.05% trypsin -EDTA (2 mg/mL) (Sigma-Aldrich) to detach the cells which are then resuspended in the complete medium (Figure 1b). A fraction of the resuspended cells (F_R) was then placed in a new flask for adherent cells and a new volume of fresh complete medium was added. The volumes of the different compounds and ratios applied during the cell subculturing are summarized in the Table 1.

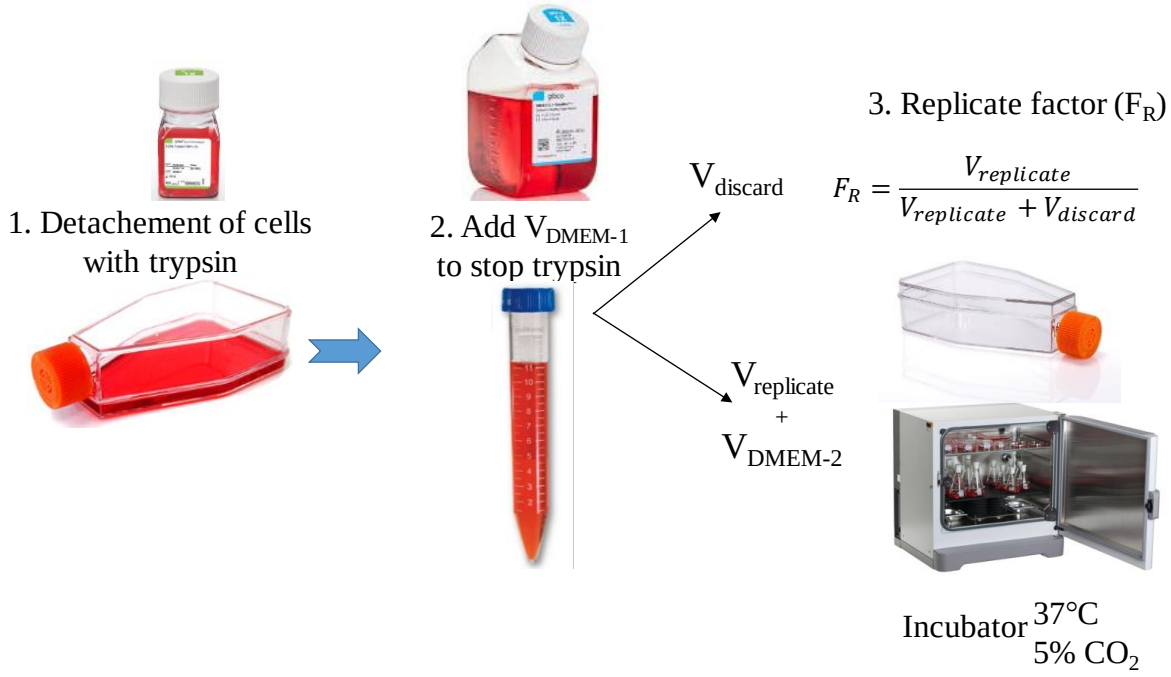

Figure 2: experimental protocol of cell culture subculturing.

Table 1: typical volumes and parameters used for the cell culture subculturing

A_{flask} (cm^2)	$V_{trypsin}$ (mL)	V_{DMEM-1} (mL)	V_{DMEM-2} (mL)	F_R	Time replicate (h)
75	1	7	15	1/10	72
25	0.5	3.5	5	1/10	72

2.1.4. Preparation of fibroblasts for cytotoxicity tests

Viability cell-based assays are often used for screening collections of compounds to determine if the test samples have effects on cell proliferation or show direct cytotoxic effects that eventually lead to cell death. To achieve that, a certain number of cells have to be attached on a support with a fixed area and treated with the studied compound. Since the cells are continuously dividing and multiplying, a control in which the cells are treated with DMEM, known as negative control, is required. Then the cytotoxicity is defined by comparison between the cells treated with the studied samples and the negative control. Moreover, the results of cell viability usually show an important variability and it is mandatory to perform a high number of repetitions for each condition and evaluated sample. For such purpose, the tests have been performed in the 96-well-plates with an area of 0.33 cm^2/well shown in Figure 4. The wells on the borders of the plate were not used since they often show abnormalities in the cell proliferation due to culture medium evaporation. The first column (green in Figure 3b) has been systematically used for the negative control and the remaining wells have been used for the studied samples (blue in Figure 3b) commonly organized by columns with 6 wells for identical samples.

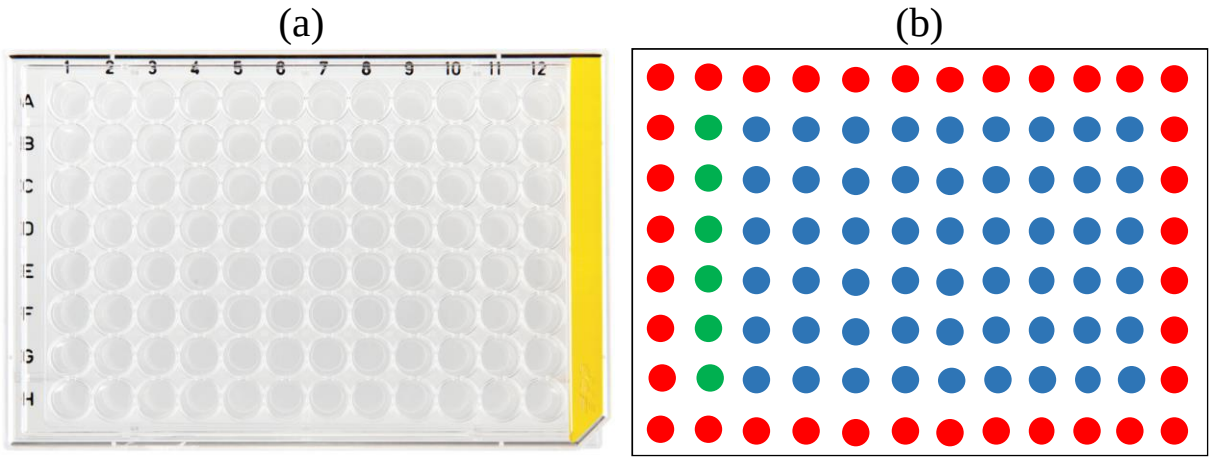

Figure 3: (a) tissue culture test plate with 96 wells (TPP) and (b) distribution of the wells in not used (red), negative control with basal medium (green) and evaluated samples (blue).

Thus, the first step is to deposite homogeneously in each of the plate wells 20.000 fibroblasts /well within 200 µL of complete medium. The concentration of cells (C_{cells}) has been determined using a counting grid (Figure 4) by the following equation:

$$C_{cells}(cells/\mu L) = \frac{n_1 + n_2 + n_3}{3} \times 10 \qquad (1)$$

where n_1, n_2 and n_3 are the quantity of cells counted by observation with an optical microscope in each of the big squares shown in red, green and blue colours in Figure 4.

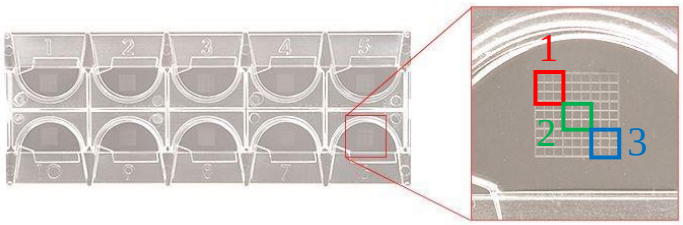

Figure 4: counting grid to determine the concentration of cells (C_{cells}) resuspended in culture medium.

Once the cell concentration has been determined, the appropriate volumes of cells and complete medium have been mixed in a Falcon tube. Finally, the cell suspension was deposited into a sterile vessel and a volume of 200 µL is transferred to each of the wells of the plate with a multichannel (6 wells/charge) micropipette, performing a mixing between each sampling and following a random filling of the wells to avoid the origination of patterns. The seeded 96-well-plate were then introduced in the incubator and cells were allowed to grow for 24 hours to ensure a homogeneous attachment before treatments.

2.1.5. Treatment of the cells with the studied samples

After 24 hours in the incubator, fibroblasts are completely attached covering the surface of each of the wells of the culture test plate as confirmed by optical microscopy. Thus, the medium can be aspirated leaving the attached cells in the plate and then filled with the samples.

Generally, the studied samples are dispersions of MNPs, polymers or mixtures of both in the culture medium The elaboration of the studied samples will be described individually further on. Once all the samples have been loaded in the wells, the culture plate is introduced again in the incubator at 37ºC and 5% CO_2 during and exposure time of 24 hours.

2.1.6. Measurement of cell activity: WST-1 assay

After the exposure time, the cells in each of the wells of the culture plate have evolved accordingly with the interactions with each of the studied samples. It is then required to apply a methodology to evaluate the number of active cells presented in each well, selecting for this study the WST-1 assay. WST-1 is a type of MTT assay consisting in a colorimetric method based in the ability of active cells, more precisely their mitochondrial dehydrogenases, to transform a tetrazolium salt in an insoluble formazan whose concentration can be quantified by absorbance measurements. Then, the larger is the number of viable cells, the higher is the activity of the mitochondrial dehydrogenases, and the greater the concentration of formazan dye determined by absorbance measurements. The step-by-step experimental protocol is listed below:

- At the end of the incubation, the samples have been aspirated from the different wells of the culture plate leaving only the attached cells and then, the cells have been washed with DMEM medium without phenol red twice to eliminate any possible sample residue.
- The WST-1 (Sigma-Aldrich) reagent has been diluted in DMEM without phenol red with a proportion 1/10 and 100 μL have been added in each wells.
- Cells were incubated during at least two hours to allow the transformation of the tetrazolium salt in formazan visually observed by an intense yellow coloration.
- The absorbance has been measured in a plate reader for the wavelengths 450 nm as well as at 630 nm as background.
- The cell viability for each well has been calculated as the difference of absorbance (A) at the two wavelengths (A_{450nm}-A_{630nm}).
- The normalized cell viability is determined individually for each sample well as the ratio between the cell viability of the sample and the mean cell viability of the negative control.

2.1.7. Data treatment

Each of the tested samples have been studied in at least 6 wells per plate and identical conditions and samples have been repeated 3 times with independent cell cultures to obtain confident results. After analysing several options for the data treatment based on the

determination of mean and confidence intervals and eliminating the outliers, it has been pointed that part of the obtained information has been lost during the analysis. Thus, it was decided to directly represent the experimental data in the form of boxplots of the cell viability normalized by the mean value of the negative control in which the data of each of the individual wells and the different plates are represented. In these plots (Figure 5), a box divided by a line at the median value represents the data from the lower to the upper quartile; corresponding to the limits that leave one quarter of the values below or above respectively. The upper and lower whiskers delimit the actual data points without considering the outliers which are the data outside 1.5 times the interquartile range (IQR). In addition, the mean value without considering the outliers has been added in the centre of the box.

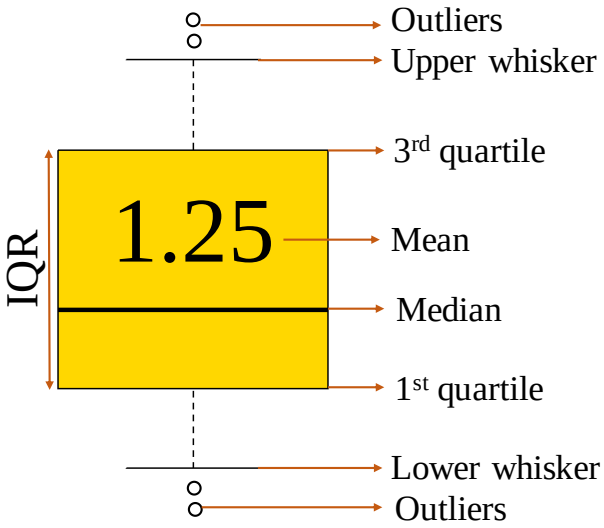

Figure 5: interpretation of the boxplot for the cell viability representation.

For statistical analysis, the experimental results were compared to their corresponding control values using an ANOVA with either Tukey's test to perform a multiple comparison or Dunnet's test to compare the result of each condition with the negative control. In all the cases a p value of < 0.05 was considered to be significant.

2.2. Cytotoxicity of the individual components

2.2.1. Introduction

The first step to test the biocompatibility of the studied nanocomposites is to evaluate the cytotoxicity of the two main individual components, sodium alginate polymer chains and citrated-MNPs. This evaluation has been carried out in NIH-3T3 fibroblasts following the experimental descriptions presented in the paragraph 2.1.

2.2.2. Sample preparation

The studied concentrations of citrated-MNPs have been selected according to the previous experiences in the BFA laboratory and were 1, 5, 10 and 20 μg/cm^2 [7,8]. The unit of concentration (μg/cm^2) represent the mass of particles per unit of area of the 2D monolayer of cells considered to be the area of each well of culture plate (0.33 cm^2), as particle tends to sediment. The samples have been prepared by mixing a volume of a concentrated aqueous dispersion of citrated-MNPs in the DMEM basal medium with only 3% of FBS to reduce interactions with the citrated-MNPs [9] named hereafter test medium. The volumes of the concentrated MNPs aqueous dispersions should be very small to avoid any effect on the dilution of the medium. In order to mix systematically the same volume of MNPs dispersion and test medium with a proportion 1:100 different intermediate aqueous dispersions of citrated-MNPs have been prepared with the concentrations shown in Table 2 from a MNPs stock dispersion with a concentration of 200 mg/mL. For the negative control, a volume of sterilized water was added to the test medium with the same proportion 1:100.

Table 2: studied concentrations of the citrated-MNPs and concentrations of the intermediate aqueous dispersions prepared from the stock dispersion (200 mg/mL).

C_{MNPs} studied (μg/cm^2)	**C_{MNPs} intermediate dispersion (mg/mL)**
20	6.60
10	3.30
5	1.65
1	0.33
Control	0

The selected concentrations of sodium alginate solutions (2.5, 5 and 10 g/L) were high enough to be in the concentrated regime with entangled polymer chains but low enough to have viscosities that allow their manipulation. Sodium alginate solutions with concentrations higher than 10 g/L (i.e., the concentration of 18 g/L selected for the elaboration of nanocomposites in the chapter IV) are too viscous to manipulate them correctly with the micropipettes used to load the samples in the culture plate. The samples have been prepared by dissolving a mass of sodium alginate powder in the test medium by magnetic stirring during 12 hours. The used sodium alginate powder (MP Biomedicals) is not a biological grade reagent and, as it has been proved in the literature [10–13], it can contain contaminants inducing adverse cell reactions or undesired and uncontrolled interactions with cells including endotoxins, protein contaminants,

elemental impurities and microbial bioburden [14]. To minimise the presence of these contaminants, two steps have been included that show experimentally good results in terms of contamination developed in the cell culture: (1) the sodium alginate powders have been sterilized by UV exposition for 20 minutes and (2) the test medium used for the preparation of sodium alginate solutions has been supplemented with a 1% of antibiotics (streptomycin and penicillin).

2.2.3. Cell viability results

Citrated-MNPs

The biocompatibility of the citrated-MNPs was tested with the cell viability WST-1 assay and the normalized results are presented in Figure 6. Whatever the concentration, there is a statistically significant decrease of the cell viability between citrated-MNPs treated cultures and the control culture. The toxicity is moderate as it never exceeds a 40% of fibroblast mortality even at the highest concentration of 20 μg/cm^2. The toxicity of iron oxide MNPs has been extensively studied in the literature but the results published are quite variable [15] including no toxicity [16], low toxicity [17] and moderate toxicity [18]. This can be explained by the dependence of toxicity on the selected cellular type and on several characteristics of the MNPs such as the shape, the hydrodynamic size, the magnetic saturation level or the type of coating or functionalization. For example, positively charged MNPs are more toxic, since they undergo interactions with the negatively charged cell membrane that increases their intracellular accumulation and affects cell membrane integrity [19]. Most of the authors relate the toxicity of iron oxide MNPs to their ability to damage DNA and induced oxidative stress [20] but also other mechanisms were described such as membrane leakage, impaired mitochondrial function, inflammation, formation of apoptotic bodies or chromosome condensation [4]. In comparison with the results found in the literature the moderate cytotoxicity found for citrated-MNPs seems reasonable taking into account their spherical shape and small size (8.6±0.1 nm) as determined by TEM and the good dispersion with small hydrodynamic sizes (9.5±3.1 nm) as determined by DLS measurements thanks to the strongly negative surface charge as presented in the Chapter I.

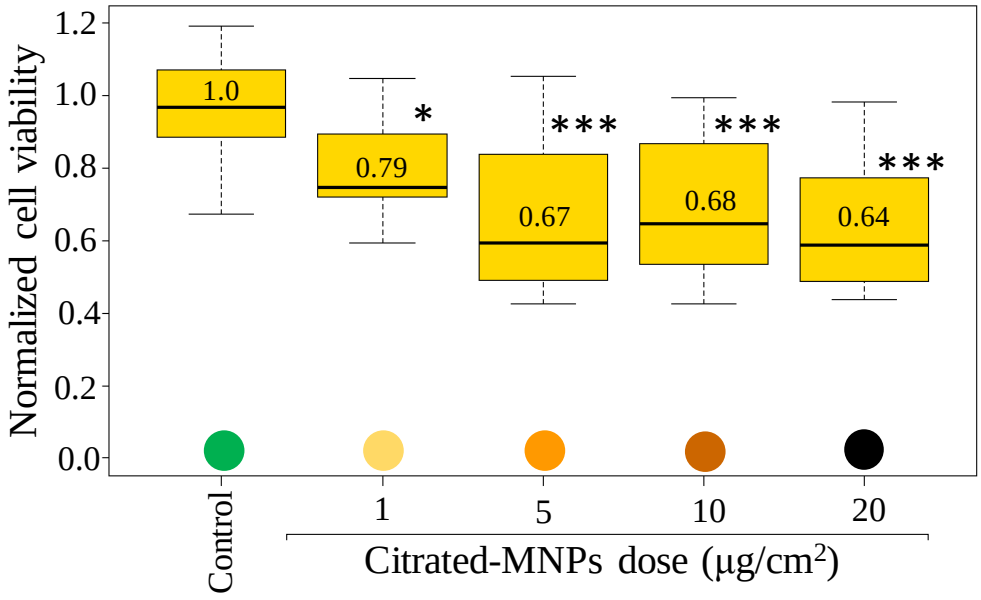

Figure 6: normalized cell viability of fibroblasts exposed to citrated-MNPs at different concentrations after 24 h of exposure (6 wells for each condition and 3 biological replicates). Significance indicated by * = p < 0.05, ** = p < 0.005 and *** = p < 0.0001, when sample treatments are compared by Dunnet's test to the control. The absence of symbol (*) means no statistically significant difference with the control.

Sodium alginate

The biocompatibility of sodium alginate was tested with the cell viability WST-1 assay and the normalized results are presented in Figure 7. There is no significant decrease of the viability of fibroblasts whatever the studied concentration. However, we observe at the lower concentration (2.5 g/L) a statistically significant increase of the viability. Sodium alginate is widely considered as a biocompatible material if it is purified appropriately [21]. The biocompatibility of a material is defined as the material property, which, after implantation in a living organism, does not produce adverse reactions and is accepted by the adjacent tissue [22]. Even if no *in vivo* studies are performed, a classical assumption is that an *in vitro* normalized cell viability value higher than 0.8 indicates good biocompatibility [23]. Thus, the studied sodium alginate solutions can be considered biocompatible in the range of studied concentrations. The increase of viability at a concentration of 2.5 g/L followed by a decrease until values close to the control at high concentration could be ascribed to the increase of viscosity as function of the sodium alginate concentration. For example, when the concentration of sodium alginate is increased from 2.5 to 10 g/L the viscosity increases from 12 to 147 mPa.s. Another explanation mentioned in the literature could be the role of proteins and polyphenolic compounds that frequently contaminate sodium alginate reagents [21].

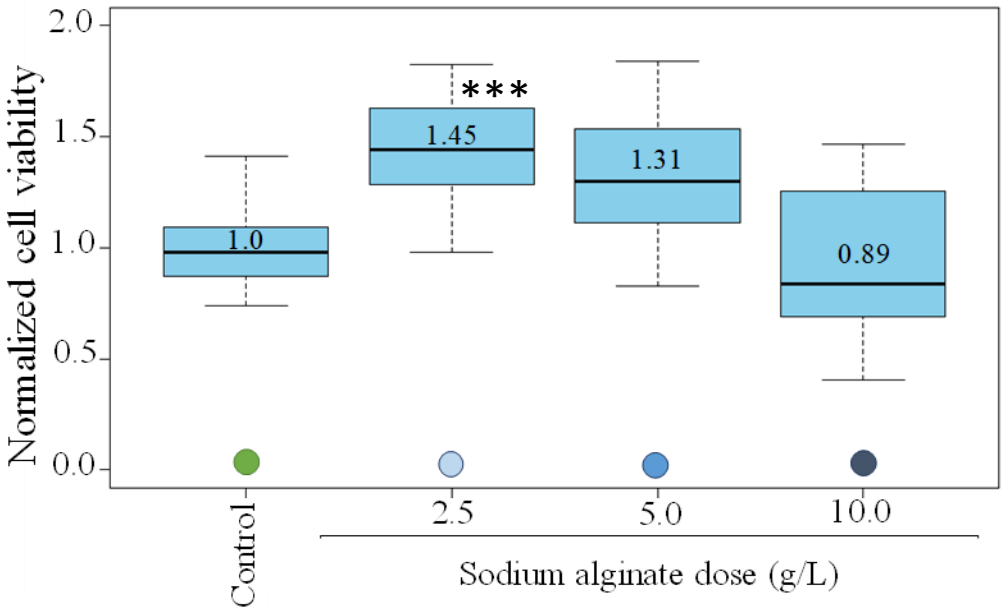

Figure 7: normalized cell viability of fibroblasts exposed to sodium alginate solutions at different concentrations after 24 h of exposure (6 wells for each condition and 3 biological replicates). Significance indicated by * = p < 0.05, ** = p < 0.005 and *** = p < 0.0001, when sample treatments are compared by Dunnet's test to the control. The absence of symbol (*) means no statistically significant difference with the control.

2.2.4. Conclusions

The biocompatibility of the main individual components for the elaboration of magnetic nanocomposites has been evaluated by *in vitro* cell viability WST-1 assay in mouse fibroblasts. In the one hand, the results obtained for citrated-MNPs show a moderate cytotoxicity even at the higher dose of 20 µg/cm^2. In the other hand, the results obtained for the sodium alginate solutions have confirmed its biocompatibility and the elimination of toxic compounds during the protocols applied for their sterilization. Moreover, a slight increase of the cell viability is observed for a concentration of sodium alginate of 2.5 g/L that comes back to a value similar to the negative control when the alginate dose is increased probably due to an important increase of the viscosity.

2.3. Cell viability of nanocomposite solutions

2.3.1. Introduction

In the nanocomposite solutions studied in the chapter IV, citrated-MNPs have been dispersed in an entangled polymer matrix either of sodium alginate (18 g/L) or PVA (100 g/L). A preliminary assumption is that sodium alginate and PVA are biocompatible polymers that can limit the moderate cytotoxicity observed in citrated-MNPs. However, polymers dissolved in the test medium at the concentrations used in the chapter IV imply high viscosities that can limit the positive effect of the biopolymers on the metabolic activity of the cells, as it has been

shown in the previous study of the cell viability of sodium alginate (Figure 7). In addition, the manipulation of solutions with high viscosity entails important difficulties for the sampling in the cell viability tests. Thus, the polymer concentrations used for the elaboration of nanocomposites in the chapter IV cannot be maintained for the cell viability tests and a concentration of 5 g/L has been selected.

2.3.2. Sample preparation

The same methodologies as for individual components (paragraph 2.2) have been used. Briefly, the polymer powders have been dissolved in the test medium by magnetic agitation and then a fixed volume of the aqueous MNPs dispersion with the concentrations presented in the Table 2 has been added and homogeneously dispersed with a vortex mixer. Cells were treated with polymer solutions (5 g/L) containing or not citrated-MNPs at different doses between 1 and 10 $\mu g/cm^2$.

2.3.3. Cell viability results

The results of the cell viability WST-1 assay obtained after exposure to polymer solutions at 5 g/L without and with citrated-MNPs at different doses are normalized and shown in Figures 8 and 9 for sodium alginate and PVA respectively.

For sodium alginate nanocomposite solutions (Figure 8), the addition of MNPs does not significantly change the cell viability leading to no statistically significant decrease for the dose of 1 and 5 $\mu g/cm^2$ compared to the control. However, at 10 $\mu g/cm^2$ we observe a slight but statistically significant decrease of viability compared to the control, but in all of the cases there is no significant differences compared to the sodium alginate solution without MNPs. Previously we found a cytotoxicity of the citrated-MNPs in the same range of concentrations (Figure 6). The decrease of the cytotoxicity of MNPs in sodium alginate can be explained by a lower diffusion of the particles due to the increment of viscosity of the basal medium induced by the entangled sodium alginate chains (1.2 mPa.s to 35.0 mPa.s) as observed in other nanoparticles with cytotoxicity negatively correlated with the viscosity of the media [24]. We can also notice a change on the cell viability of sodium alginate without citrated-MNPs from a mean value of 1.31 in Figure 7 to 0.83 for the actual results. The values obtained for the different wells and plates present also bigger variabilities leading to boxplots with larger intervals. This can be explained by the fact that experiments have been done in different periods with two different batches of sodium alginate powders and the different contaminants could change even if the specifications of the reagent were the same.

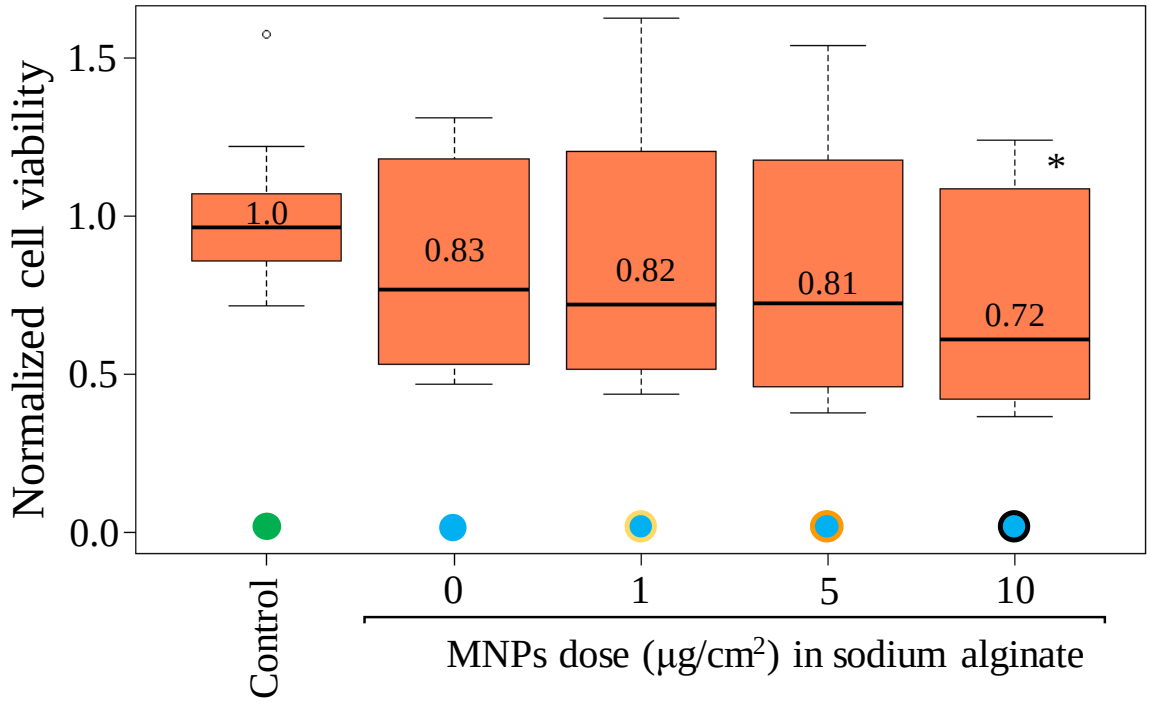

Figure 8: normalized cell viability of fibroblasts exposed to nanocomposites of sodium alginate solution (5 g/L) with different doses of citrated-MNPs after 24 h of exposure (6 wells for each condition and 3 biological replicates). Significance indicated by * = p < 0.05, ** = p < 0.005 and *** = p < 0.0001, when sample treatments are compared by Dunnet's test to the control. Significance indicated by + = p < 0.05, ++ = p < 0.005 and +++ = p < 0.0001, when the samples with different doses of MNPs added in the sodium alginate solution are compared by Dunnet's test to the sodium alginate solution without MNPs. The absence of symbol (* and +) means no statistically significant difference with the control or the sodium alginate solution respectively.

The PVA solution without MNPs shows a non-significant decrease of the viability of fibroblasts as well as sodium alginate at the same concentration of 5 g/L (Figure 9). However, the fibroblast viability is statistically decreased for all the studied concentrations of citrated-MNPs leading to a reduction of around 50% of the cell metabolic activity when compared to the control culture. Moreover, the significant decrease of the fibroblast viability is maintained for the MNPs concentrations of 5 and 10 µg/cm^2 in comparison to the culture with PVA solution without MNPs. Thus, by comparing the actual results of PVA nanocomposites (Figure 9) and those found for MNPs dispersions in test medium (Figure 6) it is observed that PVA solution with a concentration of 5 g/L is not effective to reduce the cytotoxic effect of the citrated-MNPs. This difference between PVA and sodium alginate can be explained by the smaller viscosity increase attained by the PVA at 5 g/L (1.5 mPa.s) in comparison to sodium alginate (35 mPa.s) related with the different concentration regimes determined in the chapter II Figures 16 and 17 for both polymers.

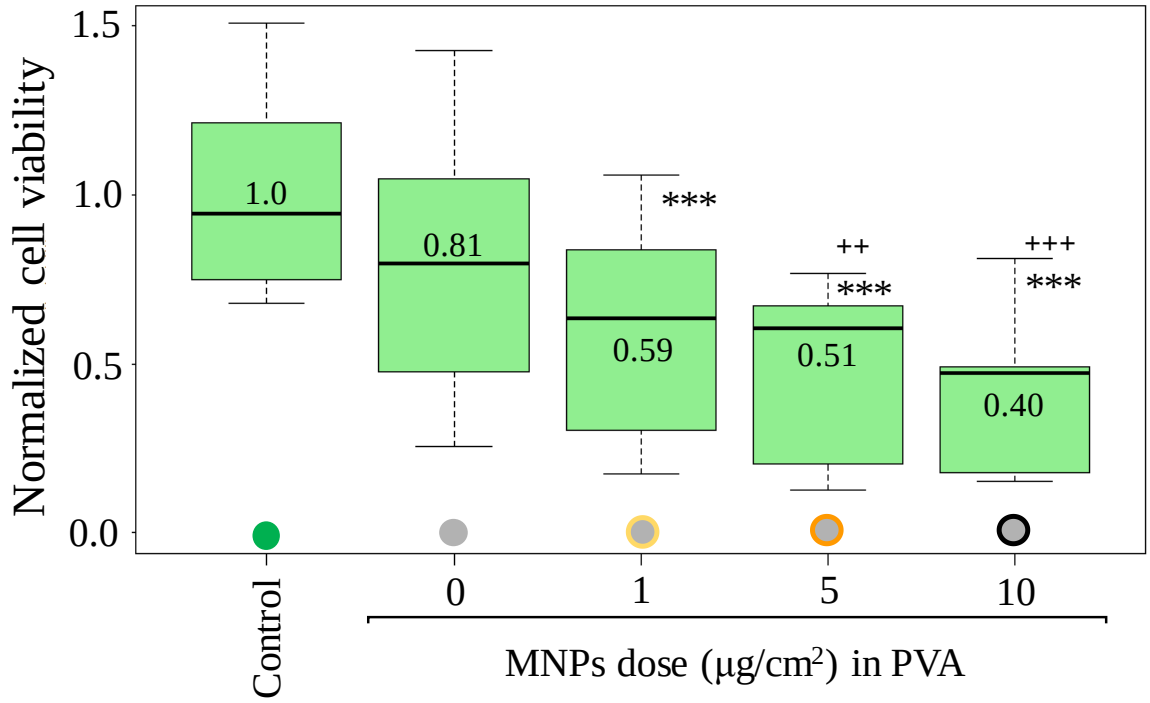

Figure 9: normalized cell viability of fibroblasts exposed to nanocomposites of PVA solution (5 g/L) with different doses of citrated-MNPs after 24 h exposure (6 wells for each condition and 3 biological replicates). Significance indicated by * = p < 0.05, ** = p < 0.005 and *** = p < 0.0001, when material treatments are compared by Dunnet's test to the control. Significance indicated by + = p < 0.05, ++ = p < 0.005 and +++ = p < 0.0001, when the samples with different doses of MNPs added in the PVA solution are compared by Dunnet's test to the PVA solution without MNPs. The absence of symbol (* and +) means no statistically significant difference with the control or the PVA solution respectively.

2.3.4. Conclusions

The biocompatibility of the magnetic nanocomposites elaborated and studied in the chapter IV consisting in the dispersion of citrated-MNPs in aqueous polymer solutions of either sodium alginate or PVA has been evaluated by *in vitro* cell viability WST-1 assay in mouse fibroblast cells. In the one hand, the introduction of citrated-MNPs in the sodium alginate solution in the test medium (5 g/L) decreases their cytotoxic effect. This could be explained by the decrease of diffusion of MNPs to the cells due to the increase of viscosity since, in these conditions, sodium alginate forms an entangled solution in the concentrated regime (Figure 10b). In the other hand, the introduction of citrated-MNPs in the PVA solution in test medium (5 g/L) leads to a decrease of the fibroblasts viability attributed to the moderate cytotoxicity of citrated-MNPs shown in Figure 6. This can be explained by the negligible increase of viscosity of the PVA at 5g/L since, in this conditions, PVA chains are isolated ones from the others in the diluted regime (Figure 10c).

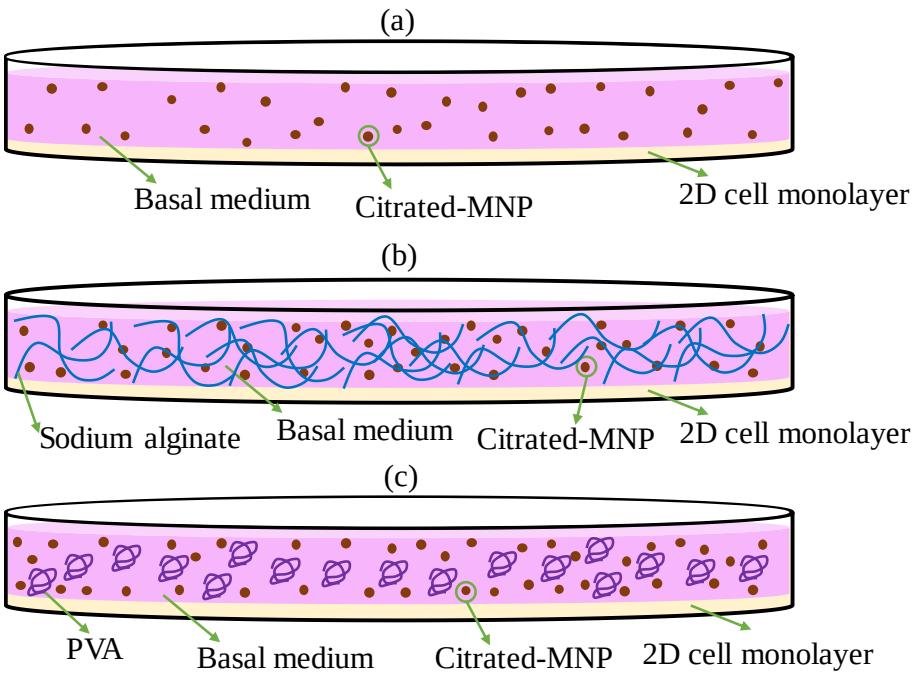

Figure 10: schematic representation of a well of the cell viability test plate to evaluate the cytotoxicity of: (a) citrated-MNPs, (b) sodium alginate 5 g/L + citrated-MNPs nanocomposite solution and (c) PVA 5g/L + citrated-MNPs nanocomposite solution.

2.4. Cell viability of nanocomposite hydrogels

2.4.1. Introduction

The applied methodology to study the individual components and the nanocomposite solutions can no longer be applied to the hydrogel samples since the crosslinked network will not allow the transfer of nutrients to the 2D cell monolayer and can induce a negative compressive effect. Then, the following methods are proposed to evaluate the biocompatibility in the hydrogel state.

2.4.2. Experimental methodology: direct contact method

The first alternative for the evaluation of the cytotoxicity of nanocomposite hydrogels is to develop a direct contact methodology. As recommended in the literature [5], a small piece of gel sample covering approximately the 20 % of a well plate has been placed on the NIH-3T3 cell monolayer and complete medium has been added in the surroundings. However, the changes of density of the nanocomposite hydrogels depending on the crosslinking degree and the loading or not of citrated-MNPs change the interactions with the cell monolayer. In some cases, the nanocomposites apply a load on the cells inhibiting the transfer of nutrients while in other cases they float in the medium losing the contact with the cells changing dramatically their effect on the cell viability. Therefore, no results are presented for this methodology

keeping as future prospect to develop a methodology to homogenize the contact between cells and nanocomposite hydrogel fragments.

2.4.3. Experimental methodology: extraction method

Due to the experimental difficulties found with the direct contact method the following extraction method has been used as alternative. This strategy is based on the evaluation of the cytotoxicity of any leachable byproducts that could be released for the nanocomposite hydrogel after immersion in test medium. It is an extensive procedure to evaluate crosslinked biomaterials by the simulation of clinical application [25]. For the present case, an important number of compounds can be released such as MNPs, citrate ions or non-crosslinked polymer chains. The procedure begins with the elaboration of calcium alginate and PVA nanocomposite hydrogels following the experimental methodologies presented in the Chapter III paragraph 2.1 with different ratios of calcium (R_{Ca} = 0.2, 0.3, 0.4) and number of freezing/thawing cycles (N_c = 1, 2, 3) respectively to modulate the degree of crosslinking. For each case, pre-gels without citrated-MNPs and with a volume fraction Φ_{MNPs} = 0.5% have been prepared. Then, 3 g of each sample have been placed in a Petri dish (diameter = 22 mm) and the corresponding crosslinking procedure has been carried out as described in chapter III. Some examples of hydrogels with and without citrated-MNPs are shown in Figure 11. The samples have been then rinsed with 5 mL of basal medium to eliminate irregularities in the surface before adding 15 mL of test medium without phenol red and to incubate them during 48h at 37ºC and 5% CO_2. At the end of the incubation period, the test medium after contact with the samples named as extracts have been collected for the evaluation of their iron content and cytotoxicity.

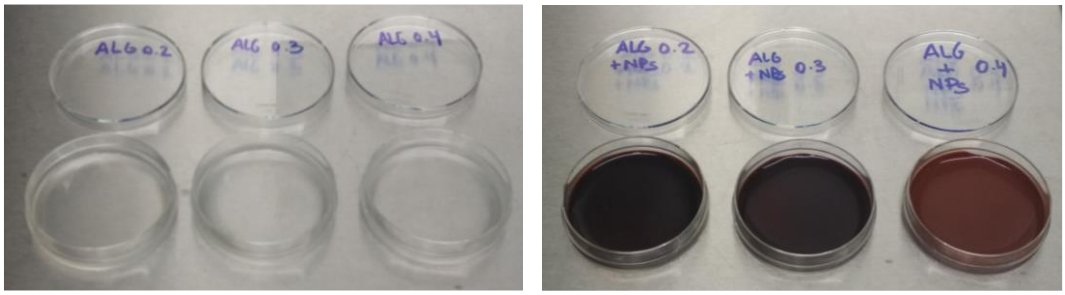

Figure 11: calcium alginate hydrogels without (left) and with (right) citrated-MNPs Φ_{MNPs} = 0.5% and different ratios of calcium (R_{Ca} = 0.2, 0.3, 0.4) before the addition of test medium.

2.4.4. Extracts iron content

The values of iron content in the different extracts have been determined by inductively-couple plasma (ICP) spectroscopy with a detection limit below 50 ppm performed in collaboration with the laboratory ITODYS (Université de Paris). The results for the extracts

collected after contact with the different hydrogel nanocomposites with Φ_{MNPs} = 0.5% and different degrees of crosslinking are shown in the Table 3. The iron content of the extracts collected from the hydrogels without MNPs have been measured to confirm the negligible iron content in the DMEM but are not shown because the values are lower than the detection limit of the technique. The results show that in all the nanocomposite hydrogels a significant amount of citrated-MNPs was released from the hydrogel network to the culture medium after 48h of contact. The amount of MNPs released is smaller for the calcium alginate than for the PVA matrices and in both cases, it decreases as the crosslinking degree is increased. The calculated values of maghemite dose ($C_{Fe_2O_3}$ - Table 3) exceed the limit of citrated-MNPs dose with measurable values of cytotoxicity established in the paragraph 2.2.3. Thus, the samples have been diluted 10 and 100 times in test medium for the calcium alginate and PVA nanocomposites respectively to be in the order of magnitude of the iron doses shown in Figure 6.

Table 3: iron content of the extracts from nanocomposite hydrogels with Φ_{MNPs} = 0.5% and polymer matrices of calcium alginate (Alg) and PVA with different degrees of crosslinking controlled by the ratio of calcium (R_{Ca}) and the number of freezing-thawing cycles (N_c).

Matrix	C_{Fe-ICP} **(mg/L)**	$C_{Fe_2O_3}$**(µg/cm²)**
Alg - R_{Ca} = 0.2	233	202
Alg - R_{Ca} = 0.3	144	124
Alg - R_{Ca} = 0.4	58	50
PVA - N_c = 1	2778	2407
PVA - N_c = 2	1454	1260
PVA - N_c = 3	481	417

2.4.5. Cell viability results

The normalized viability of fibroblasts exposed to the media collected after contact with the different hydrogel samples are shown in Figures 12 and 13 for calcium alginate and PVA matrices respectively. The extracts from hydrogels without MNPs (HY) do not induce significant decrease in cell viability compared to the negative control cultured with test medium independently of the crosslinking degree for both polymers (mean normalized cell viabilities close or higher than 1). This demonstrates that the reagents used for the crosslinking of sodium alginate ($CaCO_3$ and GDL) do not show a toxic effect. For PVA, there is only statistically significant increase of the viability of fibroblasts for the higher crosslinking degree compared to the control showing that, since the crosslinking occurs without the addition of reagents, no toxic compounds are released form the PVA network.

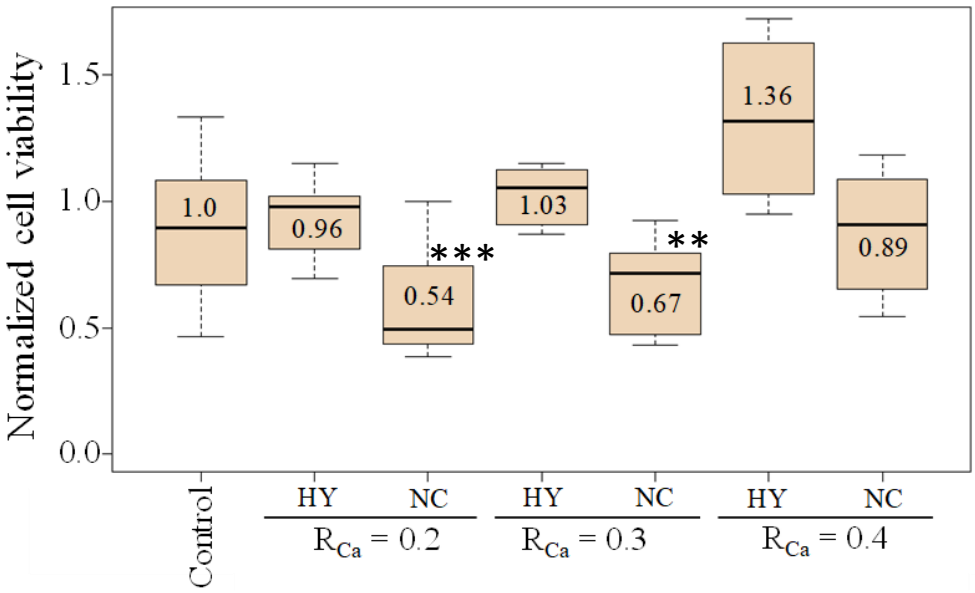

Figure 12: normalized cell viability of fibroblasts exposed to extracts of the calcium alginate hydrogels without MNPs (HY) and with Φ_{MNPs} = 0.5% (NC) with three different ratios of calcium (R_{Ca}) (6 wells for each condition and 3 biological replicates). Significance indicated by * = p < 0.05, ** = p < 0.005 and *** = p < 0.0001, when sample treatments are compared by Tukey's test to the control. The absence of symbol (*) means no statistically significant difference with the control.

The fibroblast viability after exposure to the extracts of nanocomposites with Φ_{MNPs} = 0.5% (NC) shows that calcium alginate nanocomposite hydrogels present a cytotoxic effect (Figure 12) while, surprisingly, no cytotoxic effect is found for PVA nanocomposite hydrogels (Figure 13). According to the values of the concentrations of citrated-MNPs deduced by dilution 10 and 100 times from the measured values by ICP (for Figure 12: 5.0, 12.4 and 20.2 μg/cm^2 and for Figure 13: 4.2, 12.6 and 24.1 μg/cm^2), a moderate cytotoxicity is expected assigned to the release of citrated-MNPs. In principle, this cytotoxicity should be similar to the one obtained for dispersions of citrated-MNPs in test medium seen in Figure 6 since the extracts have similar concentrations of MNPs. This expected behaviour is in a good agreement with the R_{Ca}-dependent cytotoxicity of calcium alginate nanocomposites (Figure 12). For higher R_{Ca} the network has a higher crosslinking degree releasing lower amount of MNPs and therefore presenting lower cytotoxicity. This cytotoxic effect should be related with the amount of MNPs released since the values of the mean cell viability with MNPs doses between 20.2 and 5.0 μg/cm^2 are very similar to those determined previously for equivalent concentrations of citrated-MNPs as observed in Figure 14. However, for PVA matrices, even with similar concentrations of MNPs, the cell viability does not significantly change in comparison to the negative control (mean normalized cell viabilities close or higher than 1 in Figure 13). This lack of toxic effect of citrated-MNPs released from the PVA nanocomposites can be explained by the coating of MNPs with PVA chains probably due to H-bonding between the hydroxyl groups of PVA and the carboxylate groups of citrate ions adsorbed in the surface of the citrated-MNPs.

Similar decrease of cytotoxicity is found in other studies for PVA coated maghemite MNPs [26].

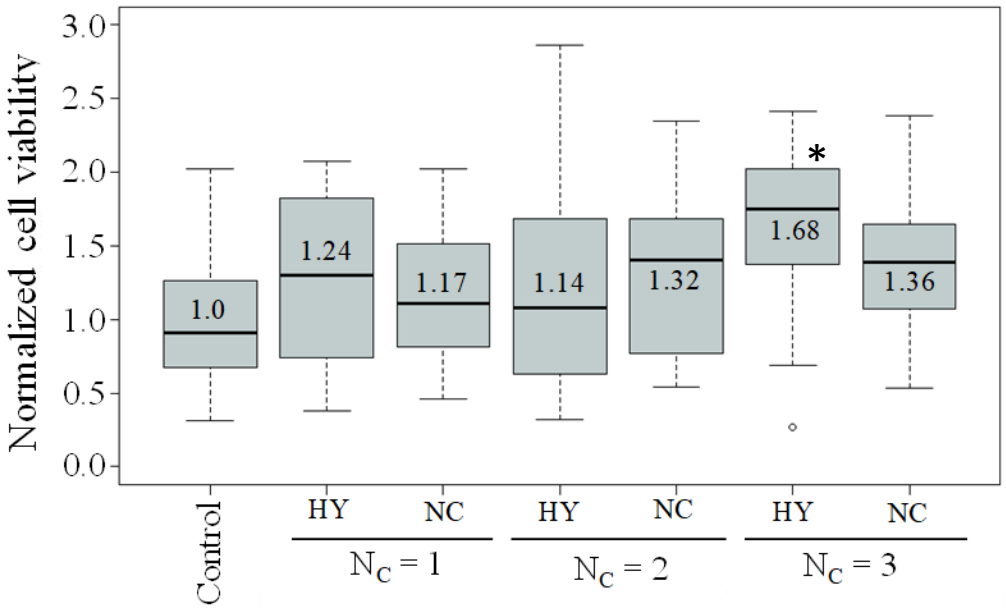

Figure 13: normalized cell viability of fibroblasts exposed to the extracts of PVA hydrogels without MNPs (HY) and with Φ_{MNPs} = 0.5% (NC) with three different number of freezing/thawing cycles (N_c) (6 wells for each condition and 3 biological replicates). Significance indicated by * = p < 0.05, ** = p < 0.005 and *** = p < 0.0001, when sample treatments are compared by Tukey's test to the control. The absence of symbol (*) means no statistically significant difference with the control.

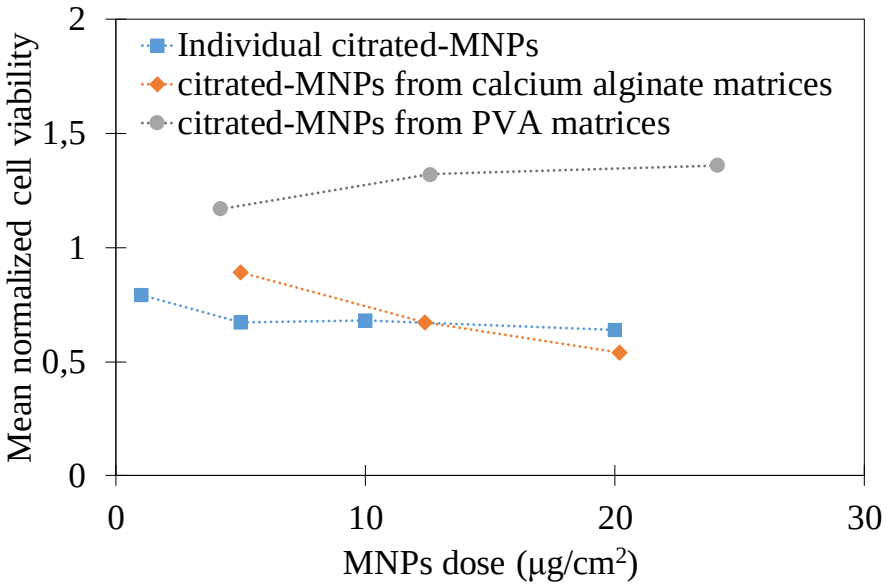

Figure 14: concentration-dependence of the normalized cell viability of fibroblasts exposed to citrated-MNPs released from the polymer matrices in comparison with individual MNPs.

2.4.6. Conclusions

The biocompatibility of the nanocomposite hydrogels studied in the chapter V has been evaluated by *in vitro* cell viability tests of the extracts collected after incubation of the hydrogels in the culture medium. Extracts obtained from both PVA and calcium alginate hydrogels

without MNPs show excellent biocompatibility with cell viabilities similar or slightly higher than the negative control cultured with fresh test medium. However, when the citrated-MNPs are loaded in those hydrogels with a volume fraction Φ_{MNPs} = 0.5% a high amount of the particles has been released by immersion in test medium leading to a potential cytotoxicity. The amounts of citrated-MNPs released are higher for the PVA than for calcium alginate and matrices and for both they decrease with the increase of the crosslinking degree (R_{Ca} or N_c) as determined by ICP spectroscopy. In addition, the results of cell viability of the media containing the released citrated-MNPs show important differences depending on the nature of the polymer matrix. For calcium alginate, a similar cytotoxic effect is found than for individual citrated-MNPs dispersed in the test medium, while for PVA matrices the cytotoxicity of the released MNPs is blocked probably due to the coating of the particles with PVA chains that acts as a barrier against the interactions of the MNPs with the cells.

3. Conclusions

The biocompatibility of the magnetic nanocomposites elaborated and studied in the previous chapters have been evaluated by *in vitro* cell viability studies with fibroblast NIH-3T3 by the WST-1 assay. The tests performed on the individual components have confirmed the biocompatibility of sodium alginate and they have shown a moderate cytotoxic effect of citrated-MNPs. By the evaluation of the cell viability of nanocomposites elaborated by dispersing the citrated-MNPs in two polymers (PVA and sodium alginate) in the form of solutions and hydrogels with different crosslinking degrees, the following conclusions for the elaboration of biocompatible nanocomposites could be deduced:

- The viscosity of the medium surrounding the cells plays an important role in the diffusion of MNPs. A sodium alginate solution in culture medium with a concentration of 5 g/L leads to a value of the viscosity of 35 Pa.s that seems suitable to decrease the diffusion of citrated-MNPs and shows a slightly increase of the viability of fibroblasts (Figure 7).
- The immersion in test medium of nanocomposites crosslinked using the protocols proposed in the chapter V shows an important release of citrated-MNPs that makes them toxic for cells. To avoid that, the parameters linked with the crosslinking degree (R_{Ca} for calcium alginate and N_c for PVA) should be increased for future studies.
- An interesting strategy has been found to decrease the cytotoxicity of the MNPs based on the interactions with the polymer chains of the matrices that can be attached to the particle surface blocking the adverse interactions with cells. This effect has been found for

citrated-MNPs dispersed in PVA matrices, but other similar strategy could be developed with calcium alginate hydrogels by a modification of the functionalization of the MNPs.

4. References

[1] J.M. Saul, D.F. Williams, CHAPTER 35 - Hydrogels in Regenerative Medicine, in: A. Atala, R. Lanza, J.A. Thomson, R. Nerem (Eds.), Princ. Regen. Med. Second Ed., Academic Press, San Diego, 2011: pp. 637–661. https://doi.org/10.1016/B978-0-12-381422-7.10035-5.

[2] S.-R. Ryoo, Y.-K. Kim, M.-H. Kim, D.-H. Min, Behaviors of NIH-3T3 Fibroblasts on Graphene/Carbon Nanotubes: Proliferation, Focal Adhesion, and Gene Transfection Studies, ACS Nano. 4 (2010) 6587–6598. https://doi.org/10.1021/nn1018279.

[3] J.M. Anderson, 9.19 - Biocompatibility, in: K. Matyjaszewski, M. Möller (Eds.), Polym. Sci. Compr. Ref., Elsevier, Amsterdam, 2012: pp. 363–383. https://doi.org/10.1016/B978-0-444-53349-4.00229-6.

[4] N. Singh, G.J.S. Jenkins, R. Asadi, S.H. Doak, Potential toxicity of superparamagnetic iron oxide nanoparticles (SPION), Nano Rev. 1 (2010) 5358. https://doi.org/10.3402/nano.v1i0.5358.

[5] J.-L. Pariente, B.-S. Kim, A. Atala, In vitro biocompatibility assessment of naturally derived and synthetic biomaterials using normal human urothelial cells, J. Biomed. Mater. Res. 55 (2001) 33–39. https://doi.org/10.1002/1097-4636(200104)55:1<33::AID-JBM50>3.0.CO;2-7.

[6] M. McLaughlin, M.J. Earle, M.A. Gîlea, B.F. Gilmore, S.P. Gorman, K.R. Seddon, Cytotoxicity of 1-alkylquinolinium bromide ionic liquids in murine fibroblast NIH 3T3 cells, Green Chem. 13 (2011) 2794–2800. https://doi.org/10.1039/C0GC00813C.

[7] M. Delaval, W. Wohlleben, R. Landsiedel, A. Baeza-Squiban, S. Boland, Assessment of the oxidative potential of nanoparticles by the cytochrome c assay: assay improvement and development of a high-throughput method to predict the toxicity of nanoparticles, Arch. Toxicol. 91 (2017) 163–177. https://doi.org/10.1007/s00204-016-1701-3.

[8] A. Kermanizadeh, S. Vranic, S. Boland, K. Moreau, A. Baeza-Squiban, B.K. Gaiser, L.A. Andrzejczuk, V. Stone, An in vitro assessment of panel of engineered nanomaterials using a human renal cell line: cytotoxicity, pro-inflammatory response, oxidative stress and genotoxicity, BMC Nephrol. 14 (2013) 96. https://doi.org/10.1186/1471-2369-14-96.

[9] H.T.R. Wiogo, M. Lim, V. Bulmus, L. Gutiérrez, R.C. Woodward, R. Amal, Insight into Serum Protein Interactions with Functionalized Magnetic Nanoparticles in Biological Media, Langmuir. 28 (2012) 4346–4356. https://doi.org/10.1021/la204740t.

[10] A. Jork, F. Thürmer, H. Cramer, G. Zimmermann, P. Gessner, K. Hämel, G. Hofmann, B. Kuttler, H.-J. Hahn, O. Josimovic-Alasevic, K.-G. Fritsch, U. Zimmermann, Biocompatible alginate from freshly collected Laminaria pallida for implantation, Appl. Microbiol. Biotechnol. 53 (2000) 224–229. https://doi.org/10.1007/s002530050012.

[11] Z. Wj, L. C, H. A, S. J, Purity of alginate affects the viability and fibrotic overgrowth of encapsulated porcine islet xenografts., Transplant. Proc. 33 (2001) 3517–3519. https://doi.org/10.1016/s0041-1345(01)02419-8.

[12] M.L. Torres, J.M. Fernandez, F.G. Dellatorre, A.M. Cortizo, T.G. Oberti, Purification of alginate improves its biocompatibility and eliminates cytotoxicity in matrix for bone tissue engineering, Algal Res. 40 (2019) 101499. https://doi.org/10.1016/j.algal.2019.101499.

[13] G. Klöck, H. Frank, R. Houben, T. Zekorn, A. Horcher, U. Siebers, M. Wöhrle, K. Federlin, U. Zimmermann, Production of purified alginates suitable for use in immunoisolated transplantation, Appl. Microbiol. Biotechnol. 40 (1994) 638–643. https://doi.org/10.1007/BF00173321.

[14] T. Andersen, P. Auk-Emblem, M. Dornish, 3D Cell Culture in Alginate Hydrogels, Microarrays. 4 (2015) 133–161. https://doi.org/10.3390/microarrays4020133.

[15] L. Arias, J. Pessan, A. Vieira, T. Lima, A. Delbem, D. Monteiro, L.S. Arias, J.P. Pessan, A.P.M. Vieira, T.M.T. de Lima, A.C.B. Delbem, D.R. Monteiro, Iron Oxide Nanoparticles for Biomedical Applications: A Perspective on Synthesis, Drugs, Antimicrobial Activity, and Toxicity, Antibiotics. 7 (2018) 46. https://doi.org/10.3390/antibiotics7020046.

[16] L.H.A. Silva, J.R. da Silva, G.A. Ferreira, R.C. Silva, E.C.D. Lima, R.B. Azevedo, D.M. Oliveira, Labeling mesenchymal cells with DMSA-coated gold and iron oxide nanoparticles: assessment of biocompatibility and potential applications, J. Nanobiotechnology. 14 (2016) 59. https://doi.org/10.1186/s12951-016-0213-x.

[17] R.P. Friedrich, J. Zaloga, E. Schreiber, I.Y. Tóth, E. Tombácz, S. Lyer, C. Alexiou, Tissue Plasminogen Activator Binding to Superparamagnetic Iron Oxide Nanoparticle—Covalent Versus Adsorptive Approach, Nanoscale Res. Lett. 11 (2016) 297. https://doi.org/10.1186/s11671-016-1521-7.

[18] S. Rajiv, J. Jerobin, V. Saranya, M. Nainawat, A. Sharma, P. Makwana, C. Gayathri, L. Bharath, M. Singh, M. Kumar, A. Mukherjee, N. Chandrasekaran, Comparative cytotoxicity and genotoxicity of cobalt (II, III) oxide, iron (III) oxide, silicon dioxide, and aluminum oxide nanoparticles on human lymphocytes in vitro, Hum. Exp. Toxicol. 35 (2016) 170–183. https://doi.org/10.1177/0960327115579208.

[19] S.C. Hong, J.H. Lee, J. Lee, H.Y. Kim, J.Y. Park, J. Cho, J. Lee, D.-W. Han, Subtle cytotoxicity and genotoxicity differences in superparamagnetic iron oxide nanoparticles coated with various functional groups, Int. J. Nanomedicine. 6 (2011) 3219–3231. https://doi.org/10.2147/IJN.S26355.

[20] M. Mahmoudi, A. Simchi, A.S. Milani, P. Stroeve, Cell toxicity of superparamagnetic iron oxide nanoparticles, J. Colloid Interface Sci. 336 (2009) 510–518. https://doi.org/10.1016/j.jcis.2009.04.046.

[21] G. Orive, A.M. Carcaboso, R.M. Hernández, A.R. Gascón, J.L. Pedraz, Biocompatibility Evaluation of Different Alginates and Alginate-Based Microcapsules, Biomacromolecules. 6 (2005) 927–931. https://doi.org/10.1021/bm049380x.

[22] R. Mihai, I. Florescu, V. Coroiu, A. Oancea, M. Lungu, In vitro biocompatibility testing of some synthetic polymers used for the achievement of nervous conduits, J. Med. Life. 4 (2011) 250–255.

[23] Magnetic Cell Separation, Volume 32 - 1st Edition, (n.d.). https://www.elsevier.com/books/magnetic-cell-separation/zborowski/978-0-444-52754-7 (accessed July 9, 2021).

[24] M. Bayal, P. Janardhanan, E. Tom, N. Chandran, S. Devadathan, D. Ranjeet, U. Unniyampurath, R. Pilankatta, S.S. Nair, Cytotoxicity of nanoparticles - Are the size and shape only matters? or the media parameters too?: a study on band engineered ZnS nanoparticles and calculations based on equivolume stress model, Nanotoxicology. 13 (2019) 1005–1020. https://doi.org/10.1080/17435390.2019.1602678.

[25] M.O. Wang, J.M. Etheridge, J.A. Thompson, C.E. Vorwald, D. Dean, J.P. Fisher, Evaluation of the In Vitro Cytotoxicity of Cross-Linked Biomaterials, Biomacromolecules. 14 (2013) 1321–1329. https://doi.org/10.1021/bm301962f.

[26] M. Mahmoudi, A. Simchi, M. Imani, M.A. Shokrgozar, A.S. Milani, U.O. Häfeli, P. Stroeve, A new approach for the in vitro identification of the cytotoxicity of superparamagnetic iron oxide nanoparticles, Colloids Surf. B Biointerfaces. 75 (2010) 300–309. https://doi.org/10.1016/j.colsurfb.2009.08.044.

Conclusions and perspectives

We have elaborated and characterized at different scales magnetic sensitive materials to progress in the understanding of soft sensitive composites until their evaluation of biocompatibility. For such purpose, we propose a methodology to elaborate magnetic nanocomposites combining polymer matrices of different natures with functionalized magnetic nanoparticles (MNPs) of maghemite (γ-Fe_2O_3) by an *ex-situ* method in which aqueous polymer solutions and MNPs dispersions are separately prepared and then mixed followed by the crosslinking to elaborate nanocomposite hydrogels.

The first step is the selection, elaboration and characterization of the individual components. In the one hand, the synthesis and characterization of the MNPs by two different methodologies lead to the production of high quality maghemite MNPs either covalently grafted with 3-Aminopropylphosphonic acid (APPA) bearing positive surface charge or stabilized by adsorption of citrate ions with negative surface charge. In the other hand, two polymers (PVA and sodium alginate) have been chosen based on a rheological study that highlights the importance of the characteristics at molecular level (chain stiffness and interactions between monomers) on the conformation of polymers in aqueous solution and therefore on their structural and viscoelastic properties. Then, the microstructure of sodium alginate aqueous solutions has been revealed through a multi-scale viscoelastic investigation combining different complementary experimental methods finding the range of concentrations to have entangled solutions with a mesh size similar to the size of the synthetized MNPs.

During the second step, hydrogels are elaborated from sodium alginate and PVA by crosslinking with Ca^{2+} or by freezing thawing cycles respectively discussing the effect of several experimental parameters to modulate their mechanical and structural properties. Firstly, the study of the sol-gel transition of calcium alginate hydrogels by time-resolved mechanical spectroscopy (TRMS) leads to the modulation of the kinetics and the properties of the critical hydrogel by the selection of the source of calcium and the amount of added calcium (R_{Ca}). Then, the determination of the compressive Young modulus (E) and the study of the swelling for the totally gelled hydrogels allow to correlate their stiffness and porosity to the changes of the crosslinking degree of the networks that can be modulated either by R_{Ca} for calcium alginate hydrogels or by the number of freezing/thawing cycles (N_c) for PVA hydrogels.

The third step is focused on the importance of the polymer-particle interaction for the elaboration of nanocomposites. Thus, MNPs either grafted with double ligand (APPA-MNPs) or stabilized by adsorption of citrate ions (citrated-MNPs) are introduced in a polyelectrolyte sodium alginate solution and in a neutral polymer PVA solution. For the three studied nanocomposite solutions we have found the conditions to obtain a fluid that is homogeneous on macroscopic scales while it is diphasic on microscopic ones, containing a microstructure that responds to an external magnetic field inducing an enhancement of the mechanical properties of the nanocomposites. This magnetic enhancement depends on both the magnetic forces that orientate the microstructures in the direction of the magnetic field perpendicular to the shear flow and the interactions between polymer chains and MNPs. More precisely we have shown a microstructure of aggregates due to the electrostatic attraction between the positively charged APPA-MNPs and negatively charged sodium alginate chains while the modification of ionic strength due to free citrate ions (not adsorbed in the MNPs surface) lead to the formation of droplets of demixion with citrated-MNPs.

The final magnetic nanocomposite hydrogels have been then elaborated in the fourth step by the addition of citrated-MNPs in calcium alginate and PVA hydrogels respectively. The sol-gel transition of calcium alginate nanocomposite hydrogels is firstly studied by TRMS finding an important increase of the gelation times as well as the obtention of softer critical gels and lower elastic modulus at long times (G'_∞) in the presence of citrated-MNP. The effect of an applied magnetic field on the sol-gel transition have been then studied for the first time showing a modulation of the viscoelastic properties before the gel point but no effect on the properties of the gel network formed at the gel point. Moreover, the mechanical and structural properties of the previous calcium alginate and new PVA nanocomposite hydrogels totally gelled have been investigated. The obtained results of shear viscoelastic properties, compressive Young modulus and swelling are all in good agreement confirming a decrease of the stiffness and the crosslinking degree when citrated-MNPs are introduced in the calcium alginate matrix. In contrast the introduction of citrated-MNPs in the PVA matrix increases the stiffness of the formed network that could be explained by H-bonding between particle and polymer.

Finally, the biocompatibility of the magnetic nanocomposites has been evaluated by *in vitro* cell viability studies in fibroblast NIH-3T3 by the WST-1 assay. This analysis allows to identify two experimental conditions of their elaboration to improve their biocompatibility: (1) sodium alginate solutions with a concentration of 5 g/L in culture medium prevent the interactions of the citrated-MNPs with the fibroblast cells decreasing their cytotoxicity and (2) the increase of the parameters to modulate the crosslinking degree of hydrogels are necessary

to prevent the release of citrated-MNPs when the hydrogel nanocomposites are immersed in the culture medium. Moreover, it has been found that the hydrogen-bonding between hydroxyl groups in PVA nanocomposite hydrogels lead to the coating of the citrated-MNPs with PVA chains decreasing their cytotoxicity.

Most cell culture studies *in vitro* of the literature are performed using cells cultured as 2D monolayers on hard plastic surfaces because of the ease, convenience and high cell viability associated with this culture method [1]. For the present case, the studies performed in cells cultured as 2D monolayers have led to the selection of the most promising methodologies for the elaboration of biocompatible magnetic hydrogels and to the understanding of the effect of the elaboration conditions on the biological entities. However, nearly all cells that make up tissue reside in an extracellular matrix (ECM) consisting in a complex 3D fibrous meshwork of collagen and elastic fibres embedded in a highly hydrated gel-like material of glycosaminoglycans, proteoglycans and glycoproteins [2]. Thus, 3D systems are biologically more relevant, and the results obtained in 3D culture studies will provide for a future work cellular responses that will be of higher biological relevance. For this purpose, a first strategy can be applied thanks to the interesting properties of calcium alginate hydrogels. They can be made to match the elasticity of most types of tissues including all types of soft tissue [3]. According to the studies performed in the previous chapters, nanocomposites with calcium alginate matrices with controlled mechanical properties can be elaborated to fit the mechanical requirements of different cell types. A preliminary attempt to seed fibroblast cells in the surface of alginate hydrogels has been done observing the formation of spherical fibroblast aggregates not attached to the hydrogel network. This can be explained by the fact that most of the cells have no receptors that recognize alginate, and then not allowing their attachment, proliferation and differentiation within alginate hydrogels. An interesting perspective could be the use of signalling molecules like RGD peptide [4] or fibronectin [5] to modify the alginate hydrogels allowing the attachment of fibroblasts.

Another possible strategy could be to study the cytotoxicity of nanocomposites by direct interaction with 3D models elaborated with other kind of matrices. A first contact has been done with the Centre of Nanotechnology and Tissue Engineering of the Photobiology and Photomedicine research Group (São Paulo University) where an interesting type of 3D models are elaborated. This later are composed of embedded fibroblasts in a matrix of collagen named 3D skin model based on the methodology firstly proposed by Bell *et al.* [6]. The studied nanocomposites can be placed in direct contact with this dermal equivalent during a certain exposure time. During this time the different components of the nanocomposite (mainly MNPs

due to their small size) can be diffused to the 3D skin model interacting with the embedded fibroblasts. Then, the cytotoxicity can be studied based on the characterization of the 3D skin model after the treatment either by a histological analysis to study the diffusion of the MNPs from the nanocomposites to the 3D model and the existing cells [7] or by confocal microscopy to study the fibroblasts morphology contained in the 3D model after the treatment.

[1] T. Andersen, P. Auk-Emblem, M. Dornish, 3D Cell Culture in Alginate Hydrogels, Microarrays. 4 (2015) 133–161. https://doi.org/10.3390/microarrays4020133.

[2] M. Lewandowska-Szumieł, S. Rumiński, 14 - Cellular response to biocomposites, in: L. Ambrosio (Ed.), Biomed. Compos. Second Ed., Woodhead Publishing, 2017: pp. 335–356. https://doi.org/10.1016/B978-0-08-100752-5.00015-9.

[3] D.E. Discher, D.J. Mooney, P.W. Zandstra, Growth Factors, Matrices, and Forces Combine and Control Stem Cells, Science. 324 (2009) 1673–1677. https://doi.org/10.1126/science.1171643.

[4] J. Rowley, G. Madlambayan, D. J. Mooney, Alginate Hydrogels As Synthetic Extracellular Matrix Materials, Biomaterials. 20 (1999) 45–53. https://doi.org/10.1016/S0142-9612(98)00107-0.

[5] J. Candiello, S.S. Singh, K. Task, P.N. Kumta, I. Banerjee, Early differentiation patterning of mouse embryonic stem cells in response to variations in alginate substrate stiffness, J. Biol. Eng. 7 (2013) 9. https://doi.org/10.1186/1754-1611-7-9.

[6] E. Bell, B. Ivarsson, C. Merrill, Production of a tissue-like structure by contraction of collagen lattices by human fibroblasts of different proliferative potential in vitro., Proc. Natl. Acad. Sci. U. S. A. 76 (1979) 1274–1278.

[7] K. Rowatt, R.E. Burns, S.F. Jr, D.M. Long, A combination Prussian blue – hematoxylin and eosin staining technique for identification of iron and other histological features, J. Histotechnol. 41 (2018) 29–34. https://doi.org/10.1080/01478885.2017.1417696